

**Quantification Of Total Alkyl Nitrates And Peroxy Nitrates Using  
Thermal Dissociation Cavity Attenuated Phase Shift Spectroscopy  
(TD-CAPS)**

A Dissertation  
Presented to  
The Academic Faculty

by

Gamze Eris

In Partial Fulfillment  
of the Requirements for the Degree  
Doctor of Philosophy in the  
School of Chemical and Biomolecular Engineering

Georgia Institute of Technology  
[August 2020]

**COPYRIGHT © 2021 BY GAMZE ERIS**

**QUANTIFICATION OF TOTAL ALKYL NITRATES AND PEROXY  
NITRATES USING THERMAL DISSOCIATION CAVITY  
ATTENUATED PHASE SHIFT SPECTROSCOPY (TD-CAPS)**

Approved by:

Dr. Nga Lee (Sally) Ng, Advisor  
School of Chemical & Biomolecular  
Engineering  
*Georgia Institute of Technology*

Dr. L. Gregory Huey, Committee  
Member  
School of Earth and Atmospheric  
Sciences  
*Georgia Institute of Technology*

Dr. Christopher W. Jones, Committee  
Member  
School of Chemical & Biomolecular  
Engineering  
*Georgia Institute of Technology*

Dr. Rodney J. Weber, Committee  
Member  
School of Earth and Atmospheric  
Sciences  
*Georgia Institute of Technology*

Dr. J. Carson Meredith, Committee Member  
School of Chemical & Biomolecular  
Engineering  
*Georgia Institute of Technology*

Date Approved: [April 30, 2020]

[To my family]

## ACKNOWLEDGEMENTS

First, I would like to thank my advisor Dr. Sally Ng for her guidance, encouragement, supervision and support throughout my graduate study. She introduced me a field of atmospheric aerosols and provided me with many opportunities such as operating instruments, working with different collaborators, presenting my research, where I learned valuable communication skills. Besides opportunities on the scientific research, she also guided about professional development including critical thinking and time management. I am grateful for her support throughout my difficult times.

I would also like to thank my committee members, Dr. L. Gregory Huey, Dr. Rodney J. Weber, Dr. Christopher W. Jones and Dr. J. Carson Meredith for their valuable time, useful comments and suggestions, which helped me investigate different perspectives regarding my research project and keep me focused on the bigger picture. Dr. L. Gregory Huey and Dr. David Tanner have been incredibly generous and supportive about the use of their laboratory equipment and in the construction of the instrument I have been building. The knowledge I gained from our discussions has been extremely valuable in the completion of this dissertation.

I would like to acknowledge my former and current group members for their support in my research and their company throughout these past five years. I would like to thank Masayuki Takeuchi for valuable discussions at different projects, laboratory and field campaigns, where we gained a lot of experiences and support each other. Yunle Chen has been a great company and gave me moral support through difficult times. Taekyu Joo was great at sharing responsibilities about parenting duties in the laboratory. Jean Rivera-Rios discussed about my project and offered support on my paper. Wing Tuet taught me to play piano, made

us great cookies. Thomas Berkemeier, Yuchen Wang, Fobang Liu and Weiqi Xu have been great to work with.

I would also like to thank to my friends Akshay Korde, Trisha Sen, Simple Kumar and Qandeel Almas, Ezgi Dogan Guner for all the enjoyable time we shared throughout these years. I would like to thank specially to my best friend, Sireesha Aluri for her great love and friendship.

Finally, I would like to thank family for their endless love and support throughout my life. They have always been there, listening to my problems, providing encouragement, and celebrating my achievements. Without their support, none of this work would have been possible.

# TABLE OF CONTENTS

<b>ACKNOWLEDGEMENTS</b>	<b>iv</b>
<b>LIST OF TABLES</b>	<b>viii</b>
<b>LIST OF FIGURES</b>	<b>ix</b>
<b>LIST OF SYMBOLS AND ABBREVIATIONS</b>	<b>xi</b>
<b>SUMMARY</b>	<b>xiv</b>
<b>CHAPTER 1. Introduction</b>	<b>iv</b>
1.1 Atmospheric organic aerosols	1
1.2 Formation and Fate of alkyl nitrates and peroxy nitrates	3
1.3 Motivation, Scope and Overview	6
<b>CHAPTER 2 Development and Characterization of TD-CAPS</b>	<b>7</b>
2.1 Background	7
2.2 Instrument Setup	12
2.3 Characterization of Potential Chemical Interferences	16
2.3.1 Chemical Interference for IPN due to Presence of NO <sub>x</sub>	16
2.3.2 Chemical Interference for PAN due to Presence of NO <sub>x</sub>	21
2.3.3 Numerical Simulations and Peroxy Radical Wall Losses	25
2.3.4 NO <sub>2</sub> Loss due to O <sub>3</sub> Thermal Decomposition Chemical Interference for IPN due to Presence of NO <sub>x</sub>	27
2.3.5 NO <sub>2</sub> Formation from O <sub>3</sub> and NO Chemical Interference for PAN due to Presence of NO <sub>x</sub>	30
2.3.6 Expression of Correction Factors and the Total Uncertainty	33
2.4 Chamber Experiment Measurements with TD-CAPS Characterization of Potential Chemical Interferences	39
2.4.1 TD-CAPS and HR-TOF-CIMS Comparison	40
2.4.2 TD-CAPS and HR-TOF-AMS Comparison	44
2.4.3 Partitioning Coefficient	47
<b>CHAPTER 3 Summary and Future Work</b>	<b>49</b>
<b>Appendix A. Supplementary for Chapter 2</b>	<b>51</b>
<b>Appendix B. Kinetic modelling of formation and evaporation of SOA from NO<sub>3</sub> oxidation of pure and mixed monoterpenes</b>	<b>60</b>
<b>Appendix C. An omnipresent diversity and variability in the chemical composition of atmospheric functionalized organic aerosol</b>	<b>138</b>
<b>REFERENCES</b>	<b>235</b>



## LIST OF TABLES

Table 2-1 Summary of Fit Equations and Uncertainties

34

## LIST OF FIGURES

Figure 1.1	Formation of secondary organic aerosol from oxidation of volatile organic compounds	3
Figure 1.2	Alkyl nitrate and peroxy nitrate formation	5
Figure 2.1	NO <sub>x</sub> cycle	8
Figure 2.2	Thermal Dissociation - Cavity Attenuated Phase Shift Spectroscopy (TD-CAPS) setup	13
Figure 2.3	Measurements of the difference signal (sampling from the 653K – reference channel) over IPN concentration when adding different amounts of NO to IPN	18
Figure 2.4	Measurements of the difference signal (sampling from the 653K – reference channel) over IPN concentration when adding different amounts of NO <sub>2</sub> to IPN.	20
Figure 2.5	Measurements of the difference signal (sampling from the 473K – reference channel) over PAN concentration when adding different amounts of NO to PAN.	22
Figure 2.6	Measurements of the difference signal (sampling from the 473K – reference channel) over PAN concentration when adding different amounts of NO <sub>2</sub> to PAN.	24
Figure 2.7	NO <sub>2</sub> Measurements at 653 K channel when adding different amounts of NO <sub>2</sub> to O <sub>3</sub> .	29
Figure 2.8	NO <sub>2</sub> Measurements at Reference channel, 473K channel and 653 K channel when adding different amounts of NO to O <sub>3</sub> .	32
Figure 2.9	Detection limit of TD-CAPS	37
Figure 2.10	NO, NO <sub>2</sub> and O <sub>3</sub> Time series at the chamber experiment where $\alpha$ -pinene is oxidized by HONO	41
Figure 2.11	Time series of gON obtained by TD-CAPS and C <sub>x</sub> H <sub>y</sub> N <sub>1-2</sub> O <sub>z</sub> by FIGEARO-CIMS	43
Figure 2.12	Scatter Plot of gON measured with TD-CAPS and AMS FIGEARO-CIMS a) 5.1 Hz/ppt b) 8 Hz/ppt	44

Figure 2.13	a) Time series of pON measured with TD-CAPS and AMS b) Scatter Plot of pON measured with TD-CAPS and AMS	47
Figure 2.14	Particle/Gas Ratio changing with the organic mass	48
Figure A. 1	Temperature profiles used in kinetic box model.	51
Figure A. 2	IPN and PAN Thermograms	51
Figure A. 3	Upper: Gas Phase TD-CAPS Setup Below: Particle Phase TD-CAPS Setup	52
Figure A. 4	Difference of NO <sub>2</sub> production from photolysis of acetone/CO/air mixture from acetone/CO/air mixture with the presence of NO	53
Figure A. 5	NO <sub>2</sub> Loss due to O <sub>3</sub> thermal decomposition	54
Figure A. 6	NO <sub>2</sub> Loss due to O <sub>3</sub> thermal decomposition where O <sub>3</sub> concentration range is 109-288 ppb and NO <sub>2</sub> concentration range is 75-196 ppb	54
Figure A. 7	Relative standard deviation of AN at 0-200 ppb NO and 0-200 ppb NO <sub>2</sub>	55
Figure A. 8	Relative standard deviation of PN at 0-200 ppb NO and 0-200 ppb NO <sub>2</sub>	55
Figure A. 9	Measurements of the difference signal (sampling from the 653K – reference channel) over IPN concentration when adding different amounts of NO to IPN at different times	56

## LIST OF SYMBOLS AND ABBREVIATIONS

AN	Alkyl nitrate
API-MS	Atmospheric Pressure Ionization Mass Spectrometry
BVOCs	Biogenic volatile organic compounds
C <sub>10</sub> H <sub>16</sub>	Monoterpene
C <sub>15</sub> H <sub>24</sub>	Sesquiterpenes
C <sub>5</sub> H <sub>8</sub>	Isoprene
CCN	Cloud condensation nuclei
CH <sub>3</sub> I	Methyl iodide
EPA	Environmental Protection Agency
EURAD-IM	European Air pollution and Dispersion-Inverse Model
F0AM	Framework for 0-D Atmospheric Modeling
FIGAERO	Filter Inlet for Gases and Aerosols
FTIR	Fourier Transform Infrared Spectroscopy
gAN	Gas phase alkyl nitrate
GC	Gas Chromatography
GC-ECD	Gas Chromatography Coupled with Electron Capture Detection
GC-MS	Gas Chromatography Coupled with Mass Spectrometry
gPN	Gas phase peroxy nitrate
GTEC	Georgia Tech Environmental Chamber
H <sub>2</sub> SO <sub>4</sub>	Sulfuric acid
HNO <sub>3</sub>	Nitric acid
HONO	Nitrous acid

HPLC	High-Pressure Liquid Chromatography
HR-ToF-AMS	High-Resolution Time-of-Flight Aerosol Mass Spectrometer
HR-ToF-CIMS	High-Resolution Time-of-Flight Chemical-Ionization Mass Spectrometer
IMR	Ion-molecule reaction
IPN	Isopropyl nitrate
MCM	Master of Chemical Mechanisms
$(\text{NH}_4)_2\text{SO}_4$	Ammonium sulfate
$\text{N}_2\text{O}_5$	Dinitrogen pentoxide
NAAQS	National Ambient Air Quality Standards
$\text{NaNO}_2$	Sodium Nitrite
NO	Nitrogen monoxide
$\text{NO}_2$	Nitrogen dioxide
$\text{NO}_3\cdot$	Nitrate radical
$\text{NO}_x$	Nitrogen oxides
$\text{NO}_y$	total reactive nitrogen
$\text{O}_3$	Ozone
OA	Organic aerosol
$\text{OH}\cdot$	Hydroxyl radical
PAN	Peroxy acetyl nitrate
PM	Particulate matter
PN	Peroxy nitrate
POA	Primary organic aerosol
pON	Particle-phase organic nitrate
PTR-MS	Proton Transfer Reaction Mass Spectrometry

$R_1=R_2$	Unsaturated hydrocarbons
R-H	Saturated hydrocarbons
RMSE	Root mean square error
$RO_2$	Peroxy radical
$RO_2NO_2$	Peroxy nitrate
$RONO_2$	Alkyl nitrate
SEAC4RS	Studies of Emissions and Atmospheric Composition, Clouds, and Climate Coupling by Regional Surveys
SMPS	Scanning Mobility Particle Sizer
SOAS	Southern Oxidant and Aerosol Study
TD	Thermal dissociation
TD-CAPS	Thermal dissociation Cavity Attenuated Phase Shift Spectroscopy
TD-CIMS	Thermal dissociation Chemical Ionization Mass Spectrometry
TD-CRDS	Thermal dissociation Cavity Ring-down Spectrometer
TD-LIF	Thermal dissociation Laser Induced Fluorescence
VOCs	Volatile organic compounds
$\sigma$	Standard deviation
$\Sigma NO_{y,i}$	sum of speciated reactive nitrogen compounds

## SUMMARY

Particulate matter or atmospheric aerosols are liquid or solid particles suspended in the air. The contribution of organic nitrates to total organic aerosols is found to be substantial from measurements conducted at various ambient sites worldwide. Alkyl nitrates (AN) and peroxy nitrates (PN), are temporary  $\text{NO}_x$  reservoirs in the troposphere, therefore understanding the formation and fate of organic nitrates is critical to determine global and regional distributions of  $\text{NO}_x$ , its cycling and impact on  $\text{O}_3$  and secondary organic aerosol production. Accurately measuring AN and PN has been challenging because they exist in low concentrations and are structurally distinct. To measure total AN and PN, a thermal dissociation (TD) inlet is typically coupled with various  $\text{NO}_y$  detection techniques such as Chemical Ionization Mass Spectrometry (TD-CIMS), Laser Induced Fluorescence (TD-LIF), Cavity Ring-down Spectrometer (TD-CRDS) and Cavity Attenuated Phase Shift Spectroscopy (TD-CAPS). TD-CAPS is advantageous since the CAPS monitor is commercially available, easy to setup and use, and requires little maintenance. Ambient measurements by TD-CAPS have been recently conducted in a remote region. However, characterization of the instrument regarding interference from other atmospheric constituents is limited. The overall objective of the propose work is to develop TD-CAPS instrument that can measure total AN and PN in gas and particle phase by making use of the thermal decomposition of these compounds. The instrument consists of two quartz tube reactors at 563 K and 473 K (enabling decomposition of AN and PN, respectively, to  $\text{NO}_2$ ) and a reference channel that measures the ambient  $\text{NO}_2$ . The  $\text{NO}_2$  concentration in each channel is measured by a CAPS monitor. The difference of  $\text{NO}_2$  between channels is used

to derive AN and PN concentration. We identified and quantified potential chemical interferences from side reactions due to presence of atmospheric constituents such as O<sub>3</sub>, NO and NO<sub>2</sub> using isopropyl nitrate (IPN) and peroxy acetyl nitrate (PAN) as representative AN and PN compounds. We compare the accuracy of our tool with the accuracy of existing/established measuring instruments by producing secondary organic aerosol in Georgia Tech Environmental Chamber (GTEC) facility. Total gas phase and particle phase AN and PN are measured with the addition of Teflon filter and activated carbon denuder to the TD-CAPS inlet. Our results show that measurements of total particle-phase AN and PN made with the TD-CAPS correlate strongly with measurements by the High-Resolution Time-of-Flight Aerosol Mass Spectrometer (HR-ToF-AMS). The measurement of total gas phase AN and PN with TD-CAPS agrees with High-Resolution Time-of-Flight Chemical-Ionization Mass Spectrometer (HR-ToF-CIMS) after accounting for measurement uncertainties in each instrument. The direct measurements of gas-phase and particle-phase organic nitrates allow us to calculate their bulk partitioning coefficients, an important parameter determining SOA formation and AN/PN fate.

# CHAPTER 1. INTRODUCTION

## 1.1 Atmospheric organic aerosols

Particulate matter or atmospheric aerosols are liquid or solid particles suspended in air. They have significant impact on climate, air quality and human health. Depending on the properties, particulate matter impacts the climate directly by scattering or absorbing solar radiation. For instance, some constituents like sulfate scatters the radiation whereas some materials like soot absorbs the radiation. It also influences the climate indirectly by acting as cloud condensation nuclei (CCN) (Kanakidou et al. 2005). In 1990, the Clean Air Act was amended to require Environmental protection Agency (EPA) to set National Ambient Air Quality Standards (NAAQS) for pollutants harmful for public health and the environment. Particulate matter (PM) is one of the six criteria pollutants. The 24 hour average standard concentration for PM 2.5 ( $<2.5 \mu\text{g}/\text{m}^3$ ) and PM 10 ( $<10 \mu\text{g}/\text{m}^3$ ) are set as  $35 \mu\text{g}/\text{m}^3$  and  $150 \mu\text{g}/\text{m}^3$  respectively.(2016) Moreover, Global Burden of Disease Study (GBD 2015) showed that the ambient particulate matter pollution is 5<sup>th</sup> risk factor causing premature death (Pinault 2017). However, in order to fully understand the its effect climate, air quality and health, detailed studies are required to understand sources, loading, composition and properties of particulate matter.

Organic aerosol (OA) is a major constituent of submicron particulate matter based on the ambient measurements such as from Aerosol Mass Spectrometer data in 37 field campaigns in the midlatitudes of the northern hemisphere which shows SOA accounts for

64%-95% of total OA on average (Zhang et al. 2007). Organic aerosol is classified into two categories due to differences in how they are formed. Primary organic aerosol (POA) is emitted directly into the atmosphere such as biomass burning, cooking, and vehicle exhaust (Hildebrandt et al. 2011). Secondary organic aerosol (SOA) is formed by the condensation of low volatility products from the oxidation of volatile organic compounds (VOCs). (Figure 1.1) SOA can also be formed from reaction of compounds in the condensed phase. (Robinson et al. 2007). A large fraction of organic aerosol is SOA therefore understanding their formation and fate is critical to address the scientific problems (Hallquist et al. 2009). The source of the VOC can be biogenic, mainly from vegetation and soil. Globally, ~90% of total nonmethane VOC emissions is biogenic VOC emissions ( $\sim 1150 \text{ TgCyr}^{-1}$ ) which consists of 44% isoprene ( $\text{C}_5\text{H}_8$ ), 11% monoterpenes ( $\text{C}_{10}\text{H}_{16}$ ), 22.5% other reactive VOC, and 22.5% other VOC (Goldstein and Galbally 2007; Guenther et al. 1995; Guenther et al. 2012). Large emissions of the  $\text{C}_5\text{H}_8$ ,  $\text{C}_{10}\text{H}_{16}$  along with sesquiterpenes ( $\text{C}_{15}\text{H}_{24}$ ) and their high reactivity with main atmospheric oxidants ozone ( $\text{O}_3$ ), hydroxyl radical (OH) and nitrate radicals ( $\text{NO}_3$ ) makes these VOCs important precursors for gas phase oxidation and thus total SOA mass. VOC can be anthropogenic, that emissions are related to transportation, industries, businesses, homes is formed from the condensation of gas phase oxidation products (Takeuchi and Ng 2018).

The contribution of organic nitrates to total OA is found to be substantial from measurements conducted at various field campaign sites in the different seasons (Ng et al. 2017). Aircraft (SEAC4RS) and ground-base (SOAS) campaigns that are done in Southeast US in Summer 2013 gives information about the speciated and total organic nitrates

derived from the biogenic VOCs and their impact on  $\text{NO}_x$  (Fisher et al. 2016; Lee et al. 2016). A year later, particle phase organic nitrates are estimated to be 5–12 % based on High Resolution Time of Flight Aerosol Mass Spectrometer (HR-ToF-AMS) measurements in summer in the southeastern USA (Xu et al. 2015b). Kiendler-Scharr et al. measured pON using AMS across Europe and compared observations with results from the European Air pollution and Dispersion-Inverse Model (EURAD-IM) chemistry transport model in to evaluate the regional extent of their results. (Kiendler-Scharr et al. 2016) They concluded that 34% to 44% fraction of measured submicron aerosol nitrate is organic nitrate.

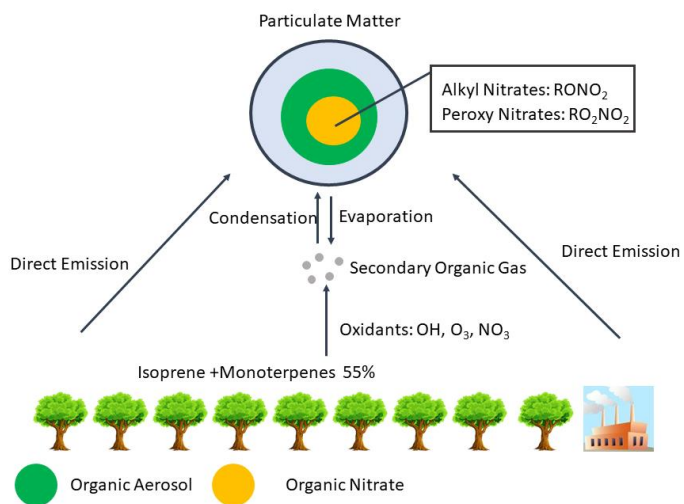


**Figure 1.1 Formation of secondary organic aerosol from oxidation of volatile organic compounds**

## 1.2 Formation and Fate of alkyl nitrates and peroxy nitrates

Organic nitrate is defined as compounds with molecular structure of  $\text{RONO}_2$  in some studies (Day et al. 2010; Rollins et al. 2009) whereas in some studies organic nitrate is used for compounds with a chemical formula of  $\text{RONO}_2$  and  $\text{RO}_2\text{NO}_2$  (Lee et al. 2016).  $\text{RONO}_2$  and  $\text{RO}_2\text{NO}_2$  compounds are also called as alkyl nitrate and peroxy nitrate, respectively. The detailed and simplified formation mechanisms of major organic nitrate derived from biogenic VOCs have been reported in previous studies (Ng et al. 2017; Perring, Pusede and Cohen 2013; Roberts 1990). Figure 1.2 shows the organic nitrate formation in daytime and nighttime. During daytime, organic nitrate is formed from the reaction between organic peroxy radicals ( $\text{RO}_2^\bullet$ ), formed from the mainly OH oxidation of VOC, and  $\text{NO}_x$ . OH radical reacts with saturated hydrocarbons (R-H) by H abstraction and produce R radical which immediate reacts with  $\text{O}_2$  to form  $\text{RO}_2^\bullet$ . OH radical reacts with unsaturated hydrocarbons ( $\text{R}_1=\text{R}_2$ ) by OH addition and produce  $\text{R}_1(\text{OH})\text{-R}_2$  radical which reacts with  $\text{O}_2$  to generate a peroxy radical  $\text{R}_1(\text{OH})\text{-R}_2\text{O}_2$ . The resulting peroxy radicals reacts with NO to produce  $\text{RONO}_2$  or RO radical depending on the abundance of VOC and  $\text{NO}_x$ . Branching ratio, ratio of reaction rate of  $\text{RONO}_2$  to the total of  $\text{RONO}_2$  or RO production, is important to find out the efficiency of  $\text{RONO}_2$  production and is found to be between 0.1-35%. Another mechanism proposed for  $\text{RONO}_2$  production is reaction of  $\text{RO}_2$  with NO.  $\text{RO}_2$  reacts with NO and forms an unstable peroxy nitrate which later decompose to RO and  $\text{NO}_2$  or forms  $\text{RONO}_2$  through unimolecular rearrangement. In the presence of  $\text{NO}_2$ ,  $\text{RO}_2$  reacts with  $\text{NO}_2$  to form  $\text{RO}_2\text{NO}_2$ .  $\text{RO}_2\text{NO}_2$  can be classified into two groups depending on the structure of  $\text{RO}_2$ .  $\text{RO}_2\text{NO}_2$  that has acyl group next to the peroxy group,  $\text{R}'\text{C}(\text{O})\text{OO}$ , is called peroxy acyl nitrates and also denoted as peroxyacetylnitric

anhydrides or PANs. Independent of the nature of R group, these compounds are thermally stable and have lifetimes can change from minutes at surface temperatures to months at upper troposphere. The other group of  $\text{RO}_2\text{NO}_2$  that does not have acyl group next to the peroxy group, peroxy-carboxylic structure, is called non-acyl peroxy nitrates. Their thermal lifetimes are shorter and only found in significant concentrations at colder regions of the atmosphere (Wooldridge et al. 2010a). During nighttime,  $\text{RONO}_2$  is formed from nitrate oxidation reactions.  $\text{NO}_3$  radical reacts with unsaturated hydrocarbons ( $\text{R}_1=\text{R}_2$ ) by  $\text{NO}_3$  addition and produce  $\text{R}_1(\text{ONO}_2)\text{-R}_2$  radical which reacts with  $\text{O}_2$  to generate a peroxy radical  $\text{R}_1(\text{ONO}_2)\text{-R}_2\text{O}_2$ . The peroxy radical later react with  $\text{NO}_3$ ,  $\text{RO}_2$  or  $\text{HO}_2$  to form  $\text{RONO}_2$ .

Laboratory studies shows that organic nitrate yield from OH oxidation of isoprene and  $\alpha$ -pinene is 4-15% and 1-26% respectively. Organic nitrate yield from  $\text{NO}_3$  oxidation of various VOCs changes from 20-80%, 0.62-0.8% for isoprene 0.10-0.29% for  $\alpha$ -pinene (Takeuchi and Ng 2018).

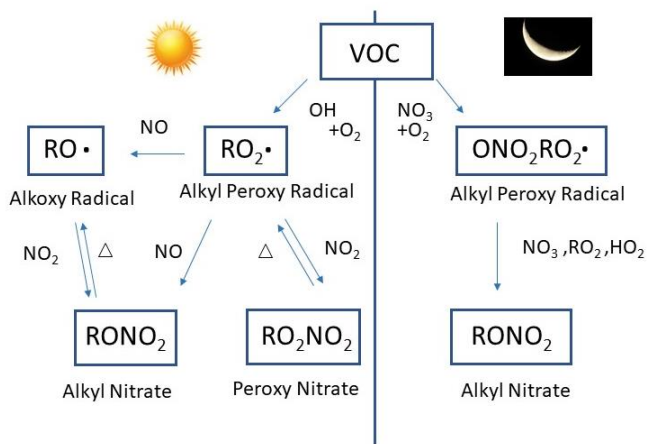


**Figure 1.2. Alkyl nitrate and peroxy nitrate formation**

### 1.3 Motivation, Scope and Overview

Alkyl nitrate (AN) and peroxy nitrate (PN) are temporary  $\text{NO}_x$  reservoirs species in the troposphere. Formation of AN and PN terminates the chain reactions of  $\text{RO}_x$  and  $\text{NO}_x$  ( $\text{NO} + \text{NO}_2$ ) radicals; therefore the quantification of these nitrates is critical to understanding the global and regional distributions of  $\text{NO}_x$  as well as its cycling and impact on ozone and SOA production (Bean and Hildebrandt Ruiz 2016; Perring, Pusede and Cohen 2013).

Quantification of speciated and total AN and PN enables us to measure the rates of chemical, physiological and removal of AN, loss or release of  $\text{NO}_x$  due to different formation and fate mechanisms of AN and PN which leads to more reliable predictions of  $\text{O}_3$  and SOA formation and thus more effective strategies for air quality control (Perring, Pusede and Cohen 2013).

The work presented in Chapter 2 of this dissertation focuses on the development and characterization of Thermal Dissociation - Cavity Attenuated Phase Shift Spectroscopy (TD-CAPS), and comparison its performance with established instruments by producing secondary organic aerosols from oxidation of biogenic organic compounds in GTEC chamber facility. Chapter 3 summarizes the main findings of this dissertation and provides recommendations for future work.

## CHAPTER 2. DEVELOPMENT AND CHARACTERIZATION OF TD-CAPS

### 2.1 Background

Nitrogen oxides ( $\text{NO}_x$ , sum of  $\text{NO}$  and  $\text{NO}_2$ ) play a critical role in atmospheric oxidation capacity, air quality, climate, and human health.  $\text{NO}_x$  levels impact the photochemical production and loss of ozone ( $\text{O}_3$ ) as well as secondary organic aerosol (SOA) formation through reactions with  $\text{RO}_x$  radicals ( $\text{RO}_x = \text{RO}_2 + \text{RO} + \text{HO}_2 + \text{HO}$ ). Therefore, it is important to understand the atmospheric life cycle of  $\text{NO}_x$  (Perring, Pusede and Cohen 2013; Roberts 1990). Figure 2.1 shows the species and the processes involved in the  $\text{NO}_x$  cycle. The sum of reservoir or sink species that enables temporary or permanent storage of  $\text{NO}_x$  is referred to as  $\text{NO}_z$  ( $\text{NO}_z = \text{HNO}_3 + \text{RO}_2\text{NO}_2 + \text{RONO}_2 + \text{HONO} + \text{N}_2\text{O}_5 + \text{NO}_3^-$ ) (Logan 1983). The sum of  $\text{NO}_x$  and  $\text{NO}_z$  is defined as  $\text{NO}_y$  (total reactive nitrogen). A significant loss pathway for  $\text{NO}_x$  is the formation of alkyl nitrate (AN) and peroxy nitrate (PN) with molecular structures of  $\text{RONO}_2$  and  $\text{RO}_2\text{NO}_2$ , respectively. The oxidation of volatile organic compounds (VOC) by atmospheric oxidants produces peroxy radicals ( $\text{RO}_2$ ).  $\text{RO}_2$  can follow different reaction pathways depending on the atmospheric conditions. The reaction of  $\text{RO}_2$  with  $\text{NO}_2$  and  $\text{NO}$  leads to the formation of PN and AN, respectively. PN species are thermally unstable at boundary layer temperatures and decompose back to  $\text{RO}_2$  and  $\text{NO}_2$  on a time scale of minutes, an exception being the longer-lived peroxyacyl nitrate (PAN). The relative importance of AN species among  $\text{NO}_y$  can be significant and depends on VOC and  $\text{NO}_x$  emissions (Perring, Pusede and Cohen 2013).

For example, (Browne and Cohen 2012) showed that AN formation is significant when biogenic VOC emissions are high and  $\text{NO}_x$  emissions are low. Owing to their semi-volatile/low-volatility nature, AN can also undergo gas-particle partitioning and contribute to SOA. The contribution of organic nitrates (referring to alkyl nitrates) to organic aerosol (OA) was found to be substantial (up to 77% by mass) from field measurements conducted at multiple sites around the world (Day et al. 2010; Fry et al. 2013; Kiendler-Scharr et al. 2016; Ng et al. 2017; Rollins et al. 2012; Rollins et al. 2013; Xu et al. 2015b).

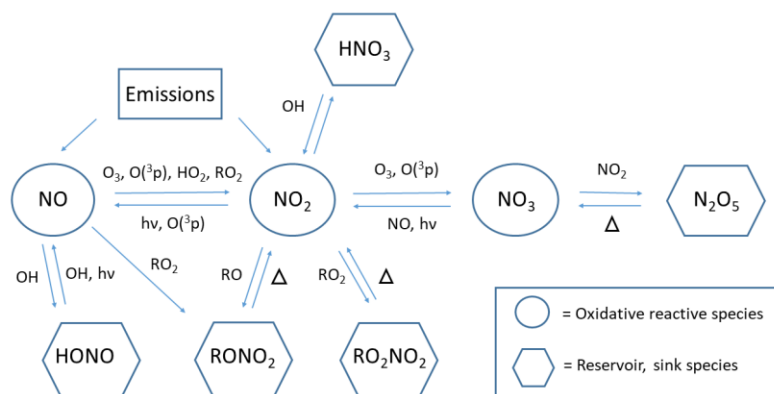


**Figure 2.1**  $\text{NO}_x$  cycle

The formation of  $\text{RONO}_2$  and  $\text{RO}_2\text{NO}_2$  terminates the chain reactions of  $\text{RO}_x$  and  $\text{NO}_x$  which affects the global and regional distributions of  $\text{NO}_x$  and thus  $\text{O}_3$  production. This makes the quantification of organic nitrates critical in  $\text{NO}_x$  and  $\text{O}_3$  budgets.  $\text{RONO}_2$  and  $\text{RO}_2\text{NO}_2$  consist of many structurally distinct compounds and are usually present in low concentrations, making their quantification challenging. In some studies, the measured total  $\text{NO}_y$  has been found to exceed the sum of speciated reactive nitrogen compounds

( $\Sigma\text{NO}_{y,i}$ ), suggesting that there are “missing” speciated reactive nitrogen species (Bradshaw, Sandholm and Talbot 1998; Buhr et al. 1990; Day et al. 2003; Fahey et al. 1986; Sparks et al. 2019; Womack et al. 2017). In general,  $\text{RONO}_2$  and  $\text{RO}_2\text{NO}_2$  have the biggest uncertainties among all  $\text{NO}_y$  species and therefore measurements of these compounds will provide improved constraints of their role in  $\text{NO}_x$  cycling,  $\text{O}_3$  and SOA production, and new insights into the unmeasured fraction of  $\text{NO}_y$ .

Individual gas-phase AN species has been measured with a variety of instrumentation. In early field measurements, short chain ( $\text{C}_3\text{--C}_5$ ) monofunctional AN were quantified with GC-ECD (Atlas 1988). Later, individual AN species were measured with GC-ECD and GC with mass spectrometric identification (GC-MS) (Luxenhofer et al. 1996; Schneider et al. 1998), high-pressure liquid chromatography (HPLC) followed by GC-ECD and GC-MS (Kastler and Ballschmiter 1998), atmospheric pressure ionization mass spectrometry (API-MS) (Kwok et al. 1996), proton transfer reaction mass spectrometry (PTR-MS) (D'Anna et al. 2005), and chemical ionization mass spectrometry (CIMS) (Beaver et al. 2012). Mass spectrometry techniques such as PTR-MS and CIMS (D'Anna et al. 2005) can measure multi-functional AN, however quantification of individual nitrates is challenging due to lack of authentic standards. In term of gas-phase PN species, peroxyacyl nitrate (PAN) is the most abundant PN, accounting for 75-90% of measured PN, with atmospheric measurements dating back to the 1960s (Carrington 1960). Early measurements were conducted with Fourier transform infrared spectroscopy (FTIR) (Niki et al. 1978) and gas chromatography (GC) followed by conversion to NO and chemiluminescence detection. However, the most common measurement technique for

PAN and its structural analogues is GC followed by electron capture detection (GC-ECD) (Darley, Kettner and Stephens 1963; Roberts 1990).

In 2002, Day and co-authors developed a method based on thermal dissociation (TD) of AN and PN to generate NO<sub>2</sub> and subsequent detection of NO<sub>2</sub> by laser-induced fluorescence (TD-LIF) (Day et al. 2002). This method differs from previous methods by measuring the sum of all AN and the sum of all PN as opposed to individual species. Since detection relies on the NO<sub>2</sub> measurement rather than the associated organic fragment, multifunctional organic nitrates can be measured by this technique as well. Later, a TD inlet was coupled with other detection techniques such as chemical ionization mass spectrometry (TD-CIMS) (Slusher et al. 2004; Zheng et al. 2011), cavity ring-down spectroscopy (TD-CRDS) (Paul, Furgeson and Osthoff 2009; Thieser et al. 2016) and Cavity Attenuated Phase Shift Spectroscopy (TD-CAPS) (Sadanaga et al. 2016). A summary of ambient measurements in urban and remote areas and comparison between different instruments for PN has been given in previous studies (Roberts 1990; Wooldridge et al. 2010b). In general, Wooldridge et al. (2010) found good overall agreements between the TD-LIF measurements and measurements of individual PN species under various environmental conditions. These TD methods have the capability of measuring particle-phase AN with modification to the instrument inlet such as the use of activated carbon denuders to remove gas phase species (Rollins et al. 2010). Total particle organic nitrates can also be quantified by aerosol mass spectrometry (AMS) by applying the following methods: NO<sup>+</sup>/NO<sub>2</sub><sup>+</sup> ratio, positive matrix factorization (PMF), and by subtraction of inorganic nitrate concentration measured by independent method from the total particulate

nitrate concentration measured by the AMS (Farmer et al. 2010; Fry et al. 2009; Hao et al. 2014; Jayne et al. 2000; Kiendler-Scharr et al. 2016; Schlag et al. 2016; Sun et al. 2012; Xu et al. 2015a; Xu et al. 2015b). Individual organic nitrates in the gas and particle phases can be measured by filter inlet for gases and aerosols coupled to high resolution time-of-flight CIMS (FIGAERO-HR-ToF-CIMS) (Chen et al. 2020; Lee et al. 2016; Nah et al. 2016; Ng et al. 2017; Takeuchi and Ng 2019).

Out of all available total AN and total PN measurement techniques, an advantage of the TD-CAPS instrument is that the CAPS monitor is commercially available. It does not require frequent calibration, although it requires frequent baseline measurements. Sadanaga et al. (2016, 2019) reported the first use of TD-CAPS for ambient measurements of AN and PN at Suzu on the North Peninsula of Japan. They analyzed the seasonal variations and diurnal variations of AN and PN and concluded that variations are mainly governed by long-range transport in the cold season and by local photochemical production in the warm season. However, there is no characterization study to quantify the limits and strengths of this technique.

In this work, we developed and characterized a TD-CAPS instrument to measure total gas-phase and particle-phase AN and PN. We used isopropyl nitrate (IPN) and peroxyacetyl nitrate (PAN) as representative AN and PN compounds to identify and quantify potential chemical interferences from side reactions due to the presence of O<sub>3</sub>, NO, and NO<sub>2</sub>. We derived correction factors for the reactions of these compounds over a wide range of concentrations representative of rural and urban environments as well as

laboratory chamber experiment conditions. Finally, we evaluated the performance the TD-CAPS instrument by making measurements of organic nitrates produced from the oxidation of biogenic VOC in the Georgia Tech Environmental Chamber (GTEC) facility and compared our results from TD-CAPS with other instruments.

## 2.2 Instrument Setup

A schematic of the TD-CAPS instrument is shown in Figure 2.2. The instrument has three channels and a CAPS monitor (Aerodyne Research Inc.) to measure  $\text{NO}_2$ . The reference channel measures the background  $\text{NO}_2$  at room temperature. The other two channels have quartz tube reactors that are heated to 653 K and 473 K, enabling decomposition of AN and PN respectively, generating  $\text{NO}_2$ . The  $\text{NO}_2$  concentration in each channel is alternatively measured by the CAPS monitor via 3-way solenoid valves. The difference in the  $\text{NO}_2$  concentration between the channels enables AN and PN measurements as shown in Eq. ((2-1)) and (2-2).

$$[\text{AN}] = [\text{NO}_2]_{653\text{K}} - [\text{NO}_2]_{473\text{K}} \quad (2-1)$$

$$[\text{PN}] = [\text{NO}_2]_{473\text{K}} - [\text{NO}_2]_{\text{Ref}} \quad (2-2)$$

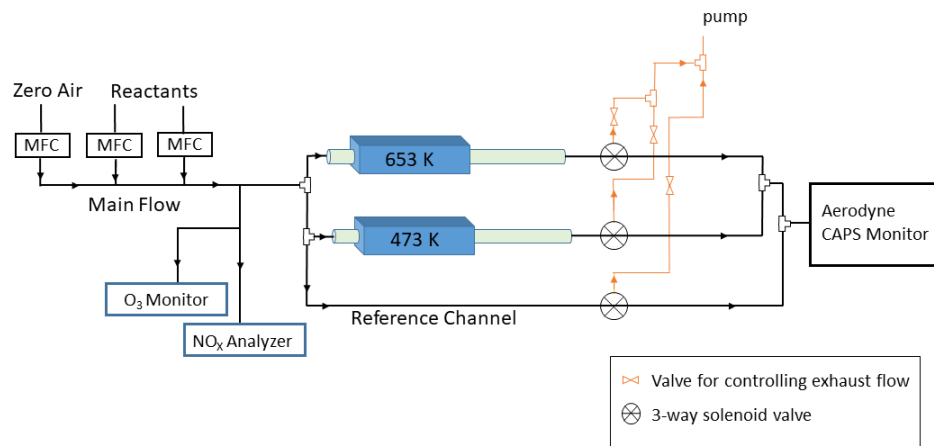


**Figure 2.2 Thermal Dissociation - Cavity Attenuated Phase Shift Spectroscopy (TD-CAPS) setup**

The quartz tube reactor has an inner diameter of 0.7 cm and a length of 28 cm. The quartz tube has heated and cooled segments. The first 12.8 cm of the quartz tube is housed inside an aluminum case, which is heated with cartridge heaters managed by a temperature controller (Omega CNi844-EIT) and insulated with FIBERFRAX. The remaining 15.2 cm of the quartz tube is cooled by fans placed around the tube. The quartz tube reactor is connected to the CAPS monitor by a Teflon tubing (0.4763 ID), where temperature of air further cools down to room temperature in this section. A  $0.91 \text{ L min}^{-1}$  flow is maintained in all channels during measurements, matching the sampling flow rate of the CAPS monitor. Solenoid valves placed after the quartz tube enable continuous flow in the channels, preventing overheating of compounds when the channel is not in use. The residence time from the heater to detection is 2 seconds.

The temperature profiles of the AN channel (653 K) and the PN channel (473 K) are shown in Figure A. 1. The temperature of the heaters in each channel is set based on the temperature range in which AN and PN are expected to thermally dissociate to produce NO<sub>2</sub> (Day et al. 2002). Thermogram measurements are conducted with representative AN and PN compounds, IPN and PAN, to validate that one mole of compound is fully dissociated to one mole of NO<sub>2</sub>. An IPN cylinder is prepared by diluting IPN vapor in nitrogen gas. PAN is produced in situ by photolysis of the acetone/air/CO mixture followed by reaction of NO. The amount of PAN generated is determined by the conversion efficiency of NO to NO<sub>2</sub>. In our measurements, the conversion efficiency is about 90%, which is consistent with the literature (Flocke et al. 2005; Warneck and Zerbach 1992). The efficiency of thermal dissociation of IPN and PAN is shown at Figure A. 2, which shows complete thermal dissociations of IPN and PAN at the expected dissociation temperatures. These results are consistent with the model NO<sub>2</sub> yields of AN and PN presented in (Day et al. 2002).

A typical measurement sequence starts with a baseline measurement at each channel using zero air, followed by measurements at the reference channel, 653 K channel, 473 K channel, and ends with another baseline measurement. The sampling duration in each channel is typically 5-10 minutes depending on the experiment. The duration is determined based on the time required to reach a stable measured NO<sub>2</sub> concentration. The baseline measurements at the beginning and the end of the measurement capture the baseline drift during the experiment, which is typically about <1 ppb in a 12-hour

experiment and corrected by interpolation between the two baseline measurements. The equation below shows how the correction is applied to each measurement.

$$\begin{aligned} [NO_2]_{\text{channel\_baseline\_corrected}} & \qquad \qquad \qquad (2-3) \\ & = [NO_2]_{\text{channel\_reading}} - [NO_2]_{\text{baseline\_interpolated}} \end{aligned}$$

Before taking measurements, the CAPS monitor is calibrated with a 1.644 ppm standard of NO<sub>2</sub>/N<sub>2</sub> gas (Airgas), diluted with zero air. The calibration factor is stable, which only varies between 0.93 and 1.1, consistent with the measurement principle of CAPS (Kebabian et al. 2008).

The gas-phase and particle-phase AN and PN from the chamber are measured by the addition of a Teflon filter and an activated charcoal denuder to the TD-CAPS inlet. (Figure A. 3) A baseline is taken by sending excess zero air to the instrument. We use a 0.45 lpm sampling rate for the particle phase measurements, dilution rate of sampling/total flow 0.44, to provide enough residence time in the denuder to remove gas phase components. The residence time in the denuder is 25.7 s. The multichannel activated carbon denuder is 15 cm in length and 4 cm in diameter. Dilution with zero air is applied to the gas phase measurements to reduce the total flow required from the chamber to the instruments. For the CAPS, the dilution is a factor of 2. A total of five channels, 3 for the gas-phase and 2 for the particle-phase, along with two CAPS monitors are used for this experiment. The sampling time for each channel is set to 2 minutes.

## 2.3 Characterization of Potential Chemical Interferences

Based on previous studies on characterization of TD-LIF and TD-CRDS instruments (Day et al. 2002; Thieser et al. 2016), we use IPN and PAN to evaluate potential chemical interferences in the TD-CAPS instrument. These interferences arise from side reactions due to presence of atmospheric constituents like  $O_3$ , NO, and  $NO_2$ . Measurements are performed by mixing various concentrations of IPN and PAN with  $NO_x$  (IPN+NO, IPN+ $NO_2$ , PAN+NO, and PAN + $NO_2$ ), and  $O_3$  with  $NO_x$  ( $O_3$ +NO and  $O_3$ + $NO_2$ ). Correction factors are derived for binary combinations of these compounds over a wide range of concentrations. The explored concentrations are representative of rural and urban environments as well as laboratory chamber reaction conditions.

Several assumptions need to be made when applying the correction factors derived from these characterization experiments. The first assumption is that all AN and PN behave like the selected representative compounds, IPN and PAN. This assumption is likely to be valid since R group in the  $RONO_2$  and  $RO_2NO_2$  has little effect on the activation energy and thus on the thermal dissociation rates of these compounds (Kirchner et al. 1999; Roberts 1990). The second assumption is that chemical interferences are additive. Here, chemical interferences are determined from binary systems and the overall interference is calculated from the addition of each interference.

### 2.3.1 Chemical Interference for IPN due to Presence of $NO_x$

IPN decomposes only in the 653 K channel. Ideally, 1 ppb of IPN produces 1 ppb of  $NO_2$ . However, deviations from the ideal case occur due to side-reaction of  $RO_2$  radicals

(produced from thermal decomposition of IPN) and HO<sub>2</sub> (from subsequent reactions) with NO to make NO<sub>2</sub> (Day et al., 2002, Thieser et al., 2016). As seen in the reactions below, two additional NO<sub>2</sub> molecules can be produced from radical reactions in addition to IPN thermal decomposition, assuming there is negligible wall loss of radicals.



We investigate chemical interference due to the presence of NO by adding NO to different concentrations of IPN systematically. The NO concentration is varied from 1 ppb to 174 ppb for IPN concentrations of 1.2, 5.8 and 11.4 ppb. Figure 2.3 shows the difference signal between the 653 K channel and reference channel divided by IPN concentration as a function of NO. Normalizing the signal by IPN concentration shows that the overestimation of NO<sub>2</sub> is dependent on IPN concentration, with a stronger dependence at low NO concentrations.

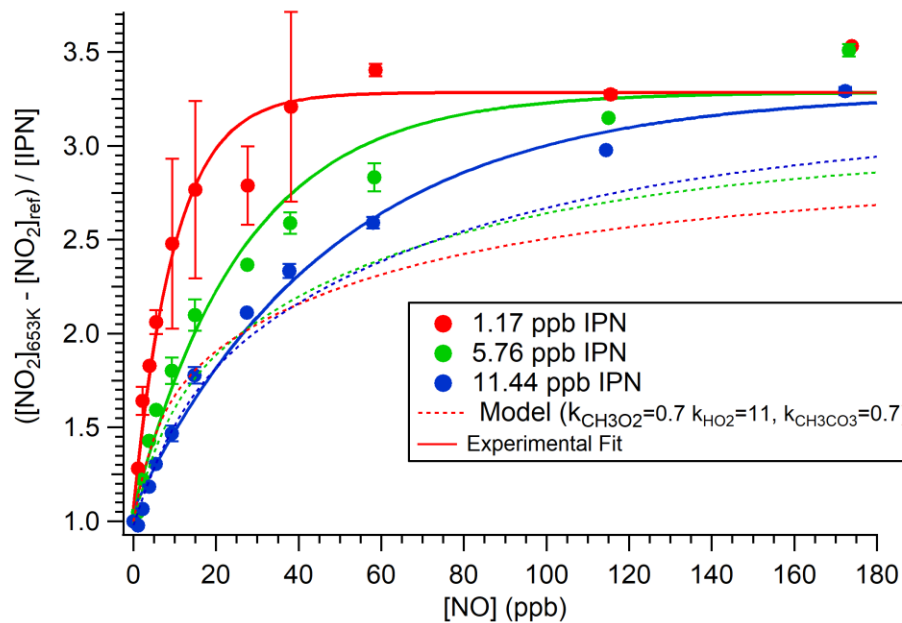


**Figure 2.3 Measurements of the difference signal (sampling from the 653K – reference channel) over IPN concentration when adding different amounts of NO to IPN**

The correction factor is derived by fitting the experimental data with an exponential equation in the form of  $y_0 + A * e^{(-NO/Tau)}$  using IGOR Pro 6.37.  $y_0$  corresponds to the peak of the curve, which has a value of 3.2837. Tau determines the shape of the curve, which is dependent on the IPN concentration. It is defined as  $Tau = m * IPN + n$ , where  $m$  and  $n$  are constants. The experimental fit equation is as follows:

$$f(NO, IPN) = 3.2837 - 2.221 * e^{\left(-\frac{[NO]}{3.694 * [IPN] + 5.5597}\right)} \quad (2-4)$$

The observed overestimation is compared with the results reported for TD-LIF (Day et al. 2002) and TD-CRDS (Thieser et al. 2016). The degree of overestimation is

found to be higher in our study than in Day et al 2002. Day et al. 2002 used a quartz tube reactor with a temperature set point of 673 K and a residence time of 200-230 ms. Their concentration of NO is up to 260 ppb for 4.9 ppb of NPN and the interference due to NO is about a factor 1.72. They concluded that the low residence time leads to incomplete conversion of NO to NO<sub>2</sub> by RO<sub>x</sub>. Moreover, they operated the LIF cells at 2-4 Torr, which will reduce rate of the bimolecular reactions. In a later study (Wooldridge et al. 2010b), they modeled the effects of pressure on the degree of interference by reducing the pressure at different parts of the inlet. Although operating at low-pressure can result in smaller interference, the CAPS monitor requires operating at ambient pressure to maintain a good sensitivity. The lowest pressure recommended by Aerodyne is 560 Torr. Reducing our sampling pressure to 580 Torr leads to a similar degree of interference, which is consistent with model predictions. Therefore, the instrument is operated at ambient pressure. The degree of overestimation in our study is also compared to the values given by Thieser et al 2016. At reactor set temperature of 723 K and 2 seconds of residence time (from heater to detector), they measured the interference due to NO for range of IPN concentrations of 0.29-5.78 ppb. They added 0-9.2 ppb of NO and expressed the interference with the  $1+1.8(1-\exp(-0.08*[NO]))$  equation. The degree of overestimation is found to be less than factor of 2 for that measured concentration range and similar to the degree of overestimation found in our study ( $\leq$  factor of 2). The interference expression in their study provides the estimate peak value of 2.8 at high NO concentrations and is less than the value that we obtained in the study. A possible reason for the differences in the interference could be the sampling history of the quartz tubing, which could affect wall loss of peroxy radicals

and consequently the degree of interference. Therefore, it is important to quantify the interference at the concentration range of IPN and NO that is interest of the subsequent measurement. The effect of radical wall loss is discussed in detail in Section 2.3.3.

We also evaluate chemical interference due to presence of NO<sub>2</sub> are explored by mixing NO<sub>2</sub> (4.1- 120.7 ppb) and IPN (4.1 ppb to 120.7 ppb) systematically. Unlike the case for NO, Figure 2.4 shows that the chemical interferences due to addition of NO<sub>2</sub> is insignificant. There is no dependency on IPN nor NO<sub>2</sub>. This trend is consistent with the behavior observed in Day et al. 2002 and Thieser et al. 2016.

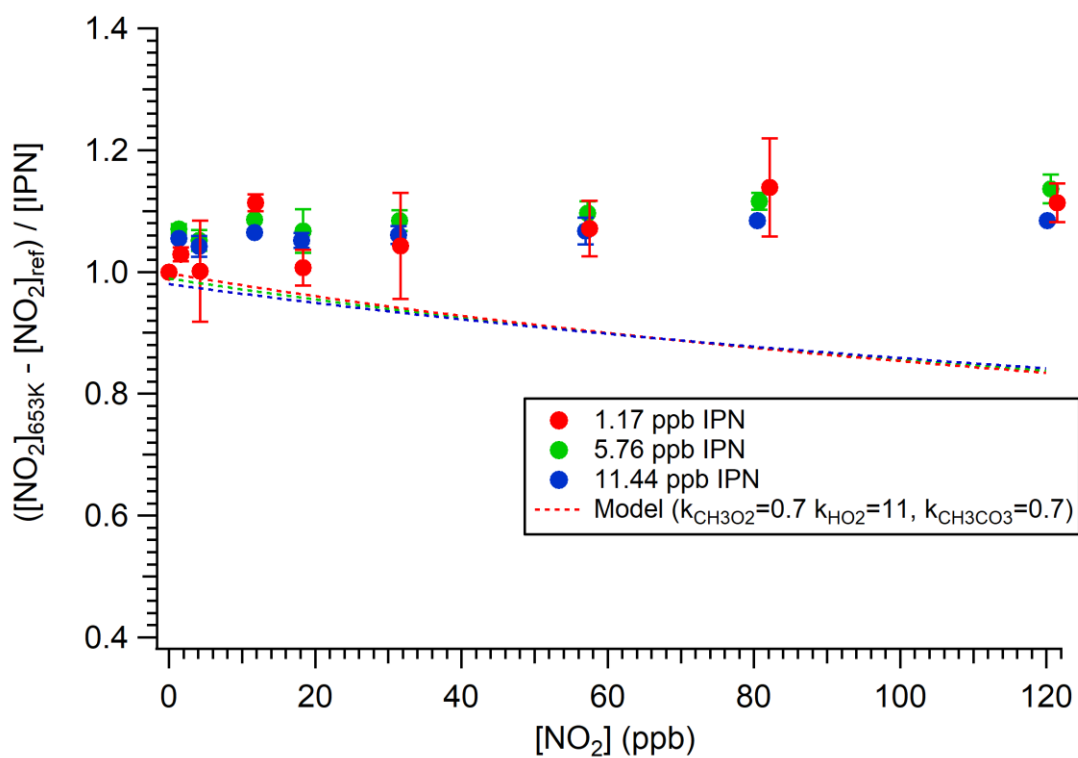


**Figure 2.4 Measurements of the difference signal (sampling from the 653K – reference channel) over IPN concentration when adding different amounts of NO<sub>2</sub> to IPN**

### 2.3.2 Chemical Interference for PAN due to Presence of $NO_x$

PAN decomposition occurs at both 473 K channel and 653 K channel; therefore, the interference is investigated in both channels. PAN thermally decomposes to  $NO_2$  and  $CH_3C(O)O_2$ . In the presence of NO,  $CH_3C(O)O_2$ ,  $CH_3O_2$ , and  $HO_2$  can react with NO to produce  $NO_2$ . This leads to up to three additional  $NO_2$  molecules from side reactions. In the presence of  $NO_2$ , recombination to PAN and reaction with  $CH_3O_2$  are important  $NO_2$  loss mechanisms.



NO is added to different concentration of PAN systematically to quantify the chemical interferences due to side reactions. NO concentration is changed from 3 ppb to 183 ppb for PAN concentration of 1.4, 1.8, 2.7, and 3.7 ppb. Figure 2.5 shows the difference signal between the 473 K channel and reference channel (see Eq (2-2)) divided by PAN concentration as a function of NO. While the interference is dependent both on NO and PAN, the dependence on PAN is more observable for NO concentrations lower

than 50 ppb. The correction factor is derived by fitting the experimental data to the following equation:

$$f(\text{NO}, \text{PAN}) = 2.7046 - 1.665 * e\left(-\frac{[\text{NO}]}{2.229 * [\text{PAN}] + 3.0527}\right) \quad (2-5)$$

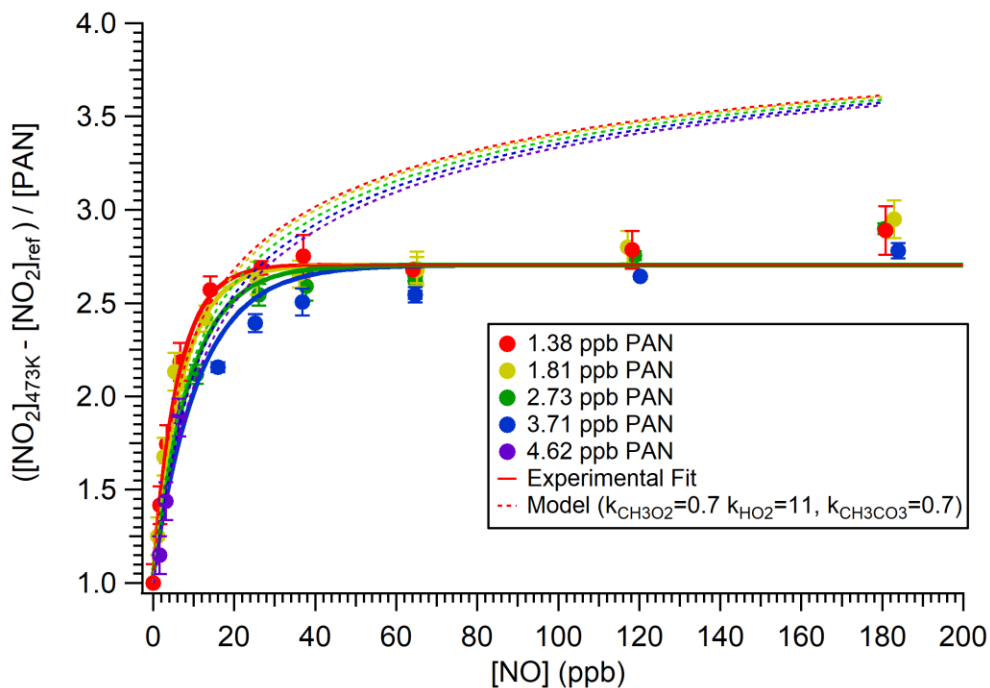


**Figure 2.5 Measurements of the difference signal (sampling from the 473K – reference channel) over PAN concentration when adding different amounts of NO to PAN.**

There is more interference in our work than the interference reported by Day et al 2002, again likely due to a longer residence time in our study. In Thieser et al 2016, the overestimation increases to the factor of 2.7 as the NO concentration increases from 0-10.1 ppb NO for 1.05 and 2.5 ppb of PAN. The interference is higher compared to our study

where it varies between the factor of 2-2.4 with PAN concentration at NO concentrations less than 14 ppb and the variation at the interference due to PAN concentration is corrected by the addition of a PAN dependency to the experimental fit.

In the 653 K channel, high concentrations of NO<sub>2</sub> are measured with the addition of NO, which was not expected. The following two cases are analyzed to understand whether this interference is due to PAN or other radicals produced in the photochemical cell. In the first case, PAN is produced by sending 42 ccm of a 20 ppm acetone/CO/air mixture and 2 ccm of a 2ppm NO tank through the photochemical cell. The output is diluted with pure air to obtain 0.77 ppb of PAN and mixed with 0-50 ppb of NO to investigate the effect of NO on the PAN measurement. In the second case, the same flow rate of acetone/CO/air is sent to the photochemical cell following same dilution rate and addition of NO concentration range. Figure A. 4 shows the difference in NO<sub>2</sub> for the two cases ( $[\text{NO}_2]_{\text{acetone/CO/air +NO}} - [\text{NO}_2]_{\text{acetone/CO/air}}$ ) which is found to be fluctuating at an average value of 0.74 ppb and does not show any trends within the uncertainty. This difference in NO<sub>2</sub> gives the PAN concentration at 0 ppb of NO and PAN concentration with the possible interference at 5.6-56 ppb of NO. Since NO<sub>2</sub> is kept constant (same as the initial PAN concentration) while increasing NO, no interference from NO is expected at 653 K channel. Since NO<sub>2</sub> production from side products is only observed in the 653 K channel, the side products are probably alkyl nitrates.

Chemical interference due to the presence of NO<sub>2</sub> are explored by adding NO<sub>2</sub> to PAN systematically. The NO<sub>2</sub> concentration is varied from 4.1 ppb to 120.7 ppb for PAN

concentrations of 1.0, 1.7, 2.9, and 4.4 ppb. Figure 2.6 shows the difference signal between the 473 K channel and reference channel (see (2-2)) divided by PAN concentration as a function of NO<sub>2</sub>. As shown in the figure, there is no dependency on PAN concentration but there is dependence on NO<sub>2</sub> concentration. The correction factor is expressed as follows:

$$f(\text{NO}_2) = 0.715 + 0.284 * e^{\left(-\frac{[\text{NO}_2]}{10.7}\right)} \quad (2-6)$$

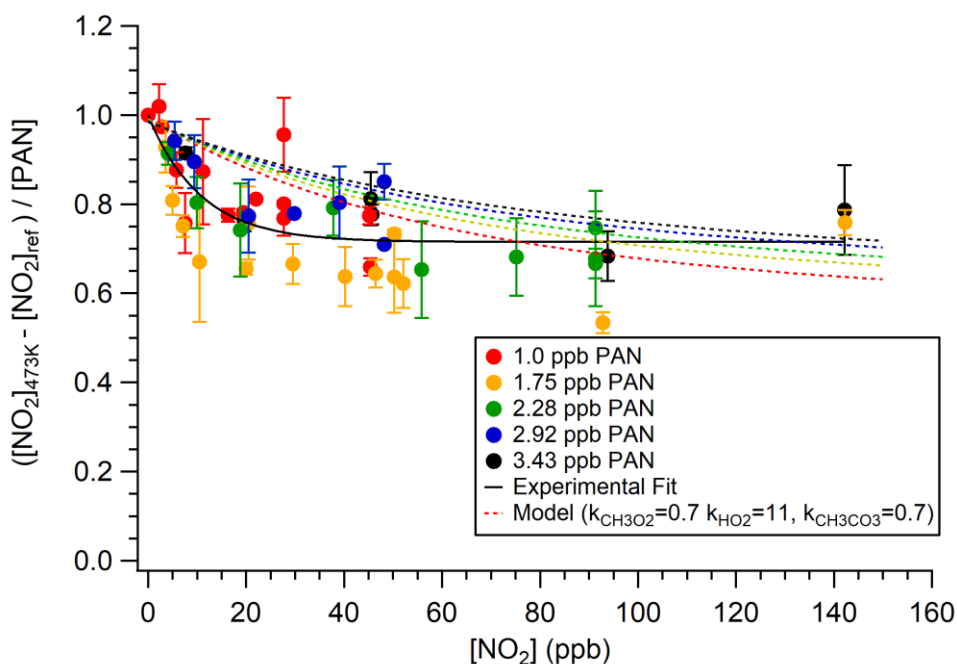


**Figure 2.6 Measurements of the difference signal (sampling from the 473K – reference channel) over PAN concentration when adding different amounts of NO<sub>2</sub> to PAN.**

The interference in Day et al. 2002 is expressed by the time-dependent bimolecular reaction of the peroxyacyl radicals and NO<sub>2</sub> where they estimated around a 4% underestimation for

1 ppb of PAN in the presence of 1 ppb of NO<sub>2</sub>. The interference is found to be smaller than that reported in Thieser et al 2016 which is underestimated up to factor of 0.4 at NO<sub>2</sub> concentrations lower than 18 ppb.

### 2.3.3 Numerical Simulations and Peroxy Radical Wall Losses

We constructed a kinetic box model to simulate and evaluate the experimental data and the reactions involved. The reactions rates are obtained primarily from the Master Chemical Mechanisms (MCM) v 3.3.1 (SI). The input of the box model simulations are reaction rates, temperature profile of each channel, residence time, and initial concentrations of the reactants. The simulations are run using Framework for 0-D Atmospheric Modeling (FOAM) v3.1. The results of the simulations are shown in Figures 2.3 – 2.6 as dotted lines. For interference from IPN+NO (Figure 2.3), the kinetic box model results show higher variation at low NO concentration that is due to loss of NO<sub>2</sub> from its reaction with OH at higher concentrations of IPN, and this loss mechanism becomes less significant as NO concentration increases. Moreover, at higher IPN concentration the model shows that relative importance of HO<sub>2</sub> reaction with OH increases which reduces the amount of NO<sub>2</sub> production from HO<sub>2</sub>+NO reaction. The Model qualitatively follows the NO and IPN dependency of NO<sub>2</sub> production. The quantitative agreement can be reached by introducing wall-loss correction of CH<sub>3</sub>O<sub>2</sub>, HO<sub>2</sub> and CH<sub>3</sub>C(O)O<sub>2</sub> radicals.

For interference from IPN+NO Although the model does not show IPN concentration effect as observed in measurements, dependency of NO<sub>2</sub> in the measurements is found different from the model results where a strong decreasing trend is

observed with increasing NO<sub>2</sub> due to combination reaction of i-C<sub>3</sub>H<sub>7</sub>O and NO<sub>2</sub> in the absence of wall-loss affects. Therefore, wall-loss for the peroxy radicals needs to be introduced to match our measurements.

The model follows the general trend of the measurements in the absence of wall-loss. However, introducing the same wall-loss rates for CH<sub>3</sub>O<sub>2</sub>, HO<sub>2</sub> and CH<sub>3</sub>C(O)O<sub>2</sub> improves the agreement.

Model results shows a larger decrease in signal compared to the experiments in the absence of radical wall-loss. Therefore, wall-loss values need to be adjusted to match the experiments.

Radical wall-losses for CH<sub>3</sub>O<sub>2</sub>, HO<sub>2</sub> and CH<sub>3</sub>C(O)O<sub>2</sub> are introduced for the kinetic box model to match the experimental data. CH<sub>3</sub>O<sub>2</sub>, HO<sub>2</sub> and CH<sub>3</sub>C(O)O<sub>2</sub> radicals are produced in IPN+NO, IPN+NO<sub>2</sub>, PAN+NO and PAN+NO<sub>2</sub> cases. Therefore, these 3 wall-loss values, k<sub>CH<sub>3</sub>O<sub>2</sub></sub>, k<sub>HO<sub>2</sub></sub> and k<sub>CH<sub>3</sub>C(O)O<sub>2</sub></sub>, are determined by minimizing the root mean square error (RMSE) of model output value and experimental data for each system. For example, for IPN+NO case:

$$RMSE_{IPN+NO} = \sqrt{\frac{\sum_i^N (f(\text{NO}, \text{IPN})_{\text{experimental}} - f(\text{NO}, \text{IPN})_{\text{model}})^2}{N}} \quad (2-7)$$

where N is the number of measurements taken for that given system.

Next, average of RMSE values are taken to select  $k_{\text{CH}_3\text{O}_2}$ ,  $k_{\text{HO}_2}$  and  $k_{\text{CH}_3\text{C}(\text{O})\text{O}_2}$  values that fits best to the 4 cases.

$$\begin{aligned}
 &RMSE_{avg} \tag{2-8} \\
 &= \frac{RMSE_{IPN+NO} + RMSE_{IPN+NO_2} + RMSE_{PAN+NO} + RMSE_{PAN+NO_2}}{4}
 \end{aligned}$$

The range of radical wall-loss values are as follows:  $k_{\text{CH}_3\text{O}_2} = 0.4\text{-}1 \text{ s}^{-1}$ ,  $k_{\text{HO}_2} = 8\text{-}14.26 \text{ s}^{-1}$  and  $k_{\text{CH}_3\text{C}(\text{O})\text{O}_2} = 0.55\text{-}0.82 \text{ s}^{-1}$ . The values for  $k_{\text{CH}_3\text{O}_2}$  and  $k_{\text{CH}_3\text{C}(\text{O})\text{O}_2}$  are similar to the values reported in Thieser et al. where radical wall-loss values vary between 0.3 and 0.8  $\text{s}^{-1}$ . These values are also comparable to the peroxy radical loss observed in Wooldridge et al. which is 0.3  $\text{s}^{-1}$  for quartz and 0.2  $\text{s}^{-1}$  for Teflon tubing. They mention that wall-loss values are likely to change between quartz tubes and through environmental exposure. We also observed changes in radical wall-loss rates that depend on sampling history.

#### 2.3.4 $\text{NO}_2$ Loss due to $\text{O}_3$ Thermal Decomposition

If the inlet stream contains  $\text{O}_3$ , its thermal decomposition to  $\text{O}_2$  and  $\text{O} (^3\text{p})$ .  $\text{O} (^3\text{p})$  atom either recombines with  $\text{O}_2$  or reacts with  $\text{NO}_2$ , resulting in a loss of  $\text{NO}_2$ .



The reaction of O with O<sub>2</sub> is instantaneous, therefore, a steady state expression can be written as:

$$[O]_{ss} = \frac{k_{12} [O_3]}{k_{13} [O_2] [M]} \quad (2-9)$$

The rate of NO<sub>2</sub> loss can be written as:

$$-\frac{d[NO_2]}{dt} = k_{14} * [NO_2] * [O]_{ss} \quad (2-10)$$

When the [O]<sub>ss</sub> is substituted into Eq (2-10)

$$-\frac{d[NO_2]}{dt} = k' * [NO_2] * [O_3] \quad (2-11)$$

where k' is  $\frac{k_{14}k_{12}}{k_{13}[O_2][M]}$ . Eq. (2-11) can further be simplified assuming of the change in [NO<sub>2</sub>] and [O<sub>3</sub>] is small, where t is the residence time.

$$[NO_2]_{Loss} = k * t * [NO_2] * [O_3] \quad (2-12)$$

We investigate this interference in the 653 K channel by mixing NO<sub>2</sub> concentrations of 4.4, 13.8, 27.6, and 36.8 ppb with O<sub>3</sub> concentrations of 22.4, 42.3, and 75.1 ppb. Figure 2.7 shows the NO<sub>2</sub> loss with the expression given by Eq. 10.

$$f(O_3, NO_2) = 0.00070574 * [NO_2] * [O_3] + 0.11082 \quad (2-13)$$

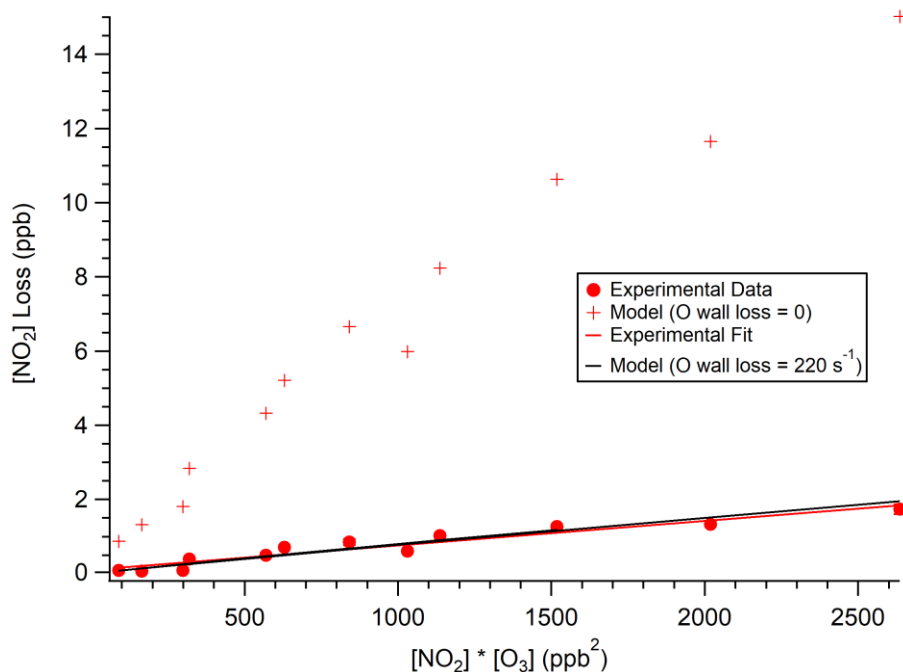


**Figure 2.7 NO<sub>2</sub> Measurements at 653 K channel when adding different amounts of NO<sub>2</sub> to O<sub>3</sub>**

In the investigated concentration ranges, the chemical interference can be expressed as a linear fit. Figure A. 5 shows the how NO<sub>2</sub> signal changes with different NO<sub>2</sub> and O<sub>3</sub> concentrations. The influences of NO<sub>2</sub> and O<sub>3</sub> are different in different concentration ranges. At small NO<sub>2</sub> concentrations, an increase in O<sub>3</sub> concentration does not change the loss of NO<sub>2</sub>. As NO<sub>2</sub> concentration increases, the effect of the O<sub>3</sub> concentration change becomes significant. Both the absolute concentration and the difference between the measured NO<sub>2</sub> and O<sub>3</sub> affects the observed NO<sub>2</sub> loss. Therefore, the expression above may not hold if the difference between the initial NO<sub>2</sub> and O<sub>3</sub> concentrations is large. In

addition, a large deviation from linear behavior is observed at high concentrations of NO<sub>2</sub> and O<sub>3</sub> (Figure A. 6).

Day et al 2002 and Thieser et al 2016 discussed the loss of NO<sub>2</sub> due to its reaction with O (<sup>3</sup>p) atom produced from the thermal decomposition of O<sub>3</sub>. Day et al 2002 investigated this loss at temperatures up to 873 K. At the residence times and the temperature of their reactor, they do not observe any change in NO<sub>2</sub> concentration. On the other hand, Thieser et al 2016 observed that O<sub>3</sub> thermal decomposition affects the NO<sub>2</sub> concentration and the interference can be quantified by a linear function of the product of NO<sub>2</sub> and O<sub>3</sub> with a slope of 7.34\*10<sup>-4</sup> which is similar to the slope we obtained in our study.

NO<sub>2</sub> loss in the 653 K channel is simulated using a kinetic box model with the addition of the thermal decomposition rate of O<sub>3</sub> is used by Thieser et al 2016. As seen Figure 2.7, NO<sub>2</sub> loss predicted by model is with much higher than the experimental data. Therefore, O wall-loss is introduced to match the model to the measurements. Wall-loss O is found to be 220 s<sup>-1</sup>. This value is within same order of magnitude as the one obtained by Thieser et al 2016 (70 s<sup>-1</sup>).

### 2.3.5 NO<sub>2</sub> Formation from O<sub>3</sub> and NO

The presence O<sub>3</sub> can also result in NO<sub>2</sub> production from the reaction of O<sub>3</sub> and NO and interfere with the measurement. NO<sub>2</sub> is produced from the reaction given below:



The rate of reaction can be written as

$$\frac{d\text{NO}_2}{dt} = k_{15} * [\text{NO}] * [\text{O}_3] \quad (2-14)$$

This can be simplified at low conversion of [NO] and [O<sub>3</sub>]

$$\text{NO}_2(\text{excess}) = k_{15} * t * [\text{NO}] * [\text{O}_3] \quad (2-15)$$

where t is the residence time.

We use combinations of NO concentrations (20.3, 45.0, and 70.0 ppb) mixed with different O<sub>3</sub> concentrations (21.6, 46.7, and 71.5 1 ppb) in order to quantify NO<sub>2</sub> formation. Figure 2.8 shows NO<sub>2</sub> production in the reference, 473 K, and 653 K channels plotted against the product of NO and O<sub>3</sub> concentrations. Fitting the experimental data to Eq. 14 yields the following equations:

$$f_{ref}(\text{O}_3, \text{NO}) = 0.00403 * [\text{NO}] * [\text{O}_3] + 1.736 \quad (2-16)$$

$$f_{473}(\text{O}_3, \text{NO}) = 0.00442 * [\text{NO}] * [\text{O}_3] + 2.045 \quad (2-17)$$

$$f_{653}(\text{O}_3, \text{NO}) = 0.00518 * [\text{NO}] * [\text{O}_3] + 6.051 \quad (2-18)$$

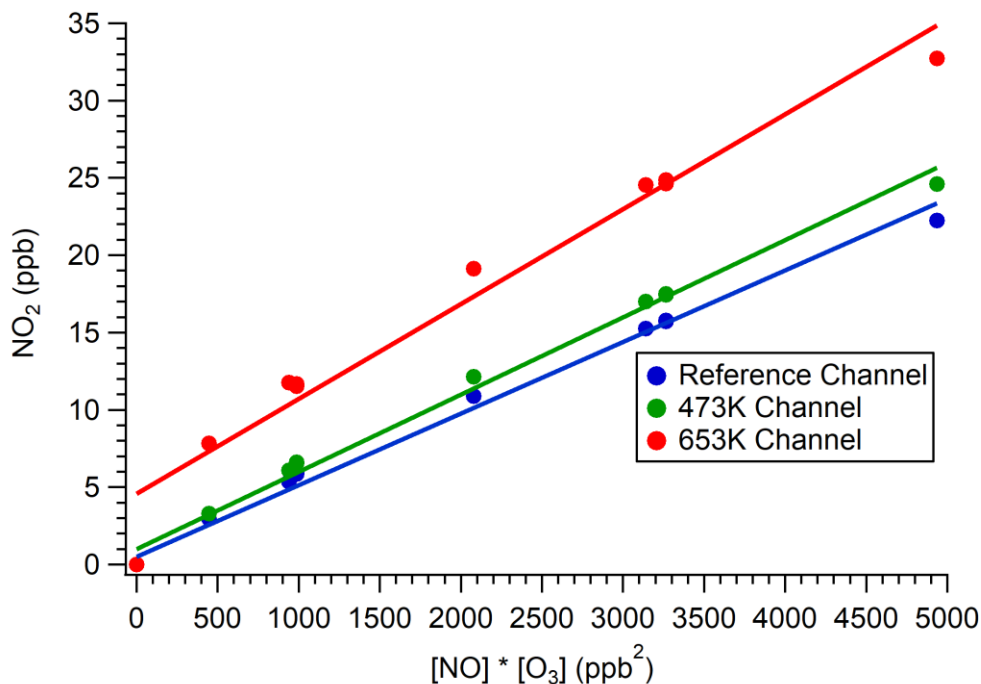


**Figure 2.8 NO<sub>2</sub> Measurements at Reference channel, 473 K channel and 653 K channel when adding different amounts of NO to O<sub>3</sub>.**

The residence time for these characterization experiments is 8.5 s. The rate constant in the reference channel ( $k_{ref}$ ) is calculated as  $1.92 \cdot 10^{-14} \text{ cm}^3 \text{ molecule}^{-1} \text{ s}^{-1}$ , which is similar to the rate in the MCM v3.1.1 ( $1.73 \cdot 10^{-14} \text{ cm}^3 \text{ molecule}^{-1} \text{ s}^{-1}$ ). Deviations from linear behavior are observed at 473 K and 653 K increasing with temperature. The reaction rate constants at 473 K ( $k_{473}$ ) and 653 K ( $k_{653}$ ) are calculated as  $2.11 \cdot 10^{-14} \text{ cm}^3 \text{ molecule}^{-1} \text{ s}^{-1}$  and  $2.48 \cdot 10^{-14} \text{ cm}^3 \text{ molecule}^{-1} \text{ s}^{-1}$ . These rate constants are comparable to the values reported in Thieser et al. (2016). As discussed in the previous section, the expression for the correction of the chemical interference (Eq 15) may not be accurate if the concentrations of O<sub>3</sub> and NO are very different from each other.

### 2.3.6 Expression of Correction Factors and the Total Uncertainty

The equations for correcting PN and AN, using the correction factors developed in previous sections, are shown below:

$$[\text{PN}] = \frac{[\text{PN}]_0 - (f_{473}(\text{O}_3, \text{NO}) - f_{\text{ref}}(\text{O}_3, \text{NO}))}{f(\text{NO}_2) f(\text{NO}, \text{PAN})} \quad (2-19)$$

where  $[\text{PN}]_0 = [\text{NO}_2]_{473} - [\text{NO}_2]_{\text{Ref}}$  is the uncorrected PN concentration, which is the difference in measured  $\text{NO}_2$  concentration between the 473 K channel and the reference channel.

$$[\text{AN}] = \frac{[\text{AN}]_0 + f(\text{O}_3, \text{NO}_2) - (f_{653}(\text{O}_3, \text{NO}) - f_{473}(\text{O}_3, \text{NO}))}{f(\text{NO}, \text{IPN})} \quad (2-20)$$

where  $[\text{AN}]_0 = [\text{NO}_2]_{653} - [\text{NO}_2]_{473}$  is the uncorrected AN concentration, which is the difference in measured  $\text{NO}_2$  concentration between the 653 K channel and the 473 K channel.

Since  $f(\text{NO}, \text{PAN})$  and  $f(\text{NO}, \text{IPN})$  are dependent on  $[\text{PN}]_0$  and  $[\text{AN}]_0$ ,  $[\text{PN}]$  and  $[\text{AN}]$  are solved iteratively.

The parameters for the correction factors (Eqns (2-4), (2-5), (2-6), (2-7), (2-16), (2-17), (2-18)) are determined by fitting the experimental data to exponential or linear equations using IGOR Pro 6.37. The uncertainties associated with each parameter are one standard deviation of the values and listed in **Error! Reference source not found..1**.

**Table 2-1 Summary of Fit Equations and Uncertainties**

System	Fit Equation	Parameter	Uncertainty of Fit Equation
IPN+NO	$f(\text{NO}, \text{IPN}) = y_0 + A$ $* e^{\left(\frac{[\text{NO}]}{m*[\text{IPN}] + n}\right)}$	$y_0 = 3.2837 \pm 0.0984$	$0.15 \pm 0.03$
		$A = -2.221 \pm 0.117$	
		$m = 3.694 \pm 0.779$	
		$n = 5.5597 \pm 2.15$	
PAN+NO	$f(\text{NO}, \text{PAN}) = y_0 + A$ $* e^{\left(\frac{[\text{NO}]}{m*[\text{PAN}] + n}\right)}$	$y_0 = 2.7046 \pm 0.0247$	$0.057 \pm 0.037$
		$A = -1.665 \pm 0.0487$	
		$m = 2.2229 \pm 0.51$	
		$n = 3.0527 \pm 1$	
PAN +NO <sub>2</sub>	$f(\text{NO}_2, \text{PAN}) = y_0 + A$ $* e^{\left(\frac{[\text{NO}_2]}{\text{Tau}}\right)}$	$y_0 = 0.715 \pm 0.0176$	$0.025 \pm 0.013$
		$A = 0.284 \pm 0.0473$	
		$\text{Tau} = 10.7 \pm 3.63$	

NO <sub>2</sub> +O <sub>3</sub>	$f(O_3, NO_2) = m * [NO_2] * [O_3]$ $+ n$	$m = .0574 * 10^{-4} \pm$ $4.41 * 10^{-5}$	
		$n = 0.11082 \pm$ $0.0509$	
NO +O <sub>3</sub>	$f_{ref}(O_3, NO) = m * [NO] * [O_3]$ $+ n$	$m = 0.004029 \pm$ $0.000113$	
		$n = 1.7362 \pm 0.415$	
	$f_{473}(O_3, NO) = m * [NO] * [O_3]$ $+ n$	$m = 0.004418 \pm$ $0.000134$	
		$n = 2.0448 \pm 0.493$	
$f_{653}(O_3, NO) = m * [NO] * [O_3]$ $+ n$	$m = 0.005184 \pm$ $0.000317$		
	$n = 6.0514 \pm 1.16$		

The detection limit is obtained by calculating the standard deviation ( $\sigma$ ) for each channel using Allan variance analysis. Since the measurements are taken as a difference, we propagate the errors to obtain the detection limit of AN and PN measurements. Allan variance is defined as half of the square of the time average of the differences between consecutive readings of  $y$ , which is the NO<sub>2</sub> concentration reading, sampled over the sampling period (T) (Allan 1966).

$$\sigma_y^2(T) = \frac{1}{2} \langle (y_{n+1} - y_n)^2 \rangle \quad (2-21)$$

The Allan variance ( $\sigma^2$ ) is calculated at two different NO<sub>2</sub> concentrations by sending a continuous flow of zero air (0 ppb of NO<sub>2</sub>) or 17 ppb of NO<sub>2</sub> through the TD-CAPS instrument for over 8 hours. Figure 2.9 shows the time series of the NO<sub>2</sub> concentration and the Allan variance as a function of integration time. As the integration time increases,  $\sigma^2$  decreases. The detection limit ( $3\sigma$  precision) of the CAPS monitor is reported as 0.060 ppb (Kebabian et al. 2008). In our study, the detection limit ( $3\sigma$  precision) of a TD-CAPS reading is 0.143 and 0.145 for 0 and 17 ppb of NO<sub>2</sub>, respectively, at a 10 s integration time. The  $3\sigma$  value did not change when going through the channels or when sampled directly from the CAPS. The value changes slightly with NO<sub>2</sub> concentration. Our detection limit is higher than the value reported in (Kebabian et al. 2008), possibly due to wear and tear of the instrument.

We use  $3\sigma=0.144$  for AN and PN measurements. Since AN and PN concentration are determined by taking the difference between two channels (Ch), the precision of AN and PN measurements becomes 0.19 after error propagation:

$$\sigma_{AN,PN} = (\text{Ch1} - \text{Ch2}) \pm \sqrt{\sigma_{\text{Ch1}}^2 + \sigma_{\text{Ch2}}^2} \quad (\text{Eq 21})$$

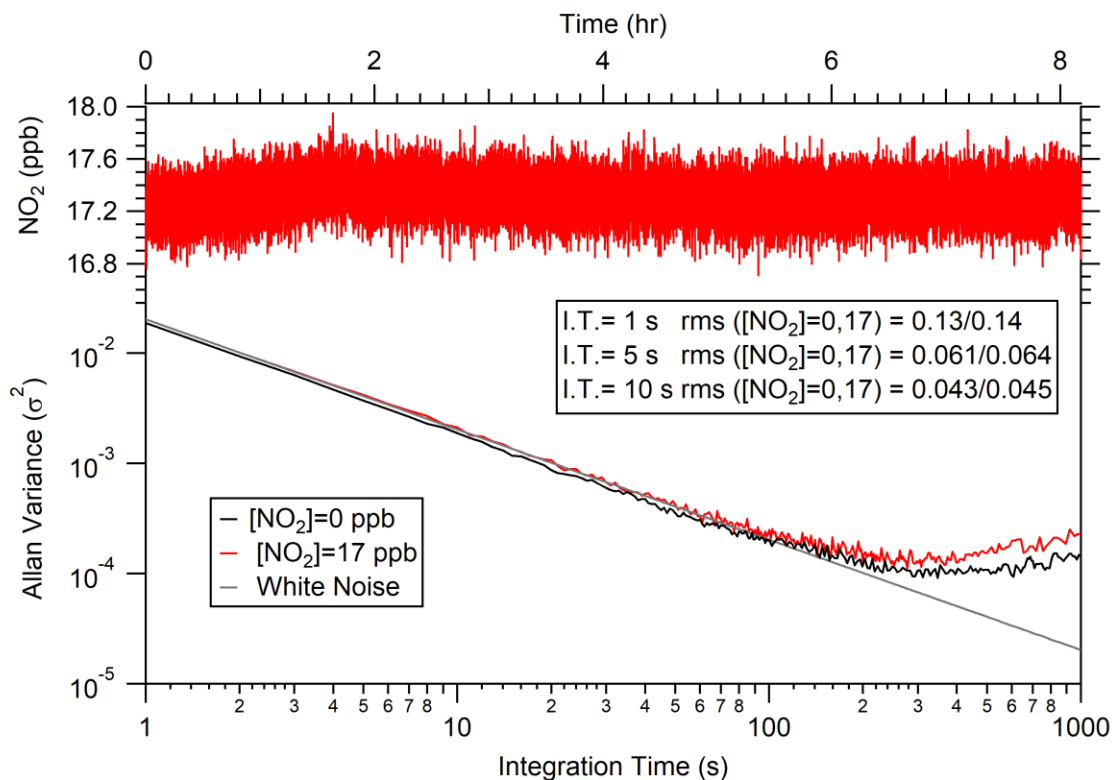


**Figure 2.9** Detection Limit of TD-CAPS

Monte Carlo Analysis is used to determine how well the experimental fit represents the data and total uncertainty. Monte Carlo Analysis is a computational technique that calculates the possible outcomes by repeatedly assigning range of values to any factor with an uncertainty, based on a probability distribution (Rubinstein and Kroese 2016). For our study, the uncertainty of each fit equation is calculated in the following steps. The fit parameters are assigned by generating normal random variables within the uncertainties shown in Table 2.1. For a given initial reactant concentration, such as IPN and NO, the standard deviation for the fit equation is obtained by running 10000 simulations. 10000 runs were selected because the computational time is fast and increasing the number of

runs did not improve the results. The simulations produce a range of possible outcomes for the fit equation. The standard deviation for the fit is then calculated by taking the average of the standard deviation for the experimental data. The uncertainty of the fit parameters is given in Table 2.1. One standard deviation represents the IPN+NO, PAN+NO case well, whereas three times the standard deviation ( $3\sigma$ ) includes the measurement points for the PAN+NO<sub>2</sub> case. Therefore, the total uncertainty of the AN and PN channels is given as  $3\sigma$ . In all cases, the experimental fit represents the data within 20% uncertainty.

The total uncertainty of the AN and PN channels is calculated as follows. The first step is to finalize the correction factors depending on the NO, NO<sub>2</sub> and O<sub>3</sub> concentrations. Second, we run the Monte Carlo simulation to calculate the uncertainty of AN and PN. Finally, the relative standard deviation of AN and PN is calculated by dividing the standard deviation by the mean PN from the simulation.

$$RelStd_{AN}(10000) = StdDev_{AN}/Mean_{AN} \quad (2-22)$$

$$RelStd_{PN}(10000) = StdDev_{PN}/Mean_{PN} \quad (2-23)$$

The relative standard deviation of AN and PN due to presence of NO and NO<sub>2</sub> is shown in Figure A. 7 and Figure A. 8. The uncertainty depends on AN<sub>0</sub> and PN<sub>0</sub>. We use 5 ppb of AN<sub>0</sub> and PN<sub>0</sub> for this example. The uncertainty in AN is higher at lower NO concentrations (<10 ppb) since the experimental fit is better at higher NO concentrations. The uncertainty does not change with NO<sub>2</sub> concentration. This is expected since IPN does not vary with the addition of NO<sub>2</sub>. The uncertainty of PN does not show any clear trend

with the NO<sub>2</sub> concentration due to the scattered experimental data observed with the addition of NO<sub>2</sub> to PAN. In the case of NO, the uncertainty is higher for NO concentrations between 10-40 ppb. In this region, the chemical interference varies more with PAN and NO concentrations and causing the experimental fit to deviate from the experimental data.

## **2.4 Chamber Experiment Measurements with TD-CAPS**

In order to evaluate the performance and further improve the TD-CAPS instrument, we measured secondary organic aerosol produced in the Georgia Tech Environmental Chamber (GTEC) facility (Boyd et al., 2015). AN and PN are produced from photooxidation of  $\alpha$ -pinene in the presence of NO<sub>x</sub>, using HONO as an OH precursor (SI) and measured by the TD-CAPS and other well-established instruments.

Gas-phase AN and PN measured by TD-CAPS are compared with observations by the Filter Inlet for Gases and AEROSols (FIGAERO) High-Resolution Time-of-Flight Chemical-Ionization Mass Spectrometer (HR-ToF-CIMS) which provides real time molecular composition of species in both the gas- and particle-phase. Details of the operation of the instrument are given in (Sanchez et al. 2016). Gas-phase species were diluted with zero air in a 1:17 ratio right before the inlet. The instrument was calibrated with an organic nitrate standard,  $\alpha$ -pinene hydroxy nitrate, to calculate the concentration of detected species. A conversion factor of 5.1-8 Hz/ppt is used to quantify the AN and PN produced in the chamber experiment. Other gas-phase measurements include O<sub>3</sub> measured by an O<sub>3</sub> analyzer (Teledyne T400) and NO concentrations measured using a Chemiluminescence NO<sub>x</sub> monitor (Teledyne 200EU).

Particle-phase organic nitrates measured by the TD-CAPS are compared with those measured by High-Resolution Time-of-Flight Aerosol Mass Spectrometer (HR-ToF-AMS). As the experiment was performed in dry conditions, all the nitrate signal is assumed to be from the organic nitrate (Takeuchi and Ng). Moreover, the collection efficiency is assumed to be 1. The collection efficiency can be calculated by using Scanning Mobility Particle Sizer (SMPS, TSI). The SMPS measures the total volume of aerosol and HR-ToF-AMS measures the mass, therefore, using an aerosol density, the mass measurement can be converted to volume and directly compared to the SMPS measurement. However, the aerosol density can vary during the experiment so this method may not be accurate.

#### 2.4.1 TD-CAPS and HR-TOF-CIMS Comparison

Since the O<sub>3</sub> concentrations in this experiment are much lower than the NO and NO<sub>2</sub> concentrations, we do not need to apply the correction factors derived for O<sub>3</sub>+NO and O<sub>3</sub>+NO<sub>2</sub> mixtures. Therefore, the equations used for correcting the gAN and gPN measurements are reduced to the following:

$$[\text{gAN}] = \frac{[\text{gAN}]_0}{f(\text{NO}, \text{IPN})} \quad (2-24)$$

$$[\text{gPN}] = \frac{[\text{gPN}]_0}{f(\text{NO}_2) f(\text{NO}, \text{PAN})} \quad (2-25)$$

We recommend that the characterization and chamber experiments to be performed within a short amount of time since the applied correction factors can change with the sampling history of the quartz tube. However, we do not have an IPN+NO measurement

close to the date of experiment. Therefore, we use average of the previous values to correct for this interference. Figure A. 9 shows two different curves, one converging at 2.1 and the other on 3.28. These were done at different times and the magnitude of the interference changed. We use the average of these two values and the uncertainty is calculated by taking the difference between the curves and the mean. In addition, Figure 2.10 shows that NO concentration increases to  $\sim 400$  ppb within 1-2 minutes. This high concentration of NO makes the IPN dependency insignificant. Therefore, the correction is reduced to the following equation which we apply to the AN channel.

$$f(\text{NO}, \text{IPN}) = 2.69 \pm 0.58 \quad (2-26)$$

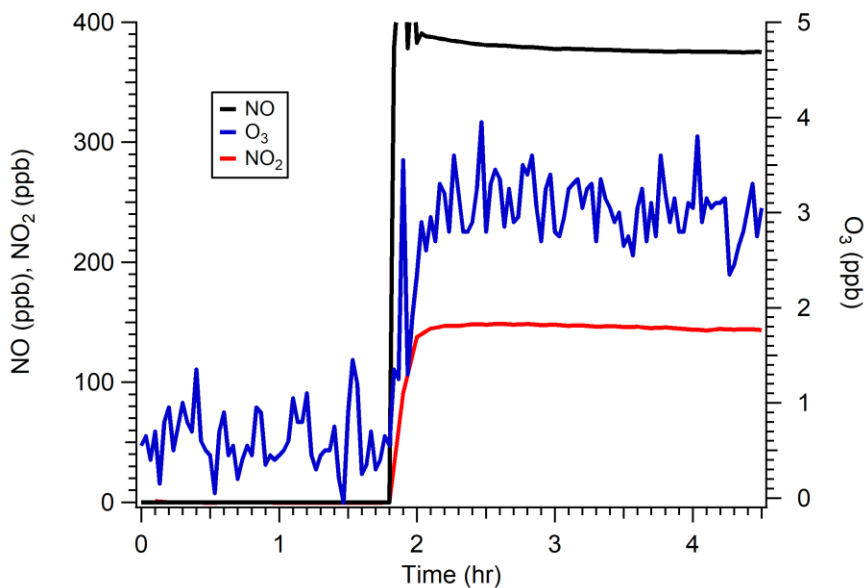


**Figure 2.10 NO, NO<sub>2</sub> and O<sub>3</sub> Time series at the chamber experiment where  $\alpha$ -pinene is oxidized by HONO**

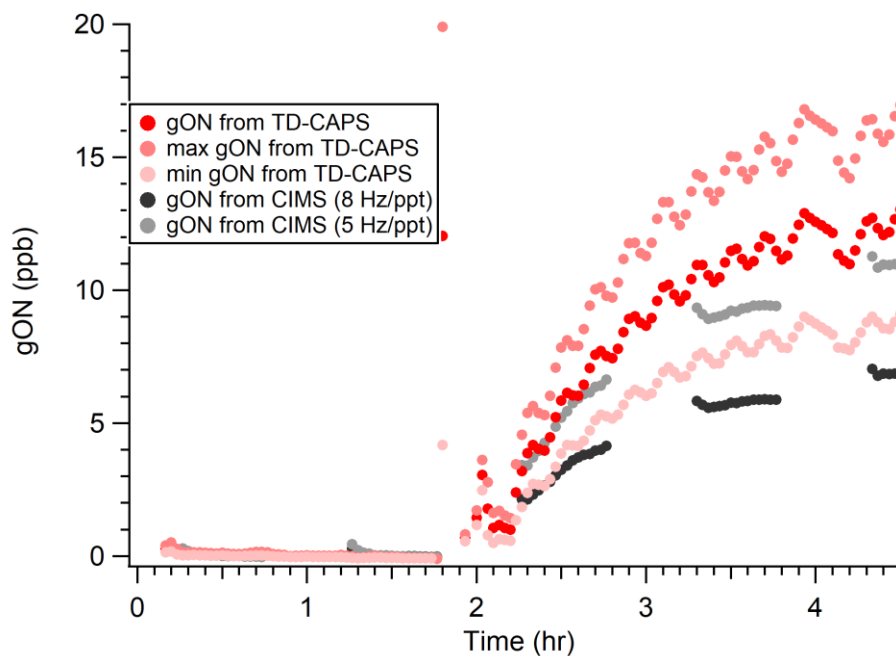
The finalized fit equations (Eq 25 and Eq 26) represent the chamber experiment conditions and used to calculate gas phase AN (gAN) and PN (gPN). Total gas phase organic nitrate is obtained by adding gAN and gPN and then correcting for dilution. Once AN and PN concentrations are determined, the uncertainty of gAN and gPN is found using Monte Carlo Analysis by following the method described in Section 3.6. Eq. 24 is used to calculate the uncertainty of the AN channel. The uncertainty of gAN and gPN ( $3*\sigma$ ) is 19 % and 47 %, respectively. The uncertainty of gAN from Eq (2-24) is consistent with the uncertainty of the reduced fit function (Eq (2-26)) which is 21 %.

The overall uncertainty of organic nitrate is calculated by propagating the error of the AN and PN measurements:

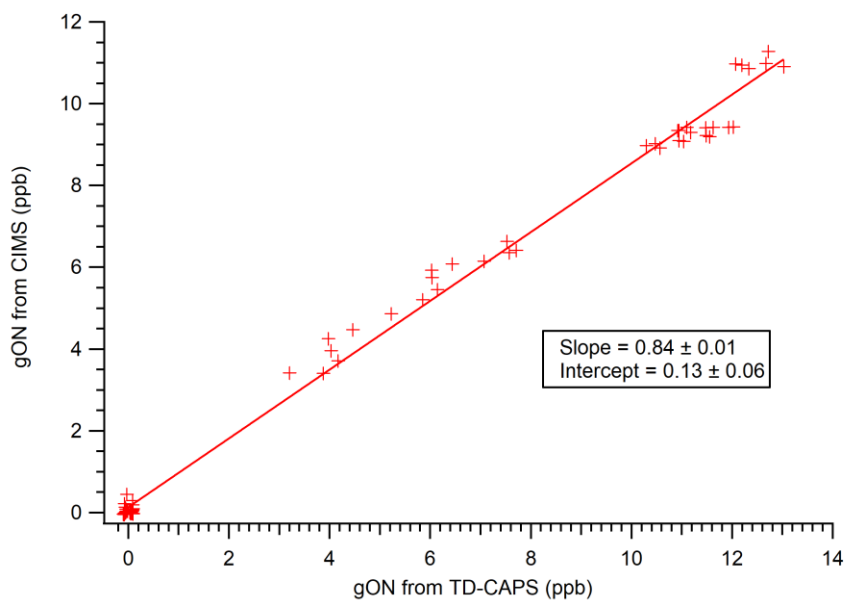
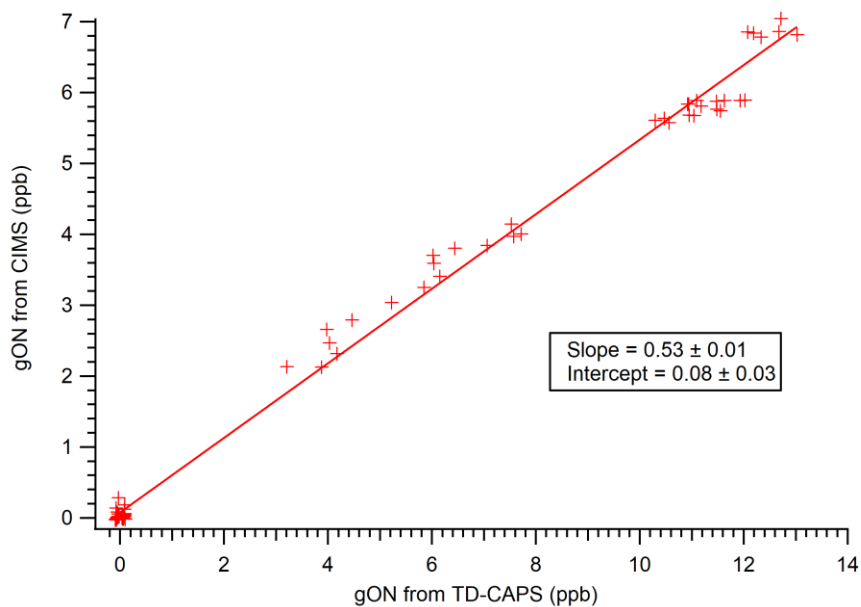
$$[\sigma_{gAN+gPN}] = \left( \sqrt{(\sigma_{gAN})^2 + (\sigma_{gPN})^2} \right) \quad (2-27)$$

Figure 2.11 shows the time series of total gAN+gPN measured by TD-CAPS and sum of  $C_xH_yN_{1-2}O_z$  measured by HR-TOF-CIMS. A scatter-plot of TD-CAPS vs HR-TOF-CIMS, using the upper and lower sensitivities (8 Hz/ppt and 5.1 Hz/ppt), gives a slope of 0.53 and 0.84, respectively (Figure 2.12). There is a good correlation between these two measurement techniques ( $R^2 = 0.994$ ). We calculate the sum of  $C_xH_yN_{1-2}O_z$  concentration measured by HR-TOF-CIMS using only one standard compound. It is noted that the sensitivity of I-CIMS varies by orders of magnitude (Aljawhary, Lee and Abbatt 2013; Lee et al. 2014) and this compound may not be representative of all the AN and PN products. In addition, CIMS is not sensitive to monofunctional AN with short carbon chains (Beaver et al. 2012), though we expect these compounds to contribute to the total ON

measured by the TD-CAPS. Beaver et al 2012 measured alkyl and multifunctional organic nitrates with TD-LIF (gas + particle phase) and  $\text{CF}_3\text{O}^-$ -CIMS during at the BEARPEX field site. There the sum of individual nitrates measured by  $\text{CF}_3\text{O}^-$ -CIMS was 85-91% of the total nitrates measured by TD-LIF which shows these instruments are in close agreement.



**Figure 2.11 Time series of gON obtained by TD-CAPS and  $\text{C}_x\text{H}_y\text{N}_{1-2}\text{O}_z$  by FIGEARO-CIMS**



**Figure 2.12 Scatter Plot of gON measured with TD-CAPS and FIGEARO-CIMS a)**

**5.1 Hz/ppt b) 8 Hz/ppt**

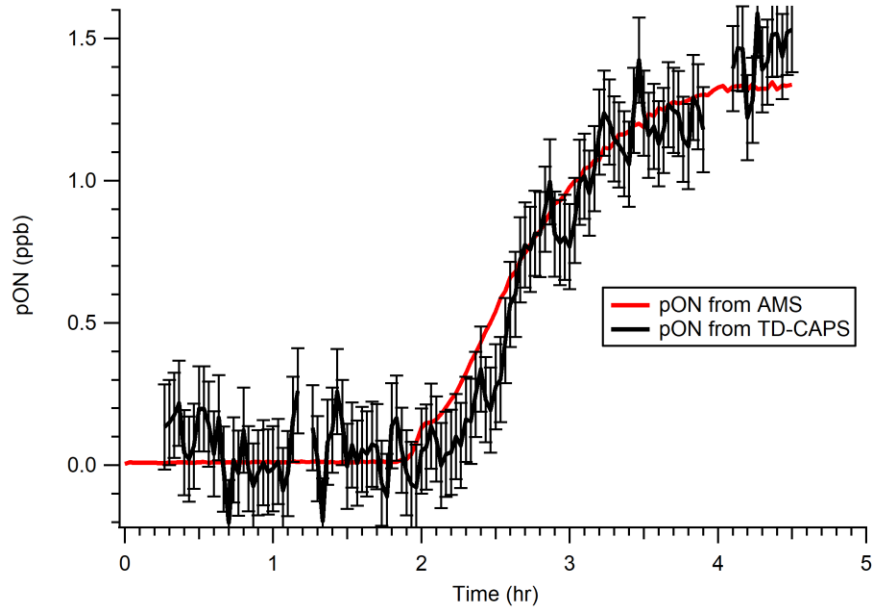
*2.4.2 TD-CAPS and HR-TOF-AMS Comparison*

Particle-phase measurements do not require any correction factors since gas species are removed by the charcoal denuder. Therefore, total particle alkyl nitrate and peroxy nitrate (pAN+pPN) is:

$$\text{pAN} + \text{pPN} = [\text{NO}_2]_{653 \text{ K}} - [\text{NO}_2]_{\text{Reference}} \quad (2-28)$$

Figure 2.13 shows the time series and scatter plot of pAN+pPN measured by TD-CAPS and HR-TOF-AMS. These figures show a good agreement between the two measurement techniques. The slope of the scatter plot is 1.01 and  $R^2$  is 0.95. Potential loss mechanisms for particle-phase measurements are due to transmission efficiency of particles through the denuder and the efficiency of evaporation and conversion of the particle organic nitrates (Rollins et al. 2010). They calculated time required for complete evaporation of the particles using a model which integrates the Hertz-Knudsen. For evaporation coefficient of 1 and particles with saturation concentration bigger than  $10^{-5} \mu\text{g}/\text{m}^{-3}$  they found particles evaporate less than 10 ms. The residence time in our heater section is 0.8 seconds which should be sufficient for complete evaporation. They also calculated the evaporation in the denuder with residence time of 9.3 s due to removal of gas phase species which changes significantly with the saturation concentration ( $C^*$ ). Transmission efficiency is found >97% for  $C^* < 1$  and 88% for  $C^*=10$  with particles > 100 nm. They also found that significant particle loss may occur for particles of  $C^* > 100$ . In our study, the residence time is 25.7 s which decreases the transmission efficiency to 91% for the particles with  $C^* < 1$  and 66% loss for the particles with  $C^*$  equal to 10. Considering the loss of particles due to evaporation in the denuder, measured pON is underestimating the actual

concentration. Assuming collection efficiency of 1 for HR-TOF-AMS also gives the underestimated concentration. The actual concentration can be as high as two times of the measured concentration considering the collection efficiency calculated from SMPS and HR-TOF-AMS.



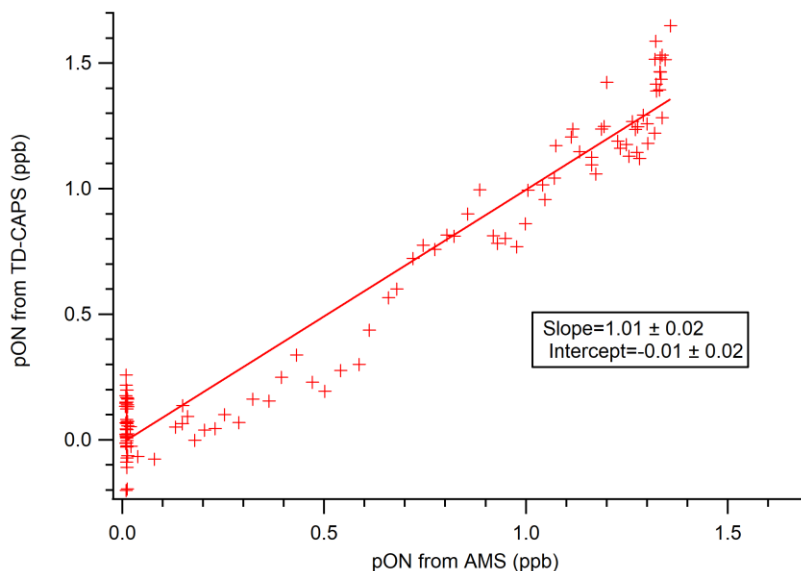


**Figure 2.13 a) Time series of pON measured with TD-CAPS and AMS b) Scatter Plot of pON measured with TD-CAPS and AMS**

### 2.4.3 Partitioning Coefficient

Direct measurements of gas and particle-phase organic nitrates enables us to calculate the bulk partitioning coefficient. Figure 2.14 shows that under typical ambient conditions,  $<40 \mu\text{g}/\text{m}^3$  of organic aerosol,  $<15\%$  of organic nitrates partition to the particle phase for these oxidation conditions (High- $\text{NO}_x$ ,  $\alpha$ -Pinene). This percentage is similar to the partitioning coefficient calculated for organic nitrates measured by (Bean and Hildebrandt Ruiz 2016) during laboratory experiments where the partitioning coefficient increases up to 20% as total organic concentration increases to  $120 \mu\text{g}/\text{m}^3$ . They used  $\text{H}_2\text{O}_2$  as the OH radical source and different NO:precursor ratios so their product distributions could be different from our study. Organic nitrate partitioning is also compared with the

values calculated by (Rollins et al. 2013) for organic nitrate measurements during the CalNex campaign where on average 21% of  $\Sigma$ ANs are in the condensed phase at of  $<10 \mu\text{g}/\text{m}^3$  of organic aerosol.

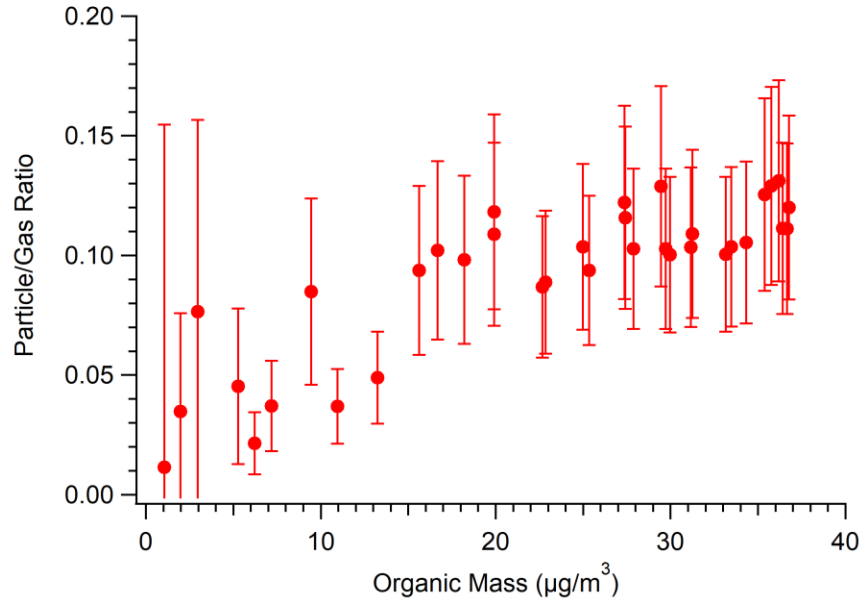


Figure 2.14 Particle/Gas Ratio changing with the organic mass

### CHAPTER 3. SUMMARY AND FUTURE WORK

We have developed a TD-CAPS instrument to measure total AN and PN in the gas and particle phases. We characterized the instrument using IPN and PAN as representative AN and PN compounds and quantify chemical interferences from side reactions due to the presence of O<sub>3</sub>, NO, and NO<sub>2</sub>. Correction factors for binary mixtures of these compounds over a wide range of concentrations that are representative of rural /urban environments and laboratory chamber reaction conditions are derived. In order to evaluate the performance of the TD-CAPS, organic nitrates are produced from the photooxidation of  $\alpha$ -pinene in the GTEC facility. The uncertainty of gAN and gPN is found as 19% and 47 % under the experimental conditions. Gas-phase organic nitrates measured by TD-CAPS and HR-TOF-CIMS have a good correlation with an R<sup>2</sup> of 0.994. Differences absolute concentrations likely due to different sensitivities and the uncertainties associated with each instrument. Particle-phase organic nitrates measured by the TD-CAPS and HR-TOF-AMS are in good quantitative agreement and correlate well (R<sup>2</sup> = 0.95).

The measurement capabilities of the TD-CAPS are shown using a chamber experiment where the gAN and gPN concentrations are in the ppb range, the time variation of these species is low and RH < 5%, which prevents possible interferences from water vapor. In future work, we will explore gAN and gPN produced under conditions that represent daytime and night-time oxidation conditions. Further characterization

experiments are warranted to quantify possible interferences from other species such as  $\text{HNO}_3$  and  $\text{N}_2\text{O}_5$ . For ambient measurements, where gAN and gPN are present at sub-ppb levels, the chemical interferences due to  $\text{NO}_x$  need to be reduced significantly. One approach could be to reduce the residence time in the reactor to decrease the extent of the side reactions in the channels. Another approach is to reduce the number of the radicals that react with  $\text{NO}_x$  by introducing glass beads in the reactors. These would increase the surface area inside the reactors enhancing radical wall-loss rates. In addition, characterization experiments can be performed with gas- and particle-phase organic nitrate standards to investigate whether more functionalized organic nitrates have similar interferences as the compounds we studied. Particle-phase measurements can be improved by quantification of particle losses in the denuder and of the efficiency of ON evaporation in the heaters. Finally, possible interferences from  $\text{NH}_4\text{NO}_3$  need to be explored for ambient measurements.

## APPENDIX A.SUPPLEMENTARY FOR CHAPTER 2

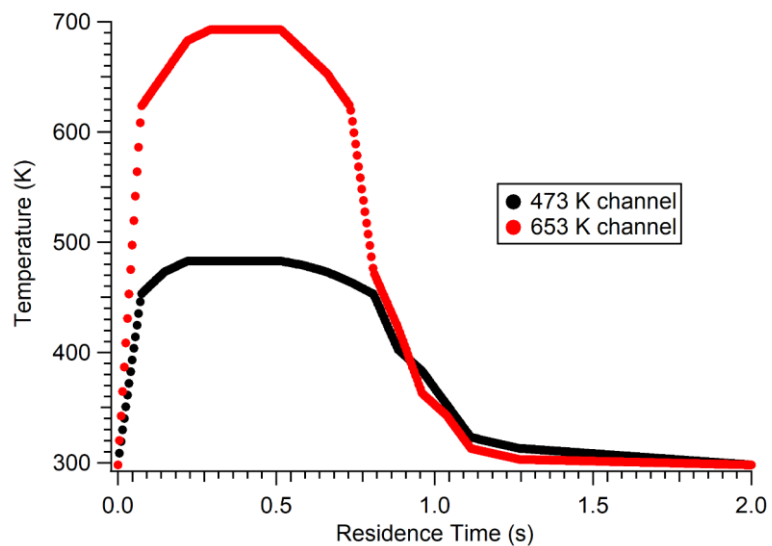


Figure A. 1 Temperature profiles of the heaters

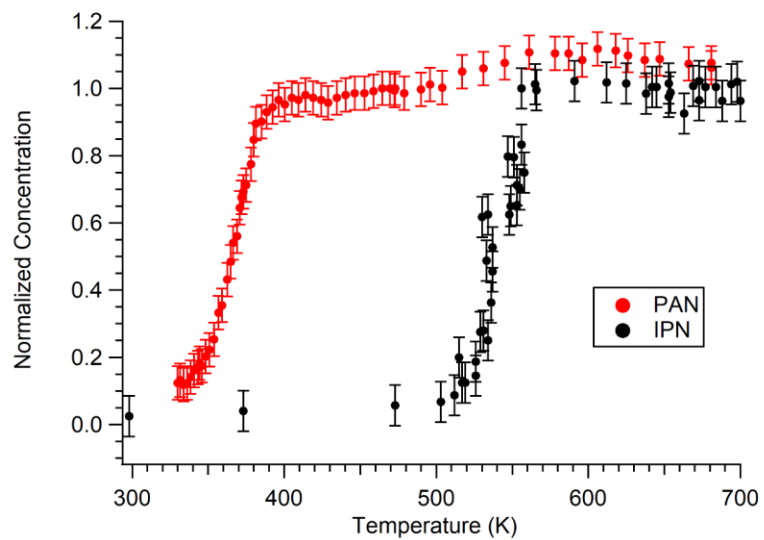
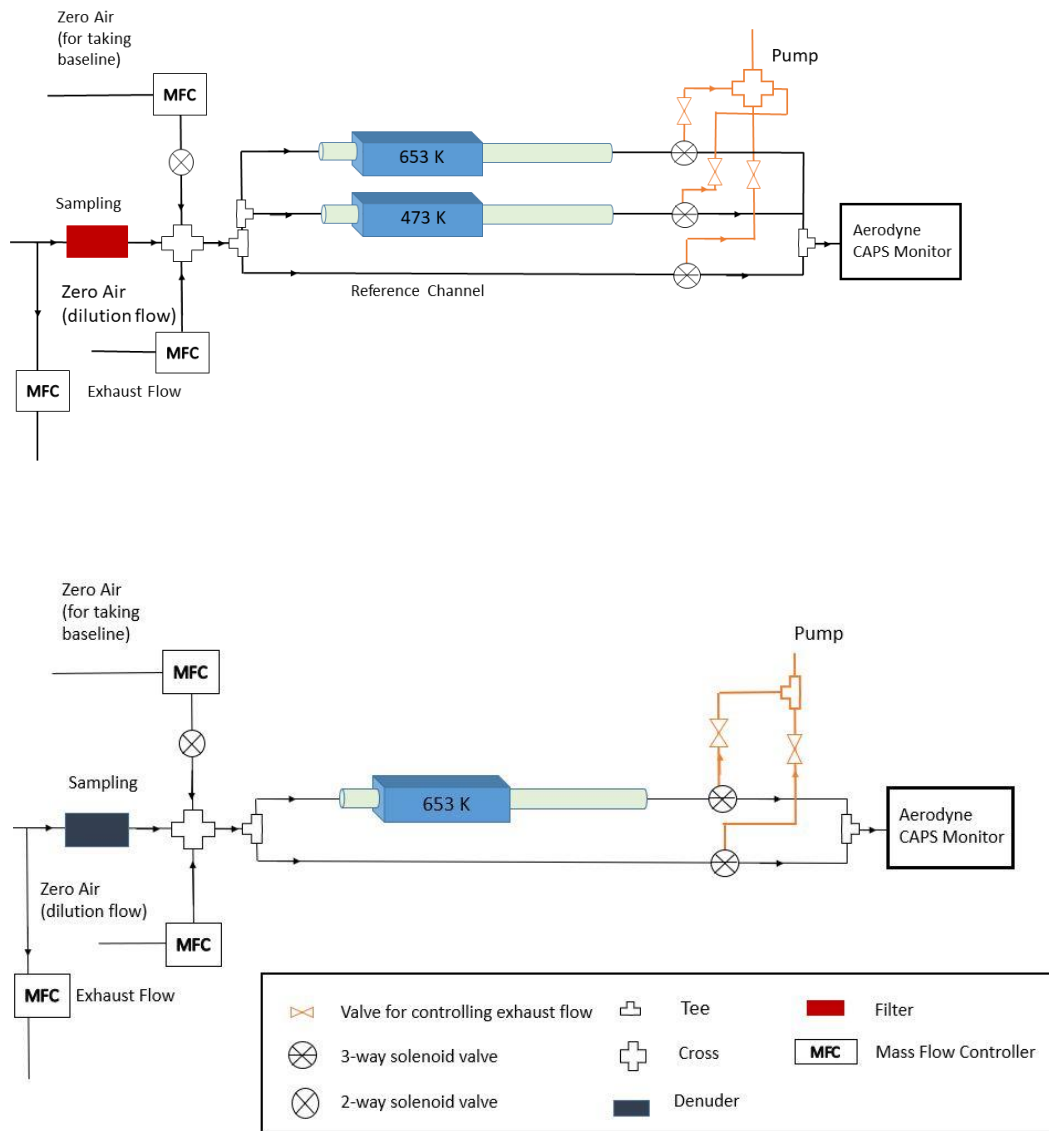
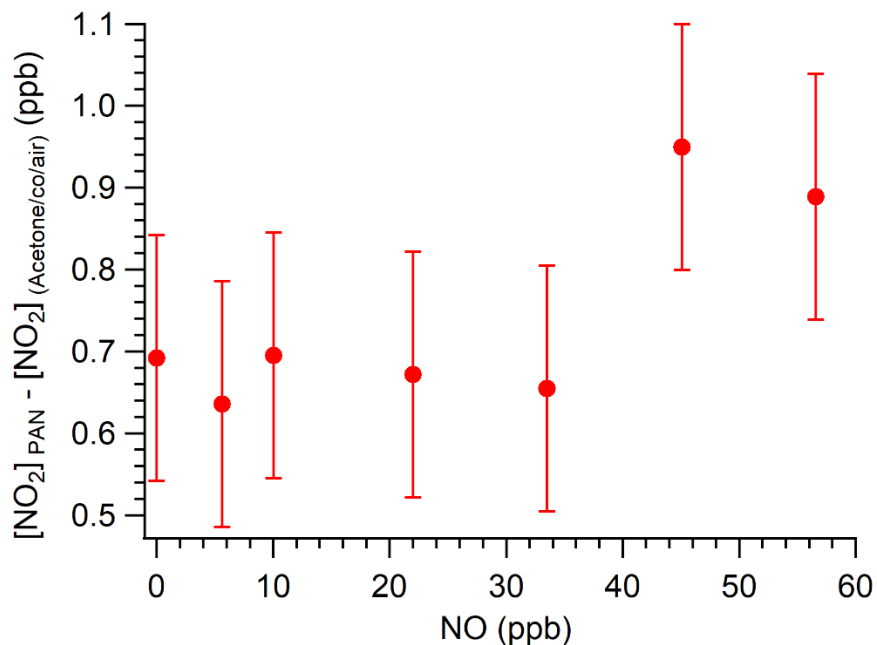


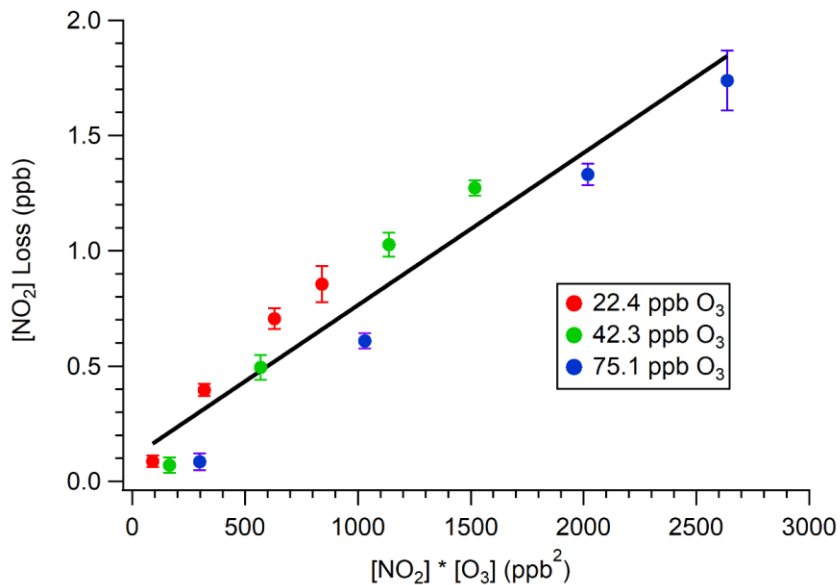
Figure A. 2 IPN and PAN Thermograms



**Figure A. 3 Upper: Gas Phase TD-CAPS Setup Below: Particle Phase TD-CAPS Setup**



**Figure A. 4** Difference of NO<sub>2</sub> production from photolysis of acetone/CO/air mixture from acetone/CO/air mixture with the presence of NO



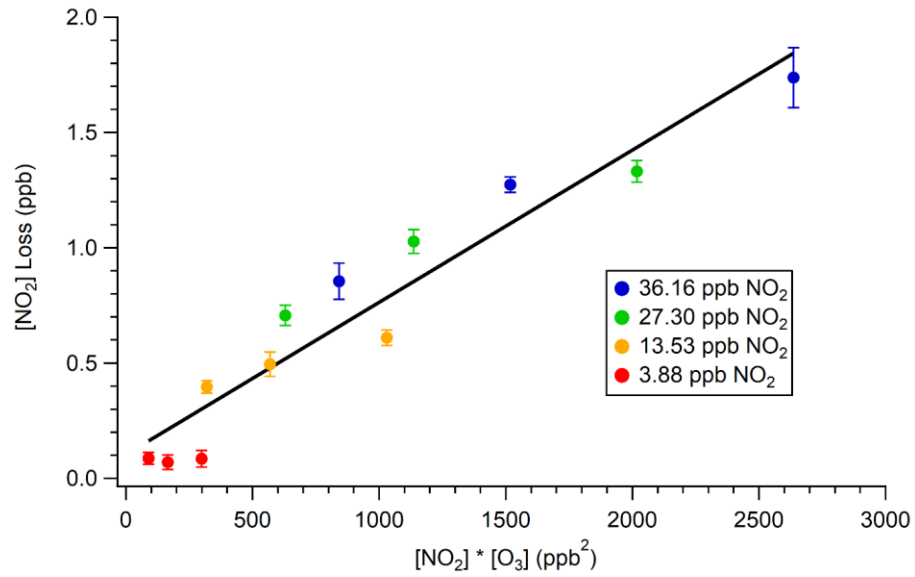


**Figure A. 5 NO<sub>2</sub> Loss due to O<sub>3</sub> thermal decomposition**

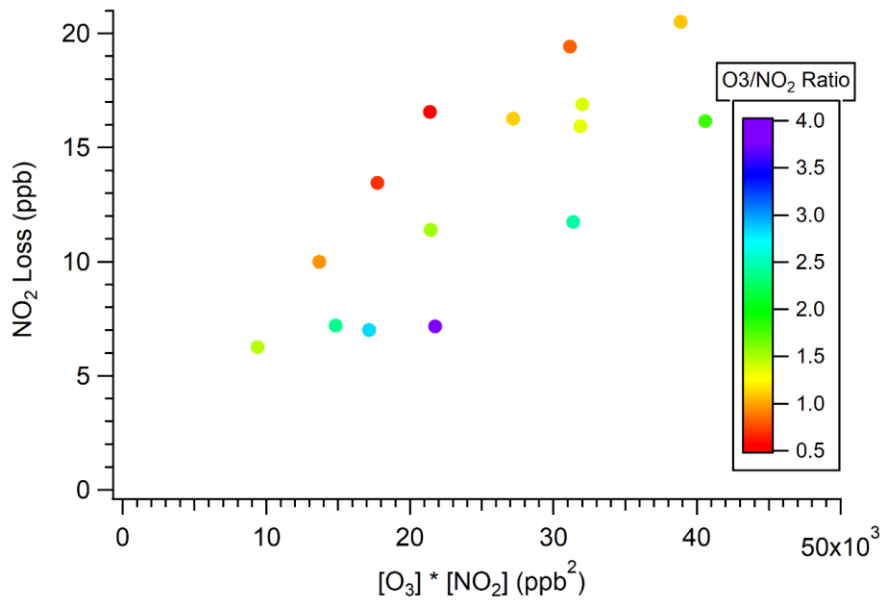


**Figure A. 6 NO<sub>2</sub> Loss due to O<sub>3</sub> thermal decomposition where O<sub>3</sub> concentration range is 109-288 ppb and NO<sub>2</sub> concentration range is 75-196 ppb**

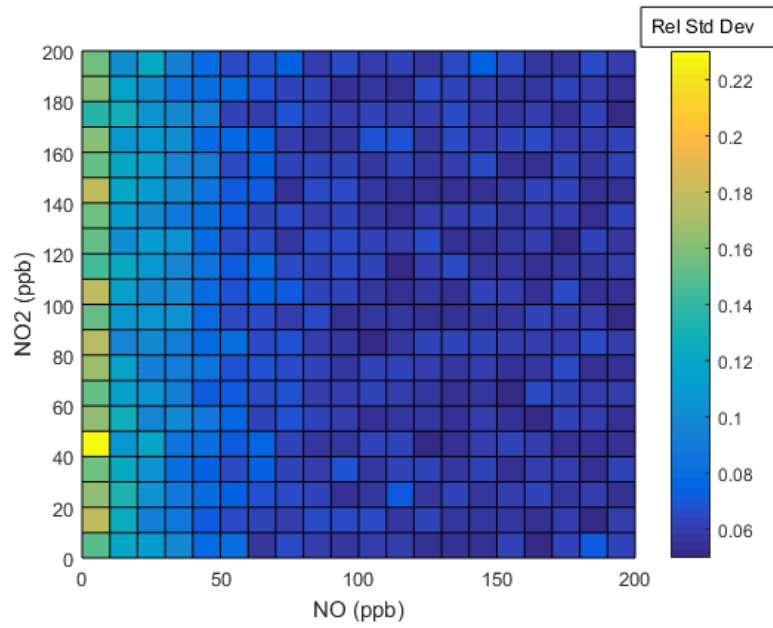


**Figure A. 7 Relative standard deviation of AN at 0-200 ppb NO and 0-200 ppb NO2**

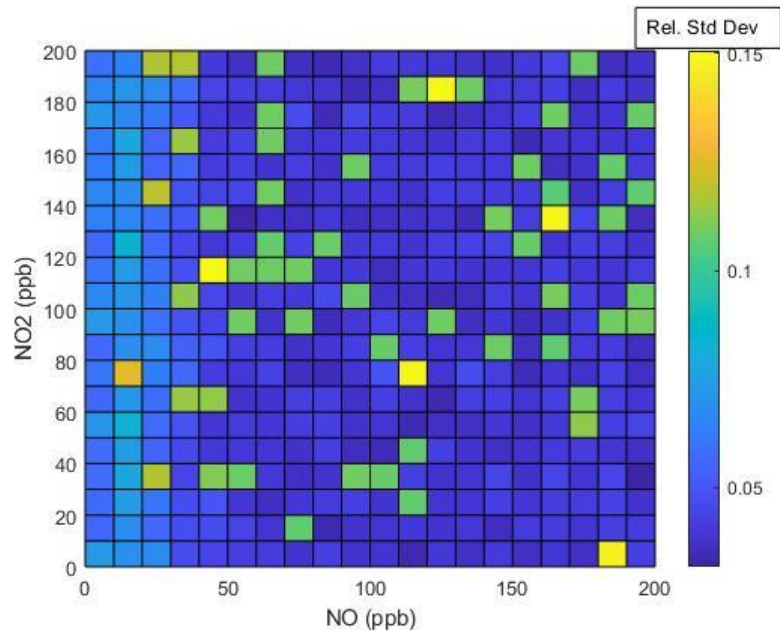


**Figure A. 8 Relative standard deviation of PN at 0-200 ppb NO and 0-200 ppb NO2**

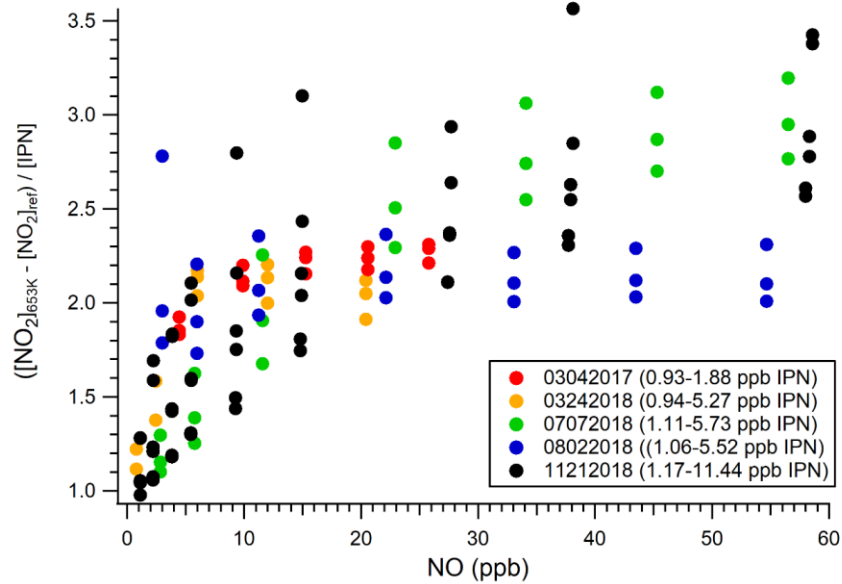


**Figure A. 9 Measurements of the difference signal (sampling from the 653K – reference channel) over IPN concentration when adding different amounts of NO to IPN at different times**

### Kinetic Box Model

- $i-C_3H_7ONO_2$  (IPN) =  $i-C_3H_7O + NO_2$  \*
- $i-C_3H_7ONO_2$  (IPN) =  $i-CH_3CHO + CH_3O_2$
- $i-C_3H_7O + O_2 = HO_2 + C_3H_6O$
- $i-C_3H_7O + NO_2 + M = i-C_3H_7ONO_2 + M$
- $CH_3O_2 + NO = CH_3O + NO_2$
- $CH_3O_2 + NO = CH_3NO_3$
- $CH_3O_2 + HO_2 = CHCO + O_2 + H_2O$
- $CH_3O_2 + HO_2 = CH_3OOH + O_2$
- $CH_3O_2 + NO_2 + M = CH_3O_2NO_2 + M$

- $\text{CH}_3\text{O} + \text{O}_2 = \text{HCHO} + \text{HO}_2$
- $\text{CH}_3\text{O}_2\text{NO}_2 = \text{CH}_3\text{O}_2 + \text{NO}_2$
- $\text{PAN} = \text{CH}_3\text{C}(\text{O})\text{O}_2 + \text{NO}_2$
- $\text{CH}_3\text{C}(\text{O})\text{O}_2 + \text{NO} = \text{CH}_3\text{O}_2 + \text{NO}_2$
- $\text{CH}_3\text{C}(\text{O})\text{O}_2 + \text{NO}_2 = \text{PAN}$
- $\text{CH}_3\text{C}(\text{O})\text{O}_2 + \text{CH}_3\text{O}_2 = \text{CH}_3\text{COOH}$
- $\text{CH}_3\text{C}(\text{O})\text{O}_2 + \text{CH}_3\text{O}_2 = \text{CH}_3\text{COO} + \text{CH}_3\text{O}_2 + \text{O}_2$
- $\text{CH}_3\text{C}(\text{O})\text{O}_2 + \text{HO}_2 = \text{CH}_3\text{COOH} + \text{O}_3$
- $\text{CH}_3\text{C}(\text{O})\text{O}_2 + \text{HO}_2 = \text{CH}_3\text{COOOH} + \text{O}_2$
- $\text{CH}_3\text{C}(\text{O})\text{O}_2 + \text{HO}_2 = \text{CH}_3\text{O}_2 + \text{OH}$

$\text{RO}_2 = \{ \text{'CH}_3\text{O}_2\text{'}; \text{'CH}_3\text{C}(\text{O})\text{O}_2\text{'}$

- $\text{CH}_3\text{O}_2 + \text{RO}_2 = \text{CH}_3\text{O}$
- $\text{CH}_3\text{O}_2 + \text{RO}_2 = \text{CH}_3\text{OH}$
- $\text{CH}_3\text{O}_2 + \text{RO}_2 = \text{HCHO}$
- $\text{CH}_3\text{C}(\text{O})\text{O}_2 + \text{RO}_2 = \text{CH}_3\text{CO}_2\text{H}$
- $\text{CH}_3\text{C}(\text{O})\text{O}_2 + \text{RO}_2 = \text{CH}_3\text{O}_2$
- $\text{NO} + \text{NO} = \text{NO}_2 + \text{NO}_2$
- $\text{HO}_2 + \text{NO} = \text{OH} + \text{NO}_2$
- $\text{OH} + \text{NO}_2 = \text{HNO}_3$
- $\text{HO}_2 + \text{NO}_2 = \text{HO}_2\text{NO}_2$
- $\text{HO}_2\text{NO}_2 = \text{HO}_2 + \text{NO}_2$
- $\text{OH} + \text{NO} = \text{HONO}$
- $\text{HO}_2 + \text{HO}_2 = \text{H}_2\text{O}_2$
- $\text{HO}_2 + \text{HO} = \text{H}_2\text{O} + \text{O}_2$
- $\text{HO}_2 + \text{NO} = \text{OH} + \text{NO}_2$

- $\text{NO} + \text{NO} = \text{NO}_2 + \text{NO}_2$
- $\text{O}_3 = \text{O}_2 + \text{O}^{**}$
- $\text{O} + \text{O}_2 + \text{M} = \text{O}_3 + \text{M}$
- $\text{O} + \text{O}_3 = 2 \text{O}_2$
- $\text{O} + \text{NO} = \text{NO}_2$
- $\text{O} + \text{NO}_2 = \text{NO} + \text{O}_2$
- $\text{O} + \text{NO}_2 = \text{NO}_3$
- $\text{NO} + \text{O}_3 = \text{NO}_2 + \text{O}_2$
- $\text{NO}_2 + \text{O}_3 = \text{NO}_3 + \text{O}_2$
- $\text{NO} + \text{NO}_3 = \text{NO}_2 + \text{NO}_2$
- $\text{NO}_2 + \text{NO}_3 = \text{NO} + \text{NO}_2$
- $\text{NO}_2 + \text{NO}_3 = \text{N}_2\text{O}_5$
- $\text{N}_2\text{O}_5 = \text{NO}_2 + \text{NO}_3$
- $\text{OH} + \text{O}_3 = \text{HO}_2$
  
- $\text{OH} + \text{H}_2\text{O}_2 = \text{HO}_2$
  
- $\text{HO}_2 + \text{O}_3 = \text{OH}$
  
- $\text{OH} + \text{NO}_3 = \text{HO}_2 + \text{NO}_2$
  
- $\text{OH} + \text{HONO} = \text{NO}_2$
  
- $\text{OH} + \text{HO}_2\text{NO}_2 = \text{NO}_2$
  
- $\text{OH} + \text{HNO}_3 = \text{NO}_3$

Reaction rate coefficients were taken from Master Chemical Mechanisms (MCM) v 3.3.1. with the exception of *{Day, 2002 #17}{Curran, 2006 #98}* and *\*\*{Peukert, 2013 #99}{Thieser, 2016 #19}*

**AN and PN are produced from photooxidation of  $\alpha$ -pinene in the presence of NO<sub>x</sub>, using HONO as an OH precursor**

Before the experiment, the reactor was flushed with zero air (Aadco, 747-14) for at least a day. Then, seed aerosol is injected into the chamber by atomizing a 0.015 M (NH<sub>4</sub>)<sub>2</sub>SO<sub>4</sub> seed solution (Sigma Aldrich) until the seed concentration is approximately 20  $\mu\text{g m}^{-3}$ . Before reaching the chamber, the seed aerosol is sent through a silica gel dryer to remove water from the particles. Next, liquid  $\alpha$ -pinene (>99%, Sigma Aldrich) is transferred to a glass bulb using a syringe. 5 lpm of zero air flow-through the bulb and carry the VOC into the chamber, reaching a concentration of 40 ppb. After seed aerosol and  $\alpha$ -pinene reach a stable concentration HONO is injected. HONO is synthesized by the dropwise addition of 20 mL of a 1% wt aqueous NaNO<sub>2</sub> (VWR International) to 40 mL of a 10% wt H<sub>2</sub>SO<sub>4</sub> (VWR International) in a glass bulb. After the addition, we flow zero air over the solution to transfer the HONO into the chamber (Tuet et al 2017). NO and NO<sub>2</sub> are also formed as byproducts of the HONO synthesis. Once HONO reaches a steady concentration, as tracked by the NO and NO<sub>2</sub> concentrations in the chamber, the UV lights are turned on to start the photooxidation.

# APPENDIX B. KINETIC MODELLING OF FORMATION AND EVAPORATION OF SOA FROM NO<sub>3</sub> OXIDATION OF PURE AND MIXED MONOTERPENES

Thomas Berkemeier<sup>1,a,\*</sup>, Masayuki Takeuchi<sup>2</sup>, Gamze Eris<sup>1</sup>, and Nga L. Ng<sup>1,3,\*</sup>

[1] School of Chemical and Biomolecular Engineering, Georgia Institute of Technology,  
Atlanta, GA, USA

[2] School of Civil and Environmental Engineering, Georgia Institute of Technology,  
Atlanta, GA, USA

[3] School of Earth and Atmospheric Sciences, Georgia Institute of Technology, Atlanta,  
GA, USA

[a] now at: Multiphase Chemistry Department, Max Planck Institute for Chemistry, Mainz,  
Germany

Correspondence to: Thomas Berkemeier (t.berkemeier@mpic.de) and Nga Lee Ng  
(ng@chbe.gatech.edu)

**Abstract.** Organic aerosol constitutes a major fraction of the global aerosol burden and is predominantly formed as secondary organic aerosol (SOA). Environmental chambers have been used extensively to study aerosol formation and evolution under controlled conditions

similar to the atmosphere, but quantitative prediction of the outcome of these experiments is generally not achieved, which signifies our lack in understanding of these results and limits their portability to large scale models. In general, kinetic models employing state-of-the-art explicit chemical mechanisms fail to describe the mass concentration and composition of SOA obtained from chamber experiments. Specifically, chemical reactions involving nitrate radical ( $\text{NO}_3$ ) oxidation of volatile organic compounds (VOCs) are a source of major uncertainty for assessing the chemical and physical properties of oxidation products. Here, we introduce a kinetic model that treats gas-phase chemistry, gas-particle partitioning, particle-phase oligomerization and chamber wall loss and use it to describe the oxidation of the monoterpenes  $\alpha$ -pinene and limonene with  $\text{NO}_3$ . The model can reproduce aerosol mass and nitration degrees in experiments using either pure precursors or their mixtures and infers volatility distributions of products, branching ratios of reactive intermediates as well as particle-phase reaction rates. The gas-phase chemistry in the model is based on the Master Chemical Mechanism (MCM), but trades speciation of single compounds for the overall ability of quantitatively describing SOA formation by using a lumped chemical mechanism. The complex branching into a multitude of individual products in MCM is replaced in this model with product volatility distributions, detailed peroxy ( $\text{RO}_2$ ) and alkoxy ( $\text{RO}$ ) radical chemistry and amended by a particle-phase oligomerization scheme. The kinetic parameters obtained in this study are constrained by a set of SOA formation and evaporation experiments conducted in the Georgia Tech Environmental Chamber (GTEC) facility. For both precursors, we present volatility distributions of nitrated and non-nitrated reaction products that are obtained by fitting the

kinetic model systematically to the experimental data using a global optimization method, the Monte Carlo Genetic Algorithm (MCGA). The results presented here provide new mechanistic insight into the processes leading to formation and evaporation of SOA. Most notably, much of the non-linear behavior of precursor mixtures can be understood by RO<sub>2</sub> fate and reversible oligomerization reactions in the particle phase, but some effects could be accredited to kinetic limitations of mass transport in the particle phase. The methodologies described in this work provide a basis for quantitative analysis of multi-source data from environmental chamber experiments with manageable computational effort.

## **1 Introduction**

Atmospheric aerosol particles play an important role in the Earth system by influencing weather and climate, enabling long-range transport of chemical compounds and negatively affecting public health (Pöschl, 2005; Fuzzi et al., 2006). A major contributor to the global aerosol burden is the oxidation of volatile organic compounds (VOCs) to condensable organic species, which leads to formation of secondary organic aerosol (SOA, Kanakidou et al., 2005). Important classes of SOA precursors include alkanes and aromatic compounds, which are often emitted from anthropogenic sources, as well as alkenes such as isoprene, monoterpenes, and sesquiterpenes, which are predominantly emitted by trees (Hallquist et al., 2009). The monoterpenes  $\alpha$ -pinene and limonene are among the most abundant and well-studied SOA precursors (Seinfeld and Pandis, 2016). Atmospheric oxidation of alkenes occurs mainly through three oxidants: the hydroxyl radical (OH), which is produced in daylight and is short-lived; the abundant, but comparatively slow

reacting ozone ( $O_3$ ); and the nitrate radical ( $NO_3$ ), which is the major source of SOA at nighttime, but also contributes to SOA formation during daytime, despite its quick photolysis (Liebmann et al., 2019). The oxidation of VOCs by  $NO_3$  results in the formation of high yields of nitrated organic compounds, alkyl nitrates and peroxy acyl nitrates, which are produced in lower quantities through other atmospheric oxidation channels such as reaction of organic peroxy radicals ( $RO_2$ ) or hydroperoxy radicals ( $HO_2$ ) with nitric oxide (NO) (Perring et al., 2013;Ng et al., 2017). These organic nitrates (ON) play an important role in the atmospheric nitrogen budget by serving as temporary or permanent sink for highly reactive nitrogen oxides ( $NO$ ,  $NO_2 = NO_x$ ). Reactive nitrogen oxides constitute an integral part of oxidation cycles in the atmosphere and are made significantly less reactive through reaction to ON.

Due to their sufficiently low volatility, ON can be taken up into atmospheric aerosol particles, where they are shielded from gas-phase chemical decomposition, causing  $NO_x$  to be temporarily removed from atmospheric oxidation cycling. While  $NO_x$  can be recycled back into the atmosphere via photolysis (Müller et al., 2014), photooxidation (Nah et al., 2016), and thermal decomposition of ON, permanent removal can occur through ON hydrolysis (Takeuchi and Ng, 2019) and deposition processes (Nguyen et al., 2015).

Furthermore, the presence of ON affects the formation and persistence of organic aerosol (OA) (Ng et al., 2017). The contribution of particulate ON mass (pON) to total organic aerosol has been investigated previously in laboratory studies by mass-spectrometric methods (Fry et al., 2009;Fry et al., 2011;Fry et al., 2014;Boyd et al., 2015;Nah et al.,

2016;Boyd et al., 2017;Faxon et al., 2018;Takeuchi and Ng, 2019) and a radioactive tracer method (Berkemeier et al., 2016), revealing that organic nitrate mass fractions can reach up to 0.8 in the particle phase under certain conditions. Although ambient measurements varied strongly temporally and regionally, the ratio of ON mass to the total organic mass has been shown to reach up to 0.77 (Ng et al., 2017 and references therein).

Despite the importance of ON to the dynamics of SOA formation, the chemical mechanism for their formation in the gas and particle phases is still under discussion (Kurtén et al., 2017;Claflin and Ziemann, 2018;Draper et al., 2019). The Master Chemical Mechanism (MCM) provides a resource of the gas phase degradation chemistry of typical SOA precursors with atmospheric oxidants (Saunders et al., 2003;Jenkin et al., 2003). However, application of MCM to the oxidation of monoterpenes with  $\text{NO}_3$  leads to a significant underestimation of particle mass and pON/OA (Boyd et al., 2017;Faxon et al., 2018).

It has been hypothesized and shown recently that a majority of SOA might exist in oligomerized form (Kalberer et al., 2004;Gao et al., 2010), which might alter their evaporation behavior (Baltensperger et al., 2005;D'Ambro et al., 2018). In that case, the evaporation time scale is determined by chemical decomposition instead of equilibrium partitioning due to volatility (Pankow, 1994). Additionally, organic aerosol particles can exhibit a highly viscous phase state (Virtanen et al., 2010;Koop et al., 2011;Reid et al., 2018), which leads to kinetic limitations in evaporation (Vaden et al., 2011), reduced particle-phase chemistry (Gatzsche et al., 2017), and non-equilibrium partitioning (Cappa and Wilson, 2011).

To describe kinetic limitations in mass transport, a number of kinetic multi-layer models have been developed recently to describe aerosol particles and cloud droplets, including KM-SUB (Shiraiwa et al., 2010), KM-GAP (Shiraiwa et al., 2012), ADCHAM (Roldin et al., 2014), and MOSAIC (Zaveri et al., 2008;Zaveri et al., 2014). These models are capable of explicitly resolving mass transport and chemical reactions within aerosol particles. Using these models, Shiraiwa et al. (2013) and Zaveri et al. (2018) were able to find evidence for diffusion limitation affecting SOA formation dynamics by inspection of the evolution of particle size distributions. Yli-Juuti et al. (2017) and Tikkanen et al. (2019) used an evaporation model based on KM-GAP to describe the interaction of volatility and viscosity during isothermal dilution as a function of different environmental conditions. However, to our best knowledge, no model has been presented that describes all aspects of gas-phase chemistry, particle-phase chemistry, gas-particle partitioning and bulk diffusion of SOA.

A model capable of describing all these aspects of SOA formation must rely on a large set of kinetic parameters, which are often not readily accessible. However, model parameters can be systematically altered so the model matches experimental data, an approach often referred to as inverse modelling. Simultaneously optimizing multiple model parameters can often be unfeasible via manual optimization and prompts the use of global optimization methods (Berkemeier et al., 2017;Berkemeier et al., 2013). As opposed to local optimization methods, global optimization algorithms are not as easily stuck in local minima and are able to reliably find solutions of difficult optimization problems. In conjunction with a kinetic model, global optimization algorithms represent a powerful tool

that allows to infer molecular level information from macroscopic data. Thus, global optimization algorithms based on differential evolution, such as the Monte Carlo Genetic Algorithm (MCGA), have become increasingly popular in the modelling of complex multiphase chemical systems (Berkemeier et al., 2017; Marshall et al., 2018; Tikkanen et al., 2019).

In a previous study, Boyd et al. (2017) showed that the retained aerosol mass from oxidation of limonene with  $\text{NO}_3$  after heating from 25 °C to 40 °C is significantly different than the mass obtained from oxidizing limonene at 40 °C. They further showed that the evaporation behavior of mixtures of limonene SOA and  $\beta$ -pinene SOA crucially depends on the order in which oxidation occurred. Limonene SOA evaporated less in the experiment where oxidation of limonene was followed by oxidation of  $\beta$ -pinene, compared to the experiment where both precursors were oxidized simultaneously. At the time, it was only postulated that diffusion limitations and/or oligomerization reactions could have led to these observations. In this work, we conduct new environmental chamber experiments and apply a novel kinetic modelling framework to investigate whether gas-phase chemistry, equilibrium partitioning, and particle-phase chemistry can describe the formation and evaporation of monoterpene SOA from oxidation of  $\alpha$ -pinene, limonene, and mixtures of both precursors with  $\text{NO}_3$ .  $\alpha$ -pinene is chosen over  $\beta$ -pinene since it shows a more distinct evaporation behavior to limonene SOA and is the overall better-understood SOA precursor. We perform experiments at a lower initial temperature compared to Boyd et al. (2017) to include a second heating stage in the experiments. We focus the modelling efforts on the experimental observables aerosol mass and organic nitrogen content (contribution of

particulate ON mass to total organic aerosol, pON/OA) as a function of time in the reaction chamber. The model uses a simplified, lumped kinetic mechanism based on MCM (Berkemeier et al., 2016), but modifies some of the branching ratios in RO<sub>2</sub> chemistry and adds chemical reactivity in the particle phase. Building on the observations of Boyd et al. (2017) in their mixed precursor experiments, we investigate the linearity of these two observables by quantitative comparison of formation and evaporation of SOA from pure and mixed monoterpene precursors. Lastly, we use the kinetic model to perform a sensitivity analysis on the potential effect of retarded bulk diffusion due to a viscous phase state. The kinetic modelling framework consisting of a kinetic multi-layer model based on KM-GAP and the MCGA algorithm is used as analysis tool to unravel the mechanistic interactions between reactive intermediates and oxidation products that can lead to non-additivity of the investigated reaction systems

## 2 Experimental and theoretical methods

### 2.1 Georgia Tech Environmental Chamber (GTEC)

The aerosol formation and evaporation experiments are performed as batch reactions in the GTEC facility, which consists of two separate 12 m<sup>3</sup> Teflon chambers in a temperature- and humidity-controlled enclosure (Boyd et al., 2015). A consistent experimental routine is maintained for all experiments presented in this study and resembles the method used by Boyd et al. (2017) with small updates. Concentrations of O<sub>3</sub> and NO<sub>x</sub> are determined with a UV absorption O<sub>3</sub> analyzer (Teledyne T400) and a chemiluminescence NO<sub>x</sub> monitor (Teledyne 200 EU), respectively. Aerosol particle number and volume concentrations are

measured using a scanning mobility particle sizer (SMPS, TSI), which consists of a differential mobility analyzer (DMA, TSI 3040) and a condensation particle counter (CPC, TSI 3775). Bulk aerosol composition is measured using a High Resolution Time-of-Flight Aerosol Mass Spectrometer (HR-ToF-AMS, DeCarlo et al., 2006).

The Teflon chamber is flushed with zero air for at least 24 h and the chamber enclosure is cooled to 5 °C several hours prior to each experiment, to ensure full equilibration with regard to temperature, pressure, and humidity. Monoterpene oxidation is initiated at 5 °C and under dry conditions (RH < 5 %). All experiments are conducted using ammonium sulfate seed particles. Seed particles are generated by atomizing a 15 mM ammonium sulfate solution into the chamber for 20 minutes, which typically results in particle number concentrations around 20 000 cm<sup>-3</sup> and mass concentrations of 28 – 41 µg/m<sup>3</sup>. Simultaneously, monoterpene precursors are injected into the chamber. Injection volumes of the precursors are chosen to achieve consistent total aerosol mass concentrations around 100 µg/m<sup>3</sup> in all experiments, based on knowledge about aerosol yields in trial experiments for this study. For  $\alpha$ -pinene, we use a micro syringe to inject a known volume of liquid into a mildly heated glass bulb from which a 5 L/min zero air flow carries the evaporating fumes into the chamber. For limonene, the required liquid volume is so low that the use of micro syringes is a source of non-negligible uncertainty and hence a gas cylinder filled with 0.85 ppm limonene, calibrated and confirmed using gas chromatography with flame ionization detection (GC-FID), is used to inject a known volume of gas into the chamber over the course of several minutes. NO<sub>3</sub> is produced by oxidation of NO<sub>2</sub> with O<sub>3</sub> (generated by passing zero air through a photochemical ozone generator) in a 1.5 L flow tube (0.9 L/min

flow, 100 s residence time). The reaction mixture is optimized so  $\text{NO}_3$  and  $\text{N}_2\text{O}_5$  are produced in high yields, with no significant amount of  $\text{O}_3$  entering the chamber. This is achieved by using a 2:1 ratio of  $\text{NO}_2$  and  $\text{O}_3$ .  $\text{N}_2\text{O}_5$  decomposes in the chamber to release  $\text{NO}_3$  over time. Injection of  $\text{NO}_3/\text{N}_2\text{O}_5$  marks the beginning of the reaction.

When peak SOA growth is reached, which is typically achieved in under 4 hours of the experiment, the chamber enclosure temperature is raised to 25 °C and, after another waiting period, to 42 °C. The temperature changes take approximately 90 minutes in both cases. Temperature profiles are reported alongside the experimental results in Fig. 2.

In total, four experiments are conducted, either with a single monoterpene precursor, pure  $\alpha$ -pinene (APN) and pure limonene (LIM), or with a mixture of both precursors. In the case where both precursors are used, the oxidation occurred in one of two variants: simultaneous (MIX) or sequential oxidation (SEQ). In case of the MIX experiment, both precursors are injected simultaneously into the chamber prior to  $\text{NO}_3/\text{N}_2\text{O}_5$  injection. In case of the SEQ experiment, peak growth of the first precursor oxidation is first awaited. The first oxidation is followed by a second  $\text{NO}_3/\text{N}_2\text{O}_5$  injection and injection of the second VOC precursor shortly thereafter. An 8-fold excess of  $\text{N}_2\text{O}_5$  is used for pure limonene experiments, and a 4-fold excess used for pure  $\alpha$ -pinene experiments. In the mixed precursor experiments, the amount of injected  $\text{NO}_3/\text{N}_2\text{O}_5$  is determined using the same ratios proportionately. A summary of all experimental conditions, including injected precursor amounts, aerosol mass, organic aerosol mass excluding seed, and SOA yields can be found in Table 2. It is noted that we refer to the total aerosol mass concentration

(sum of inorganic seed mass concentration and organic aerosol mass concentration) in the chamber simply as “aerosol mass” in our discussions. “SOA yield” refers to the ratio of produced organic aerosol mass concentration to the reacted VOC mass concentration (Odum et al., 1996).

## **2.2 Kinetic model**

The kinetic model calculations in this study are performed with a multi-compartmental model akin to the KM-SUB/KM-GAP model family (Shiraiwa et al., 2010; Shiraiwa et al., 2012). The model code is set up as a generator script that uses an input chemical mechanism to generate a system of differential equations that is able to describe the key physical and chemical processes in the GTEC chamber. The model compartments include the chamber wall, the chamber gas phase, the particle near-surface gas phase, the particle surface and the particle bulk. The processes explicitly described in the model include injection of chemical compounds, wall loss of gas phase species, temperature change, gas diffusion to particles, condensation and evaporation at the particle surface, as well as chemical reaction in the gas and particle phases. Wall loss of particles is implicitly accounted for in this study by using wall loss-corrected SMPS data (Keywood et al., 2004; Nah et al., 2017).

All product molecules with volatility lower than  $10^{-5}$  Pa are allowed to partition into the topmost layer of the particles, according to their volatility. Gas-particle partitioning is explicitly treated in the model and equilibration between the particle near-surface gas phase and the particle surface is achieved by balancing surface adsorption and desorption rates. This way, evaporation and condensation kinetics are treated more realistically than in a

model assuming instantaneous equilibrium partitioning. The adsorption flux  $J_{ads,X}$  of a molecule  $X$  is calculated from the collision flux from the particle near-surface gas phase to the particle surface, which in turn is calculated from the mean thermal velocity  $w_X$  and the accommodation coefficient  $\alpha_{s,X}$ .  $\alpha_{s,X}$  is assumed to be 0.1 for all organic species in this study, in line with previous investigations (Julin et al., 2013).

$$J_{ads,X} = \alpha_{s,X} \cdot \frac{w_X}{4} \cdot [X]_{gs} \quad (1)$$

The desorption flux from the particle surface to the gas phase  $J_{des,X}$  is dependent on the vapor pressure  $p_{vap,X}$  and the ratio of the concentration of  $X$  in the particle near-surface bulk layer  $[X]_{b1}$  and the sum of all other species  $Y_j$  in that layer.

$$J_{des,X} = \frac{\alpha_{s,X} \cdot w_X \cdot p_{vap,X} \cdot N_A \cdot [X]_{b1}}{4 \cdot R \cdot T \cdot \sum [Y_j]_{b1}} \quad (2)$$

Here,  $R$  is the universal gas constant,  $T$  the temperature, and  $N_A$  is Avogadro's number. The vapor pressure of product compounds is assumed to be temperature dependent with a precursor-dependent effective enthalpy of volatilization,  $\Delta H_{vap,Z}$  in kJ/mol, where  $Z$  is the precursor of  $X$  and  $T_0$  refers to the reference temperature 298 K. We assume this single effective enthalpy to be representative for the entire product spectrum and hence independent of  $C^*$ .

$$p_{vap,X}(T) = p_{vap,X}(T_0) \cdot \exp \frac{-\Delta H_{vap,Z}}{R \cdot (T - 298)} \quad (3)$$

Note that in this study only a single well-mixed layer is used to describe the aerosol phase. New particle formation from low-volatility vapors is not treated in this model, so seed particles have to be pre-defined. Seed particles are initialized as covered with a very small amount of non-volatile organics (0.005 ppb gas phase mixing ratio) to aid in computation of gas-particle partitioning.

The model can be run in two modes: lumped mode, in which only vapor pressure bins are defined, and explicit mode, in which vapor pressures must be pre-supplied for all participating species. In the following, we will describe the specific lumped mode used in this study.

### **2.3 Lumped Chemical Mechanism**

The gas-phase chemical mechanism, summarized in Fig. 1a, is modeled after the initial reaction steps in the MCM, but does not assume specific sum or structural formulas of product molecules. The validity of this approach has been shown in previous work (Berkemeier et al., 2016). For limonene SOA, we apply the same general chemistry, but consider the oxidation of both double bonds individually, which leads to the more complex reaction scheme shown in Fig. S1. Note that oxidation of the second double bond of limonene with  $\text{NO}_3$  is not considered in MCM. However, we have shown previously that including oxidation of the second double bond leads to a significantly improved correlation between a kinetic model and chamber experiments (Boyd et al., 2017).

To account for chemical identity, the major product classes, nitrated and non-nitrated organic molecules, are subdivided into volatility bins (Fig. 1b) following the concept of a

volatility basis set (VBS; Donahue et al., 2011). The six volatility bins employed in this study are chosen to have increased resolution and hence achieve maximum sensitivity around the experimental range of 10-100  $\mu\text{g}/\text{m}^3$ , but still cover a wider range of volatilities: (1)  $1.32 \cdot 10^{-12}$  Pa ( $C^* = 0.01 \mu\text{g}/\text{m}^3$ ), (2)  $1.32 \cdot 10^{-10}$  Pa ( $C^* = 1 \mu\text{g}/\text{m}^3$ ), (3)  $1.32 \cdot 10^{-9}$  Pa ( $C^* = 10 \mu\text{g}/\text{m}^3$ ), (4)  $1.32 \cdot 10^{-8}$  Pa ( $C^* = 100 \mu\text{g}/\text{m}^3$ ), (5)  $1.32 \cdot 10^{-7}$  Pa ( $C^* = 1000 \mu\text{g}/\text{m}^3$ ) and (6)  $1.32 \cdot 10^{-5}$  Pa ( $C^* = 100\,000 \mu\text{g}/\text{m}^3$ ) at 298 K.  $C^*$  is the saturation mass concentration, which indicates the organic aerosol mass at which a semi-volatile organic substance would be in the gas and particle phase in equal parts. Oligomeric species are chosen to be fully non-volatile and hence technically form a seventh volatility bin. The average molar mass of molecules in the organic aerosol phase is assumed to be 250 g/mol, which is similar to assumptions in previous publications (Berkemeier et al., 2016) and consistent with our measurements using chemical ionization high-resolution time-of-flight mass spectrometry with a special filter inlet that samples both the aerosol and gas phase (FIGAERO-HRToF-CIMS, Lopez-Hilfiker et al., 2014) that were conducted alongside this study (Takeuchi and Ng, 2019).

A specific aim of this study is the mechanistic analysis of ON formation. Therefore, the gas-phase formation of ON is treated in detail and has been expanded from the MCM template, which is detailed in Fig. S2. We assume that chemical reaction of  $\text{NO}_3$  with the terpenic precursor yields a nitrated peroxy radical ( $\text{R}^{\text{N}}\text{O}_2$ ). The fate of the nitrate group ( $-\text{ONO}_2$ ) in this radical is dependent on its radical branching ratios. Following MCM, we assume that the reaction of  $\text{R}^{\text{N}}\text{O}_2$  with  $\text{HO}_2$  yields a stable organic nitrate product, whereas reaction with  $\text{NO}$ ,  $\text{NO}_3$ ,  $\text{RO}_2$ , or unimolecular decay leads to formation of a nitrated alkoxy

radical ( $R^{\text{NO}}$ ), which can further stabilize under elimination of the nitrate group. Reaction of two  $RO_2$  may also yield dimers. Another channel of ON formation is the reaction of a non-nitrated peroxy radical ( $RO_2^{\text{II}}$ ) with NO. Following MCM, we assume that only  $RO_2^{\text{II}}$ , which is the main intermediate in monoterpene OH oxidation and a secondary intermediate of monoterpene ozonolysis, can undergo this reaction and is in that regard distinct from  $RO_2^{\text{I}}$ , which is the main intermediate in monoterpene ozonolysis. However, this  $RO_2^{\text{II}} + \text{NO}$  reaction channel has only minor implications in this study due to the low prevalence of NO under the employed reaction conditions, i.e., injection of  $\text{NO}_3/\text{N}_2\text{O}_5$  as well as no irradiance with UV lights.

Particle-phase chemistry is included as formation and decomposition of oligomers from monoterpene oxidation products. Possible reaction pathways for oligomerization include the formation of esters, aldols, hemiacetals, acetals, peroxyhemiacetals, and peroxyacetals from alcohol, aldehyde, hydroperoxide, and carboxylic acid moieties in the monoterpene oxidation products (Ziemann and Atkinson, 2012), but are lumped into a single reaction for simplicity. These oligomers are assumed to be non-volatile, but can re-partition back to the gas phase after decomposition into the monomeric building blocks. The information about volatility and nitration degree of monomers is retained during oligomerization and reinstated after their decomposition. This process is outlined in Fig. 1c. A detailed discussion of the oligomerization scheme is provided in the Supplement, Sect. S1 and Fig. S3. An overview of all reactions of the lumped model in the gas and particle phases is given in Table S1.

## 2.4 Global Optimization

The Monte Carlo Genetic Algorithm (MCGA; Berkemeier et al., 2017) is applied for inverse fitting of the kinetic model to the experimental data and determining the non-prescribed kinetic parameters listed in Table 1. The MCGA method consists of two steps: a Monte Carlo step and a genetic algorithm step. During the Monte Carlo step, kinetic parameter sets are randomly sampled from a defined parameter range and the residue between the model result and the experimental data is determined for each parameter set through evaluation of the kinetic model. During the genetic algorithm step, the parameter sets are optimized mimicking processes known from natural evolution: a survival mechanism retains best-fitting parameter sets, the recombination mechanic generates new parameter sets by combing parameters of high scoring sets, and the mutation step prevents early homogenization of the sample of parameter sets. To determine the model-experiment correlation, we use a least-squares approach that minimizes the sum of the squares of the residuals, Eq. 4. The estimator is normalized to the magnitude of the largest data point in a given sample,  $\max(Y_{\text{data},i})$ , and the number of data points  $n_i$  of data set  $i$ . Additionally, optional weighting factors  $w_i$  can be used to guide the optimization process.

$$f_i = w_i \sqrt{\frac{1}{n_i} \sum \left( \frac{Y_{\text{model}} - Y_{\text{data},i}}{\max(Y_{\text{data},i})} \right)^2} \quad (4)$$

After an optimization result is returned, a 1-dimensional golden-section search (Press et al., 2007, Sect. 10.2) is used to ensure conversion into a minimum of the optimization hypersurface. The simplex method (Press et al., 2007, Sect. 10.5) is used to find other

combinations of parameters that lead to equivalent model results (test of uniqueness). Weighting factors  $w_i$  can be used to assign a lower importance to data sets that e.g., exhibit large scatter due to experimental noise, represent experimental artifacts or are deemed only supplementary for the purpose of the optimization.

Note that for the experiments discussed in this manuscript, multiple model solutions can be obtained, dependent not only on the choice of data sets that is optimized to, but also on the choice of weighting factors. In the following sections, only one fit of the model to experimental data will be discussed as de-facto fit as it scored best in our choice of model-experiment correlation estimator. The fit is obtained by fitting to total aerosol mass and aerosol organic nitrate fraction (pON/OA) data of three experimental data sets (LIM, APN, and SEQ). The fourth experiment (MIX) is intentionally left out from the fitting process for cross-validation. We will discuss the dependence of the best fit on weighting factors and the uniqueness of the obtained model solution in a separate section, Sect. 3.5.

### 3 Results and discussion

#### 3.1 Pure limonene oxidation (LIM)

##### 3.2.1 Experimental observations (LIM)

Fig. 2a shows the total aerosol mass concentration (denoted as “aerosol mass”) during an experiment of limonene oxidation with  $\text{NO}_3$  in the presence of ammonium sulfate seed particles, and subsequent evaporation in the GTEC chamber, here referred to as “LIM” experiment. Oxidation at 5 °C initially causes a fast increase in aerosol mass (black open markers, left axis) from 29  $\mu\text{g}/\text{m}^3$  of seed mass to about 70  $\mu\text{g}/\text{m}^3$  of aerosol mass within the first 20 minutes of the experiment. Afterwards, aerosol growth slows down considerably, so that the peak aerosol mass of 110  $\mu\text{g}/\text{m}^3$  is reached only after 5 hours. The slow increase in aerosol mass in the beginning of the experiment is likely an important feature of the experimental data for determination of mass transfer and chemical reaction rates.

The produced aerosol mass corresponds to a SOA yield of 130 % (Table 2) and is observed to be constant in the chamber for several hours at 5 °C. Note that this observation is different from previous experiments conducted at 25 °C and 40 °C (Boyd et al., 2017), where peak aerosol mass was achieved swiftly and SOA yields at aerosol mass loading similar to this study were determined to be 174 % (constant yield) and 124 %, respectively. While the lower SOA yield at 40 °C compared to 25 °C can be explained with equilibrium partitioning theory, the lower mass yield observed at 5 °C in this study cannot.

After 7 hours of total experiment time, the temperature set point of the chamber enclosure is increased to 25 °C. The new temperature plateau is reached inside the Teflon chamber 90 minutes later (grey dashed line, right axis). The temperature change causes a slight reduction in aerosol mass from 110 to about 104  $\mu\text{g}/\text{m}^3$ . At the new temperature set point, aerosol mass is not constant, but rather decays at a constant rate. After about 19 hours, the temperature set point is increased to 42 °C, which again causes an immediate slight reduction in aerosol mass from 90 to about 83  $\mu\text{g}/\text{m}^3$ . At the new temperature plateau of 42 °C, aerosol mass once again decays at a constant rate that is comparable to the one previously observed.

### **3.2.2 Kinetic modelling results (LIM)**

In the following, kinetic modelling results are discussed in terms of a best fit that is obtained using the Monte Carlo Genetic Algorithm (MCGA). The uniqueness of this fit and potential pitfalls of the optimization process are discussed in Sects. 3.3.2 and 4. The kinetic model (red solid line in Fig. 2a) is able to reproduce the observed aerosol formation and evaporation behavior. In the model run at hand, the initial quick increase in aerosol mass is due to condensation of dimers formed in the gas phase through the  $\text{RO}_2 + \text{RO}_2$  channel (from now on referred to as “gas-phase dimers”), making up about 50 % of condensing material in the initial seconds and minutes. Subsequent growth is due to condensation of monomeric oxidation products (from now on referred to as “monomers”) of sufficiently low volatility. After 20 minutes, half of the aerosol mass at peak growth is

reached and the particle phase is mostly comprised of monomeric compounds, cf. Fig. 2b, panel (i), about one third of which still contain an C-C double bond (Fig. S4). These mono-unsaturated oxidation products either partition back into the gas phase where they can be oxidized further, or co-oligomerize in the particle phase with other oxidation products. The vapor pressure of the non-nitrated and nitrated mono-unsaturated oxidation products were fitted during the MCGA optimization and determined to have saturation mass concentrations  $C^*$  of 1560 and 292  $\mu\text{g}/\text{m}^3$  at 298 K, respectively. During peak growth, 27 % of oxidation products still contain a double bond in this model run, almost all of which are nitrated and present in the oligomer phase. Note that this is possible because we do not consider the oxidation of unsaturated compounds in the particle phase.

The volatility distributions determined with the global optimization can be found in Fig. S5a. The majority of limonene oxidation products in this model run occupies the 4<sup>th</sup> and 5<sup>th</sup> volatility bins ( $C^* = 100, 1000 \mu\text{g}/\text{m}^3$  at 298 K), which are mostly present in the gas phase under these reaction conditions. In the model, the slow increase in aerosol mass from 20 minutes to 5 hours of oxidation is due to oligomerization of monomers forming higher molecular weight structures through accretion reactions in the particle phase (from now on referred to as “oligomers”). According to the model fit, oligomerization occurs at a rate of  $1 \text{ h}^{-1}$ , hereby slowly removing semi-volatile species in the particle phase from the partitioning equilibrium and causing a slow drift of semi-volatiles from the gas phase into the particle phase. At peak growth, most of the organic material in the particle phase exists in an oligomeric state, cf. Fig. 2b, panel (ii), which explains the lack of initial evaporation caused by an increase in chamber temperature.

A potential justification for the observed lower SOA yield at 5 °C in this study compared to experiments performed at 25°C (Boyd et al., 2017) could be the temperature-dependence of the oligomerization rate constant. In chamber experiments, condensation of vapors onto the particles stands in competition with irreversible loss to the chamber walls, which we assume to be mostly temperature-independent. When oligomerization occurs more slowly, oxidation products from the 100 and 1000  $\mu\text{g}/\text{m}^3$  volatility bins are increasingly lost to the walls instead of being incorporated into the particle oligomer phase. Furthermore, Boyd et al. (2017) observed a lower aerosol mass when forming limonene SOA at 40 °C compared to first forming limonene SOA at 25 °C and then heating to 40 °C. Also here, a possible explanation is the formation of oligomers of semi-volatile vapors: the fractional amount of chemical species from the 100 and 1000  $\mu\text{g}/\text{m}^3$  volatility bins that partitions into the particle phase is much smaller at 40 °C and hence prevents mass accumulation through oligomerization.

The slow decay of aerosol mass between 6 and 24 hours of the experiment is attributed in the model to a slow unimolecular decay of oligomeric material with a rate constant of 0.04  $\text{h}^{-1}$  and subsequent evaporation of monomers at elevated temperatures, followed by irreversible deposition of vapors onto the chamber walls. The observed decomposition rate is slightly slower than the rate of 0.06-0.2  $\text{h}^{-1}$  reported by D'Ambro et al. (2018) for SOA formed from ozonolysis of  $\alpha$ -pinene. Following Le Chatelier's principle, removal of monomers from the equilibrium causes a constant drift of organic matter from oligomeric to monomeric state. Since the volatility of the monomeric subunit is retained in the model (for details see oligomerization mechanism in Fig. S3), this process is faster for monomers

that have higher volatilities because they partition into the gas phase more quickly and readily, causing an enrichment of low-volatility monomeric subunits in the particle phase. The (meta-)stability of organic material in the particle phase can hence be attributed not only to the stability of the oligomer bond, but also the volatility of the monomeric building blocks at this temperature.

Monomers are removed from the system by loss to the chamber walls, which is the main driver of loss of organic mass. The loss coefficient of gas-phase molecules to the chamber wall is determined to be  $3.3 \times 10^{-7}$ . This number is interpreted as a vapor-wall accommodation coefficient of molecules colliding with the chamber wall and is used for all organic molecules independent of their chemical structure. In this study, it is assumed that molecules adsorbed to the chamber walls are irreversibly lost for the time scale of the experiment. This can be explained by slow diffusion of molecules into the inner layer of the Teflon wall (Huang et al., 2018). In the geometry of the GTEC and for 250 g/mol molecules at 298 K, a loss coefficient of  $2.8 \times 10^{-7}$  corresponds to a loss rate of  $0.12 \text{ h}^{-1}$  or an equilibration time scale  $\tau_{\text{gwe}}$  of  $3.0 \times 10^4 \text{ s}$ , respectively. This number falls in-between values previously reported in the literature. Krechmer et al. (2016) as well as Yeh and Ziemann (2015) reported a  $\tau_{\text{gwe}}$  around  $1 \times 10^3 \text{ s}$  in their Teflon chamber, whereas vapor wall equilibration timescales measured in the CalTech chamber typically range from  $3 \times 10^4 \text{ s}$  and  $5 \times 10^5 \text{ s}$ , depending on the chemical identity of the investigated substance (Loza et al., 2010; Shiraiwa et al., 2013; Zhang et al., 2015a).

### **3.2 Pure $\alpha$ -pinene oxidation (APN)**

### 3.2.1 Experimental observations (APN)

Fig. 3a shows the aerosol mass during the corresponding experiment of  $\alpha$ -pinene oxidation with  $\text{NO}_3$ , here referred to as “APN” experiment. Similar to the LIM experiment described above, oxidation at 5 °C initially causes a fast increase in aerosol mass (black open markers), however, peak aerosol mass is reached already after 3 hours of oxidation at 109  $\mu\text{g}/\text{m}^3$ . Due to the larger amount of injected precursor, SOA yield is at 25.2 % significantly lower than observed in the limonene oxidation experiment (Table 2). However, this yield appears to be larger than previously reported for the oxidation of  $\alpha$ -pinene with  $\text{NO}_3$ : Hallquist et al. (1999) measured a 7 % yield (corresponding to 52.9  $\mu\text{g}/\text{m}^3$  organic aerosol) at 15 °C. Nah et al. (2016) measured a yield of 3.6 % (corresponding to 2.4  $\mu\text{g}/\text{m}^3$  organic aerosol) at room temperature. Fry et al. (2014) reported no significant aerosol growth at room temperature. This is indicative of the low temperature employed in the experiments having a significant impact on SOA yield.

After about 4 hours of total experiment time, the temperature set point of the chamber enclosure is increased to 25 °C, leading to a sharp and significant evaporation of organic material from aerosol particles. When the new temperature plateau is reached after 7 hours, aerosol mass has decreased to 80  $\mu\text{g}/\text{m}^3$ . Since evaporation has hardly slowed down by that time, heating to the new temperature set point of 42 °C is initiated after 8 hours of experiment time (i.e., without long waiting time at the 25 °C temperature plateau) to avoid losing too much volatile aerosol mass from evaporation. After a chamber temperature of 42 °C is reached after 10 hours, evaporation slows down considerably and continues at a

slow rate until the end of the experiment, where a minimum aerosol mass of  $57 \mu\text{g}/\text{m}^3$  is observed. With a seed mass of  $37.3 \mu\text{g}/\text{m}^3$ , this corresponds to a retained organic aerosol mass of about  $20 \mu\text{g}/\text{m}^3$  (cf. Table 2).

### 3.2.2 Kinetic modelling results (APN)

The kinetic model (blue solid line in Fig. 3a) shows a reasonable correlation to the experimental data. The detailed model analysis in Fig. 3b reveals that at peak growth, the aerosol is composed of about 57 % of monomers and an aggregate 43 % of higher molecular weight structures, i.e., 33 % oligomers and 11 % gas-phase dimers (Fig. 3b (i)). Upon increase in chamber temperature, the gas-phase dimer content increases considerably from 11 % to 31 % (panel ii) due to evaporation of monomers in volatility bins  $C^* = 1\text{-}100 \mu\text{g}/\text{m}^3$  and decomposition of oligomers. Hence, the slower evaporation of organic material toward the end of the experiment can be attributed to the fact that the remaining organic aerosol is only comprised of gas-phase dimers ( $C^* = 0.01 \mu\text{g}/\text{m}^3$ ), low-volatile monomers ( $C^* = 0.01\text{-}1 \mu\text{g}/\text{m}^3$  volatility bins) and oligomers composed of low-volatile monomer building blocks (Fig. 3b (ii)). The volatility distributions of the monomers produced from gas-phase chemistry (Fig. S5b) reveal that a large fraction of nitrated monomers occupy the highest volatility bin and does not partition into the particle phase. Since the majority of the oxidation products of the reaction of  $\alpha$ -pinene with  $\text{NO}_3$  are nitrated organics, this could explain the lower SOA yield compared to the reaction of  $\alpha$ -pinene with  $\text{O}_3$  or OH (Hoffmann et al., 1997;Griffin et al., 1999;Ng et al., 2007;Eddingsaas et al., 2012;Nah et al., 2017) since non-nitrated monomers also occupy lower volatility bins in this specific global optimization result.

Compared to the LIM experiment, peak aerosol mass is reached more quickly in the APN experiment. In the model solution, this is due to the determined oligomer formation rate being comparatively high at  $17.4 \text{ h}^{-1}$ , which is an order of magnitude faster than determined for the LIM experiment. On the other hand, the oligomer decomposition rate is determined to be  $3.3 \text{ h}^{-1}$ , which is two orders of magnitude quicker than that determined for the LIM experiment and one order of magnitude quicker than the rates reported by D'Ambro et al. (2018) for  $\alpha$ -pinene ozonolysis. This leads to an overall lower, more quickly formed, but labile oligomer content for the APN experiment. The higher gas-phase dimer concentration can be explained by the higher initial precursor concentration used in the APN experiment that leads to a more pronounced  $\text{RO}_2 + \text{RO}_2$  gas-phase chemistry.

Evaporation in the model slows down once the  $25 \text{ }^\circ\text{C}$  temperature plateau is reached and picks up again after temperature is raised. This behavior is not observed in the experiment, where the evaporation rate remains almost constant, irrespective of chamber temperature between hours 5 and 9 of the experiment. The behavior cannot be reproduced in any model run and the implications of these findings will be discussed in Sect. 3.4.3.

### **3.3 Simultaneous and sequential oxidation experiments (MIX and SEQ)**

In addition to oxidation experiments with single precursors, experiments are performed where  $\alpha$ -pinene and limonene are oxidized simultaneously (MIX) or in sequence (SEQ) to investigate whether their co-existence affects growth or evaporation of SOA. In Figs. 4a (MIX) and 4b (SEQ), aerosol mass is displayed for these two scenarios alongside kinetic modelling results. The experiments are set up in a way that the produced aerosol mass is

comparable in magnitude to the pure precursor experiments and both precursors contribute to the produced mass in equal parts. Table 2 lists the experimental SOA yields along with injected precursor amounts.

### **3.3.1 Experimental observations (MIX and SEQ)**

In the MIX experiment (Fig. 4a), most of the initial increase in aerosol mass (black open markers) is rapid and peak growth is reached after about 3 hours, comparable to the pure  $\alpha$ -pinene oxidation experiment. The evaporation pattern upon chamber heating shows a less pronounced decrease in particle mass compared to the APN experiment, but is more pronounced than observed in the LIM experiment. Overall, the mass loss during the 5 °C to 25 °C evaporation step is more pronounced than mass loss during the 25 °C to 42 °C step.

In the SEQ experiment (Fig. 4b), initial growth of  $\alpha$ -pinene SOA onto the inorganic seed particles is rapid. After subsequent injection of limonene precursor, the second increase in aerosol mass is more gradual, as would be expected from the pure LIM experiment. The evaporation pattern in the SEQ experiment is less pronounced than the one of the MIX experiment during the 5 °C to 25 °C temperature increase and equally marginal from 25 °C to 42 °C.

### **3.3.2 Kinetic modelling results (MIX and SEQ)**

The model result of the best fit modelling scenario (solid green and purple lines) lacks in correlation to the experimental data for both, MIX, and SEQ experiments. Strikingly, the

mass at peak aerosol growth is overestimated by the model in both scenarios. Furthermore, initial evaporation is overestimated such that aerosol mass in the middle and late stages of the experiments agrees between model and experiment. Towards the end of the experiment, evaporation is further overestimated in the SEQ experiment, such that predicted aerosol mass becomes lower than the experimentally observed mass.

The best fit modelling result is generated from optimization to aerosol mass and pON/OA data from experimental data sets LIM, APN, and SEQ; experiment MIX is left out for cross-validation. Furthermore, pure precursor experiments are each weighted twice as high as the MIX experiment. pON/OA data is weighted by a factor of 4 less than aerosol mass data. The model optimization is hence intentionally biased towards aerosol mass of the pure precursor experiments. The premise of this decision is to investigate the potentially non-linear effects of mixing precursors, which cannot be accomplished if the pure precursor experiments are not accurately represented in the first place. We note that fitting to all four data sets with equal weighting coefficients does not yield a subjectively better optimization result and only shifted insufficient model-experiment correlation to the pure precursor experiments APN and LIM.

Figs. 4a and 4b also show a different modelling scenario that is obtained by only optimizing to the APN and LIM experiments (dashed green and purple lines), with experiments MIX and SEQ left out for cross-validation. This scenario shows agreement between model and mixed precursor experiments during peak growth, but significantly underestimates aerosol mass after the first increase in chamber temperature. If applied to all data sets, this fit scores

worse in the least-squares residue between model and experiment (Eq. 4) than the best fit scenario described above, however, overestimation of evaporation in the mixed precursor experiment is a common theme between modelling scenarios that were able to reproduce both the growth and evaporation of the pure precursor experiments. Of note, evaporation is generally more strongly overestimated in the SEQ experiment, where limonene SOA is deposited onto  $\alpha$ -pinene SOA that has already formed.

These results are similar to the findings of Boyd et al. (2017), who showed less evaporation of limonene SOA and more evaporation of  $\beta$ -pinene SOA in a SEQ-type experiment ( $\beta$ -pinene SOA condensing on preformed limonene SOA) compared to their MIX-type experiment. The study postulated a core-shell morphology of a limonene SOA core and a  $\beta$ -pinene SOA shell that is sustained due to incomplete mixing, though oligomerization between limonene and  $\beta$ -pinene oxidation products could also play a role. Here, we show in a proof of concept that oligomerization mechanics alone cannot explain the evaporation of monoterpene SOA mixtures. In the following, we will take a closer look at further possible explanations.

### **3.4 Deviation between model and experiment**

We can conclude that while peak aerosol mass can be reconciled between the four simulated experiments with the kinetic model, the evaporation pattern in experiments MIX and SEQ cannot be brought fully into agreement with the pure precursor experiments LIM and APN. Hence, the kinetic model must lack a process that leads to resistance in

evaporation in the mixed precursor scenarios compared to the pure precursor experiments.

Possible mechanisms introducing such non-linearity include:

1. Non-linear gas-phase chemistry
2. Augmented particle-phase oligomerization chemistry
3. Mass transfer limitations

In general, none of these points can be fully excluded based on the results presented in this manuscript. However, in the following, we will go through the obtained evidence and evaluate these points to make an informed guess on how likely they are to affect aerosol formation and evaporation.

### **3.4.1 Gas-phase chemistry**

Non-linear effects in gas-phase chemistry branching ratios could lead to a mixture of oxidation products that is more readily oxidized or dimerized and hence would show a reduced evaporation rate upon increase in chamber temperature. One possible mechanism for this is an increased yield of gas-phase dimers due to bimolecular reaction of two RO<sub>2</sub> radicals from different precursors, forming hetero-dimers of oxidation products. Formation of hetero-dimers is considered in the model, however, the branching ratio is assumed to be similar for limonene- and  $\alpha$ -pinene-derived molecules and hence self-reactions are of the same speed as cross-reactions. Berndt et al. (2018) showed that cross-reactions of two different  $\alpha$ -pinene-derived RO<sub>2</sub> radicals can be faster than the respective self-reaction rates. Such an effect would cause a higher dimer fraction in the product spectrum, which in turn would lead to reduced evaporation of SOA from precursor mixtures due to overall

lower volatility. Since the number of RO<sub>2</sub> radicals in precursor mixtures is diversified, more cross-reactions could occur naturally, which would lead to more gas-phase dimers and in turn explain the slower evaporation in the MIX experiment. The SEQ experiment, however, also shows slow evaporation compared to the pure precursor experiment. Since oxidation occurred separately and cross-reactions are not enhanced by diversification of RO<sub>2</sub> radicals, formation of hetero-dimers in the gas phase cannot be the cause for reduced product volatility in the SEQ experiment.

### **3.4.2 Oligomerization**

Augmented oligomerization in the particle phase is a possible explanation of reduced evaporation rates in case mixtures of oxidation products from different precursors oligomerize more readily together than the pure components in isolation. Unlike the gas-phase chemistry scenarios described above, these effects could be observed in both MIX and SEQ experiments since particle-phase oligomerization may occur retroactively after the second oxidation step in the sequential oxidation experiment. Moreover, oligomerization of already low-volatile products would not alter SOA yields as strongly as gas-phase chemical effects would, but could have a pronounced influence on evaporation rates.

In general, an augmentation effect leading to a higher oligomerization degree in mixtures could be achieved if the hetero-oligomers were formed more efficiently than a linear combination of formation rates of both homo-oligomers. A similar effect would be achieved when oxidation products of one of the two precursors were such efficient

oligomer-formers that they would cause the oxidation products of the other precursors to oligomerize more readily and pull them into the oligomer phase. Therefore, during development of the model, we tested an implementation of the oligomerization scheme where formation of hetero-oligomers occurs at a combined rate using their logarithmic mean value, but first-order decomposition rates remain unaffected by the precursor type. The model solution exhibited a large discrepancy in oligomerization rates of a few orders of magnitudes, with limonene oxidation products oligomerizing quickly and readily and  $\alpha$ -pinene oxidation products hardly oligomerizing in isolation. As a result, mixtures of oxidation products still oligomerized significantly, driven by the high individual oligomer formation rate of limonene oxidation products. Equilibrium oligomerization degree is governed by both oligomer formation and decomposition rates, but is also naturally capped to a value of 100 %. Hence, in conclusion, mixing a strong oligomer former that reaches this cap in isolation with a weak oligomer former can lead to a higher combined oligomerization degree of the mixture. However, this pure theoretical result seems unphysical as it requires a very high oligomerization degree of pure limonene SOA and a very small degree of oligomerization in pure  $\alpha$ -pinene SOA, which has not been observed in experimental studies (Faxon et al., 2018; Takeuchi and Ng, 2019).

### **3.4.3 Mass transfer limitations**

Increased mass transfer limitations caused by high viscosity can cause a reduction of volatilization. This is due to surface concentrations of the evaporating components being depleted when the mixing time scale in the particle is longer than the evaporation time

scale. Mass transfer limitation is not treated in the model runs previously shown in this study. Instead, a well-mixed bulk phase is assumed and any resistance in evaporation is explained with oligomerization reactions. The slow evaporation of limonene SOA is hence solely caused by significant oligomerization in the model runs previously presented, but could also be caused by mass transfer limitations induced by a high bulk-phase viscosity, especially if a high fraction of particle-phase oligomers would have formed that depresses mobility of molecules in the condensed phase (Baltensperger et al., 2005; D'Ambro et al., 2018). Hence, limonene SOA might exhibit a more viscous phase state than  $\alpha$ -pinene SOA. The high viscosity caused by limonene oxidation products might in turn affect evaporation in the mixed precursor experiments and cause the observed non-linear effects. In a first approximation, viscosities of mixtures can be assumed to be a linear combination of the individual viscosities and follow a logarithmic mixing rule (Gervasi et al., 2019). This entails that the change in the rate of mass transport between pure compounds and their mixtures can reach orders of magnitudes. This would be in line with volatilization rates observed in the mixed precursor experiments being more similar to the pure LIM experiment, which was observed in this and a previous study (Boyd et al., 2017). Notably, while evaporation steps immediately following a change in chamber temperature are overall similar between the MIX and SEQ experiments, the slope of the aerosol mass versus time curve is steeper in the MIX experiments. This might suggest that in the SEQ experiment, limonene SOA might be covering the preformed  $\alpha$ -pinene oxidation products in a core-shell morphology and thus hampering their volatilization.

To test the effect of impeded bulk diffusivity on the evaporation of SOA, we perform a sensitivity study in which we increase viscosity in the model to evaluate whether the evaporation rates in the MIX experiment can be brought into agreement with observations. We use the alternative fitting scenario shown in Fig. 4 (dashed lines) and raise the viscosity in the simulation to  $2 \cdot 10^6$ ,  $2 \cdot 10^7$ , and  $2 \cdot 10^8$  Pa·s, respectively, in three separate model runs (Fig. 5). These viscosities are in the typical range for SOA under dry conditions and fall into the semi-solid phase state region (Koop et al., 2011; Shiraiwa et al., 2011; Abramson et al., 2013; Zhang et al., 2015b; Grayson et al., 2016; Gervasi et al., 2019). Using the Stokes-Einstein relation (Einstein, 1905) and an effective molecular radius of 2 nm, these viscosities correspond to bulk diffusion coefficients of  $5 \times 10^{-16}$  to  $5 \times 10^{-18}$  cm<sup>2</sup>/s at 298 K. The effective radius is approximated from geometric considerations assuming spherical molecular shape, a molar mass of 250 g/mol and density of 1.55 g/cm<sup>3</sup>. The temperature-dependence of this diffusion coefficient is approximated with a constant activation enthalpy of diffusion  $\Delta H_{\text{dif}} = 50$  kJ/mol according to Eq. (5).

$$D_b(T) = D_b(298 \text{ K}) \cdot \exp \frac{-\Delta H_{\text{dif}}}{R \left( \frac{1}{T} - \frac{1}{298} \right)} \quad (5)$$

Fig. 5 shows that in the selected viscosity range, the model output is quite sensitive to changes in bulk diffusivity. Evaporation is almost unimpeded in the highest diffusion case, but considerably slowed at the lowest simulated diffusivity. At a bulk diffusion coefficient of  $5 \times 10^{-17}$  cm<sup>2</sup>/s, the correlation with the evaporation pattern in the MIX experiment is much improved. This model result insinuates that the co-presence of limonene SOA and

$\alpha$ -pinene SOA might strongly reduce the mobility of  $\alpha$ -pinene oxidation products so that the fast evaporation of  $\alpha$ -pinene oxidation products observed in the pure  $\alpha$ -pinene oxidation experiment does not take place.

The outcome of this sensitivity study has to be treated with caution since slow diffusion of limonene oxidation products also causes a change in the simulation outcome for the pure limonene experiment, which the employed parameter set is based on. With this parameter set, the slow evaporation of limonene SOA in the model is purely attributed to oligomer formation. The sensitivity study hence suggests that the high oligomerization degree observed for limonene SOA in the previous best fit solutions might be overestimated. In fact, a particularly high oligomer content was not observed for limonene SOA from oxidation with  $\text{NO}_3$  in measurements using FIGAERO-CIMS (Faxon et al., 2018). Distinction of these two effects (oligomerization vs. mass transfer limitation) could be possible with the model and the MCGA, but is not attempted in this study due to the prohibitive computational cost of model calculations at low diffusivities and will be subject of future studies.

Taken together, it is possible that increased mass transfer limitation led to the observed reduced evaporation rates of the SOA mixtures as postulated in Boyd et al. (2017). However, there are still large uncertainties and a high computational expense associated with a model treatment of highly viscous SOA systems. While frameworks for the determination of viscosity of mixtures have recently been developed (Gervasi et al., 2019), these rely on structural information about individual compounds. Furthermore, while the

Stokes-Einstein relation seems to hold for similar systems at viscosities of up to  $10^4$  Pa·s (Ullmann et al., 2019), it is not clear whether it also holds for viscosities of  $\sim 10^7$  Pa·s derived in this study (Evoy et al., 2019).

Additionally, treatment of slow particle-phase diffusion requires many model layers to describe the steep concentrations gradients arising at the particle surface upon evaporation. In combination with the multitude of tracked species in the particle phase, computational costs quickly reach unfeasible ranges. Ideally, the spatial resolution model layers would have to be generated upon model runtime by an algorithm that detects steep concentration gradients. This detailed description will be presented in a forthcoming publication.

### **3.5 Organic nitrate fractions**

In this study, the organic nitrate fraction (pON/OA) is presented as ratio of the total mass concentration of particulate ON (which includes the organic part and nitrate part of the ON compounds) to the total mass concentration of organic aerosol (which includes both ON and non-nitrated organics) (Takeuchi and Ng, 2019). It can be inferred from AMS data using Eq. 6. In this formula, it is assumed that all organic aerosol mass is found in the organic and nitrate signal of the AMS ( $AMS_{ORG}$  and  $AMS_{NO_3}$ ) and all AMS nitrate is ON. When  $MW_{pON}$  is the average molar mass of the ON (i.e., 250 g/mol in this study) and  $MW_{NO_3}$  the molar mass of the nitrate group (i.e., 62 g/mol), the pON mass can be determined by scaling the AMS signal with the ratio of these molar masses.

$$\frac{pON}{OA} = \frac{AMS_{NO_3} \cdot \frac{MW_{pON}}{MW_{NO_3}}}{AMS_{NO_3} + AMS_{ORG}} \approx \frac{4.03}{1 + \frac{AMS_{ORG}}{AMS_{NO_3}}} \quad (6)$$

Fig. 6 depicts measured and modelled values for pON/OA for all four experiments. Panel a shows that in the LIM experiment, pON/OA is high, with a mass ratio of about 0.8 in the particle phase, and only slightly increases over time, which is reproduced in the model. Note that the average molar mass of ON might change during the experiment, e.g., by evaporation of lower molecular weight components, which is not considered in our calculation. In the model, the slow evaporation of limonene SOA is caused by oligomer decomposition followed by evaporation of volatile monomers. The fact that nitrate groups are rather evenly distributed across monomers from the predominantly evaporating volatility bins is reflected in the constant pON/OA returned by the model. We note that this result gives no evidence that decomposition rates of oligomers consisting of nitrated or non-nitrated monomeric building blocks might differ and we use the same oligomer decomposition rate irrespective of nitration state of the respective product bin.

Panel b shows pON/OA in the APN experiment. The initial nitrate content is lower than in the LIM experiment with a value of about 0.45. During the first temperature increase in the APN experiment, ON content increases with the reduction in organic mass, indicating predominant evaporation of non-nitrated oxidation products. During the second evaporation step, ON content decreases, indicating predominant evaporation of nitrated oxidation product. The best fit model run (solid blue line) captures the overall magnitude

of the ON content, but lacks the time dependence of a reduction followed by an increase in pON/OA. This is probably due to the model parameter optimization being stuck in a local minimum and the relatively low weighting coefficients assigned to the pON/OA data sets in this study. pON/OA data were weighted by a factor of 4 less than aerosol mass data in this study.

The measured and simulated ON contents for the experiments with multiple precursors are shown in panels c and d of Fig. 6 for the MIX and SEQ experiment, respectively. While both experiments use approximately the same concentrations of  $\alpha$ -pinene and limonene, the measured pON/OA are slightly different. Simultaneous oxidation (MIX) leads to an initial pON/OA of 0.53, which is surprisingly low and closer to the value measured for pure  $\alpha$ -pinene SOA. Sequential oxidation (SEQ) leads to an initial pON/OA of 0.52 after  $\alpha$ -pinene oxidation, and increases to 0.6 after oxidation of limonene has concluded. This value in the SEQ experiment is closer to the expected value when assuming linear additivity of ON content. The unexpectedly low ON content in the MIX experiment points towards non-linear effects in chemistry that are not captured by the model. The time- and temperature-dependence of the ON fraction is qualitatively similar for both experiments and overall captured by the model. Predominant evaporation of  $\alpha$ -pinene oxidation products, which are the more-volatile and less-nitrated components of the mixture, leads to an overall increase of pON/OA.

A notable observation from modelling is that dimers from the gas-phase reaction of  $\text{RO}_2 + \text{RO}_2$  are mainly nitrates because most  $\text{RO}_2$  radicals originate from the reaction of alkene

with  $\text{NO}_3$  and are hence nitrated. This is especially significant for the  $\alpha$ -pinene +  $\text{NO}_3$  reaction system since the high momentary  $\text{RO}_2$  radical concentrations in these experiments lead to a high estimated contribution of gas-phase dimers to aerosol mass of 11 % at peak growth and close to 31 % after heating to 42 °C (cf. Fig. 3).

In summary, the experimental and modelling results in this study confirm previous studies and report a high efficiency of nitration in the reaction of monoterpenes with  $\text{NO}_3$ , with a nitrated SOA fraction larger than 50 % under most experimental conditions studies (Ng et al., 2017 and references therein). Limonene SOA shows overall higher nitration degrees than  $\alpha$ -pinene SOA, which can be understood by the higher number of double bonds of the VOC precursor compound itself and hence more possibilities to introduce a nitrate group during oxidation. An increase in temperature from 5 °C to 25 °C leads to an increase in ON content of the SOA in all observed systems, which can be explained by the slightly elevated nitration degree in the dimer fraction and hence less volatile fraction of the organic aerosol. By heating above 25 °C, pON/OA is in general slightly reduced. A potential reason for this might be accelerated thermal decomposition of ON.

#### **4 Conclusions and Outlook**

In this study, an inverse modelling approach is utilized alongside laboratory chamber experiments to gain insights into the molecular-level processes which occur during the formation and evaporation of SOA from the oxidation of  $\alpha$ -pinene, limonene, and mixtures of both precursors with  $\text{NO}_3$ . We find  $\alpha$ -pinene SOA to form and evaporate rather quickly and limonene SOA to form and evaporate more slowly. Both SOA types, however, show

retardation in evaporation compared to instantaneous equilibration, which can be explained by the presence of particle-phase oligomers. The oxidation products of both SOA types are found to be heavily nitrated. A mixed and a sequential oxidation of both precursors shows the expected linear additivity of SOA yields, but a non-linear reduction in evaporation behavior, which could not be explained without diffusion limitations in the particle phase. These results highlight the significance of  $\text{NO}_3$  as oxidant in SOA formation and the importance of ON as products of monoterpene oxidation. This study finds evidence for non-equilibrium partitioning caused by slow particle-phase chemistry and slow diffusion, which is currently not considered in global models and may lead to underestimation of SOA persistence and hence underestimated global SOA burden in these models.

The modelling approach applied in this study comprises a combination of the kinetic multi-layer model based on KM-GAP (Shiraiwa et al., 2012) with the automated global optimization suite MCGA (Berkemeier et al., 2017) and details the full chemistry and physics of SOA particle growth and shrinkage. The underlying SOA formation and evaporation mechanism uses a simplified and lumped version of the Master Chemical Mechanism (MCM; Jenkin et al., 2003; Saunders et al., 2003; Berkemeier et al., 2016), extends it with a reversible particle-phase oligomerization and gas-phase dimerization scheme, and treats gas-particle partitioning with a volatility basis set approach (Donahue et al., 2006; Donahue et al., 2011) for each product bin. This study focuses on  $\text{NO}_3$  oxidation of monoterpenes and their mixtures, but the model framework can be ported to other chemical systems. The depth resolution capabilities of the multi-layer model allow for a sensitivity study of the influence of particle phase state on the evaporation of these

particles. A full treatment of composition-dependent, depth-resolved viscosity as global optimization parameter is ultimately needed to disentangle the interactions of particle-phase diffusion and particle-phase chemistry. Due to the computational expense of finely-resolved computational layers and the general uncertainty in the physical and chemical parameters, this will be subject of follow-up studies. In such studies, offline analysis of the oligomerization degree of SOA material can help to constrain oligomerization and oligomer decomposition rates and thermodynamic models can be used to provide estimates for composition-dependence of viscosities and diffusivities (DeRieux et al., 2018; Gervasi et al., 2019).

In general, the model parameters that are returned by the inverse modelling approach applied in this work must be evaluated in the context of the model and experimental data that are employed. With a simplified multi-parameter model and experimental data sets that are aggregate observables and subject to uncertainty, the concept of a single global minimum and multiple local minima on the optimization hypersurface can become blurred and several extended areas on the optimization hypersurface can exhibit a minimal function value. This effect is enhanced when model parameters behave non-orthogonally, i.e., one parameter can be expressed to some extent by another one (or combinations of others). The existence of numerous and extended minima on the optimization hypersurface makes the process of finding an optimal parameter set computationally expensive. For example, repeated execution of an automated fitting algorithm can help to assess the flexibility of an undetermined system. Fig. S5 includes an estimation of the uncertainty in volatility distributions obtained in this study. The error bars in Fig. S5 are standard deviations of

individual re-fits of volatility distributions and hence quantify the uniqueness (or lack thereof) of the fitted volatility distributions. Beyond the technical intricacies of the parameter optimization process, the uniqueness of the obtained parameter set can be enhanced by inclusion of more experimental data at different conditions or by *a priori* determination of model parameters such as measurements of volatility distributions, oligomerization degrees or particle viscosities.

The modelling suite presented here constitutes a step forward in the computational, data-driven evaluation of SOA formation with kinetic models. In this work, only a small set of laboratory chamber data is utilized for optimization as proof of concept. We postulate that, by reconciling and cross-comparing large sets of experimental data we will be able to significantly enhance our understanding of SOA and close the gap between our expanding theoretical knowledge about the detailed gas-phase chemistry, gas-particle partitioning, particle phase state of SOA, and the application of this knowledge in chemical transport models.

Associated Content

**Supporting Information**

Author Information

**Corresponding Author**

\*Tel: 0049-6131-305-7010, e-mail: t.berkemeier@mpic.de.

\*Tel: 001-404-385-2148, e-mail: ng@chbe.gatech.edu.

## **Notes**

**The authors declare no competing financial interest.**

## Acknowledgements

This work was supported by NSF CAREER AGS-1555034. T. Berkemeier acknowledged support by the Eckert Postdoctoral Fellowship from the School of Chemical and Biomolecular Engineering at Georgia Institute of Technology.

## Figures

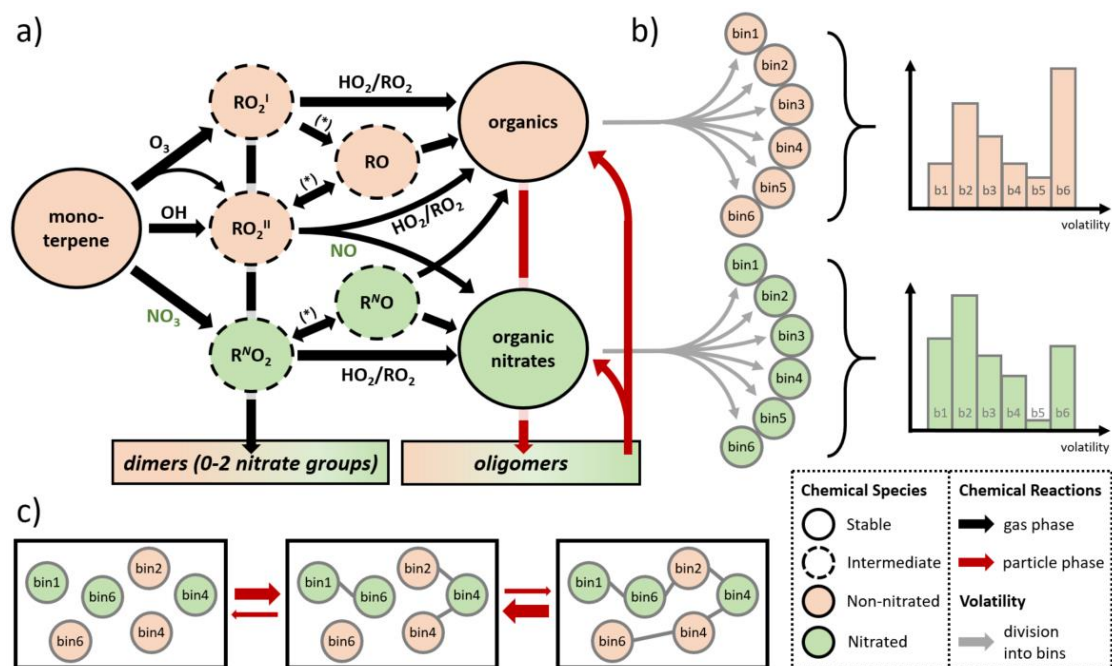


**Figure 1.** (a) Schematic representation of the lumped chemical mechanism for oxidation of monoterpenes with one double bond (e.g.,  $\alpha$ -pinene). The asterisk stands for chemical reaction with NO, NO<sub>3</sub>, and RO<sub>2</sub>. (b) The stable products are divided into 6 product bins each with a different volatility (grey arrows; bin1-bin6), according to a probability distribution (exemplary graphs on the right). (c) Oligomerization occurs in equilibrium reactions in the particle phase under conservation of precursor origin and volatility bin.

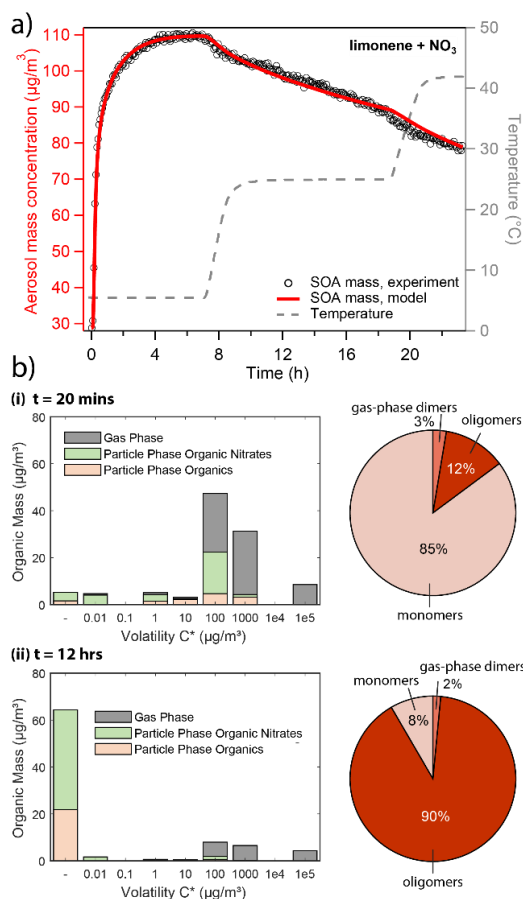


**Figure 2.** (a) Comparison of experimental and modelling results for oxidation of limonene with NO<sub>3</sub>. Open black markers are experimental aerosol mass obtained using an SMPS. The red solid line represents the model result and the grey dashed line corresponds to the experimental temperature profile. (b) Analysis of the occupation of volatility bins of all products (bar plot) and oligomerization state of particle-phase products (pie chart) in the model (i) 20 minutes and (ii) 12 hours after the beginning of the experiment. Shadings in the bar plot denote where molecules of a certain volatility bin reside: gas phase (grey) or particle phase (colored). Products in the particle phase are further distinguished as organic nitrates (green) and non-nitrated organics (orange).

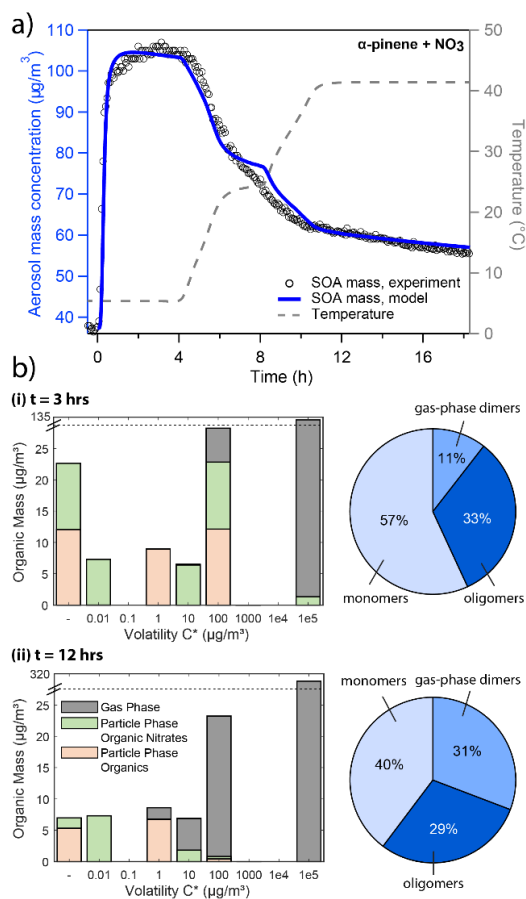
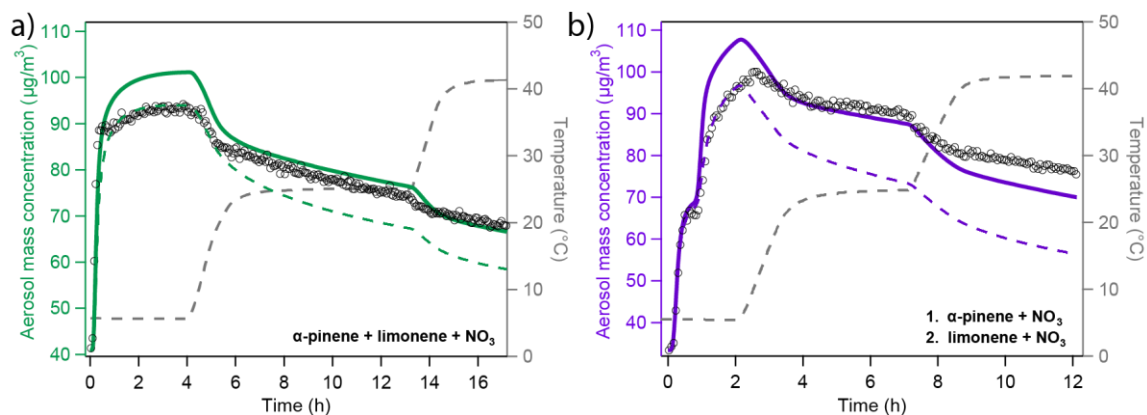


Figure 3. (a) Comparison of experimental and modelling results of aerosol mass for oxidation of  $\alpha$ -pinene with NO<sub>3</sub>. Open black markers are experimental aerosol masses obtained using an SMPS. The blue solid line represents a model result and the grey dashed line corresponds to the experimental temperature profile. (b) Analysis of the occupation of volatility bins of all products (bar plot) and oligomerization state of particle-phase products (pie chart) in the model (i) 3 hours and (ii) 12 hours after the beginning of the experiment. Shadings in the bar plot denote where molecules of a certain volatility bin reside: gas phase (grey) or particle phase (colored). Products in the particle phase are further distinguished as organic nitrates (green) and non-nitrated organics (orange).



**Figure 4.** Overview of experimental and modelling results of aerosol mass for experiments with mixed monoterpene precursors. The experiments in the two panels differ in the way the precursors were added: (a) simultaneous oxidation of a mixture of  $\alpha$ -pinene and limonene, (b) sequential oxidation of firstly  $\alpha$ -pinene and secondly limonene with  $\text{NO}_3$ . Open black markers are experimental aerosol mass obtained using an SMPS. The colored solid and dashed lines represent model results from two different fits to the experimental data. The grey dashed line indicates the experimental temperature profile.

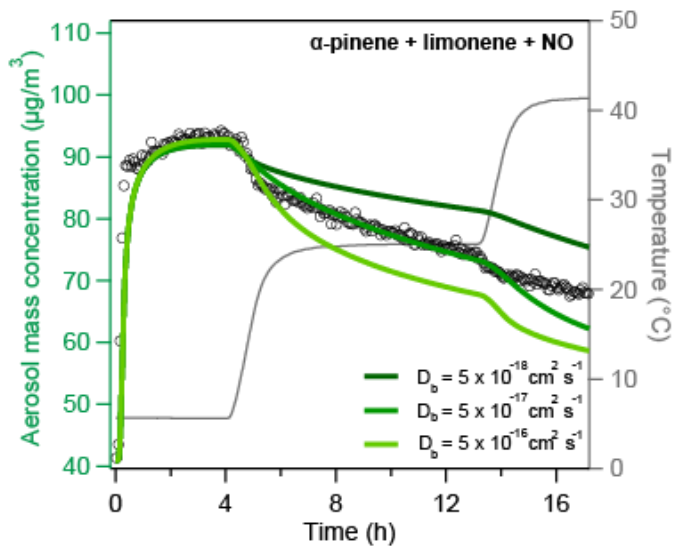
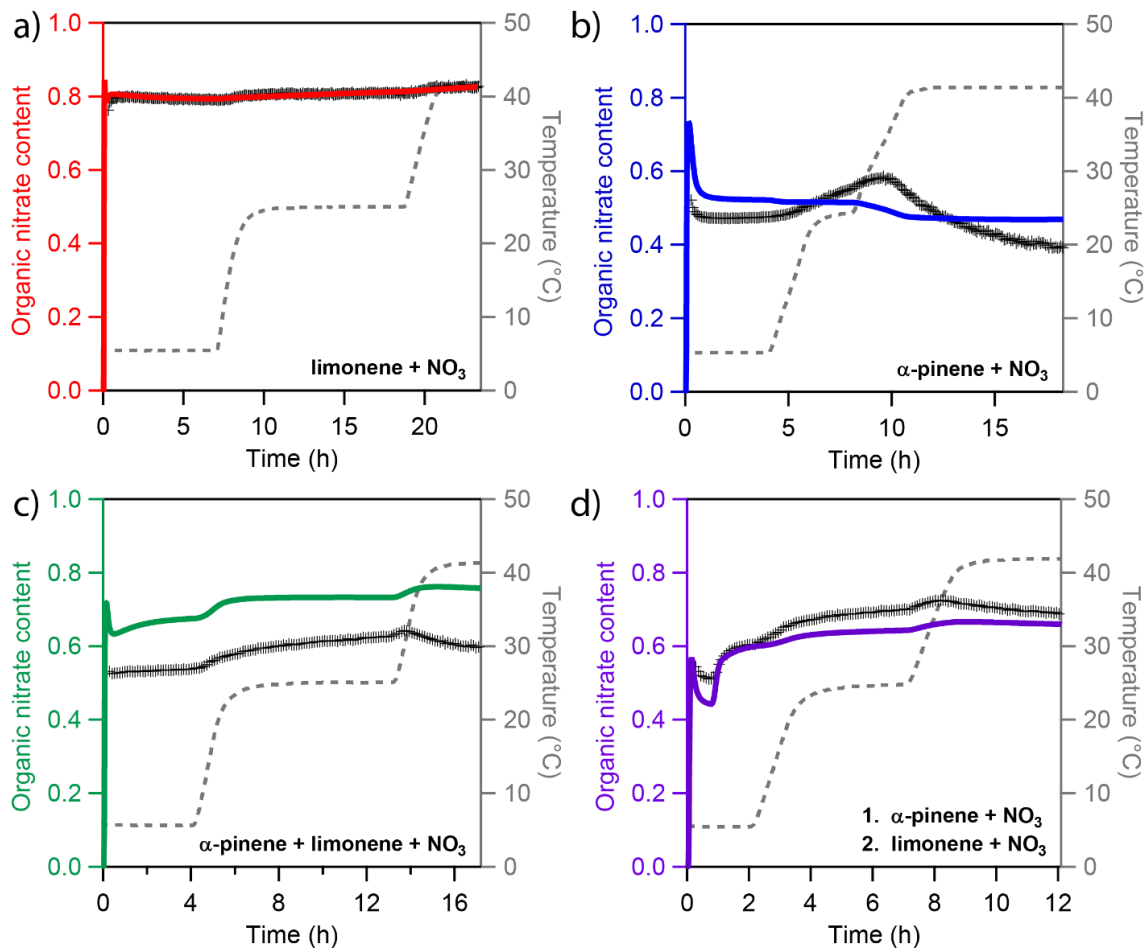


Figure 5. Influence of viscosity on model simulation results based on the alternative fitting scenario and the MIX experiment. Model simulations were performed at different diffusivity coefficients  $5 \times 10^{-18}$  -  $5 \times 10^{-16} \text{ cm}^2/\text{s}$ , corresponding to bulk viscosities of  $2 \cdot 10^6$  -  $2 \cdot 10^8 \text{ Pa}\cdot\text{s}$  according to the Stokes-Einstein relation, Eq. (5).



**Figure 6.** Experimental and modelling results of particulate organic nitrate content (pON/OA) for four different types of chamber-generated SOA. (a) only limonene, (b) only  $\alpha$ -pinene, (c) a mixture of  $\alpha$ -pinene and limonene and (d) sequential oxidation of firstly  $\alpha$ -pinene and secondly limonene. Cross markers are experimental nitration degrees inferred using a High Resolution Time-of-Flight Aerosol Mass Spectrometer (HR-ToF-AMS). The colored solid lines represent results of the kinetic model. The grey dashed line indicates the experimental temperature profile.

## Tables

**Table 1.** Fit parameters of the kinetic model. Error estimates for the volatility distribution (parameters  $f_{\text{apin}}$  and  $f_{\text{lim}}$ ) can be found in Fig. S5 in the supplement, error estimates for all other parameters are ranges in which a parameter can be varied until the model-experiment correlation decreases by 10 %. For a full list of kinetic parameters, see Table S1.

# of parameters	Parameter	Value of best fit	Description
6	$f_{\text{apin,org,b1}} - f_{\text{apin,org,b6}}$	see Fig. S5	Volatility distribution of non-nitrated monomeric $\alpha$ -pinene oxidation products
6	$f_{\text{apin,nitr,b1}} - f_{\text{apin,nitr,b6}}$	see Fig. S5	Volatility distribution of nitrated monomeric $\alpha$ -pinene oxidation products
6	$f_{\text{lim,org,b1}} - f_{\text{lim,org,b6}}$	see Fig. S5	Volatility distribution of non-nitrated monomeric limonene oxidation products
6	$f_{\text{lim,nitr,b1}} - f_{\text{lim,nitr,b6}}$	see Fig. S5	Volatility distribution of nitrated monomeric limonene oxidation products
1	gpwl	$2.80 \times 10^{-7}$ (2.31 – $3.34 \times 10^{-7}$ )	Gas-phase wall loss rate
1	$\Delta H_{\text{vap}}$ ( $\alpha$ -pinene)	76.7 (62.9 – 88.5)	Effective enthalpy of vaporization of $\alpha$ -pinene SOA products (kJ/mol)
1	$\Delta H_{\text{vap}}$ (limonene)	69.2 (66.0 – 72.2)	Effective enthalpy of vaporization of limonene SOA products (kJ/mol)
1	$p_{\text{vap,intermed1}}$ (limonene)	$2.06 \times 10^{-7}$ ( $1.38 \times 10^{-7}$ – $4.70 \times 10^{-7}$ )	Vapor pressure, non-nitrated limonene SOA intermediate (Pa)

1	$p_{\text{vap,intermed2}}$ (limonene)	$3.86 \times 10^{-8}$ (3.16 – $4.48 \times 10^{-7}$ )	Vapor pressure, nitrated limonene SOA intermediate (Pa)
1	$c_1$	0.0139 (0.0106 – 0.0168)	Branching ratio, gas-phase dimer yield from $\text{RO}_2 +$ $\text{RO}_2$
1	$c_2$	0.141 (0.102 – 0.0171)	Branching ratio, RO yield from $\text{RO}_2 + \text{RO}_2$
1	$c_{3,\text{apin}}$	0.0691 (0.0630 – 0.0746)	Branching ratio, product yield from RO, $\alpha$ -pinene
1	$c_{3,\text{lim}}$	0.774 (0.578 – 0.972)	Branching ratio, product yield from RO, limonene
1	$c_{4,\text{apin}}$	0 (0 – 0.0965)	Product ratio of non- nitrated to nitrate ratio species from RO, $\alpha$ -pinene
1	$c_{4,\text{lim}}$	0.230 (0.190 – 0.272)	Product ratio of non- nitrated to nitrate ratio species from RO, limonene
1	$k_{\text{form,apin}}$	17.4 (9.5 – 27.0)	Oligomerization rate coefficient, $\alpha$ -pinene ( $\text{h}^{-1}$ )
1	$k_{\text{form,lim}}$	1.11 (1.01 – 1.22)	Oligomerization rate coefficient, limonene ( $\text{h}^{-1}$ )
1	$k_{\text{decom,apin}}$	3.28 (2.13 – 6.04)	Oligomer decomposition rate coefficient, $\alpha$ -pinene ( $\text{h}^{-1}$ )
1	$k_{\text{decom,lim}}$	0.0392 (0.0356 – 0.0428)	Oligomer decomposition rate coefficient, limonene ( $\text{h}^{-1}$ )
1	$\text{TF}(k_{\text{decom,apin}})$	620 (492 – 801)	Temperature-dependence factor of oligomer decomposition, $\alpha$ -pinene (kJ/mol)
1	$\text{TF}(k_{\text{decom,lim}})$	244 (214 – 269)	Temperature-dependence factor of oligomer

			decomposition, limonene (kJ/mol)
--	--	--	-------------------------------------

**Table 2.** Experimental conditions for environmental chamber experiments presented in this study alongside aerosol masses and SOA yields during peak growth at 5 °C.

Exp	VOC 1 (ppb)	VOC 2 (ppb)	Experiment variant	Seed mass <sup>†</sup> ( $\mu\text{g} / \text{m}^3$ )	Peak aerosol mass <sup>†</sup> ( $\mu\text{g} / \text{m}^3$ )	Peak organic aerosol mass <sup>†</sup> ( $\mu\text{g} / \text{m}^3$ )	SOA yield (%)
LIM	limonene (10.5 $\pm$ 1.1)		pure limonene	28.8 $\pm$ 1.4	110.1 $\pm$ 5.5	81.3 $\pm$ 5.7	129.6 $\pm$ 15.8
APN	$\alpha$ -pinene (47.5 $\pm$ 4.8)		pure $\alpha$ - pinene	37.3 $\pm$ 1.9	108.7 $\pm$ 5.4	71.4 $\pm$ 5.7	25.2 $\pm$ 3.2
SEQ	$\alpha$ -pinene (24 $\pm$ 2.4)	limonene (5 $\pm$ 0.5)	sequential	33.4 $\pm$ 1.7	100.1 $\pm$ 5.0	66.7 $\pm$ 5.3	38.5 $\pm$ 4.9
MIX	$\alpha$ -pinene (22.5 $\pm$ 2.3)	limonene (5 $\pm$ 0.5)	simultaneous	40.9 $\pm$ 2.0	93.8 $\pm$ 4.7	52.9 $\pm$ 5.1	32.2 $\pm$ 4.5

<sup>†</sup>: Aerosol masses are calculated from aerosol volume concentrations using a density of the organic phase of 1.64 g/cm<sup>3</sup> for limonene SOA (Boyd et al., 2017), 1.46 g/cm<sup>3</sup> for  $\alpha$ -pinene SOA (Nah et al., 2016), and 1.55 g/cm<sup>3</sup> for the mixtures. All the reported masses are wall-loss corrected

## References

- Abramson, E., Imre, D., Beranek, J., Wilson, J. M., and Zelenyuk, A.: Experimental determination of chemical diffusion within secondary organic aerosol particles, *Physical Chemistry Chemical Physics*, 15, 2983-2991, 10.1039/c2cp44013j, 2013.
- Baltensperger, U., Kalberer, M., Dommen, J., Paulsen, D., Alfarra, M. R., Coe, H., Fisseha, R., Gascho, A., Gysel, M., Nyeki, S., Sax, M., Steinbacher, M., Prevot, A. S. H., Sjögren,

S., Weingartner, E., and Zenobi, R.: Secondary organic aerosols from anthropogenic and biogenic precursors, *Faraday Discussions*, 130, 265-278, 10.1039/B417367H, 2005.

Berkemeier, T., Huisman, A. J., Ammann, M., Shiraiwa, M., Koop, T., and Pöschl, U.: Kinetic regimes and limiting cases of gas uptake and heterogeneous reactions in atmospheric aerosols and clouds: a general classification scheme, *Atmos. Chem. Phys.*, 13, 6663-6686, 10.5194/acp-13-6663-2013, 2013.

Berkemeier, T., Ammann, M., Mentel, T. F., Pöschl, U., and Shiraiwa, M.: Organic Nitrate Contribution to New Particle Formation and Growth in Secondary Organic Aerosols from  $\alpha$ -Pinene Ozonolysis, *Environmental Science & Technology*, 50, 6334-6342, 10.1021/acs.est.6b00961, 2016.

Berkemeier, T., Ammann, M., Krieger, U. K., Peter, T., Spichtinger, P., Pöschl, U., Shiraiwa, M., and Huisman, A. J.: Technical note: Monte Carlo genetic algorithm (MCGA) for model analysis of multiphase chemical kinetics to determine transport and reaction rate coefficients using multiple experimental data sets, *Atmos. Chem. Phys.*, 17, 8021-8029, 10.5194/acp-17-8021-2017, 2017.

Berndt, T., Mentler, B., Scholz, W., Fischer, L., Herrmann, H., Kulmala, M., and Hansel, A.: Accretion Product Formation from Ozonolysis and OH Radical Reaction of  $\alpha$ -Pinene: Mechanistic Insight and the Influence of Isoprene and Ethylene, *Environmental Science & Technology*, 52, 11069-11077, 10.1021/acs.est.8b02210, 2018.

Boyd, C. M., Sanchez, J., Xu, L., Eugene, A. J., Nah, T., Tuet, W. Y., Guzman, M. I., and Ng, N. L.: Secondary organic aerosol formation from the beta-pinene+NO<sub>3</sub> system: effect of humidity and peroxy radical fate, *Atmospheric Chemistry and Physics*, 15, 7497-7522, 10.5194/acp-15-7497-2015, 2015.

Boyd, C. M., Nah, T., Xu, L., Berkemeier, T., and Ng, N. L.: Secondary Organic Aerosol (SOA) from Nitrate Radical Oxidation of Monoterpenes: Effects of Temperature, Dilution, and Humidity on Aerosol Formation, Mixing, and Evaporation, *Environmental Science & Technology*, 51, 7831-7841, 10.1021/acs.est.7b01460, 2017.

Cappa, C. D., and Wilson, K. R.: Evolution of organic aerosol mass spectra upon heating: implications for OA phase and partitioning behavior, *Atmospheric Chemistry and Physics*, 11, 1895-1911, 10.5194/acp-11-1895-2011, 2011.

Claflin, M. S., and Ziemann, P. J.: Identification and Quantitation of Aerosol Products of the Reaction of  $\beta$ -Pinene with NO<sub>3</sub> Radicals and Implications for Gas- and Particle-Phase Reaction Mechanisms, *The Journal of Physical Chemistry A*, 122, 3640-3652, 10.1021/acs.jpca.8b00692, 2018.

D'Ambro, E. L., Schobesberger, S., Zaveri, R. A., Shilling, J. E., Lee, B. H., Lopez-Hilfiker, F. D., Mohr, C., and Thornton, J. A.: Isothermal Evaporation of  $\alpha$ -Pinene Ozonolysis SOA: Volatility, Phase State, and Oligomeric Composition, *ACS Earth and Space Chemistry*, 2, 1058-1067, 10.1021/acsearthspacechem.8b00084, 2018.

DeCarlo, P. F., Kimmel, J. R., Trimborn, A., Northway, M. J., Jayne, J. T., Aiken, A. C., Gonin, M., Fuhrer, K., Horvath, T., Docherty, K. S., Worsnop, D. R., and Jimenez, J. L.: Field-Deployable, High-Resolution, Time-of-Flight Aerosol Mass Spectrometer, *Analytical Chemistry*, 78, 8281-8289, 10.1021/ac061249n, 2006.

DeRieux, W. S. W., Li, Y., Lin, P., Laskin, J., Laskin, A., Bertram, A. K., Nizkorodov, S. A., and Shiraiwa, M.: Predicting the glass transition temperature and viscosity of secondary organic material using molecular composition, *Atmos. Chem. Phys.*, 18, 6331-6351, 10.5194/acp-18-6331-2018, 2018.

Donahue, N. M., Robinson, A. L., Stanier, C. O., and Pandis, S. N.: Coupled partitioning, dilution, and chemical aging of semivolatile organics, *Environmental Science & Technology*, 40, 2635-2643, 10.1021/es052297c, 2006.

Donahue, N. M., Epstein, S. A., Pandis, S. N., and Robinson, A. L.: A two-dimensional volatility basis set: 1. organic-aerosol mixing thermodynamics, *Atmospheric Chemistry and Physics*, 11, 3303-3318, 10.5194/acp-11-3303-2011, 2011.

Draper, D. C., Myllys, N., Hyttinen, N., Møller, K. H., Kjaergaard, H. G., Fry, J. L., Smith, J. N., and Kurtén, T.: Formation of Highly Oxidized Molecules from NO<sub>3</sub> Radical Initiated Oxidation of  $\Delta$ -3-Carene: A Mechanistic Study, *ACS Earth and Space Chemistry*, 3, 1460-1470, 10.1021/acsearthspacechem.9b00143, 2019.

Eddingsaas, N. C., Loza, C. L., Yee, L. D., Chan, M., Schilling, K. A., Chhabra, P. S., Seinfeld, J. H., and Wennberg, P. O.:  $\alpha$ -pinene photooxidation under controlled chemical conditions &ndash; Part 2: SOA yield and composition in low- and high-NO<sub>x</sub> environments, *Atmos. Chem. Phys.*, 12, 7413-7427, 10.5194/acp-12-7413-2012, 2012.

Einstein, A.: Über die von der molekularkinetischen Theorie der Wärme geforderte Bewegung von in ruhenden Flüssigkeiten suspendierten Teilchen, *Annalen der Physik*, 322, 549-560, 10.1002/andp.19053220806, 1905.

Evoy, E., Maclean, A. M., Rovelli, G., Li, Y., Tsimpidi, A. P., Karydis, V. A., Kamal, S., Lelieveld, J., Shiraiwa, M., Reid, J. P., and Bertram, A. K.: Predictions of diffusion rates of large organic molecules in secondary organic aerosols using the Stokes–Einstein and fractional Stokes–Einstein relations, *Atmos. Chem. Phys.*, 19, 10073-10085, 10.5194/acp-19-10073-2019, 2019.

Faxon, C., Hammes, J., Le Breton, M., Pathak, R. K., and Hallquist, M.: Characterization of organic nitrate constituents of secondary organic aerosol (SOA) from nitrate-radical-initiated oxidation of limonene using high-resolution chemical ionization mass spectrometry, *Atmos. Chem. Phys.*, 18, 5467-5481, 10.5194/acp-18-5467-2018, 2018.

Fry, J. L., Kiendler-Scharr, A., Rollins, A. W., Wooldridge, P. J., Brown, S. S., Fuchs, H., Dubé, W., Mensah, A., dal Maso, M., Tillmann, R., Dorn, H. P., Brauers, T., and Cohen, R. C.: Organic nitrate and secondary organic aerosol yield from NO<sub>3</sub> oxidation of  $\beta$ -pinene

evaluated using a gas-phase kinetics/aerosol partitioning model, *Atmos. Chem. Phys.*, 9, 1431-1449, 10.5194/acp-9-1431-2009, 2009.

Fry, J. L., Kiendler-Scharr, A., Rollins, A. W., Brauers, T., Brown, S. S., Dorn, H. P., Dubé, W. P., Fuchs, H., Mensah, A., Rohrer, F., Tillmann, R., Wahner, A., Wooldridge, P. J., and Cohen, R. C.: SOA from limonene: role of NO<sub>3</sub> in its generation and degradation, *Atmospheric Chemistry and Physics*, 11, 3879-3894, 10.5194/acp-11-3879-2011, 2011.

Fry, J. L., Draper, D. C., Barsanti, K. C., Smith, J. N., Ortega, J., Winkler, P. M., Lawler, M. J., Brown, S. S., Edwards, P. M., Cohen, R. C., and Lee, L.: Secondary Organic Aerosol Formation and Organic Nitrate Yield from NO<sub>3</sub> Oxidation of Biogenic Hydrocarbons, *Environmental Science & Technology*, 48, 11944-11953, 10.1021/es502204x, 2014.

Fuzzi, S., Andreae, M. O., Huebert, B. J., Kulmala, M., Bond, T. C., Boy, M., Doherty, S. J., Guenther, A., Kanakidou, M., Kawamura, K., Kerminen, V. M., Lohmann, U., Russell, L. M., and Pöschl, U.: Critical assessment of the current state of scientific knowledge, terminology, and research needs concerning the role of organic aerosols in the atmosphere, climate, and global change, *Atmospheric Chemistry and Physics*, 6, 2017-2038, 2006.

Gao, Y., Hall, W. A., and Johnston, M. V.: Molecular Composition of Monoterpene Secondary Organic Aerosol at Low Mass Loading, *Environmental Science & Technology*, 44, 7897-7902, 10.1021/es101861k, 2010.

Gatzsche, K., Iinuma, Y., Tilgner, A., Mutzel, A., Berndt, T., and Wolke, R.: Kinetic modeling studies of SOA formation from  $\alpha$ -pinene ozonolysis, *Atmos. Chem. Phys.*, 17, 13187-13211, 10.5194/acp-17-13187-2017, 2017.

Gervasi, N. R., Topping, D. O., and Zuend, A.: A predictive group-contribution model for the viscosity of aqueous organic aerosol, *Atmos. Chem. Phys. Discuss.*, 2019, 1-32, 10.5194/acp-2019-699, 2019.

Grayson, J. W., Zhang, Y., Mutzel, A., Renbaum-Wolff, L., Böge, O., Kamal, S., Herrmann, H., Martin, S. T., and Bertram, A. K.: Effect of varying experimental conditions on the viscosity of  $\alpha$ -pinene derived secondary organic material, *Atmos. Chem. Phys.*, 16, 6027-6040, 10.5194/acp-16-6027-2016, 2016.

Griffin, R. J., Cocker Iii, D. R., Flagan, R. C., and Seinfeld, J. H.: Organic aerosol formation from the oxidation of biogenic hydrocarbons, *Journal of Geophysical Research: Atmospheres*, 104, 3555-3567, 10.1029/1998JD100049, 1999.

Hallquist, M., Wängberg, I., Ljungström, E., Barnes, I., and Becker, K.-H.: Aerosol and Product Yields from NO<sub>3</sub> Radical-Initiated Oxidation of Selected Monoterpenes, *Environmental Science & Technology*, 33, 553-559, 10.1021/es980292s, 1999.

Hallquist, M., Wenger, J. C., Baltensperger, U., Rudich, Y., Simpson, D., Claeys, M., Dommen, J., Donahue, N. M., George, C., Goldstein, A. H., Hamilton, J. F., Herrmann, H., Hoffmann, T., Iinuma, Y., Jang, M., Jenkin, M. E., Jimenez, J. L., Kiendler-Scharr, A.,

Maenhaut, W., McFiggans, G., Mentel, T. F., Monod, A., Prevot, A. S. H., Seinfeld, J. H., Surratt, J. D., Szmigielski, R., and Wildt, J.: The formation, properties and impact of secondary organic aerosol: current and emerging issues, *Atmospheric Chemistry and Physics*, 9, 5155-5235, 2009.

Hoffmann, T., Odum, J. R., Bowman, F., Collins, D., Klockow, D., Flagan, R. C., and Seinfeld, J. H.: Formation of Organic Aerosols from the Oxidation of Biogenic Hydrocarbons, *Journal of Atmospheric Chemistry*, 26, 189-222, 10.1023/A:1005734301837, 1997.

Huang, Y., Zhao, R., Charan, S. M., Kenseth, C. M., Zhang, X., and Seinfeld, J. H.: Unified Theory of Vapor–Wall Mass Transport in Teflon-Walled Environmental Chambers, *Environmental Science & Technology*, 52, 2134-2142, 10.1021/acs.est.7b05575, 2018.

Jenkin, M. E., Saunders, S. M., Wagner, V., and Pilling, M. J.: Protocol for the development of the Master Chemical Mechanism, MCM v3 (Part B): tropospheric degradation of aromatic volatile organic compounds, *Atmos. Chem. Phys.*, 3, 181-193, 10.5194/acp-3-181-2003, 2003.

Julin, J., Shiraiwa, M., Miles, R. E. H., Reid, J. P., Pöschl, U., and Riipinen, I.: Mass Accommodation of Water: Bridging the Gap Between Molecular Dynamics Simulations and Kinetic Condensation Models, *The Journal of Physical Chemistry A*, 117, 410-420, 10.1021/jp310594e, 2013.

Kalberer, M., Paulsen, D., Sax, M., Steinbacher, M., Dommen, J., Prevot, A. S. H., Fisseha, R., Weingartner, E., Frankevich, V., Zenobi, R., and Baltensperger, U.: Identification of polymers as major components of atmospheric organic aerosols, *Science*, 303, 1659-1662, 2004.

Kanakidou, M., Seinfeld, J. H., Pandis, S. N., Barnes, I., Dentener, F. J., Facchini, M. C., Van Dingenen, R., Ervens, B., Nenes, A., Nielsen, C. J., Swietlicki, E., Putaud, J. P., Balkanski, Y., Fuzzi, S., Horth, J., Moortgat, G. K., Winterhalter, R., Myhre, C. E. L., Tsigaridis, K., Vignati, E., Stephanou, E. G., and Wilson, J.: Organic aerosol and global climate modelling: a review, *Atmospheric Chemistry and Physics*, 5, 1053-1123, 2005.

Keyword, M. D., Varutbangkul, V., Bahreini, R., Flagan, R. C., and Seinfeld, J. H.: Secondary organic aerosol formation from the ozonolysis of cycloalkenes and related compounds, *Environmental Science & Technology*, 38, 4157-4164, 10.1021/es.035363o, 2004.

Koop, T., Bookhold, J., Shiraiwa, M., and Pöschl, U.: Glass transition and phase state of organic compounds: dependency on molecular properties and implications for secondary organic aerosols in the atmosphere, *Physical Chemistry Chemical Physics*, 13, 19238-19255, 2011.

Krechmer, J. E., Pagonis, D., Ziemann, P. J., and Jimenez, J. L.: Quantification of Gas-Wall Partitioning in Teflon Environmental Chambers Using Rapid Bursts of Low-

Volatility Oxidized Species Generated in Situ, *Environmental Science & Technology*, 50, 5757-5765, 10.1021/acs.est.6b00606, 2016.

Kurtén, T., Møller, K. H., Nguyen, T. B., Schwantes, R. H., Misztal, P. K., Su, L., Wennberg, P. O., Fry, J. L., and Kjaergaard, H. G.: Alkoxy Radical Bond Scissions Explain the Anomalously Low Secondary Organic Aerosol and Organonitrate Yields From  $\alpha$ -Pinene + NO<sub>3</sub>, *The Journal of Physical Chemistry Letters*, 8, 2826-2834, 10.1021/acs.jpcllett.7b01038, 2017.

Liebmann, J., Sobanski, N., Schuladen, J., Karu, E., Hellén, H., Hakola, H., Zha, Q., Ehn, M., Riva, M., Heikkinen, L., Williams, J., Fischer, H., Lelieveld, J., and Crowley, J. N.: Alkyl nitrates in the boreal forest: formation via the NO<sub>3</sub>-, OH- and O<sub>3</sub>-induced oxidation of biogenic volatile organic compounds and ambient lifetimes, *Atmos. Chem. Phys.*, 19, 10391-10403, 10.5194/acp-19-10391-2019, 2019.

Lopez-Hilfiker, F. D., Mohr, C., Ehn, M., Rubach, F., Kleist, E., Wildt, J., Mentel, T. F., Lutz, A., Hallquist, M., Worsnop, D., and Thornton, J. A.: A novel method for online analysis of gas and particle composition: description and evaluation of a Filter Inlet for Gases and AEROSols (FIGAERO), *Atmos. Meas. Tech.*, 7, 983-1001, 10.5194/amt-7-983-2014, 2014.

Loza, C. L., Chan, A. W. H., Galloway, M. M., Keutsch, F. N., Flagan, R. C., and Seinfeld, J. H.: Characterization of vapor wall loss in laboratory chambers, *Environmental Science & Technology*, 44, 5074-5078, 10.1021/es100727v, 2010.

Marshall, F. H., Berkemeier, T., Shiraiwa, M., Nandy, L., Ohm, P. B., Dutcher, C. S., and Reid, J. P.: Influence of particle viscosity on mass transfer and heterogeneous ozonolysis kinetics in aqueous-sucrose-maleic acid aerosol, *Physical Chemistry Chemical Physics*, 20, 15560-15573, 10.1039/C8CP01666F, 2018.

Müller, J. F., Peeters, J., and Stavrou, T.: Fast photolysis of carbonyl nitrates from isoprene, *Atmos. Chem. Phys.*, 14, 2497-2508, 10.5194/acp-14-2497-2014, 2014.

Nah, T., Sanchez, J., Boyd, C. M., and Ng, N. L.: Photochemical Aging of  $\alpha$ -pinene and  $\beta$ -pinene Secondary Organic Aerosol formed from Nitrate Radical Oxidation, *Environmental Science & Technology*, 50, 222-231, 10.1021/acs.est.5b04594, 2016.

Nah, T., McVay, R. C., Pierce, J. R., Seinfeld, J. H., and Ng, N. L.: Constraining uncertainties in particle-wall deposition correction during SOA formation in chamber experiments, *Atmos. Chem. Phys.*, 17, 2297-2310, 10.5194/acp-17-2297-2017, 2017.

Ng, N. L., Chhabra, P. S., Chan, A. W. H., Surratt, J. D., Kroll, J. H., Kwan, A. J., McCabe, D. C., Wennberg, P. O., Sorooshian, A., Murphy, S. M., Dalleska, N. F., Flagan, R. C., and Seinfeld, J. H.: Effect of NO<sub>x</sub> level on secondary organic aerosol (SOA) formation from the photooxidation of terpenes, *Atmos. Chem. Phys.*, 7, 5159-5174, 10.5194/acp-7-5159-2007, 2007.

- Ng, N. L., Brown, S. S., Archibald, A. T., Atlas, E., Cohen, R. C., Crowley, J. N., Day, D. A., Donahue, N. M., Fry, J. L., Fuchs, H., Griffin, R. J., Guzman, M. I., Herrmann, H., Hodzic, A., Iinuma, Y., Jimenez, J. L., Kiendler-Scharr, A., Lee, B. H., Luecken, D. J., Mao, J., McLaren, R., Mutzel, A., Osthoff, H. D., Ouyang, B., Picquet-Varrault, B., Platt, U., Pye, H. O. T., Rudich, Y., Schwantes, R. H., Shiraiwa, M., Stutz, J., Thornton, J. A., Tilgner, A., Williams, B. J., and Zaveri, R. A.: Nitrate radicals and biogenic volatile organic compounds: oxidation, mechanisms, and organic aerosol, *Atmos. Chem. Phys.*, 17, 2103-2162, 10.5194/acp-17-2103-2017, 2017.
- Nguyen, T. B., Crounse, J. D., Teng, A. P., St. Clair, J. M., Paulot, F., Wolfe, G. M., and Wennberg, P. O.: Rapid deposition of oxidized biogenic compounds to a temperate forest, *Proceedings of the National Academy of Sciences*, 112, E392, 10.1073/pnas.1418702112, 2015.
- Odum, J. R., Hoffmann, T., Bowman, F., Collins, D., Flagan, R. C., and Seinfeld, J. H.: Gas/particle partitioning and secondary organic aerosol yields, *Environmental Science & Technology*, 30, 2580-2585, 1996.
- Pankow, J. F.: An absorption model of gas-particle partitioning of organic-compounds in the atmosphere, *Atmospheric Environment*, 28, 185-188, 1994.
- Perring, A. E., Pusede, S. E., and Cohen, R. C.: An Observational Perspective on the Atmospheric Impacts of Alkyl and Multifunctional Nitrates on Ozone and Secondary Organic Aerosol, *Chemical Reviews*, 113, 5848-5870, 10.1021/cr300520x, 2013.
- Pöschl, U.: Atmospheric aerosols: Composition, transformation, climate and health effects, *Angewandte Chemie-International Edition*, 44, 7520-7540, 10.1002/anie.200501122, 2005.
- Press, W. H., Teukolsky, S. A., Vetterling, W. T., and Flannery, B. P.: *Numerical Recipes 3rd Edition: The Art of Scientific Computing*, Cambridge University Press, 1256 pp., 2007.
- Reid, J. P., Bertram, A. K., Topping, D. O., Laskin, A., Martin, S. T., Petters, M. D., Pope, F. D., and Rovelli, G.: The viscosity of atmospherically relevant organic particles, *Nature Communications*, 9, 956, 10.1038/s41467-018-03027-z, 2018.
- Roldin, P., Eriksson, A. C., Nordin, E. Z., Hermansson, E., Mogensen, D., Rusanen, A., Boy, M., Swietlicki, E., Svenningsson, B., Zelenyuk, A., and Pagels, J.: Modelling non-equilibrium secondary organic aerosol formation and evaporation with the aerosol dynamics, gas- and particle-phase chemistry kinetic multilayer model ADCHAM, *Atmospheric Chemistry and Physics*, 14, 7953-7993, 10.5194/acp-14-7953-2014, 2014.
- Saunders, S. M., Jenkin, M. E., Derwent, R. G., and Pilling, M. J.: Protocol for the development of the Master Chemical Mechanism, MCM v3 (Part A): tropospheric degradation of non-aromatic volatile organic compounds, *Atmos. Chem. Phys.*, 3, 161-180, 10.5194/acp-3-161-2003, 2003.

Seinfeld, J. H., and Pandis, S. N.: Atmospheric Chemistry and Physics: From Air Pollution to Climate Change, John Wiley & Sons, Inc., New York, 2016.

Shiraiwa, M., Pfrang, C., and Pöschl, U.: Kinetic multi-layer model of aerosol surface and bulk chemistry (KM-SUB): the influence of interfacial transport and bulk diffusion on the oxidation of oleic acid by ozone, *Atmos. Chem. Phys.*, 10, 3673-3691, 2010.

Shiraiwa, M., Ammann, M., Koop, T., and Pöschl, U.: Gas uptake and chemical aging of semisolid organic aerosol particles, *Proceedings of the National Academy of Sciences*, 108, 11003-11008, 10.1073/pnas.1103045108, 2011.

Shiraiwa, M., Pfrang, C., Koop, T., and Pöschl, U.: Kinetic multi-layer model of gas-particle interactions in aerosols and clouds (KM-GAP): linking condensation, evaporation and chemical reactions of organics, oxidants and water, *Atmos. Chem. Phys.*, 12, 2777-2794, 10.5194/acp-12-2777-2012, 2012.

Shiraiwa, M., Yee, L. D., Schilling, K. A., Loza, C. L., Craven, J. S., Zuend, A., Ziemann, P. J., and Seinfeld, J. H.: Size distribution dynamics reveal particle-phase chemistry in organic aerosol formation, *Proceedings of the National Academy of Sciences of the United States of America*, 110, 11746-11750, 10.1073/pnas.1307501110, 2013.

Takeuchi, M., and Ng, N. L.: Chemical composition and hydrolysis of organic nitrate aerosol formed from hydroxyl and nitrate radical oxidation of  $\alpha$ -pinene and  $\beta$ -pinene, *Atmos. Chem. Phys.*, 19, 12749-12766, 10.5194/acp-19-12749-2019, 2019.

Tikkanen, O. P., Hämäläinen, V., Rovelli, G., Lipponen, A., Shiraiwa, M., Reid, J. P., Lehtinen, K. E. J., and Yli-Juuti, T.: Optimization of process models for determining volatility distribution and viscosity of organic aerosols from isothermal particle evaporation data, *Atmos. Chem. Phys.*, 19, 9333-9350, 10.5194/acp-19-9333-2019, 2019.

Ullmann, D. A., Hinks, M. L., Maclean, A. M., Butenhoff, C. L., Grayson, J. W., Barsanti, K., Jimenez, J. L., Nizkorodov, S. A., Kamal, S., and Bertram, A. K.: Viscosities, diffusion coefficients, and mixing times of intrinsic fluorescent organic molecules in brown limonene secondary organic aerosol and tests of the Stokes–Einstein equation, *Atmos. Chem. Phys.*, 19, 1491-1503, 10.5194/acp-19-1491-2019, 2019.

Vaden, T. D., Imre, D., Beranek, J., Shrivastava, M., and Zelenyuk, A.: Evaporation kinetics and phase of laboratory and ambient secondary organic aerosol, *Proceedings of the National Academy of Sciences of the United States of America*, 108, 2190-2195, 10.1073/pnas.1013391108, 2011.

Virtanen, A., Joutsensaari, J., Koop, T., Kannosto, J., YliPirilä, P., Leskinen, J., Mäkelä, J. M., Holopainen, J. K., Pöschl, U., Kulmala, M., Worsnop, D. R., and Laaksonen, A.: An amorphous solid state of biogenic secondary organic aerosol particles, *Nature*, 467, 824-827, doi:10.1038/nature09455, 2010.

Yeh, G. K., and Ziemann, P. J.: Gas-Wall Partitioning of Oxygenated Organic Compounds: Measurements, Structure–Activity Relationships, and Correlation with Gas Chromatographic Retention Factor, *Aerosol Science and Technology*, 49, 727-738, 10.1080/02786826.2015.1068427, 2015.

Yli-Juuti, T., Pajunoja, A., Tikkanen, O.-P., Buchholz, A., Faiola, C., Väisänen, O., Hao, L., Kari, E., Peräkylä, O., Garmash, O., Shiraiwa, M., Ehn, M., Lehtinen, K., and Virtanen, A.: Factors controlling the evaporation of secondary organic aerosol from  $\alpha$ -pinene ozonolysis, *Geophysical Research Letters*, 44, 2562-2570, 10.1002/2016GL072364, 2017.

Zaveri, R. A., Easter, R. C., Fast, J. D., and Peters, L. K.: Model for Simulating Aerosol Interactions and Chemistry (MOSAIC), *Journal of Geophysical Research-Atmospheres*, 113, 10.1029/2007jd008782, 2008.

Zaveri, R. A., Easter, R. C., Shilling, J. E., and Seinfeld, J. H.: Modeling kinetic partitioning of secondary organic aerosol and size distribution dynamics: representing effects of volatility, phase state, and particle-phase reaction, *Atmos. Chem. Phys.*, 14, 5153-5181, 10.5194/acp-14-5153-2014, 2014.

Zaveri, R. A., Shilling, J. E., Zelenyuk, A., Liu, J., Bell, D. M., D'Ambro, E. L., Gaston, C. J., Thornton, J. A., Laskin, A., Lin, P., Wilson, J., Easter, R. C., Wang, J., Bertram, A. K., Martin, S. T., Seinfeld, J. H., and Worsnop, D. R.: Growth Kinetics and Size Distribution Dynamics of Viscous Secondary Organic Aerosol, *Environmental Science & Technology*, 52, 1191-1199, 10.1021/acs.est.7b04623, 2018.

Zhang, X., Schwantes, R. H., McVay, R. C., Lignell, H., Coggon, M. M., Flagan, R. C., and Seinfeld, J. H.: Vapor wall deposition in Teflon chambers, *Atmos. Chem. Phys.*, 15, 4197-4214, 10.5194/acp-15-4197-2015, 2015a.

Zhang, Y., Sanchez, M. S., Douet, C., Wang, Y., Bateman, A. P., Gong, Z., Kuwata, M., Renbaum-Wolff, L., Sato, B. B., Liu, P. F., Bertram, A. K., Geiger, F. M., and Martin, S. T.: Changing shapes and implied viscosities of suspended submicron particles, *Atmos. Chem. Phys.*, 15, 7819-7829, 10.5194/acp-15-7819-2015, 2015b.

Ziemann, P. J., and Atkinson, R.: Kinetics, products, and mechanisms of secondary organic aerosol formation, *Chemical Society Reviews*, 41, 6582-6605, 2012.

## **Supporting Information**

### **S.1 Particle-Phase Oligomerization Scheme**

Gas-phase oxidation products may undergo reversible oligomerization in the particle phase, which is treated in the kinetic model. The volatility information of the monomeric building blocks is tracked in their oligomeric state and regained after decomposition into monomers. We assume both, formation and decomposition of oligomers, to be pseudo-first order processes that occur with a rate depending on the precursor material. Formation of hetero-oligomers is hence implicitly considered, but occurs with the speed of product from either precursor, not with a combined rate. This means that molecule  $A$  oligomerizes with molecule  $B$  with the (pseudo-first order) oligomerization rate coefficient  $k_{\text{form},A} = k'_{\text{form},A} \cdot ([A_{\text{monomer}}] + [B_{\text{monomer}}])$ , where  $k'_{\text{form},A}$  is the second-order oligomerization rate coefficient of molecule  $A$  and  $[A_{\text{monomer}}]$ ,  $[B_{\text{monomer}}]$  are particle-phase monomer concentrations of molecules  $A$  and  $B$ , respectively.



Furthermore, gradual oligomerization will affect the availability of reaction sites for oligomerization reactions. This is accounted for with a conservatively chosen factor that can reduce the oligomer formation rate by up to a factor of 0.5, depending on the oligomer fraction,  $f_{\text{oligomer}}$ .

$$k_{\text{form},A}^* = k_{\text{form},A} \cdot (1 - 0.5 \cdot f_{\text{oligomer}}) \quad (3)$$

This assumes that every monoterpene oxidation product has two possible reaction sites for oligomerization, but for simplicity, there is no further oligomerization beyond the dimer level. The real reduction in formation rate will depend on the exact number of reaction sites and average chain length of the oligomer in solution. A schematic representation of the oligomer formation and decomposition processes employed in the kinetic model is shown in Fig. S3.

### SI Figures

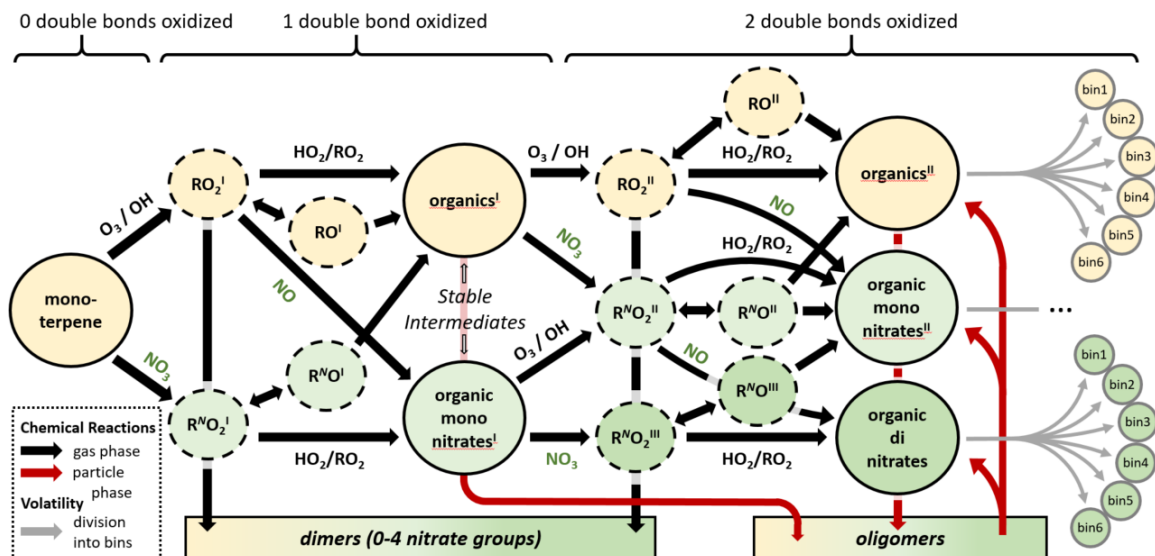


**Fig. S1.** Schematic representation of the extended lumped chemical mechanism for monoterpenes with two double bonds (e.g. limonene). Yellow colors denote non-nitrated products, while green colors denote mono-nitrated organics (light green), di-nitrated organics (green), and nitrogen oxides (dark green), respectively. Stable products are divided into product bins analogous to Fig. 1 (not depicted for clarity).

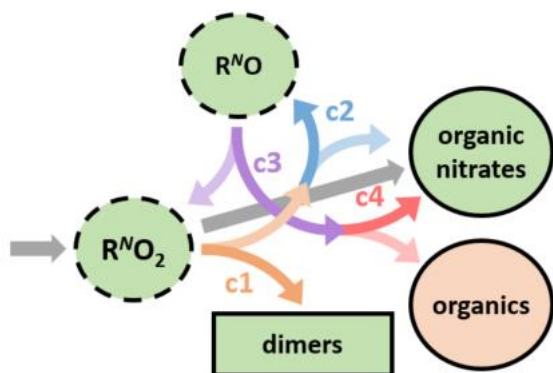
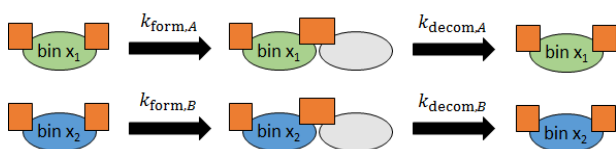
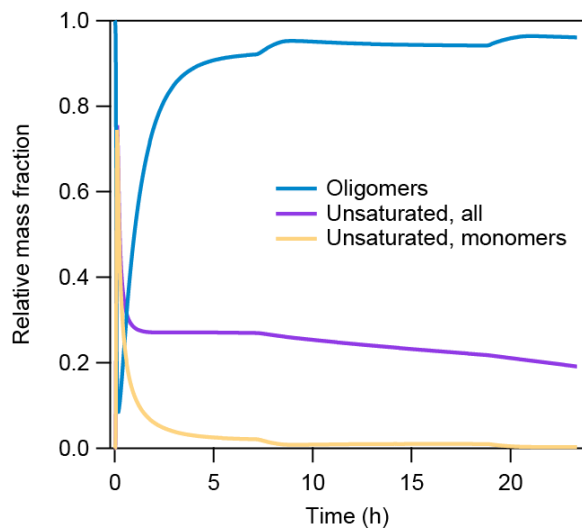


Fig. S2. Scheme detailing the branching ratios  $c1$ - $c4$  of  $RO_2$  and  $RO$  radical chemistry used in the oxidation of  $\alpha$ -pinene. The branching ratios detail the success of dimer formation ( $c1$ ),  $RO$  yield from not-dimer-forming  $RO_2$  self-reaction ( $c2$ ), success of  $RO$  making product upon unimolecular decay ( $c3$ ) and the branching between nitrated and non-nitrated products from stabilization of  $RO$  ( $c4$ ). The darker color in the arrow pairs indicates which of the two branches is increased with increasing numerical value of the branching ratio. The formation of  $\alpha$ -pinene oxidation products from  $RO_2^{II}$  and limonene oxidation products from  $RO_2^{IV}$  and  $RO_2^V$  was treated analogous.



**Fig. S3.** Schematic representation of the oligomer formation and decomposition scheme A employed in the kinetic model presented in this study. Chemical reaction of the oxidation products from precursor 1 (green ellipsoid) and precursor 2 (blue ellipsoid) occurs at specific reaction sites (orange squares) under formation of dimers.



**Fig. S4.** Detailed composition highlighting saturation and oligomerization degree of oxidation products of the particle phase during the LIM experiment according to the model in the best fit simulation.

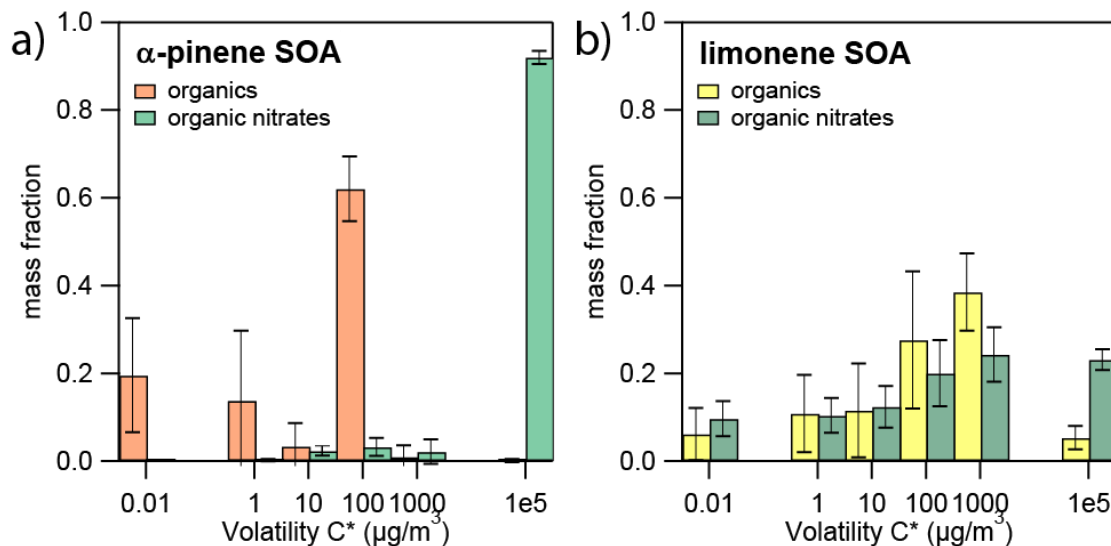


Fig. S5. Volatility distributions of monoterpene oxidation products as derived from kinetic model optimization to experimental data. These distribution keys are used to divide stable monomeric oxidation products into volatility bins. Volatility distributions were differentiated between nitrated and non-nitrated products as well as their precursor origin: (a) nitrated and non-nitrated  $\alpha$ -pinene oxidation products ( $f_{\text{apin,org,bi}}$ ,  $f_{\text{apin,nitr,bi}}$ ), (b) nitrated and non-nitrated limonene products ( $f_{\text{lim,org,bi}}$ ,  $f_{\text{lim,nitr,bi}}$ ). Dinitrated and mononitrated molecules were considered as following the same volatility distribution. The bars show arithmetic means obtained from multiple model optimizations that each optimized six volatility bins while keeping all other model parameters constant. All fits possessed similar model-experiment correlation. Error bars represent standard deviations.

## SI Tables

Table S1. Lumped gas-phase chemical mechanism employed in this study. Rate coefficients of gas phase reactions involving inorganic reactants are ported from MCM and unless explicitly indicated displayed for a temperature of 5.5 °C and 1 bar pressure. Note that all stable organic products are further subdivided into 6 volatility bins according to a fitted volatility distribution.  $[\text{RO}_2]$  stands for the total concentration of  $\text{RO}_2$  radicals, T is temperature,  $f_{\text{oligomer}}$  the oligomer fraction,  $c_1$ - $c_4$  are fittest branching ratios, and  $\text{TF}_{\text{apin}}$  and  $\text{TF}_{\text{lim}}$  are temperature-dependence factors for  $\alpha$ -pinene and limonene, respectively. In the names of chemical species, the suffix “org” denotes a non-nitrated product, the suffix “orgnitr” denotes an organic nitrate. Among these, a superscript “1N” denotes a mononitrated compound, a superscript “2N” denotes a dinitrated compound, etc.

Number	Reaction Equation	Rate coefficients (s <sup>-1</sup> or cm <sup>3</sup> /s)
Gas Phase Reactions Involving Inorganics		
1	$O \rightarrow O_3$	$6.27 \cdot 10^4 \cdot (T/300)^{-2.6}$
2	$O \rightarrow O_3$	$1.78 \cdot 10^4 \cdot (T/300)^{-2.6}$
3	$O + O_3 \rightarrow$	$8.00 \cdot 10^{-12} \cdot \exp(-2060/T)$
4	$O + NO \rightarrow NO_2$	$2.63 \cdot 10^{-12}$
5	$O + NO_2 \rightarrow NO$	$5.50 \cdot 10^{-12} \cdot \exp(188/T)$
6	$O + NO_2 \rightarrow NO_3$	$2.33 \cdot 10^{-12}$
7	$O_3 + NO \rightarrow NO_2$	$1.40 \cdot 10^{-12} \cdot \exp(-1310/T)$
8	$O_3 + NO_2 \rightarrow NO_3$	$1.40 \cdot 10^{-13} \cdot \exp(-2470/T)$
9	$NO + NO \rightarrow NO_2 + NO_2$	$1.79 \cdot 10^{-20} \cdot \exp(530/T)$

10	$\text{NO} + \text{NO}_3 \rightarrow \text{NO}_2 + \text{NO}_2$	$1.80 \cdot 10^{-11} \cdot \exp(110/T)$
11	$\text{NO}_2 + \text{NO}_3 \rightarrow \text{NO} + \text{NO}_2$	$4.50 \cdot 10^{-14} \cdot \exp(-1260/T)$
12	$\text{NO}_2 + \text{NO}_3 \rightarrow \text{N}_2\text{O}_5$	$1.28 \cdot 10^{-12}$
13	$\text{O}_3 + \text{OH} \rightarrow \text{HO}_2$	$1.70 \cdot 10^{-12} \cdot \exp(-940/T)$
14	$\text{OH} + \text{CO} \rightarrow \text{HO}_2$	$2.33 \cdot 10^{-13}$
15	$\text{OH} + \text{H}_2\text{O}_2 \rightarrow \text{HO}_2$	$2.9 \cdot 10^{-12} \cdot \exp(-160/T)$
16	$\text{O}_3 + \text{HO}_2 \rightarrow \text{OH}$	$2.03 \cdot 10^{-16} \cdot (T/300)^{4.57} \cdot \exp(693/T)$
17	$\text{OH} + \text{HO}_2 \rightarrow$	$4.80 \cdot 10^{-11} \cdot \exp(250/T)$
18	$\text{HO}_2 + \text{HO}_2 \rightarrow \text{H}_2\text{O}_2$	$2.20 \cdot 10^{-13} \cdot \exp(600/T)$
19	$\text{HO}_2 + \text{HO}_2 \rightarrow \text{H}_2\text{O}_2$	$4.94 \cdot 10^{-14} \cdot \exp(980/T)$
20	$\text{NO} + \text{OH} \rightarrow \text{HONO}$	$1.12 \cdot 10^{-11}$

21	$\text{NO}_2 + \text{OH} \rightarrow \text{HNO}_3$	$1.15 \cdot 10^{-11}$
22	$\text{NO}_3 + \text{OH} \rightarrow \text{NO}_2 + \text{HO}_2$	$2.00 \cdot 10^{-11}$
23	$\text{NO} + \text{HO}_2 \rightarrow \text{NO}_2 + \text{OH}$	$3.45 \cdot 10^{-12} \cdot \exp(270/T)$
24	$\text{NO}_2 + \text{HO}_2 \rightarrow \text{HO}_2\text{NO}_2$	$8.55 \cdot 10^{-13}$
25	$\text{OH} + \text{HO}_2\text{NO}_2 \rightarrow \text{NO}_2$	$3.20 \cdot 10^{-13} \cdot \exp(690/T)$
26	$\text{NO}_3 + \text{HO}_2 \rightarrow \text{NO}_2 + \text{OH}$	$4.00 \cdot 10^{-12}$
27	$\text{OH} + \text{HONO} \rightarrow \text{NO}_2$	$2.50 \cdot 10^{-12} \cdot \exp(260/T)$
28	$\text{OH} + \text{HNO}_3 \rightarrow \text{NO}_3$	$5.00 \cdot 10^{-3}$
29	$\text{HNO}_3 \rightarrow \text{NA}$	$6.00 \cdot 10^{-6}$
30	$\text{N}_2\text{O}_5 \rightarrow \text{NA} + \text{NA}$	$4.00 \cdot 10^{-4}$
31	$\text{N}_2\text{O}_5 \rightarrow \text{NO}_2 + \text{NO}_3$	$3.50 \cdot 10^{-3}$
32	$\text{HO}_2\text{NO}_2 \rightarrow \text{NO}_2 + \text{HO}_2$	$5.00 \cdot 10^{-3}$

Gas Phase Reactions Involving Organics		
34	$O_3 + \text{APINENE} \rightarrow \text{OH} + \text{APINENE\_RO}_2^{\text{I}}$	$0.85 \cdot 8.05 \cdot 10^{-16} \cdot e^{-640/T}$
35	$O_3 + \text{APINENE} \rightarrow \text{APINENE\_RO}_2^{\text{II}}$	$0.15 \cdot 8.05 \cdot 10^{-16} \cdot e^{-640/T}$
36	$\text{OH} + \text{APINENE} \rightarrow \text{APINENE\_RO}_2^{\text{II}}$	$1.2e^{-11} \cdot e^{440/T}$
37	$\text{NO}_3 + \text{APINENE} \rightarrow \text{APINENE\_RO}_2^{\text{III}}$	$1.2e^{-12} \cdot e^{490/T}$
38	$\text{NO} + \text{APINENE\_RO}_2^{\text{I}} \rightarrow \text{NO}_2 + \text{APINENE\_RO}^{\text{I}}$	$9.10 \cdot 10^{-12}$
39	$\text{NO}_3 + \text{APINENE\_RO}_2^{\text{I}} \rightarrow \text{NO}_2 + \text{APINENE\_RO}^{\text{I}}$	$2.30 \cdot 10^{-12}$
40	$\text{HO}_2 + \text{APINENE\_RO}_2^{\text{I}} \rightarrow \text{APINENE\_org}$	$2.20 \cdot 10^{-11}$
41	$\text{NO} + \text{APINENE\_RO}_2^{\text{II}} \rightarrow \text{APINENE\_orgnitr}^{\text{1N}}$	$9.10 \cdot 10^{-12}$
42	$\text{NO} + \text{APINENE\_RO}_2^{\text{II}} \rightarrow \text{NO}_2 + \text{APINENE\_RO}^{\text{I}}$	$9.10 \cdot 10^{-12}$
43	$\text{NO}_3 + \text{APINENE\_RO}_2^{\text{II}} \rightarrow \text{NO}_2 + \text{APINENE\_RO}^{\text{I}}$	$2.30 \cdot 10^{-12}$
44	$\text{HO}_2 + \text{APINENE\_RO}_2^{\text{II}} \rightarrow \text{APINENE\_org}$	$2.20 \cdot 10^{-11}$

45	$\text{NO} + \text{APINENE\_RO}_2^{\text{III}} \rightarrow \text{NO}_2 + \text{APINENE\_RO}^{\text{II}}$	$9.10 \cdot 10^{-12}$
46	$\text{NO}_3 + \text{APINENE\_RO}_2^{\text{III}} \rightarrow \text{NO}_2 + \text{APINENE\_RO}^{\text{II}}$	$2.30 \cdot 10^{-12}$
47	$\text{HO}_2 + \text{APINENE\_RO}_2^{\text{III}} \rightarrow \text{APINENE\_orgnitr}^{\text{1N}}$	$2.20 \cdot 10^{-11}$
48	$\text{APINENE\_RO}_2^{\text{I}} \rightarrow \text{APINENE\_RO}^{\text{I}}$	$[\text{RO}_2] \cdot (1-c_1) \cdot c_2 \cdot 10^{-13}$
49	$\text{APINENE\_RO}_2^{\text{I}} \rightarrow \text{APINENE\_org}$	$[\text{RO}_2] \cdot (1-c_1) \cdot (1-c_2) \cdot 10^{-13}$
50	$\text{APINENE\_RO}_2^{\text{II}} \rightarrow \text{APINENE\_RO}^{\text{I}}$	$[\text{RO}_2] \cdot (1-c_1) \cdot c_2 \cdot 10^{-14}$
51	$\text{APINENE\_RO}_2^{\text{II}} \rightarrow \text{APINENE\_org}$	$[\text{RO}_2] \cdot (1-c_1) \cdot (1-c_2) \cdot 10^{-14}$
52	$\text{APINENE\_RO}_2^{\text{III}} \rightarrow \text{APINENE\_RO}^{\text{II}}$	$[\text{RO}_2] \cdot (1-c_1) \cdot c_2 \cdot 10^{-14}$
53	$\text{APINENE\_RO}_2^{\text{III}} \rightarrow \text{APINENE\_orgnitr}^{\text{1N}}$	$[\text{RO}_2] \cdot (1-c_1) \cdot (1-c_2) \cdot 10^{-14}$
54	$\text{APINENE\_RO}^{\text{I}} \rightarrow \text{HO}_2 + \text{APINENE\_org}$	$c_{3\_apin} \cdot 10^6$
55	$\text{APINENE\_RO}^{\text{I}} \rightarrow \text{APINENE\_RO}_2^{\text{II}}$	$(1 - c_{3\_apin}) \cdot 10^6$
56	$\text{APINENE\_RO}^{\text{II}} \rightarrow \text{NO}_2 + \text{APINENE\_org}$	$c_{3\_apin} \cdot (1 - c_{4\_apin}) \cdot 10^6$

57	$\text{APINENE\_RO}^{\text{II}} \rightarrow \text{APINENE\_orgnitr}^{\text{IN}}$	$c_{3\_apin} \cdot c_{4\_apin} \cdot 10^6$
58	$\text{APINENE\_RO}^{\text{II}} \rightarrow \text{APINENE\_RO}_2^{\text{III}}$	$(1-c_{3\_apin}) \cdot 10^6$
59	$\text{APINENE\_RO}_2^{\text{I}} \rightarrow \text{APINENE\_dimer\_org}$	$c_1 \cdot [\text{RO}_2] \cdot 10^{-13}$
60	$\text{APINENE\_RO}_2^{\text{II}} \rightarrow \text{APINENE\_dimer\_org}$	$c_1 \cdot [\text{RO}_2] \cdot 10^{-14}$
61	$\text{APINENE\_RO}_2^{\text{III}} \rightarrow \text{APINENE\_dimer\_orgnitr}^{\text{IN}}$	$c_1 \cdot [\text{RO}_2] \cdot 10^{-14}$
62	$\text{O}_3 + \text{LIMONENE} \rightarrow \text{OH} + \text{LIMONENE\_RO}_2^{\text{I}}$	$0.865 \cdot 2.80 \cdot 10^{-15} \cdot \exp(-770/T)$
63	$\text{O}_3 + \text{LIMONENE} \rightarrow \text{LIMONENE\_RO}_2^{\text{I}}$	$0.135 \cdot 2.80 \cdot 10^{-15} \cdot \exp(-770/T)$
64	$\text{OH} + \text{LIMONENE} \rightarrow \text{LIMONENE\_RO}_2^{\text{I}}$	$4.28 \cdot 10^{-11} \cdot \exp(401/T)$
65	$\text{NO}_3 + \text{LIMONENE} \rightarrow \text{LIMONENE\_RO}_2^{\text{II}}$	$1.22 \cdot 10^{-11}$
66	$\text{NO} + \text{LIMONENE\_RO}_2^{\text{I}} \rightarrow$ $\text{LIMONENE\_intermed\_orgnitr}^{\text{IN}}$	$0.228 \cdot 2.70 \cdot 10^{-12} \cdot \exp(360/T)$
67	$\text{NO} + \text{LIMONENE\_RO}_2^{\text{I}} \rightarrow \text{NO}_2 +$ $\text{LIMONENE\_RO}^{\text{I}}$	$0.772 \cdot 2.70 \cdot 10^{-12} \cdot \exp(360/T)$

68	$\text{NO}_3 + \text{LIMONENE\_RO}_2^{\text{I}} \rightarrow \text{NO}_2 + \text{LIMONENE\_RO}^{\text{I}}$	$2.30 \cdot 10^{-12}$
69	$\text{HO}_2 + \text{LIMONENE\_RO}_2^{\text{I}} \rightarrow \text{LIMONENE\_intermed\_org}$	$0.914 \cdot 2.91 \cdot 10^{13} \cdot \exp(1300/T)$
70	$\text{NO} + \text{LIMONENE\_RO}_2^{\text{II}} \rightarrow \text{LIMONENE\_intermed\_orgnitr}^{1\text{N}}$	$0.228 \cdot 2.70 \cdot 10^{-12} \cdot \exp(360/T)$
71	$\text{NO} + \text{LIMONENE\_RO}_2^{\text{II}} \rightarrow \text{NO}_2 + \text{LIMONENE\_RO}^{\text{II}}$	$0.772 \cdot 2.70 \cdot 10^{-12} \cdot \exp(360/T)$
72	$\text{NO}_3 + \text{LIMONENE\_RO}_2^{\text{II}} \rightarrow \text{NO}_2 + \text{LIMONENE\_RO}^{\text{II}}$	$2.30 \cdot 10^{-12}$
73	$\text{HO}_2 + \text{LIMONENE\_RO}_2^{\text{II}} \rightarrow \text{LIMONENE\_intermed\_orgnitr}^{1\text{N}}$	$0.914 \cdot 2.91 \cdot 10^{13} \cdot \exp(1300/T)$
74	$\text{LIMONENE\_RO}_2^{\text{I}} \rightarrow \text{LIMONENE\_RO}^{\text{I}}$	$[\text{RO}_2] \cdot (1-c_1) \cdot c_2 \cdot 8.80 \cdot 10^{-13}$
75	$\text{LIMONENE\_RO}_2^{\text{I}} \rightarrow \text{LIMONENE\_intermed\_org}$	$[\text{RO}_2] \cdot (1-c_1) \cdot (1-c_2) \cdot 8.80 \cdot 10^{13}$
76	$\text{LIMONENE\_RO}_2^{\text{II}} \rightarrow \text{LIMONENE\_RO}^{\text{II}}$	$[\text{RO}_2] \cdot (1-c_1) \cdot c_2 \cdot 9.20 \cdot 10^{-14}$

77	LIMONENE_RO <sub>2</sub> <sup>II</sup> → LIMONENE_intermed_orgnitr_ <sup>1N</sup>	[RO <sub>2</sub> ]·(1-c <sub>1</sub> )·(1-c <sub>2</sub> )·9.20·10 <sup>-14</sup>
78	LIMONENE_RO <sup>I</sup> → HO <sub>2</sub> + LIMONENE_intermed_org	c <sub>3,lim</sub> · 10 <sup>6</sup>
79	LIMONENE_RO <sup>I</sup> → LIMONENE_RO <sub>2</sub> <sup>II</sup>	(1-c <sub>3,lim</sub> ) · 10 <sup>6</sup>
80	LIMONENE_RO <sup>II</sup> → NO <sub>2</sub> + LIMONENE_intermed_org	c <sub>3,lim</sub> · 10 <sup>6</sup>
81	LIMONENE_RO <sup>II</sup> → LIMONENE_RO <sub>2</sub> <sup>III</sup>	(1-c <sub>3,lim</sub> ) · 10 <sup>6</sup>
82	O <sub>3</sub> + LIMONENE_intermed_org → OH + LIMONENE_RO <sub>2</sub> <sup>III</sup>	0.67·8.30·10 <sup>-18</sup>
83	O <sub>3</sub> + LIMONENE_intermed_org → LIMONENE_RO <sub>2</sub> <sup>III</sup>	0.33·8.30·10 <sup>-18</sup>
84	OH + LIMONENE_intermed_org → LIMONENE_RO <sub>2</sub> <sup>III</sup>	1.10·10 <sup>-10</sup>
85	NO <sub>3</sub> + LIMONENE_intermed_org → LIMONENE_RO <sub>2</sub> <sup>IV</sup>	2.60·10 <sup>-13</sup>

86	$O_3 + \text{LIMONENE\_intermed\_orgnitr}^{1N} \rightarrow \text{OH} + \text{LIMONENE\_RO}_2^{IV}$	$0.67 \cdot 8.30 \cdot 10^{-18}$
87	$O_3 + \text{LIMONENE\_intermed\_orgnitr}^{1N} \rightarrow \text{LIMONENE\_RO}_2^{IV}$	$0.33 \cdot 8.30 \cdot 10^{-18}$
88	$\text{OH} + \text{LIMONENE\_intermed\_orgnit}^{1N} \rightarrow \text{LIMONENE\_RO}_2^{IV}$	$1.10 \cdot 10^{-10}$
89	$\text{NO}_3 + \text{LIMONENE\_intermed\_orgnitr}^{1N} \rightarrow \text{LIMONENE\_RO}_2^V$	$2.60 \cdot 10^{-13}$
90	$\text{HO}_2 + \text{LIMONENE\_RO}_2^{III} \rightarrow \text{LIMONENE\_org}$	$0.914 \cdot 2.91 \cdot 10^{-13} \cdot \exp(1300/T)$
91	$\text{NO}_3 + \text{LIMONENE\_RO}_2^{III} \rightarrow \text{NO}_2 + \text{LIMONENE\_RO}^{III}$	$2.30 \cdot 10^{-12}$
92	$\text{NO} + \text{LIMONENE\_RO}_2^{III} \rightarrow \text{NO}_2 + \text{LIMONENE\_RO}^{III}$	$0.772 \cdot 2.70 \cdot 10^{-12} \cdot \exp(360/T)$
93	$\text{NO} + \text{LIMONENE\_RO}_2^{III} \rightarrow \text{LIMONENE\_orgnitr}^{1N}$	$0.228 \cdot 2.70 \cdot 10^{-12} \cdot \exp(360/T)$

94	LIMONENE_RO <sub>2</sub> <sup>III</sup> → LIMONENE_RO <sup>III</sup>	[RO <sub>2</sub> ]·(1-c <sub>1</sub> )·c <sub>2</sub> ·9.20·10 <sup>-14</sup>
95	LIMONENE_RO <sub>2</sub> <sup>III</sup> → LIMONENE_org	[RO <sub>2</sub> ]·(1-c <sub>1</sub> )·(1-c <sub>2</sub> )·9.20·10 <sup>-14</sup>
96	HO <sub>2</sub> + LIMONENE_RO <sub>2</sub> <sup>IV</sup> → LIMONENE_ornitr <sup>1N</sup>	0.914·2.91·10 <sup>-13</sup> ·exp(1300/T)
97	NO <sub>3</sub> + LIMONENE_RO <sub>2</sub> <sup>IV</sup> → NO <sub>2</sub> + LIMONENE_RO <sup>IV</sup>	2.30·10 <sup>-12</sup>
98	NO + LIMONENE_RO <sub>2</sub> <sup>IV</sup> → NO <sub>2</sub> + LIMONENE_RO <sup>IV</sup>	2.70·10 <sup>-12</sup> ·exp(360/T)
99	NO + LIMONENE_RO <sub>2</sub> <sup>IV</sup> → LIMONENE_ornitr <sup>2N</sup>	2.70·10 <sup>-12</sup> ·exp(360/T)
100	LIMONENE_RO <sub>2</sub> <sup>IV</sup> → LIMONENE_RO <sup>IV</sup>	[RO <sub>2</sub> ]·(1-c <sub>1</sub> )·c <sub>2</sub> ·9.20·10 <sup>-14</sup>
101	LIMONENE_RO <sub>2</sub> <sup>IV</sup> → LIMONENE_ornitr <sup>1N</sup>	[RO <sub>2</sub> ]·(1-c <sub>1</sub> )·(1-c <sub>2</sub> )·9.20·10 <sup>-14</sup>
102	HO <sub>2</sub> + LIMONENE_RO <sub>2</sub> <sup>V</sup> → LIMONENE_ornitr <sup>2N</sup>	0.914·2.91·10 <sup>-13</sup> ·exp(1300/T)

103	$\text{NO}_3 + \text{LIMONENE\_RO}_2^{\text{V}} \rightarrow \text{NO}_2 + \text{LIMONENE\_RO}^{\text{V}}$	$2.30 \cdot 10^{-12}$
104	$\text{NO} + \text{LIMONENE\_RO}_2^{\text{V}} \rightarrow \text{NO}_2 + \text{LIMONENE\_RO}^{\text{V}}$	$2.70 \cdot 10^{-12} \cdot \exp(360/T)$
105	$\text{LIMONENE\_RO}_2^{\text{V}} \rightarrow \text{LIMONENE\_RO}^{\text{V}}$	$[\text{RO}_2] \cdot (1-c_1) \cdot c_2 \cdot 9.20 \cdot 10^{-14}$
106	$\text{LIMONENE\_RO}_2^{\text{V}} \rightarrow \text{LIMONENE\_orgnitr}^{2\text{N}}$	$[\text{RO}_2] \cdot (1-c_1) \cdot (1-c_2) \cdot 9.20 \cdot 10^{-14}$
107	$\text{LIMONENE\_RO}^{\text{III}} \rightarrow \text{HO}_2 + \text{LIMONENE\_org}$	$c_{3,\text{lim}} \cdot 10^6$
108	$\text{LIMONENE\_RO}^{\text{III}} \rightarrow \text{LIMONENE\_RO}_2^{\text{III}}$	$(1 - c_{3,\text{lim}}) \cdot 10^6$
109	$\text{LIMONENE\_RO}^{\text{IV}} \rightarrow \text{NO}_2 + \text{LIMONENE\_org}$	$c_{3,\text{lim}} \cdot (1 - c_{4,\text{lim}}) \cdot 10^6$
110	$\text{LIMONENE\_RO}^{\text{IV}} \rightarrow \text{LIMONENE\_orgnitr}^{1\text{N}}$	$c_{3,\text{lim}} \cdot c_{4,\text{lim}} \cdot 10^6$
111	$\text{LIMONENE\_RO}^{\text{IV}} \rightarrow \text{LIMONENE\_RO}_2^{\text{IV}}$	$(1-c_{3,\text{lim}}) \cdot 10^6$
112	$\text{LIMONENE\_RO}^{\text{V}} \rightarrow \text{NO}_2 + \text{LIMONENE\_orgnitr}^{1\text{N}}$	$c_{3,\text{lim}} \cdot (1 - c_{4,\text{lim}}) \cdot 10^6$

113	LIMONENE_RO <sup>V</sup> → LIMONENE_ornitr <sup>2N</sup>	$c_{3,lim} \cdot c_{4,lim} \cdot 10^6$
114	LIMONENE_RO <sup>V</sup> → LIMONENE_RO2 <sup>V</sup>	$(1 - c_{3,lim}) \cdot 10^6$
115	LIMONENE_RO <sub>2</sub> <sup>I</sup> → LIMONENE_dimer_org	$c_1 \cdot [RO_2] \cdot 9.20 \cdot 10^{-14}$
116	LIMONENE_RO <sub>2</sub> <sup>II</sup> → LIMONENE_dimer_ornitr <sup>1N</sup>	$c_1 \cdot [RO_2] \cdot 9.20 \cdot 10^{-14}$
117	LIMONENE_RO <sub>2</sub> <sup>III</sup> → LIMONENE_dimer_org	$c_1 \cdot [RO_2] \cdot 9.20 \cdot 10^{-14}$
118	LIMONENE_RO <sub>2</sub> <sup>IV</sup> → LIMONENE_dimer_ornitr <sup>1N</sup>	$c_1 \cdot [RO_2] \cdot 9.20 \cdot 10^{-14}$
119	LIMONENE_RO <sub>2</sub> <sup>V</sup> → LIMONENE_dimer_ornitr <sup>2N</sup>	$c_1 \cdot [RO_2] \cdot 9.20 \cdot 10^{-14}$
Particle Phase Reactions		
120	LIMONENE_intermed_org → LIMONENE_olig_intermed_org	$k_{form,lim} \cdot (1 - f_{oligomer}/2)$
121	LIMONENE_intermed_ornitr <sup>1N</sup> → LIMONENE_olig_intermed_ornitr <sup>1N</sup>	$k_{form,lim} \cdot (1 - f_{oligomer}/2)$

122	APINENE_org $\rightarrow$ APINENE_olig_org	$k_{\text{form,apin}} \cdot (1 - f_{\text{oligomer}}/2)$
123	APINENE_ornitr <sup>1N</sup> $\rightarrow$ APINENE_olig_ornitr <sup>1N</sup>	$k_{\text{form,apin}} \cdot (1 - f_{\text{oligomer}}/2)$
124	APINENE_olig_org $\rightarrow$ APINENE_org	$k_{\text{decom,apin}} \cdot \exp(\text{TF}_{\text{apin}}/T)$
125	APINENE_olig_ornitr <sup>1N</sup> $\rightarrow$ APINENE_ornitr <sup>1N</sup>	$k_{\text{decom,apin}} \cdot \exp(\text{TF}_{\text{apin}}/T)$
126	LIMONENE_org $\rightarrow$ LIMONENE_olig_org	$k_{\text{form,lim}} \cdot (1 - f_{\text{oligomer}}/2)$
127	LIMONENE_ornitr <sup>1N</sup> $\rightarrow$ LIMONENE_olig_ornitr <sup>1N</sup>	$k_{\text{form,lim}} \cdot (1 - f_{\text{oligomer}}/2)$
128	LIMONENE_ornitr <sup>2N</sup> $\rightarrow$ LIMONENE_olig_ornitr <sup>2N</sup>	$k_{\text{form,lim}} \cdot (1 - f_{\text{oligomer}}/2)$
129	LIMONENE_olig_org $\rightarrow$ LIMONENE_org	$k_{\text{decom,lim}} \cdot \exp(\text{TF}_{\text{lim}}/T)$
130	LIMONENE_olig_ornitr <sup>1N</sup> $\rightarrow$ LIMONENE_ornitr <sup>1N</sup>	$k_{\text{decom,lim}} \cdot \exp(\text{TF}_{\text{lim}}/T)$
131	LIMONENE_olig_ornitr <sup>2N</sup> $\rightarrow$ LIMONENE_ornitr <sup>2N</sup>	$k_{\text{decom,lim}} \cdot \exp(\text{TF}_{\text{lim}}/T)$

132	LIMONENE_olig_intermed_org → LIMONENE_intermed_org	$k_{\text{decom\_lim}} \cdot \exp(\text{TF}_{\text{lim}}/T)$
133	LIMONENE_olig_intermed_orgnitr <sup>1N</sup> → LIMONENE_intermed_orgnitr <sup>1N</sup>	$k_{\text{decom\_lim}} \cdot \exp(\text{TF}_{\text{lim}}/T)$

**APPENDIX C. AN OMNIPRESENT DIVERSITY AND  
VARIABILITY IN THE CHEMICAL COMPOSITION OF  
ATMOSPHERIC FUNCTIONALIZED ORGANIC AEROSOL**

Jenna C. Ditto<sup>1</sup>, Emily B. Barnes<sup>1,a</sup>, Peeyush Khare<sup>1</sup>, Masayuki Takeuchi<sup>2</sup>, Taekyu Joo<sup>3</sup>,  
Alexander A.T. Bui<sup>4</sup>, Julia Lee-Taylor<sup>5,6</sup>, Gamze Eris<sup>7</sup>, Yunle Chen<sup>3</sup>, Bernard Aumont<sup>8</sup>,  
Jose L. Jimenez<sup>5</sup>, Nga Lee Ng<sup>3,7</sup>, Robert J. Griffin<sup>4</sup>, Drew R. Gentner<sup>1,\*</sup>

<sup>1</sup> Dept. of Chemical and Environmental Engineering, Yale University, New Haven CT  
06511 USA

<sup>2</sup> School of Civil and Environmental Engineering, Georgia Institute of Technology,  
Atlanta, GA 30332 USA

<sup>3</sup> School of Earth and Atmospheric Sciences, Georgia Institute of Technology, Atlanta, GA  
30332 USA

<sup>4</sup> Dept. of Civil and Environmental Engineering, Rice University, Houston, TX 77005 USA

<sup>5</sup> Dept. of Chemistry and Cooperative Institute for Research in the Environmental Sciences  
(CIRES), University of Colorado at Boulder, Boulder, CO 80309 USA

<sup>6</sup> National Center for Atmospheric Research, Boulder, CO 80307 USA

<sup>7</sup> School of Chemical and Biomolecular Engineering, Georgia Institute of Technology, Atlanta, GA 30332 USA

<sup>8</sup> Laboratoire Interuniversitaire des Systèmes Atmosphériques, UMR 7583, CNRS, Université Paris-Est-Créteil et Université Paris Diderot, Institut Pierre Simon Laplace, Créteil, France

<sup>a</sup> Now at: Dept. of Civil and Environmental Engineering, University of California, Berkeley, CA 94710 USA

\* Corresponding author: [drew.gentner@yale.edu](mailto:drew.gentner@yale.edu)

## **Abstract**

The atmospheric life cycles of organic compounds occur amongst the evolution of 10,000's of compounds spread across wide ranges of volatility, polarity, and water solubility. The molecular-level chemical composition of this mixture plays a major, yet uncertain, role in its transformations, fates, and impacts. Here, we perform an extensive untargeted molecular-level intercomparison of functionalized organic aerosol (OA) from three diverse

field sites and an environmental chamber. Despite similar bulk OA composition, we report large molecular-level variability between ambient samples at each field site, with  $66 \pm 13\%$  of functionalized OA compounds in a sample differing between consecutive multi-hour samples. Single precursor laboratory experiments and fully chemically-explicit modeling confirm this variability is due to changes in emitted precursor mixtures, chemical age, and/or oxidation conditions. These molecular-level results demonstrate much greater compositional variability than less-speciated measurements, which tend to show consistent diurnal profiles for descriptors of elemental composition (e.g. O/C ratio). This has potential implications for fundamental and applied atmospheric chemistry studies, and should be considered in future work to evaluate the effects of compositional variability on OA properties measured at a broader array of sites and to ultimately inform strategic OA parameterizations for air quality and climate models.

## **Introduction**

Organic aerosol (OA) is a major component of ambient fine particulate matter (20-90%),<sup>1</sup> which has significant detrimental health effects and climate forcings.<sup>2,3</sup> Primary OA (POA) is emitted directly from anthropogenic and biogenic sources, while secondary OA (SOA) is formed through the oxidation of reactive gas-phase precursors in the atmosphere (including volatile organic compounds (VOCs)). The oxidation of both gas- and particle-phase organic compounds occurs via a diverse set of oxidation pathways, depending on molecular structure and atmospheric conditions. These reactions and their divergent branching ratios convert an often complicated mixture of emitted reactants into an

increasingly diverse mixture of oxidation products, which is broadly characterized as SOA or “oxidized OA”.<sup>1,4,5</sup> Products span a wide polarity and volatility space, with diverse oxygen-, nitrogen-, and sulfur-containing functionality.<sup>6</sup>

Molecular identity and structure are tied to the atmospheric transformations of organic compounds, and the ultimate health and environmental impacts of OA.<sup>7–13</sup> Thus, detailed molecular-level speciation is necessary to advance fundamental understanding of atmospheric processes and chemical life cycles, and to provide effective parameterizations for air quality-climate models and detailed chemical mechanisms. This is challenging, however, because the number of potential oxidation products and isomers to catalogue rapidly increases with molecular size and elemental constituents.<sup>4</sup>

Knowledge of OA chemical composition has advanced considerably in recent years through online and offline measurement studies, but major uncertainties remain at the molecular level. Chemically-detailed online measurement capabilities have improved through applications of mass spectrometry (MS) (e.g. aerosol MS (AMS), chemical ionization MS (CIMS), ion mobility spectrometry–MS) and gas chromatography (GC) with MS detectors.<sup>1,14–17</sup> Some recent studies have combined data from multiple mass spectrometers to measure across wider volatility and polarity ranges,<sup>15,18</sup> even achieving mass closure at one forested site (i.e.  $\Sigma(\text{individual measured species}) \approx \text{total observed carbon mass}$ ).<sup>15</sup>

However, the current state of knowledge from both online and offline measurements is far from chemically-comprehensive. Most online methods have limited

molecular-level speciation due to limited MS resolution and isomer differentiation.<sup>19,20</sup> Also, many online OA instruments can only characterize the bulk OA mixture, which greatly reduces chemical detail. Still, these useful bulk measurements are central to most OA source apportionment studies (where “oxidized OA” is a common reported factor)<sup>1</sup> and atmospheric chemistry models. For example, AMS data on bulk elemental ratios (O/C and H/C) from chambers and ambient measurements across the globe are often used to parameterize the overall composition and photochemical age of OA in models.<sup>1,21,22</sup> Offline characterization of OA filter samples with MS is common and sometimes includes GC or liquid chromatography (LC) separation,<sup>23–26</sup> but is often limited to targeted analyses of a smaller subset of compounds. Very few studies have looked at compositional variability for either chamber or laboratory samples via a non-targeted approach with a sufficiently powerful MS, and those that have were limited by sample size and did not include LC.<sup>6,27,28</sup>

This study is the most extensive non-targeted multi-platform survey to date of functionalized OA compositional variability via LC and high resolution MS, with more temporal resolution and a larger sample size than previous offline studies. With the objective of advancing the state of knowledge on molecular-level OA composition, variability, and dynamics, we: (a) carry out a non-targeted molecular-level speciation of complex OA mixtures from 3 diverse field sites and a set of environmental chamber experiments, resolving isomers using LC and identifying the molecular formula of each observed LC peak using high resolution MS; (b) perform an unprecedented intercomparison of functionalized OA composition in environmental chamber experiments and at each field site to examine sample-to-sample variability in each data set and explore

potential causes of this molecular-level variability; (c) model the multi-generational evolution of molecular-level variability in OA composition using chemically-explicit mechanisms, and compare this data to our other results. Results from all platforms are supported by a sensitivity analysis to strengthen conclusions.

### **Limited temporal variability in bulk chemical speciation of functionalized OA at 3 diverse field sites**

To capture OA chemical complexity with increased levels of atmospheric oxidation, summertime measurements were made at three field sites: a remote forest in Northern Michigan (PROPHET site), near downtown Atlanta, and New York City (Queens Co.). Particulate matter (PM<sub>10</sub>) samples were collected on PTFE membrane filters using a passivated stainless steel sampler with a minimal inlet surface area to reduce sampling artifacts and losses. Multi-hour samples were separately collected during day and night (site-dependent, 8 hours on average), avoiding dusk and dawn to focus on daytime or nighttime chemistry. OA was extracted from the filters with methanol, and characterized via high performance LC with electrospray ionization (ESI) in positive and negative mode, with high resolution quadrupole time-of-flight MS (LC-ESI-Q-TOF).

Data collection was extensively quality-controlled through the use of field and laboratory blanks, spiking filter samples with deuterated internal standards, and consistent sample handling and analytical procedures. Similarly, data processing was thoroughly quality controlled, and a conservative threshold for peak inclusion in the subsequent

analyses was implemented (i.e. limit of detection (LOD) threshold). Observed analytes were assigned a molecular formula using high mass accuracy molecular ion  $m/z$  ratios and isotopic distributions. Then, peaks and their assigned formulas were rigorously scrutinized via a series of rules and standards (see Methods), and catalogued based on their molecular formula and LC retention time. To ensure an accurate interpretation of all results, data collection and processing methods were validated with replicate runs of standards and samples, and run-to-run variability of identified compounds was reduced to less than 8% (see Methods, Figure S1, Table S1). Unless otherwise specified, all data presented here are based on compound count (see SI for additional intensity-weighted data).

The focus of this study was functionalized OA; many of these functionalized compounds are readily protonated/deprotonated, or can interact with other ions to form adducts, making them well-suited for electrospray ionization.<sup>29,30</sup> This includes SOA and functionalized POA, though the majority of the compounds sampled is expected to be SOA, as these samples were all collected during the summer. Henceforth, all references to the OA characterized by LC-ESI-Q-TOF are labelled as “OA”, but represent functionalized POA and SOA observed with the methods discussed here. The vast majority of compounds observed at each field site contain at least 1 oxygen atom (92%-94%), with minor contributions of nitrogen-containing compounds without oxygen, which ionize well via ESI.<sup>29,31</sup> Sulfur-containing compounds without oxygen do not ionize well via ESI, and are thus omitted here, along with non-functionalized OA.<sup>29,31,32</sup> Overall, the average sum of speciated components represents approximately  $2.6 \pm 1.3 \mu\text{g}/\text{m}^3$ ,  $0.5 \pm 0.3 \mu\text{g}/\text{m}^3$ , and  $1.0 \pm 0.3 \mu\text{g}/\text{m}^3$ , in the forest, Atlanta, and New York City, respectively (see Supplemental

Information), but this does not include any sulfur-containing compounds without oxygen or non-functionalized OA.

The bulk composition of OA filter samples at each site exhibits limited variance and is particularly consistent for the forested site, for both daytime and nighttime samples (Figures 1, S2, S3). Mean elemental ratios of oxygen-to-carbon (O/C), oxygen-to-nitrogen (O/N), and oxygen-to-sulfur (O/S) show minor changes at each site, but contributing compounds demonstrate a diverse mix of functionality, similar to previous high-resolution OA characterization.<sup>6,23,27</sup> Limited variance in average O/C ratio was also observed via AMS in the forest and in Atlanta (Figures S2-S4). Such behavior is typical of many past AMS studies, where there is some variance in high-time resolution data, but diurnal profiles are consistent day-to-day, often falling within a narrow O/C range.<sup>33,34</sup> Approximately 50%-65% of observed compounds contain nitrogen or sulfur, including organonitrates and organosulfates, whose average molecular weights have been previously unconstrained and are provided in Figure S2. Compounds containing oxygen, nitrogen, and sulfur (CHONS), which have been detected previously in the ambient atmosphere,<sup>26,35,36</sup> were prevalent at the three sites (10% on average).

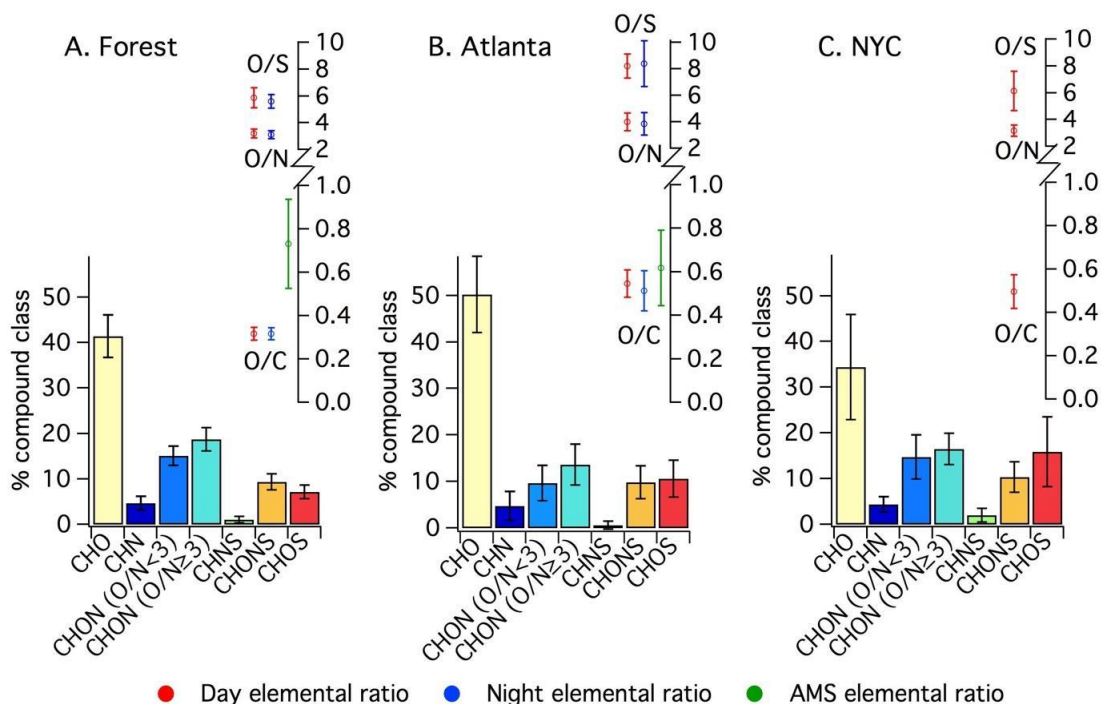


**Figure 1.** Average bulk mixture composition and elemental ratios for each field site show limited variability between multi-hour samples. Elemental ratios (points on upper scales) are displayed as daytime (red) and nighttime (blue) values for LC-ESI-Q-TOF data, and shown along with AMS ratios (green). Error bars represent 1 standard deviation (LC-ESI-Q-TOF data) and 28% error (AMS data, as determined by Canagaratna et al. for improved-ambient analysis<sup>22</sup>). Values presented here are unweighted. O/N and O/S ratios are computed for compounds with 1 or more N or S atoms. Bar charts show the fraction of compounds in each compound class, denoted by the elements present in each class (daily compound class distributions are shown in Figures S7 and S8). Oxygen and nitrogen-containing organic compounds are split into two classes depending on their O/N ratio: CHON with  $O/N < 3$ , and CHON with  $O/N \geq 3$  (includes organic nitrates). In Atlanta, the LC-ESI-Q-TOF O/C ratio agrees well with the AMS O/C ratio. However, there is a larger discrepancy between these values in the forest, which decreases slightly in the abundance-weighted results (Figure S3) (see Section S2 for further discussion).

## Molecular-level speciation reveals extensive temporal variability in functionalized OA composition

Despite relatively constant overall composition, an isomer-specific molecular-level analysis shows ubiquitous sample-to-sample variability in chemical composition of OA at

all three sites (Figures 2, S5, S6). With 1620-8100 compounds measured at each site, variability at the molecular-level was regularly 60-80%, meaning that 60-80% of compounds in a given sample were distinct and typically only 20-40% of compounds overlapped between any two compared samples. This reached a minimum of only 40% distinct compounds (60% overlapping) in two Atlanta comparisons. For each site, we compared subsets of similar samples (e.g. all daytime to all daytime) and all consecutive samples (e.g. day-to-day, day-to-night). Compounds were cataloged by both their molecular formula and LC retention time to differentiate isomers. Here, the definitions of “distinct” and “overlapping” are the percentages of observed compounds in a given sample that are either different or shared, respectively, in a comparison of 2 samples (see Methods, Equations 1 and 2). “Distinct” compounds are present above the LOD in one of the two compared samples, but absent or below the LOD in the other, and therefore contribute a negligible amount of mass to the second sample.

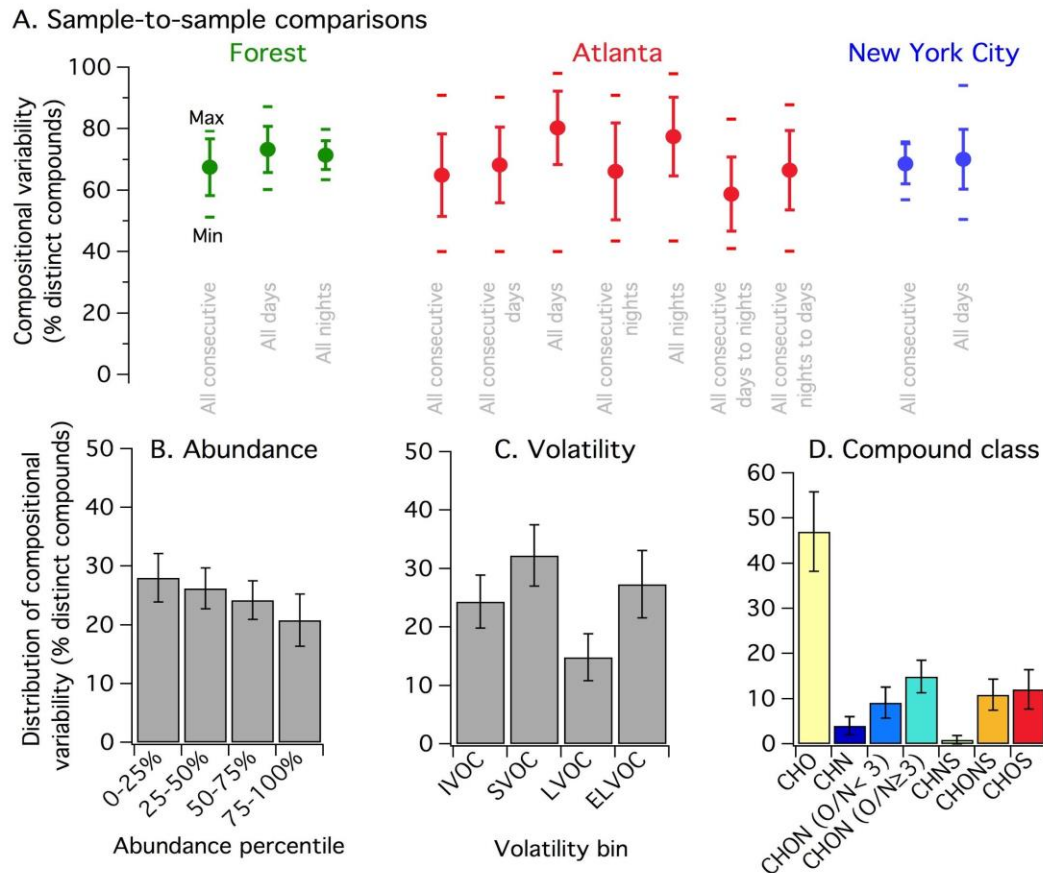


**Figure 2.** Molecular-level composition varies greatly between multi-hour samples at 3 diverse field sites, and this variability occurs across abundances, volatilities, and compound classes. (A) The average ( $\pm$  standard deviation, shown as error bars) percentage of distinct compounds for sample-to-sample comparisons is shown across various sample subsets at each field site, where overlapping compounds are determined by comparing molecular formulas and LC retention times. Markers above and below each average and standard deviation represent the minimum and maximum values of distinct compounds for each set of comparisons. All other sample-to-sample comparisons in each set fell in the range set by the minimum and maximum displayed here. “All consecutive samples” includes consecutive days, consecutive nights, consecutive day-night pairs, and consecutive night-next day pairs. Day- and night-only comparisons for all samples and consecutive samples are also shown. (B-D) Molecular-level variability in all sample comparisons across all 3 sites is shown as the distribution of compositional variability (i.e. distinct compounds) across (B) abundance ranges, (C) volatility bins (i.e. intermediate/semi/low/extremely-low volatility organic compounds: IVOCs, SVOCs, LVOCs, ELVOCs, respectively), and (D) compound classes.

On average,  $73\pm 8\%$ ,  $78\pm 13\%$ ,  $70\pm 9\%$  of compounds were distinct between any compared samples in the forest, Atlanta, and New York City, respectively. Large sample-

to-sample variability was observed even with minimal changes in overall composition (Figures S5-S6, S10-S11). Daytime and nighttime comparisons were equally variable. For all 3 sites, comparisons of consecutive samples had only slightly more overlap than comparisons of all samples, but were within standard deviations (Figure 2), with consecutive sample-to-sample variability of  $67\pm 9\%$ ,  $65\pm 13\%$ ,  $69\pm 7\%$  in the forest, Atlanta, and New York City. Comparisons between daytime and nighttime samples are expected to vary somewhat, due to the distinctly different oxidation conditions in the presence or absence of sunlight (i.e.  $\text{OH}^\bullet$ - versus  $\text{NO}_3^\bullet$ -oxidation pathways). However, comparisons between consecutive daytime samples and consecutive nighttime samples also show significant variability, despite similar oxidation conditions from day-to-day and night-to-night. These highly variable results are notable in contrast to Figure 1, which shows relatively consistent bulk aerosol properties (elemental ratios and elemental composition) across each field campaign.

The observed sample-to-sample compositional variability is due to differences in both detected molecular ions and isomeric structures differentiated by LC. In the midst of this variability, there are still prominent molecular formulas in our datasets spread across multiple isomers, including common, known markers of monoterpene, isoprene, and PAH oxidation (Table S3). There are also compounds that appear relatively frequently at each site, but few compounds are above LOD thresholds in all samples (Figure S12). Compounds were observed with up to 8 isomers at the 3 field sites (Figure S13). However, the majority of compounds at each site were present as only one isomer above LODs (Figures S12-S13).

The observed compositional variability occurs across a distribution of abundances, volatilities, and compound classes (Figures 2b-d, site specific distributions in S15-S16). Though not displayed in Figure 2, similar trends were observed for the laboratory chamber experiments. Distinct compounds from each sample-to-sample comparison are similarly spread across abundance quartiles, highlighting that this variability exists across a range of concentrations and is not attributed just to low abundance compounds. Individual compounds observed exist at  $\sim\text{ng}/\text{m}^3$  concentrations in the atmosphere. Furthermore, the distinct compounds contribute significantly to the total analyzed mass in the OA samples, representing  $59 \pm 17\%$  of the abundance (i.e. mass) in the comparisons of all consecutive samples (e.g. Figure S6b, for the Atlanta campaign).

The volatility of each observed compound was computed according to a parameterization by Li et al.,<sup>37</sup> and compounds were then binned as intermediate-volatility (IVOC), semivolatile (SVOC), low-volatility (LVOC), and extremely low volatility (ELVOC) organic compounds. Distinct compounds span a wide volatility space, with similar contributions from IVOCs, SVOCs, ELVOCs, and fewer distinct LVOCs at all sites (Figures 2c, S15, S16). IVOCs represent 21% of observed variability on average; their presence in OA can be attributed to either: highly-polar water-soluble compounds often observed in OA (e.g. 2-methylglyceric acid ( $\text{C}_4\text{H}_8\text{O}_5$ ) from isoprene oxidation), misattribution without structural consideration in the above parameterization,<sup>38</sup> or fragments of larger species. Finally, distinct compounds occur across all compound classes (Figures 2d, S15, S16), similar to the overall distributions in Figure 1, and there is no

statistically significant difference in the relative occurrence of compositional variability within each class (Figure S17).

There are several considerations in the interpretation of these results. First, non-functionalized hydrocarbons (i.e. unoxidized precursor gases or unoxidized OA) are outside the scope of this study, but the presence of fresh emissions could either homogenize OA if there are continuous sources, or exacerbate variability if there are intermittent diverse sources. The relative effect of any given intermittent source through non-functionalized hydrocarbons or their SOA is going to depend on the complexity of emissions (e.g. motor vehicle exhaust).<sup>14,39</sup> Second, it is possible that longer duration samples (e.g. 24 hours) with greater averaging times could reduce sample-to-sample variability by collapsing diurnal variations into a single aggregate sample. Here, sampling times vary depending on the site (4.5-10 hours), but comparisons were always between samples of similar duration.

Third, the OA mass collected and instrument LOD will affect the total number of compounds observed in a given sample, regardless of instrumentation. Our ambient results show that the variability is distributed across abundances (Figure 2b). However, we more thoroughly investigated the influence of LOD via a sensitivity analysis of ambient, chamber, and modeling results. Our sensitivity analysis (Figures 3a and S18) demonstrates that the outcomes of this study are not prone to bias based on the LOD threshold, number of analytes detected, or sample mass collected. Improved instrument sensitivity (e.g. attogram-level) could enable the measurement of very minor compounds, which may reduce sample-to-sample variability in ambient data. However, this study demonstrates that

variability occurs across a range of abundances, even in the most abundant OA components, which are most influential on OA properties and associated impacts.

Similarly, the number of compounds and fraction of OA mass observed in each sample in this study must be considered. The data quality control discussed above allows only high quality peaks with assigned molecular formulas that pass a strict set of standards to be considered in this analysis (see Methods); this resulted in an average of  $553 \pm 146$  compounds per sample for the forest samples (mean  $\pm$  standard deviation),  $128 \pm 41$  compounds per sample for the Atlanta samples,  $161 \pm 66$  compounds per sample for the New York City samples, and  $240 \pm 35$  compounds per sample for the environmental chamber samples. These numbers increase as the inclusion threshold is dropped (which was set conservatively and in the LOD sensitivity analysis it was still always above the instrument LOD determined by a signal-to-noise ratio of 3 – refer to Methods and SI for additional discussion). Though there are 10,000's of compounds estimated to be present in the atmosphere, many of these compounds are present at concentrations below our conservative thresholds for formula assignment and inclusion in this study (i.e.  $\sim 0.1$  ppt LOD threshold). Similarly, though GECKO-A produces roughly 83,700 possible compounds for  $\alpha$ - and  $\beta$ -pinene oxidation, most of these theoretical compounds exist at minimal concentrations (i.e.  $\ll$  ppq); only  $\sim 1000$  particle phase compounds from each precursor are present above 1 ppt. However, there is no guarantee that all of them will form in a given ambient atmosphere due to variable chemical conditions, precursor/oxidant concentrations, or further particle-phase processing. Refer to the GECKO-A methods section for further discussion. We acknowledge that the functionalized OA compounds

discussed here may not be representative of all particle-phase organic compounds at each of the sites we sampled, but rather represent a subset of compounds that are functionalized with oxygen, nitrogen, and/or sulfur. However, filter extraction and analysis techniques (discussed in the Methods section) were tailored based on best-practices in the literature to focus on this functionalized fraction. There is some uncertainty regarding the representativeness of the fraction of compounds we observe compared to the rest of OA present (especially POA), and results should be interpreted in this context. However, this highly functionalized fraction has been understudied, and warrants further characterization and assessment for its possible effects on the chemical physical properties and impacts of SOA.

A comparison of mass differences between OA components in this study and other forested sites using both CIMS and offline ultra-high resolution MS shows a large fraction of compounds that would not be resolved by online MS methods due to interferences from other analytes (Figure 3b).<sup>20</sup> This renders a significant fraction of the chemical diversity observed or modeled in this study inaccessible via current online MS measurements. In contrast, our offline LC-ESI-Q-TOF analysis has the advantage of isolating analyte peaks in LC space for accurate mass detection and formula assignment, without interference from other mass spectral peaks.

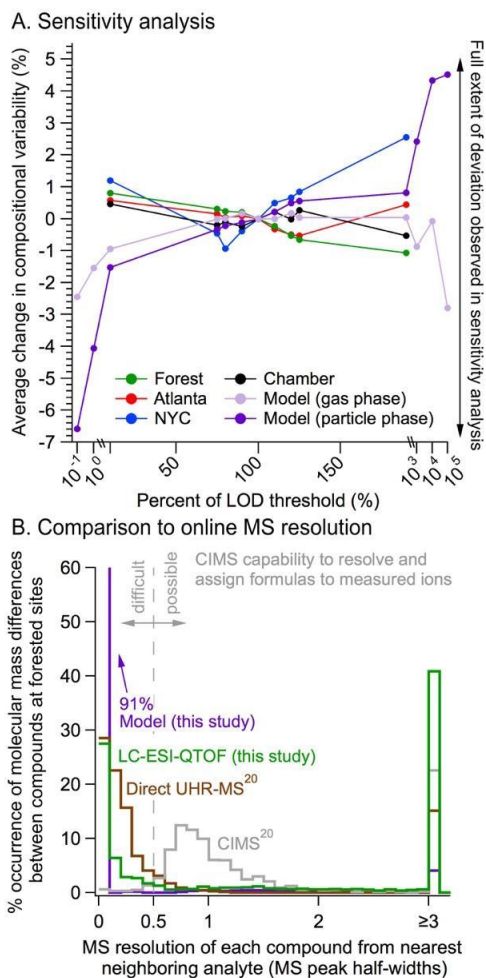


**Figure 3.** (A) A sensitivity analysis demonstrates minimal change in compositional variability results from the base case (“100% of LOD threshold”) with changes in LOD threshold for field, chamber, and modeling results. LOD thresholds were increased to 110%, 120%, 125%, and 190%, and decreased to 10%, 20%, 25% and 90%. The model threshold was set to a baseline of 0.5 ppq. The model threshold was varied as above, and was also reduced and increased by 1-3 orders of magnitude, resulting in less than 6.6% change in compositional variability. For each LOD threshold, all sample-to-sample comparisons were performed, and compositional variability values averaged to yield an average change in compositional variability from the base case threshold. The range denoted by the arrow on the right denotes the full extent of variability observed in the sensitivity analysis when varying all relevant threshold parameters together (3A) and independently (Figure S18). (B) The distributions of molecular mass differences between compounds modeled or measured at forested sites in this study, and in another published ultra-high resolution (UHR) offline filter study, demonstrate small mass differences between many compounds that could be missed with typical online MS.<sup>20</sup> They are compared to published CIMS compound lists with demarcation of necessary mass differences for CIMS or other online MS to resolve peaks and assign formulas.<sup>20</sup> All measured or modeled data have been normalized to CIMS mass resolution ( $M/\Delta M=4000$ ) for comparison, but CIMS resolution limits do not

## Potential driving factors explored via field, chamber, and modeling data

To constrain the factors driving the observed ambient OA variability, we examine the effects of diversity in precursor emissions, chemical oxidation conditions, and air parcel history, via a combination of environmental chamber experiments, chemically-explicit modeling, and backward trajectory analysis. Currently, molecular-level variability in primary emissions from both biogenic and anthropogenic sources is well understood.<sup>40</sup> Gas- and particle-phase emissions, both locally and regionally, are chemically-diverse across source types (e.g. trees versus motor vehicles), but differences also exist between source sub-types (e.g. orange versus pine trees), and composition of emissions can vary temporally. This has all become more evident with increasingly speciated measurements.<sup>14,41,42</sup>

To investigate molecular-level variability in oxidation products, a set of “nighttime” environmental chamber experiments was performed using either  $\alpha$ -pinene or  $\beta$ -pinene precursors. Precursor compounds were initially oxidized by  $\text{NO}_3^\bullet$  radicals to form  $\text{RO}_2^\bullet$  radicals, and then chemistry was varied between experiments, and either controlled by  $\text{RO}_2^\bullet + \text{NO}_3^\bullet$  or  $\text{RO}_2^\bullet + \text{HO}_2^\bullet$  pathways. With our molecular-level speciation, we observe significantly different product distributions between  $\alpha$ -pinene and  $\beta$ -pinene experiments (84% distinct on average) in similar chemical conditions, while changing oxidation conditions with the same precursor produces more product overlap (60% distinct on average) (Table 1, Figure S19).<sup>28</sup> Isomers were observed in sets of up to 4 in the environmental chamber experiments (Figure S13). Average O/C ratios for overlapping

compounds ranged from 0.2-0.34, which are lower than (but not statistically significantly) the overall average O/C of all observed compounds in each comparison.

**Table 1.** Chamber experiment and model run intercomparisons with molecular-level variability. Bolded entries represent comparisons with either the same precursor or chemical pathway.

Chamber experiment comparisons				
Experiment	$\alpha$ -pinene RO <sub>2</sub> *+ HO <sub>2</sub> *	$\alpha$ -pinene RO <sub>2</sub> *+ NO <sub>3</sub> *	$\beta$ -pinene RO <sub>2</sub> *+ HO <sub>2</sub> *	$\beta$ -pinene RO <sub>2</sub> *+ NO <sub>3</sub> *
$\alpha$ -pinene RO <sub>2</sub> *+ HO <sub>2</sub> *	0%	<b>63%</b>	<b>83%</b>	88%
$\alpha$ -pinene RO <sub>2</sub> *+ NO <sub>3</sub> *		0%	75%	<b>85%</b>
$\beta$ -pinene RO <sub>2</sub> *+ HO <sub>2</sub> *			0%	<b>56%</b>
$\beta$ -pinene RO <sub>2</sub> *+ NO <sub>3</sub> *				0%
Modeling comparisons (gas-phase / initial particle-phase)				
Model run	$\alpha$ -pinene RO <sub>2</sub> *+ HO <sub>2</sub> *	$\alpha$ -pinene RO <sub>2</sub> *+ NO <sub>3</sub> *	$\beta$ -pinene RO <sub>2</sub> *+ HO <sub>2</sub> *	$\beta$ -pinene RO <sub>2</sub> *+ NO <sub>3</sub> *
$\alpha$ -pinene RO <sub>2</sub> *+ HO <sub>2</sub> *	0%	<b>43% / 41%</b>	<b>87% / 98%</b>	90% / 99%
$\alpha$ -pinene RO <sub>2</sub> *+ NO <sub>3</sub> *		0%	90% / 99%	<b>83% / 97%</b>
$\beta$ -pinene RO <sub>2</sub> *+ HO <sub>2</sub> *			0%	<b>41% / 39%</b>
$\beta$ -pinene RO <sub>2</sub> *+ NO <sub>3</sub> *				0%

Note: A comparison of model simulations with OH\* oxidation of  $\alpha$ -pinene versus  $\beta$ -pinene (in forest conditions) results in 60% (gas) and 69% (particle) distinct compounds after 8 hours of simulation time. Initial particle-phase composition refers to particle-phase composition directly after gas-particle partitioning (no particle-phase chemistry is included in GECKO-A).

Interestingly, the abundances of most overlapping compounds are similar between chamber experiments (Figure S19). Compounds that are common to both experiments tend to fall near a 1:1 abundance line, suggesting the presence of shared prominent products across oxidation conditions for nighttime  $\alpha$ - or  $\beta$ -pinene chemistry, and potentially other precursors or chemical conditions. This trend was not evident in the model chamber simulations, discussed below (Figure S20).

To supplement these chamber experiments, we modeled the gas-phase product distribution of the same single precursors ( $\alpha$ - and  $\beta$ -pinene), and their initial particle-phase composition after partitioning using GECKO-A (Table 1). Here, chemical structures were tracked between modeling experiments. With an average of  $2296 \pm 2911$  individual

compounds above a 0.5 ppq LOD threshold at each final model simulation time, the results demonstrate similar molecular-level variability as in the chamber and field data. It is important to note that 0.5 ppq is below our instrument LOD threshold for ambient and laboratory chamber analyses, but was selected as a threshold for the GECKO-A simulated data because it provided an opportunity to further extend the LOD sensitivity analysis beyond the range of our ambient/laboratory chamber measurements (Figure 3A).

We tested nighttime ( $\text{NO}_3^\bullet$ ) oxidation with either  $\text{RO}_2^\bullet + \text{NO}_3^\bullet$  or  $\text{RO}_2^\bullet + \text{HO}_2^\bullet$  reaction pathways, similar to the chamber experiments (“chamber simulations”), as well as daytime  $\text{OH}^\bullet$ -initiated oxidation under ambient conditions (“forest simulations”). Model runs with  $\text{RO}_2^\bullet + \text{NO}_3^\bullet$  controlled reactivity showed a significantly more diverse set of oxidation products than the product distribution from  $\text{RO}_2^\bullet + \text{HO}_2^\bullet$  chemistry. The chamber and model results are in agreement that variations in precursor structure are more influential contributors to compositional variability than the oxidation conditions tested. However, this chamber and modeling study was limited to  $\alpha$ - and  $\beta$ -pinene, and should not be extrapolated to other precursors or oxidation conditions without further testing. Other precursor comparisons with greater difference in structure or formula are extremely likely to cause greater variability in OA composition. The inclusion of these modeling results acts as an independent verification of our ambient and laboratory chamber observations, as the model results are not subject to any of our analytical procedures. The variability observed in the simulated data strongly supports the results by replicating the variability observed in ambient and laboratory data.

Modeling results suggest that SOA compositional variability can be partially attributed to the preceding composition of oxidized organic gases, which, along with the initial particle-phase composition, provides a lower limit of variability just after partitioning but before additional particle-phase chemistry takes place (such chemistry is excluded from GECKO-A). The subsequent contributions of compositional variability from particle- and/or aqueous-phase chemistry cannot not be determined from this modeling analysis. The LOD sensitivity analysis with modeling data also shows little sensitivity to changes in threshold (Figures 3a, S18), down to LODs several orders of magnitude below the ambient or chamber LODs.

Time-resolved modeling results show that the evolution of compositional variability over time varies with chemistry and precursors (Figure 4a-b), with variability increasing or decreasing over time for comparisons with like versus differing precursors, respectively. Additional intra-comparisons of individual model runs at fresh versus old “ages” (i.e. product generation) (Figure 4c) demonstrates that air parcel “age” likely plays a role in accentuating compositional variability since reaction precursors are frequently not emitted and reacted at a uniform time in the ambient atmosphere. The precursor-dependent increase in potential compounds in chemically-explicit models has been shown previously to reach  $10^5$ - $10^6$  over several generations, including diverse isomers.<sup>5,18</sup> The chemical diversity of a single precursor or simple mixture is expected to grow exponentially and peak with a diverse population of larger oxidized compounds, and ultimately converge on a smaller number of oxidized fragments at the end of the oxidation life cycle.<sup>5,43</sup> The extent to which

this decrease in variability might occur in the ambient atmosphere is subject to the effects of aerosol deposition and emissions of fresh precursors.

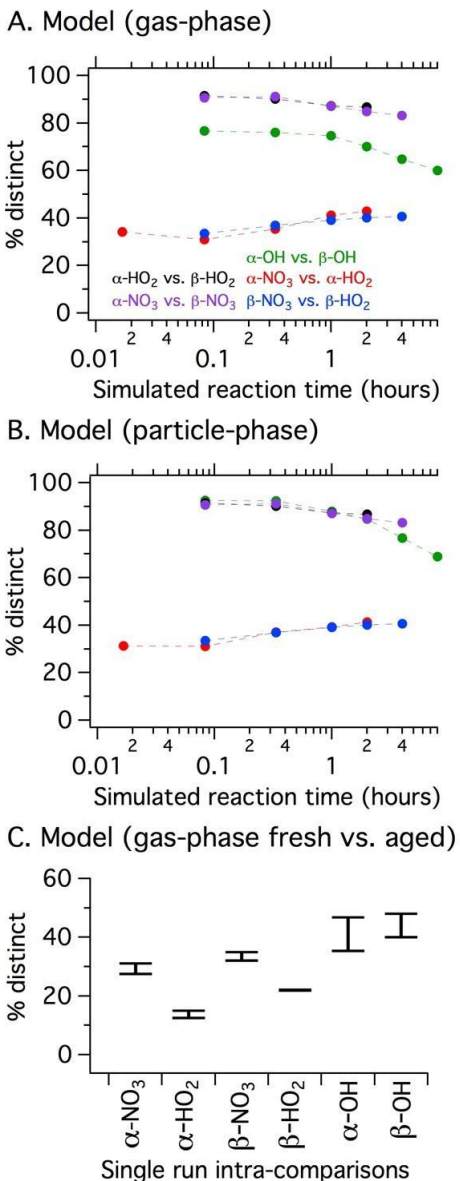


**Figure 4.** Modeling results with the dynamics of SOA compositional variability for  $\alpha$ - or  $\beta$ -pinene daytime OH<sup>•</sup> oxidation (“OH”) or nighttime NO<sub>3</sub> oxidation with RO<sub>2</sub><sup>•</sup> radical reacting predominantly with HO<sub>2</sub><sup>•</sup> or NO<sub>3</sub><sup>•</sup> (“HO<sub>2</sub>”, “NO<sub>3</sub>”). (A-B) Model results show the evolution of compositional variability over reaction time, with variability increasing or decreasing over time for comparisons with like versus differing precursors, respectively. Oxidant exposure values for each modeling experiment are shown in Figure S18, and the evolution of gas- and particle-phase mass and elemental ratios in the modeling experiments are shown in Figure S19. (C) Intra-run comparisons of fresh (5 min simulation time) versus aged (last 2 simulation time points) compounds in the gas-phase GECKO-A output show compositional variability within single simulations.

To investigate the role of air parcel history in contributing to the observed OA compositional variability, we modeled hourly backward trajectories covering all air parcels' 24-hour history for each sample using HYSPLIT.<sup>44,45</sup> For each site, we compared the statistical distribution of backward trajectories separately for all daytime and nighttime samples with 20×20 km<sup>2</sup> resolution and observed a diverse range of unique versus overlapping air parcel histories (Figure S25). Despite some prevailing backward trajectories observed at each site, there is no observed correlation between dissimilar backward trajectories and chemical compositional variability (Figure S26,  $r=0.02-0.5$ ). However, there is clustering around very high backward trajectory variability and very high OA compositional variability, meaning most sample-to-sample comparisons with significantly different backward trajectories do not share many compounds. This suggests that changes in air parcel backward trajectories may contribute to compositional variability, but do not control it.

Our observations are not without supporting evidence from other studies. Source apportionment via PMF with bulk OA measurements at the forested site shows major shifts in the relative source contributions of 3 broadly-defined factors representing more oxidized oxygenated OA, IEPOX-derived OA, and monoterpene-derived OA (Figure S14). All 3 factors frequently approach negligible prevalence over long time periods, and at least two of the factors may also have significant variability in precursors or oxidation pathways. Similar shifts in the prevalence of PMF factors has been observed in other regions including the Southeastern U.S, though interpretation has been limited without chemical speciation.<sup>46-48</sup> In addition, our molecular-level compositional variability results (Figure 2)

are supported by two recent analogous studies using high resolution mass spectrometry without LC separation. First, laboratory experiments on aqueous photochemistry of SOA from terpene precursors found that >50% of all observed oxidation products were unique to a single precursor.<sup>28</sup> Second, a comparison of 4 ambient OA samples from Los Angeles and Bakersfield, CA report 35-65% compositional variability between sites, and 35-91% when compared to chamber experiments with diesel fuel or isoprene.<sup>27</sup> These values are all lower limits of variability, since no LC separation was employed in either of these two studies to distinguish between isomers.

### **Conclusions, potential implications and opportunities for fundamental understanding, monitoring, and modeling**

In conclusion, we present a multiplatform analysis of compositional variability in the atmosphere, and show significant temporal variability in ambient, laboratory, and modeled functionalized OA composition. Our observations highlight the complex interplay between precursor emissions, chemistry, and air parcel history in determining molecular-level functionalized OA composition, which is likely primarily composed of SOA. The atmosphere combines variability in precursor emissions with variability in the measured air parcels' ages, and multiple levels of variability in multiphase chemical oxidation conditions (e.g. day versus night; concentrations of oxidants, NO<sub>x</sub>, and co-reactants (e.g. HNO<sub>3</sub>, H<sub>2</sub>SO<sub>4</sub>, NH<sub>3</sub>); concentration and composition of existing POA/SOA; particle acidity; relative humidity and aqueous chemistry;<sup>49</sup> solar intensity; temperature).

Additionally, differences in transport and meteorology can also affect dry and wet deposition timescales and OA lifetime. In all, the combination of these factors produces a much larger number of divergent chemical species, whose presence varies with changes in these underlying factors. Shifts in one or more of these factors can significantly alter ambient molecular-level OA composition day-to-day, despite other factors, such as the presence of major precursors, remaining constant. This and future molecular-level studies on aerosol composition should be used to strategically parameterize aerosol composition in models, or to inform strategic model simplifications to more efficiently yet accurately describe complex aerosol mixtures. Future research is required to expand on this study of aerosol variability and observe temporal trends in molecular-level aerosol composition at these sites and others throughout different seasons. Gas-phase composition should also be assessed to determine the link between variability in gas-phase precursors and resulting SOA. The variability of non-functionalized POA should also be considered, and its possible effect on compositional variability (See discussion above). Finally, the impacts on aerosol properties should be assessed, using molecular-level data to study mixture-wide aerosol viscosity and resulting phase state, solubility, hygroscopicity, volatility, among other properties of interest.

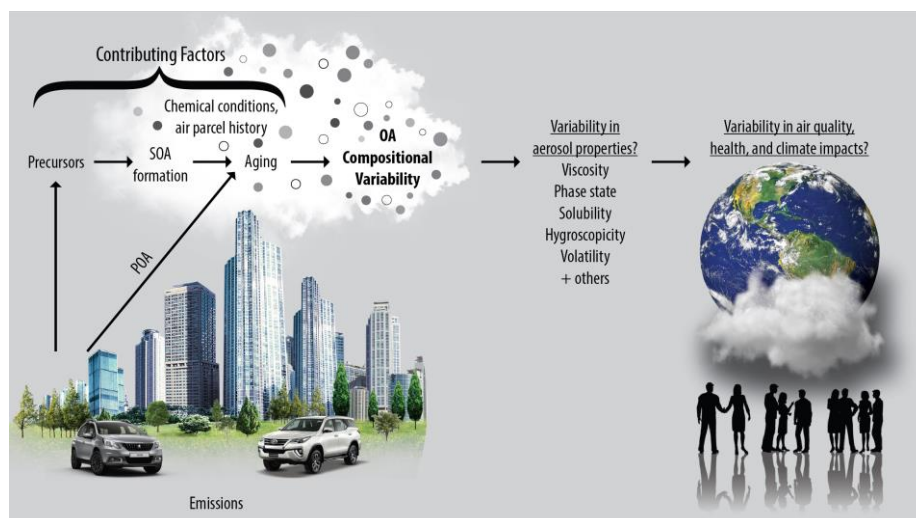


**Figure 5.** Summary of the hypothesized causes and effects of OA compositional variability

*Potential Implications and Opportunities for Future Work:* Our findings reveal that the molecular-level chemical composition of functionalized OA mixtures in the atmosphere is highly variable, with the specific combination of factors driving SOA formation constantly changing, and their combined effects on aerosol properties underconstrained. These results are important for fundamental understanding, monitoring and modeling practices, and air quality management policies for several main reasons.

First, this molecular-level study reveals significant temporal variability in OA composition, in contrast with common bulk OA composition metrics which seemingly collapse variability in OA evolution within and between studies, and thus tend to oversimplify the underlying variability of complex OA mixtures. For example, tracking elemental ratios from our LC-ESI-Q-TOF analysis (e.g. O/C, O/N, O/S in Figure 1) shows minimal temporal variability (Figure 1), while molecular level data show major changes in chemical composition with time (Figure 2). Molecular-level data should be used in

combination with bulk metrics to evaluate, constrain, and improve the use of simplified metrics to represent aerosol composition, as well as age, evolution, and properties. SOA parameterizations in 3-D chemistry and climate models should be informed by these results and incorporate strategic simplifications that capture key changes in molecular-level composition. Existing bulk composition metrics include elemental ratios,<sup>34</sup> bulk carbon oxidation state,<sup>43</sup> mass spectral fragments (e.g.  $m/z$  43/44),<sup>50</sup> functional group fractions,<sup>51</sup> or often generic statistically-derived source apportionment factors (e.g. “semivolatile oxygenated OA”).<sup>1,50</sup> Non-targeted molecular-level speciation should be used to elucidate variations between seemingly similar bulk metric values within data sets, between studies, and in model evaluations. If such non-targeted data are unavailable, studies should avoid basing analyses on single “representative” days because they are uncertain to include “typical” OA composition for a given site.

Second, the molecular-level composition of OA (both elemental and structural) is a determining factor for its oxidation chemistry, its chemical/physical properties, the multiphase evolution of the whole organic mixture, and its interactions with aerosol inorganic species and water. A constantly changing aerosol composition may imply constantly changing oxidation chemistry and resulting aerosol properties, though this must be the subject of future research. For example, aerosol miscibility is strongly dependent on chemical structure.<sup>52</sup> Metrics like O/C, which do not reflect changes in the isomeric composition of a mixture, may be misleading in characterizing an aerosol mixture because overall O/C may remain fairly consistent with time, and therefore seemingly indicate consistent chemical composition. However, when chemical structure is taken into account

to study structure-dependent properties, like aerosol miscibility, these properties may begin to show significant variability. Therefore, to develop effective air quality and climate management strategies, it is essential that we understand the underlying processes that control this variability and thus influence the impacts of the coupled emissions-chemistry system. OA compositional variability could modify (and signify changes in) its impacts, such as urban air quality (i.e. SOA formation/evolution),<sup>1,52</sup> human health (e.g. structurally dependent toxicity, carcinogenicity, and *in vivo* reactive oxygen species (ROS) generation),<sup>3,53</sup> climate (e.g. changes in aerosol phase state, cloud condensation nuclei<sup>52</sup>), and feedbacks to chemical composition evolution through changes in aerosol phase state (e.g. glassy versus aqueous layer) that will affect chemistry in all phases.

For example, a recent study with  $\alpha$ - and  $\beta$ -pinene showed that precursor structure caused greater variations in *in vivo* ROS generation than reaction conditions.<sup>53</sup> Similarly, molecular-level characterization is valuable because it can enable detailed estimates of physical/chemical properties like aerosol phase state, viscosity, solubility, hygroscopicity, and volatility, and allow for assessments of their ambient variability.<sup>52,54</sup> Future work should determine which chemical/physical properties are most prone to changes with compositional variability, and how observed compositional changes at different locations will affect SOA properties. For example, while there is some correlation between hygroscopicity and overall O/C ratio,<sup>55-57</sup> the importance of O/C distributions (rather than just the average O/C ratio) in determining volatility has been shown.<sup>56,58</sup> For these and other properties, understanding molecular-level variability will further advance understanding and improve our predictive capacity.

Third, these data-rich molecular-level characterizations of compositional variability represent an incredible statistical resource and opportunity to develop a fundamental understanding of the chemical evolution of complex OA mixtures and its driving factors. A broad survey and intercomparison of ambient sites and laboratory experiments is needed to provide data to enable computationally-intense source apportionment and factor analysis studies with machine learning, neural networks, and other statistical methods. These offline methods and results are not intended to supplant, but rather augment, the valuable data produced by online methods and bulk characterization. Together with powerful, high-time resolution instruments (i.e. AMS, CIMS), future molecular-level compositional variability studies with greater temporal resolution and structural characterization of analytes with tandem MS can further deconvolve the factors that drive SOA formation and transformations.

## **Methods**

The methods combined in this study each have strong foundations discussed in numerous previous studies, including filter handling and extraction, LC-ESI-Q-TOF analysis of OA extracts including QC/QA for formula assignment and formula evaluation, and non-targeted approaches to chemical characterization (all references herein).

## **Site descriptions**

Ambient particle-phase samples were collected at three field sites. The first set of samples was collected in a remote forest at the PROPHET research tower (University of Michigan Biological Station, 45.33°N, 84.42°W) during PROPHET 2016 (Program for Research on Oxidants: PHotochemistry, Emissions and Transport). The campaign ran from July 1 to July 31, 2016, and samples were collected from July 11 to July 31. This remote, mixed forest contains a variety of coniferous and deciduous trees, including types of aspen, northern hardwood, and pine.<sup>59</sup> It is well isolated from major urban areas; Pellston, MI is the nearest town (5.5 km from the PROPHET tower, population < 900), and major metropolitan areas such as Detroit, Milwaukee, and Toronto are more than 400 km away. This site was selected because of its prominent biogenic emissions with minimal anthropogenic influence, allowing a focused study of BVOC oxidation products. This was a collaborative field campaign, with a variety of other measurements collected, including online particle-phase characterization data via AMS that are used in this study.

Samples were also collected near downtown Atlanta (33.78°N, 84.41°W), at the Jefferson Street SEARCH site (Southeastern Aerosol Research and Characterization). These measurements were collected from July 26 to August 18, 2017. The Atlanta site was selected because of its mix of anthropogenic and biogenic precursors and conditions; there is significant anthropogenic influence expected with high NO<sub>x</sub> concentrations and other anthropogenic pollutants (e.g. SO<sub>2</sub>), as well as high concentrations of biogenic organic compounds such as isoprene and monoterpenes, observed during similar field campaigns in the Southeast US.<sup>60,61</sup> Using the established SEARCH site infrastructure, these

measurements were once again part of a collaborative mission, and we use online particle-phase measurements collected via AMS in this study.

Finally, samples were collected in Queens, New York, at the New York State Department of Environmental Conservation Air Monitoring Station (40.74°N, 73.83°W). Measurements were collected from September 1 to September 21, 2017. This site is located in a densely populated area, and anthropogenic emissions are expected to be dominant. These measurements are supported by PM<sub>2.5</sub> and other trace gas pollutant measurements made by the New York State Department of Environmental Conservation.

## **Sampling**

Particle-phase samples were collected with a custom built passivated stainless steel sampler for simultaneous collection of offline gas- and particle-phase samples with a very low surface area inlet (minimal or no upstream tubing) to minimize sampling artifacts and losses. The sampler was designed using passivated stainless steel filter holders (Pall Corporation) and an 84 mesh stainless steel screen (McMaster Carr). The screen was installed over the opening of the filter holders to limit particle size to a PM<sub>10</sub> size cut (mesh size determined by aerosol penetration efficiency at 1 m<sup>3</sup>/hour, accounting for losses to the screen by diffusion, impaction, and interception). Particle-phase samples were collected on PTFE membrane filters (47 mm diameter, 1.0 µm pores, Tisch Environmental) at 1 m<sup>3</sup>/hour according to federal reference methods.<sup>62</sup> Field blanks were collected with all samples. All filters were spiked with deuterated standards (containing benzene-d<sub>6</sub>, ethylbenzene-d<sub>10</sub>,

diethyl phthalate-d4 (all from AccuStandard), N-dodecanol-d25, octanoic acid-d15, N-hexadecane-d34, and N-octane-d18 (all from Cambridge Isotope Laboratories)), stored at -30°C to -80°C, and transported using expedited shipping in insulated coolers with multiple ice packs to ensure good sample quality upon analysis.

At PROPHET (forested field site), particle-phase samples were collected on the research tower, 28 m above the ground and 6 m above the canopy. The sampler was facing west on the tower, and no inlet tubing was used. Samples were collected both during the day (9:00am-5:00pm) and at night (9:30pm-5:30am), avoiding sunrise and sunset periods to capture distinct daytime and nighttime chemistry. At the Atlanta site, the inlet was positioned 4.5 m above the ground, facing west. Minimal inlet tubing was used in this sampling setup (18" of 5/8" stainless steel tubing), so that the sampler could be housed out of direct sunlight, in an air conditioned trailer at the site. Samples were collected during the day (9:00am-7:00pm) and overnight (10:30pm-5:00am), once again avoiding transitional periods. At the New York site, the sampler was positioned 4.5 m above the ground, facing west. Minimal inlet tubing was used here (9" of 5/8" stainless steel tubing), also to house the sampler away from direct sunlight and with temperature control. Samples were collected during the day only (7:00am-4:00pm, referred to as "all day" samples, or 1:00pm-5:30pm, referred to as "afternoon" samples).

*PROPHET AMS Measurements:* At PROPHET, a high-resolution time-of-flight aerosol mass spectrometer (HR-TOF-AMS, Aerodyne Research Inc.) was used to measure non-refractory submicron aerosols.<sup>63</sup> In brief, particles are sampled through a 100-micron

critical orifice and are focused into a particle beam using an aerodynamic lens. After traversing a vacuum chamber, the particles in the beam are impacted onto a porous tungsten vaporizer heated to 600°C. Vapors are subsequently ionized by electron impact ionization (70 eV). The resulting ions are detected using a high resolution time-of-flight mass spectrometer. The HR-TOF-AMS was operated in a high sensitivity mode, referred to as “V-mode”. Sampling inlets for HR-TOF-AMS measurements were located at two different heights, 6 m and 30 m, and data from the 30 m inlet on the PROPHET tower are considered in this study. Both inlets were fitted with PM<sub>2.5</sub> cyclones to remove dust and prevent instrument clogging. The results presented here are of PM<sub>1</sub>, due to the transmission efficiency of PM<sub>1</sub> through the AMS aerodynamic lens. Measurements were alternated between the 6 m and 30 m heights at 10 minute intervals. Ionization efficiency (IE) HR-TOF-AMS calibrations were performed at the beginning and end of this field campaign, according to standard protocols.<sup>64,65</sup> The IE calibrations were performed using monodisperse 300-nm ammonium nitrate particles.

*Atlanta AMS Measurements:* Another Aerodyne HR-ToF-AMS (referred to as GT-AMS hereafter) was deployed at the Atlanta Jefferson Street site. The sampling was done continuously with an inlet facing west at 4.5 m above the ground, and the inlet was coupled with a PM<sub>2.5</sub> cyclone to remove coarse particles. However, as above, the data presented here is for PM<sub>1</sub>.

For the AMS instruments at both sites, a nafion dryer was attached upstream of the AMS to dry the particles to below a relative humidity of 20%, because humidity has the

potential to affect particle collection efficiency at the vaporizer. IE calibrations were performed every week. The composition dependent collection efficiency (CDCE) was applied to HR-TOF-AMS data from both sites, according to Middlebrook et al.<sup>66</sup> Data analysis was performed in Igor Pro v6.37 (Wavemetrics, Inc.) using the Squirrel v1.16H and Pika v1.57I packages.<sup>67</sup> High resolution mass spectral fitting was performed on the HR-TOF-AMS V-mode data. Elemental analyses were performed to find the atomic ratios of oxygen to carbon (O/C) according to the “improved-ambient” method by Canagaratna et al.<sup>22</sup>

Four chamber experiments were performed in the Georgia Tech Environmental Chamber facility.<sup>69</sup> Experiments were performed at 70% relative humidity at 25°C with seed aerosols generated by atomization of a sulfuric acid (0.01 M) and magnesium sulfate (0.005 M) solution.  $\alpha$ -pinene and  $\beta$ -pinene (12 ppb) were used as precursor VOCs and were oxidized by  $\text{NO}_3^\bullet$ . These experiments were designed to study nighttime VOC oxidation chemistry as it has been shown that nitrate radical oxidation of monoterpenes can contribute substantially to nighttime aerosol production in the southeastern U.S. The experiments are included in this study because they present an opportunity to explore the effects of precursor identity and chemical conditions on compositional variability in a controlled manner. Here,  $\alpha$ -pinene and  $\beta$ -pinene were selected as precursors because they are prevalent monoterpenes observed at the forested site and Atlanta site. Their difference in structure presents an opportunity to study the effects that these structural differences have on oxidation chemistry. Future research will include a broader selection of biogenic and anthropogenic VOC precursors. Two experiments were run for each precursor, with

RO<sub>2</sub>• fate controlled primarily either by NO<sub>3</sub>• (“RO<sub>2</sub>•+NO<sub>3</sub>• experiments”) or by HO<sub>2</sub>• (“RO<sub>2</sub>•+HO<sub>2</sub>• experiments”), following experimental protocols similar to those in Boyd et al.<sup>69</sup> Briefly, seed aerosols and a precursor VOC were injected into the chamber prior to the introduction of N<sub>2</sub>O<sub>5</sub>, which serves as a source of NO<sub>3</sub>•. For RO<sub>2</sub>•+HO<sub>2</sub>• experiments, 25 ppm formaldehyde was also injected. N<sub>2</sub>O<sub>5</sub> was premade in a flow tube by mixing O<sub>3</sub> and NO<sub>2</sub> and was introduced to the chamber, which marked the beginning of an experiment. Approximately 60 ppb N<sub>2</sub>O<sub>5</sub> was added to the chamber for RO<sub>2</sub>•+ NO<sub>3</sub>• experiments, and 80 ppb N<sub>2</sub>O<sub>5</sub> was added for RO<sub>2</sub>•+ HO<sub>2</sub>• experiments. Filter samples were collected on PTFE membrane filters (47 mm diameter, 0.45 μm pores, Maine Manufacturing LLC) 3-4 hours after the beginning of each experiment for 100-120 minutes at 28-30 L/min.

Model simulations use GECKO-A, an explicit chemical mechanism generator that applies observed structure-activity relationships (SARs) to predict as fully as possible the atmospheric chemistry of precursor hydrocarbons.<sup>5,70</sup> SOA formation is described via gas-particle partitioning,<sup>71</sup> using vapor pressure relationships.<sup>72,73</sup> The completed mechanisms are implemented in a box model. To maintain a tractable mechanism size, the following standard thresholds are imposed: (1) for any given reaction, pathways with branching ratio <5% are ignored and the reaction rates of the other pathways are incremented proportionally so that the overall reaction rate is unchanged; (2) we lump together products contributing <5% to the total yield from a reaction, by substituting them with their highest-yield positional isomer (GECKO-A does not account for stereoisomers). The model has been tested with these thresholds for the oxidation of α-pinene.<sup>74,75</sup> In this study we also

apply the GECKO-A SARs to the oxidation of  $\beta$ -pinene. Here,  $\alpha$ -pinene and  $\beta$ -pinene were selected for consistency with the laboratory chamber experiments discussed above. The resulting combined mechanism contains ~83700 unique non-radical species, including ~18500 lumped species which represent the contributions of an additional ~128000 very low-yield isomers. These species should be regarded as potential products. Not all possible reaction pathways are relevant to any given set of experimental conditions. The effective diversity of the model is best assessed by applying experimentally-relevant “detection limits” to the model output.

Six different single precursor modeling experiments were performed, either as chamber simulations ( $\alpha$ - or  $\beta$ -pinene precursor with  $\text{NO}_3^\bullet$  oxidation, and subsequent  $\text{RO}_2^\bullet$  fate controlled by  $\text{NO}_3^\bullet$  or  $\text{HO}_2^\bullet$ ) or as ambient (forest) simulations ( $\alpha$ - or  $\beta$ -pinene precursor,  $\text{OH}^\bullet$  oxidation). Chamber simulations were run for 2-4 hours of simulated oxidant exposure, and ambient simulations were run for 8 hours of simulated exposure under constant noontime conditions. All runs were performed at 295 K, with 70% relative humidity. Initial precursor concentration was 12 ppb in all cases, to match the chamber experiments discussed previously. For the GECKO-A chamber simulations, runs started with 60 ppb  $\text{N}_2\text{O}_5$  (as  $\text{NO}_3^\bullet$  source), with 25 ppm of formaldehyde added for the  $\text{RO}_2^\bullet + \text{HO}_2^\bullet$  experiment. In the ambient simulations, 30 ppb  $\text{O}_3$  and 0.1 ppb of  $\text{NO}_x$  were added. After applying an abundance threshold of 0.5 ppq, as previously discussed, an average of  $2296 \pm 2911$  compounds remained for each simulation.

## Analysis

All filters were extracted in 2 mL of methanol ( $\geq 99.9\%$  purity, Sigma-Aldrich). Various solvents were considered and tested for filter extraction (e.g. acetonitrile, dichloromethane), but methanol was selected because of its well-documented use in extraction of oxidized organics, organonitrates, and organosulfates.<sup>25,26,76-78</sup> It is important to note that only reasonably polar organic compounds will dissolve in methanol, so non-polar compounds may be left behind. However, non-polar compounds do not ionize well via electrospray ionization (discussed below), and are therefore not observed during analysis anyway.

Extracts were sonicated at room temperature for 60 minutes, and were exposed to gentle nitrogen flow to reduce their volume to 200  $\mu\text{L}$  methanol ( $\geq 99.9\%$  purity, Sigma-Aldrich), thereby increasing analyte concentration.<sup>26,49-52</sup> Extracts were stored at  $-30^\circ\text{C}$  until analysis. Field and laboratory blanks were extracted using these same methods. All filters from each campaign were extracted at the same time and subsequently analyzed together.

Samples were analyzed on an Agilent 1260 Infinity HPLC with electrospray ionization (ESI), and an Agilent 6550 Q-TOF tandem mass spectrometer. Separation was performed with an Agilent Poroshell 120 SB-Aq reverse phase column column (2.1 $\times$ 50mm, 2.7  $\mu\text{m}$  particle size). Formic acid at 0.1% (98-100%, Sigma-Aldrich) was used as a modifier in the PROPHET sample set to promote ionization in the ESI source. In the Atlanta and New York City sample sets, 0.1% acetic acid (for HPLC, Sigma-Aldrich) was

used as a modifier. Methanol ( $\geq 99.9\%$  purity, Sigma-Aldrich) and water at ambient temperature were used as LC solvents.

In all analyses, 5  $\mu\text{L}$  aliquots of each sample were injected to the LC column. For the PROPHET sample set, the following solvent gradient was applied: from 0 to 2 minutes, 95% water (A) and 5% methanol (B); from 2-10 minutes, increase B to 90%; from 10-17 minutes, hold at 90% B; then decrease to 5% B to prepare for the next run, similar to previously established methods.<sup>79</sup> For the Atlanta and New York City sample sets, the above gradient was slightly extended: from 0 to 2 minutes, 95% water (A) and 5% methanol (B); from 2-22 minutes, increase B to 90%; from 22-27 minutes, hold at 90% B; then decrease to 5% B to prepare for the next run. A flow rate of 0.2 mL/min was used in all cases.

The electrospray source was run in both positive and negative ionization mode at the following source conditions, optimized for small molecule identification with our Q-TOF: drying gas temperature and flow of 225°C and 13 L/min (PROPHET) or 17 L/min (Atlanta/New York City), respectively; fragmentor voltage at 365 V and capillary voltage at 4000 V; sheath gas flow and temperature at 400°C and 12 L/min, respectively; nebulizer pressure at 20 psig. The fragmentor voltage was lowered to investigate possible compound fragmentation caused by this voltage, leading to the observation of IVOCs (as discussed above). However, there was no difference in the volatility distribution observed when this value was lowered.

ESI ionization allows for measurement of compounds that are efficiently ionized in the source. Oxygen-containing compounds are prominent, as are nitrogen-containing compounds (e.g. amines, as they are sufficiently basic and thus readily ionized via ESI)<sup>29,31</sup>, and compounds containing a combination of oxygen, nitrogen, and sulfur atoms. We observe nitrogen- and sulfur-containing compounds without oxygen, though they contribute minimally to observed abundance. Sulfur-containing compounds without oxygen are difficult to detect without specialized pre-treatment, and thus omitted here.<sup>29,31,32</sup> We note that the organic compounds we observe during this analysis do not reflect the full range of organic compounds present as particles in the atmospheres we sampled, but rather a fraction that is functionalized with oxygen, nitrogen, and/or sulfur.

To ensure accurate mass results, a solution of reference masses was introduced to the ESI source throughout analysis, containing compounds with extremely high purity and predictable ionization in positive and negative mode: 5 mM purine and 2.5 mM HP-0921 (in 95% acetonitrile ( $\geq 99.9\%$  purity, Honeywell), 5% water (18.2 M $\Omega$ -cm), Agilent Technologies). The Q-TOF was tuned and calibrated for optimal performance in its low mass range ( $m/z < 1700$ ), and data were collected for ions ranging from  $m/z$  50-1000.

Data were initially processed with Agilent Mass Hunter software. Mass Hunter was selected for automated peak finding and identification because it has been optimized to work with the Agilent LC-Q-TOF data output, and because of its strengths in feature identification and formula generation (see below). We carefully evaluated Mass Hunter's performance at multiple points in our analyses with analytical standards, to verify its

efficacy at feature and formula identification. This software has been used extensively in previously published work, in the field of atmospheric chemistry (e.g. Zhang et al.<sup>79</sup>) and in others (e.g. Chen et al.,<sup>80</sup> Witherspoon et al.<sup>81</sup>).

For all samples, ions from  $m/z$  50-600 were extracted and assigned masses, allowing for  $[M+H]^+$  and  $[M+Na]^+$  addition in ESI positive mode,  $[M-H]^-$  and  $[M+HCOO]^-$  or  $[M+CH_3COO]^-$  in negative mode, as well as neutral water loss. To ensure high quality data, only ions with strong signal (isotope height of 1000 counts and compound height of 5000 counts to confidently surpass instrument noise) and strong peak quality score ( $>70\%$ , a score produced by Mass Hunter, including criteria such as signal-to-noise ratio, retention time peak width, retention time peak shape, and isotope pattern) were selected. Formulas were assigned to the resulting masses, constraining elements according to  $C_{3-60}H_{4-122}O_{0-20}N_{0-3}S_{0-1}$ . The formula with the best formula match score for each compound was selected. Only formulas with formula quality scores greater than 75% were retained for subsequent untargeted analysis (formula quality score is a score produced by Mass Hunter, incorporating mass match, isotope spacing, and isotope abundance). Samples and blanks were processed identically. The high mass accuracy (sub 1-2 ppm) and mass resolution ( $>25000$ ) of the Q-TOF, paired with accurate adduct assignment and the use of isotopic distribution (pattern and spacing) ensures accurate molecular formula identification for the analytes observed in this untargeted analysis, similar to previous work.<sup>82-84</sup> Compared to online methods, our instrumentation has the advantage of isolating analyte peaks in LC space for mass detection and formula assignment without interference from other mass spectral peaks (as is typical with direct-MS analysis), therefore increasing the likelihood

of a high mass accuracy formula assignment well beyond the mass resolution (i.e.  $M/\Delta M$ ) of the MS.

*Data Quality Control and Quality Assurance:* We performed extensive data quality control using external code written in R, following best practices established in the literature.<sup>82,85</sup>

*Blank subtraction:* Masses appearing in both a sample and its corresponding blank (using a conservative 5 ppm tolerance) with an abundance ratio of less than 5:1 were eliminated from the results. Masses appearing in both a sample and its corresponding blank with a ratio larger than 5 were retained, and the abundance of the blank was subtracted from the abundance of the sample in these cases. Positive and negative mode data were then combined, and abundances of any compounds appearing in both ionization modes were averaged.

*Molecular formula evaluation:* For further data quality control, all molecular formulas were screened to identify possible incorrect assignments. The number of C, H, O, N, and S atoms were further limited according to values presented by Kind and Fiehn (e.g. for masses below 500 Da, to no more than 39 C, 72 H, 20 O, etc.<sup>82</sup>). Compounds were additionally flagged based on a disagreement with the “Nitrogen rule” (molecules with an odd number of N-atoms must have an odd nominal mass<sup>86</sup>), non-integer double bond equivalent values, large mass differences between the observed mass and proposed mass for a particular formula, and outlier H/C ratios ( $H/C < 0.2$  or  $H/C > 3.1$ )<sup>82</sup>. Alternative molecular formulas proposed by the Agilent software for these flagged compounds were

evaluated, and if no reasonable alternative formula existed, the compounds were omitted from analysis.

Conservative abundance thresholds: An additional screening step was added to reduce variability from sample to sample caused by low abundance impurities in the LC solvents. Here, frequently occurring impurity ions were excluded and a conservative abundance threshold was implemented to far surpass the instrument LOD (ion height > 15000 counts or peak abundance > 100000 counts); see Supplemental Information for additional details. This threshold is unrelated to the threshold used in the GECKO-A analysis, discussed above. All together, our LC-ESI-Q-TOF's capabilities, in combination with strict quality control on peak assignment, formula assignment, and blank subtraction enable confident mass and formula identification for compounds in complex aerosol mixtures and follows best practices from the literature.

To study sample-to-sample compositional variability, molecular formulas and retention times were compared. The fraction of overlapping compounds was computed by comparing the number of compounds occurring in both samples (with a formula and retention time match, " $N_{\text{Shared}}$ ") in a set of two by the number of compounds present in each sample in the set (" $N_1$ " and " $N_2$ " for samples 1 and 2 in the set), and averaging the two values to provide the percent of distinct or overlapping compounds in a given sample comparison, as show in Equations 1 and 2. Compound-specific model results were treated in the same way. However, instead of tracking isomers with molecular formula and LC

retention time for the model results, chemical structures were used to compare across modeling experiments.

Additional data analyses performed in this study include a sensitivity analysis and a statistical backward trajectory analysis using HYSPLIT. Briefly, a sensitivity analysis was performed to evaluate the effect of LOD thresholds on the results of the sample-to-sample compositional variability analysis presented here. In addition, a backward trajectory analysis with 24-hour HYSPLIT trajectories was performed to evaluate the effect of air parcel history (and associated transport, chemistry, and meteorology) on the compositional variability observed at each field site. Additional details for both analyses can be found in the Supplemental Information.

### **Data availability**

The data that support the findings presented here are available from the authors upon request.

### **Code availability**

Basic R code for data processing and sample comparison are described in the Methods and Supplemental Information, but are available upon request. The chemical mechanism from GECKO-A modeling is also available upon request.

## **Acknowledgements**

We thank the University of Michigan Biological Station and the New York State Department of Environmental Conservation for enabling us to collect samples at these two locations. We gratefully acknowledge the NOAA Air Resources Laboratory (ARL) for the provision of the HYSPLIT transport and dispersion model and READY website (<http://www.ready.noaa.gov>) used in this publication. We also thank Dr. Harald Stark and Dr. Lynn Mazzoleni for CIMS and ultra-high resolution data shown in Figure 3, and Dr. Jason Surratt for synthesizing standards used in this work. D.R. Gentner acknowledges support from National Science Foundation Award 1622389. J. Lee-Taylor and J.L. Jimenez are grateful for support under EPA STAR 83587701-0 and DOE (BER/ASR) DE-SC0016559. This publication has not been formally reviewed by EPA. The views expressed in this document are solely those of the authors and do not necessarily reflect those of the Agency. EPA does not endorse any products or commercial services mentioned in this publication. The National Center for Atmospheric Research is sponsored by the National Science Foundation. A. Bui and R. Griffin acknowledge support of the National Science Foundation through AGS-1552086. M. Takeuchi, T. Joo, G. Eris, Y. Chen, and N. L. Ng acknowledge support from National Science Foundation CAREER AGS-1555034.

## **Author contributions**

J.C.D and D.R.G. designed the study and led analyses. J.C.D. collected filter samples at the forested site. A.A.T.B. and R.J.G. collected and analyzed AMS data at the forested site. T.J. collected filter samples and T.J., Y.C., and N.L.N. collected and analyzed AMS data in Atlanta. P.K. collected filter samples in NYC. M.T. and G.E. ran environmental chamber experiments and collected samples. J.L.-T., J.L.J., and B.A. developed and ran GECKO-A simulations. E.B.B. contributed to initial filter data analysis, method development, and observations. J.C.D. analyzed all filter data and compiled all results. J.C.D. and D.R.G. wrote the paper, with relevant methods contributions from co-authors. All authors commented on and discussed the manuscript to help refine the interpretation and presentation of results.

## References

1. Jimenez, J. L. *et al.* Evolution of Organic Aerosols in the Atmosphere. *Science*. **326**, 1525–1529 (2009).
2. Hallquist, M. *et al.* The formation, properties and impact of secondary organic aerosol: current and emerging issues. *Atmos. Chem. Phys.* **9**, 5155–5236 (2009).
3. Pöschl, U. & Shiraiwa, M. Multiphase Chemistry at the Atmosphere-Biosphere Interface Influencing Climate and Public Health in the Anthropocene. *Chem. Rev.* **115**, 4440–4475 (2015).
4. Goldstein, A. H. & Galbally, I. E. Known and Unexplored Organic Constituents in the Earth's Atmosphere. *Environ. Sci. Technol.* **41**, 1515–1521 (2007).
5. Aumont, B., Szopa, S. & Madronich, S. Modelling the evolution of organic carbon during its gas-phase tropospheric oxidation: development of an explicit model based

- on a self generating approach. *Atmos. Chem. Phys.* **5**, 2497–2517 (2005).
6. O'Brien, R. E. *et al.* Molecular characterization of organic aerosol using nanospray desorption/electrospray ionization mass spectrometry: CalNex 2010 field study. *Atmos. Environ.* **68**, 265–272 (2013).
  7. World Health Organization. Burden of disease from ambient and household air pollution: database estimates. (2015).
  8. Cohen, A. J. *et al.* The global burden of disease due to outdoor air pollution. *J. Toxicol. Environ. Health* **68**, 1301–1307 (2005).
  9. Pope, C. A. & Dockery, D. D. Health Effects of Fine Particulate Air Pollution: Lines that Connect. *J. Air Waste Manage. Assoc.* **56**, 709–742 (2006).
  10. Jerrett, M. *et al.* Long-term ozone exposure and mortality. *N. Engl. J. Med.* **360**, 1085–1095 (2009).
  11. Tao, F., Gonzalez-Flecha, B. & Kobzik, L. Reactive oxygen species in pulmonary inflammation by ambient particulates. *Free Radic. Biol. Med.* **35**, 327–340 (2003).
  12. Gurgueira, S. A., Lawrence, J., Coull, B., Murthy, G. G. K. & González-Flecha, B. Rapid increases in the steady-state concentration of reactive oxygen species in the lungs and heart after particulate air pollution inhalation. *Environ. Health Perspect.* **110**, 749–755 (2002).
  13. Voter, K. Z. *et al.* Ozone exposure and the production of reactive oxygen species by bronchoalveolar cells in humans. *Inhal. Toxicol.* **13**, 465–483 (2001).
  14. Gentner, D. R. *et al.* Elucidating secondary organic aerosol from diesel and gasoline vehicles through detailed characterization of organic carbon emissions. *Proc. Natl. Acad. Sci.* **109**, 18318–18323 (2012).
  15. Hunter, J. F. *et al.* Comprehensive characterization of atmospheric organic carbon at a forested site. *Nat. Geosci.* **10**, 748–753 (2017).
  16. Zhang, X. *et al.* Highly Oxygenated Multifunctional Compounds in  $\alpha$ -Pinene Secondary Organic Aerosol. *Environ. Sci. Technol.* **51**, 5932–5940 (2017).
  17. Krechmer, J. E. *et al.* Ion mobility spectrometry-mass spectrometry (IMS-MS) for on- and offline analysis of atmospheric gas and aerosol species. *Atmos. Meas. Tech.* **9**, 3245–3262 (2016).
  18. Isaacman-VanWertz, G. *et al.* Using advanced mass spectrometry techniques to fully characterize atmospheric organic carbon: current capabilities and remaining gaps. *Faraday Discuss.* **200**, 579–598 (2017).

19. Nozière, B. *et al.* The Molecular Identification of Organic Compounds in the Atmosphere: State of the Art and Challenges. *Chem. Rev.* **115**, 3919–3983 (2015).
20. Stark, H. *et al.* Methods to extract molecular and bulk chemical information from series of complex mass spectra with limited mass resolution. *Int. J. Mass Spectrom.* **389**, 26–38 (2015).
21. Heald, C. L. *et al.* A simplified description of the evolution of organic aerosol composition in the atmosphere. *Geophys. Res. Lett.* **37**, (2010).
22. Canagaratna, M. R. *et al.* Elemental ratio measurements of organic compounds using aerosol mass spectrometry: characterization, improved calibration, and implications. *Atmos. Chem. Phys.* **15**, 253–272 (2015).
23. O’Brien, R. E. *et al.* Molecular characterization of S- and N-containing organic constituents in ambient aerosols by negative ion mode high-resolution Nanospray Desorption Electrospray Ionization Mass Spectrometry: CalNex 2010 field study. *J. Geophys. Res. Atmos.* **119**, 12,706–12,720 (2014).
24. Budisulistiorini, S. H. *et al.* Examining the effects of anthropogenic emissions on isoprene-derived secondary organic aerosol formation during the 2013 Southern Oxidant and Aerosol Study (SOAS) at the Look Rock, Tennessee ground site. *Atmos. Chem. Phys.* **15**, 8871–8888 (2015).
25. Riva, M., Barbosa, T. D. S., Lin, Y., Stone, E. A. & Gold, A. Characterization of organosulfates in secondary organic aerosol derived from the photooxidation of long-chain alkanes. *Atmos. Chem. Phys.* **16**, 11001–11018 (2016).
26. Surratt, J. D. *et al.* Organosulfate Formation in Biogenic Secondary Organic Aerosol. *J. Phys. Chem. A* **112**, 8345–8378 (2008).
27. O’Brien, R. E. *et al.* Probing molecular associations of field-collected and laboratory-generated SOA with nano-DESI high-resolution mass spectrometry. *J. Geophys. Res. Atmos.* **118**, 1042–1051 (2013).
28. Romonosky, D. E., Laskin, A., Laskin, J. & Nizkorodov, S. A. High-Resolution Mass Spectrometry and Molecular Characterization of Aqueous Photochemistry Products of Common Types of Secondary Organic Aerosols. *J. Phys. Chem. A* **119**, 2594–2606 (2015).
29. Oss, M., Krueve, A., Herodes, K. & Leito, I. Electrospray Ionization Efficiency Scale of Organic Compound. *Anal. Chem.* **82**, 2865–2872 (2010).
30. Bateman, A. P., Laskin, J., Laskin, A. & Nizkorodov, S. A. Applications of High-Resolution Electrospray Ionization Mass Spectrometry to Measurements of Average Oxygen to Carbon Ratios in Secondary Organic Aerosols. *Environ. Sci. Technol.*

- 46**, 8315–8324 (2012).
31. Pudenzi, M. A. & Eberlin, M. N. Assessing Relative Electrospray Ionization, Atmospheric Pressure Photoionization, Atmospheric Pressure Chemical Ionization, and Atmospheric Pressure Photo- and Chemical Ionization Efficiencies in Mass Spectrometry Petroleomic Analysis via Pools and Pairs. *Energy and Fuels* **30**, 7125–7133 (2016).
  32. Purcell, J. M. *et al.* Sulfur speciation in petroleum: Atmospheric pressure photoionization or chemical derivatization and electrospray ionization Fourier transform ion cyclotron resonance mass spectrometry. *Energy and Fuels* **21**, 2869–2874 (2007).
  33. Hayes, P. L. *et al.* Organic aerosol composition and sources in Pasadena, California, during the 2010 CalNex campaign. *J. Geophys. Res. Atmos.* **118**, 9233–9257 (2013).
  34. Aiken, A. C., DeCarlo, P. F., Kroll, J. H., Huffman, J. A. & Docherty, K. S. O/C and OM/OC Ratios of Primary, Secondary, and Ambient Organic Aerosols with High-Resolution Time-of-Flight Aerosol Mass Spectrometry. *Environ. Sci. Technol.* **42**, 4478–4485 (2008).
  35. Wang, X. K. *et al.* Molecular characterization of atmospheric particulate organosulfates in three megacities at the middle and lower reaches of the Yangtze River. *Atmos. Chem. Phys.* **16**, 2285–2298 (2016).
  36. Lin, P., Yu, J. Z., Engling, G. & Kalberer, M. Organosulfates in humic-like substance fraction isolated from aerosols at seven locations in East Asia: A study by ultra-high-resolution mass spectrometry. *Environ. Sci. Technol.* **46**, 13118–13127 (2012).
  37. Li, Y., Pöschl, U. & Shiraiwa, M. Molecular corridors and parameterizations of volatility in the chemical evolution of organic aerosols. *Atmos. Chem. Phys.* **16**, 3327–3344 (2016).
  38. D'Ambro, E. L. *et al.* Molecular composition and volatility of isoprene photochemical oxidation secondary organic aerosol under low and high NO<sub>x</sub> conditions. *Atmos. Chem. Phys.* **17**, 159–174 (2017).
  39. Worton, D. R. *et al.* Lubricating oil dominates primary organic aerosol emissions from motor vehicles. *Environ. Sci. Technol.* **48**, 3698–3706 (2014).
  40. Gentner, D. R. *et al.* Review of Urban Secondary Organic Aerosol Formation from Gasoline and Diesel Motor Vehicle Emissions. *Environ. Sci. Technol.* **51**, 1074–1093 (2017).
  41. Gentner, D. R. *et al.* Emissions of terpenoids, benzenoids, and other biogenic gas-

- phase organic compounds from agricultural crops and their potential implications for air quality. *Atmos. Chem. Phys.* **14**, 5393–5413 (2014).
42. Park, J. H. *et al.* Active Atmosphere-Ecosystem Exchange of the Vast Majority of Detected Volatile Organic Compounds. *Science*. **341**, 643–647 (2013).
  43. Kroll, J. H. *et al.* Carbon oxidation state as a metric for describing the chemistry of atmospheric organic aerosol. *Nat. Chem.* **3**, 133–139 (2011).
  44. Polissar, A. V., Hopke, P. K. & Harris, J. M. Source Regions for Atmospheric Aerosol Measured at Barrow, Alaska. *Environ. Sci. Technol.* **35**, 4214–4226 (2001).
  45. Gentner, D. R. *et al.* Emissions of organic carbon and methane from petroleum and dairy operations in California’s San Joaquin Valley. *Atmos. Chem. Phys.* **14**, 4955–4978 (2014).
  46. Budisulistiorini, S. H. *et al.* Real-time Continuous Characterization of Secondary Organic Aerosol Derived from Isoprene Epoxydiols in Downtown Atlanta, Georgia, Using the Aerodyne Aerosol Chemical Speciation Monitor. *Environ. Sci. Technol.* **47**, 5686–5694 (2013).
  47. Karambelas, A., Pye, H. O. T., Budisulistiorini, S. H., Surratt, J. D. & Pinder, R. W. Contribution of Isoprene Epoxydiol to Urban Organic Aerosol: Evidence from Modeling and Measurements. *Environ. Sci. Technol. Lett.* **1**, 278–283 (2014).
  48. Rutter, A. P. *et al.* Sources of air pollution in a region of oil and gas exploration downwind of a large city. *Atmos. Environ.* **120**, 89–99 (2015).
  49. Ervens, B., Turpin, B. J. & Weber, R. J. Secondary organic aerosol formation in cloud droplets and aqueous particles (aqSOA): A review of laboratory, field and model studies. *Atmos. Chem. Phys.* **11**, 11069–11102 (2011).
  50. Ng, N. L. *et al.* Organic aerosol components observed in Northern Hemispheric datasets from Aerosol Mass Spectrometry. *Atmos. Chem. Phys.* **10**, 4625–4641 (2010).
  51. Russell, L. M., Bahadur, R. & Ziemann, P. J. Identifying organic aerosol sources by comparing functional group composition in chamber and atmospheric particles. *Proc. Natl. Acad. Sci.* **108**, 3516–3521 (2011).
  52. Koop, T., Bookhold, J., Shiraiwa, M. & Pöschl, U. Glass transition and phase state of organic compounds: dependency on molecular properties and implications for secondary organic aerosols in the atmosphere. *Phys. Chem. Chem. Phys.* **13**, 19238–19255 (2011).
  53. Tuet, W. Y. *et al.* Chemical oxidative potential of secondary organic aerosol (SOA)

- generated from the photooxidation of biogenic and anthropogenic volatile organic compounds. *Atmos. Chem. Phys.* **17**, 839–853 (2017).
54. Ye, J., Gordon, C. A. & Chan, A. W. H. Enhancement in Secondary Organic Aerosol Formation in the Presence of Preexisting Organic Particle. *Environ. Sci. Technol.* **50**, 3572–3579 (2016).
  55. Rickards, A. M. J., Miles, R. E. H., Davies, J. F., Marshall, F. H. & Reid, J. P. Measurements of the Sensitivity of Aerosol Hygroscopicity and the  $\kappa$  Parameter to the O/C ratio. *J. Phys. Chem. A* **117**, 14120–14131 (2013).
  56. Kostenidou, E. *et al.* Organic aerosol in the summertime Southeastern United States: components and their link to volatility distribution, oxidation state and hygroscopicity. *Atmos. Chem. Phys.* **18**, 5799–5819 (2017).
  57. Thalman, R. *et al.* CCN activity and organic hygroscopicity of aerosols downwind of an urban region in central Amazonia: seasonal and diel variations and impact of anthropogenic emissions. *Atmos. Chem. Phys.* **17**, 11779–11801 (2017).
  58. Xu, L. *et al.* Wintertime aerosol chemical composition, volatility, and spatial variability in the greater London area. *Atmos. Chem. Phys.* **16**, 1139–1160 (2016).
  59. Carroll, M. A., Bertman, S. B. & Shepson, P. B. Overview of the Program for Research on Oxidants: PHotochemistry, Emissions, and Transport (PROPHET) summer 1998 measurements intensive. *J. Geophys. Res.* **106**, 24275–24288 (2001).
  60. Edwards, P. M. *et al.* Transition from high- to low-NO<sub>x</sub> control of night-time oxidation in the southeastern US. *Nat. Geosci.* **10**, 490–495 (2017).
  61. Xu, L. *et al.* Effects of anthropogenic emissions on aerosol formation from isoprene and monoterpenes in the southeastern United States. *Proc. Natl. Acad. Sci.* **112**, 37–42 (2014).
  62. eCFR — Electronic Code of Federal Regulations. (2018). Available at: <https://www.ecfr.gov/cgi-bin/retrieveECFR?gp=&SID=0f3bfa16342b3e5b858743bbbbcfa4f&r=PART&n=40y6.0.1.1.1>. (Accessed: 22nd July 2018)
  63. DeCarlo, P. F. *et al.* Field-deployable, high-resolution, time-of-flight aerosol mass spectrometer. *Anal. Chem.* **78**, 8281–8289 (2006).
  64. Jayne, J. T. *et al.* Development of an aerosol mass spectrometer for size and composition analysis of submicron particles. *Aerosol Sci. Technol.* **33**, 49–70 (2000).
  65. Jimenez, J. L. Ambient aerosol sampling using the Aerodyne Aerosol Mass

- Spectrometer. *J. Geophys. Res.* **108**, 8425 (2003).
66. Middlebrook, A. M., Bahreini, R., Jimenez, J. L. & Canagaratna, M. R. Evaluation of composition-dependent collection efficiencies for the Aerodyne aerosol mass spectrometer using field data. *Aerosol Sci. Technol.* **46**, 258–271 (2012).
  67. Sueper, D. ToF-AMS Data Analysis Software. (2018). Available at: [http://cires1.colorado.edu/jimenez-group/wiki/index.php/ToF-AMS\\_Analysis\\_Software](http://cires1.colorado.edu/jimenez-group/wiki/index.php/ToF-AMS_Analysis_Software).
  68. Matthew, B. M., Middlebrook, A. M. & Onasch, T. B. Collection efficiencies in an aerodyne aerosol mass spectrometer as a function of particle phase for laboratory generated aerosols. *Aerosol Sci. Technol.* **42**, 884–898 (2008).
  69. Boyd, C. M. *et al.* Secondary organic aerosol (SOA) formation from the  $\beta$ -pinene + NO<sub>3</sub> system: effect of humidity and peroxy radical fate. *Atmos. Chem. Phys.* **15**, 7497–7522 (2015).
  70. Lee-Taylor, J. *et al.* Multiday production of condensing organic aerosol mass in urban and forest outflow. *Atmos. Chem. Phys.* **15**, 595–615 (2015).
  71. Camredon, M., Aumont, B., Lee-Taylor, J. & Madronich, S. The SOA/VOC/NO<sub>x</sub> system: an explicit model of secondary organic aerosol formation. *Atmos. Chem. Phys.* **7**, 5599–5610 (2007).
  72. Nannoolal, Y., Rarey, J., Ramjugernath, D. & Cordes, W. Estimation of pure component properties: Part 1. Estimation of the normal boiling point of non-electrolyte organic compounds via group contributions and group interactions. *Fluid Phase Equilib.* **226**, 45–63 (2004).
  73. Nannoolal, Y., Rarey, J. & Ramjugernath, D. Estimation of pure component properties: Part 3. Estimation of the vapor pressure of non-electrolyte organic compounds via group contribution and group interactions. *Fluid Phase Equilib.* **269**, 117–133 (2008).
  74. Valorso, R. *et al.* Explicit modelling of SOA formation from  $\alpha$ -pinene photooxidation: Sensitivity to vapour pressure estimation. *Atmos. Chem. Phys.* **11**, 6895–6910 (2011).
  75. McVay, R. C. *et al.* SOA formation from the photooxidation of  $\alpha$ -pinene: Systematic exploration of the simulation of chamber data. *Atmos. Chem. Phys.* **16**, 2785–2802 (2016).
  76. Hamilton, J. F., Lewis, A. C., Carey, T. J. & Wenger, J. C. Characterization of Polar Compounds and Oligomers in Secondary Organic Aerosol Using Liquid Chromatography Coupled to Mass Spectrometry. *Anal. Chem.* **80**, 474–480 (2008).

77. Ng, N. L. *et al.* Secondary organic aerosol (SOA) formation from reaction of isoprene with nitrate radicals (NO<sub>3</sub>). *Atmos. Chem. Phys.* **8**, 4117–4140 (2008).
78. Riva, M. *et al.* Chemical Characterization of Secondary Organic Aerosol from Oxidation of Isoprene Hydroxyhydroperoxides. *Environ. Sci. Technol.* **50**, 9889–9899 (2016).
79. Zhang, H., Surratt, J. D., Lin, Y. H., Bapat, J. & Kamens, R. M. Effect of relative humidity on SOA formation from isoprene/NO photooxidation: enhancement of 2-methylglyceric acid and its corresponding oligoesters under dry conditions. *Atmos. Chem. Phys.* **11**, 6411–6424 (2011).
80. Chen, Q. *et al.* Untargeted plasma metabolite profiling reveals the broad systemic consequences of xanthine oxidoreductase inactivation in mice. *PLoS One* **7**, (2012).
81. Witherspoon, M., Chen, Q., Kopelovich, L., Gross, S. S. & Lipkin, S. M. Unbiased metabolite profiling indicates that a diminished thymidine pool is the underlying mechanism of colon cancer chemoprevention by alpha-difluoromethylornithine. *Cancer Discov.* **3**, 1072–1081 (2013).
82. Kind, T. & Fiehn, O. Seven Golden Rules for heuristic filtering of molecular formulas obtained by accurate mass spectrometry. *BMC Bioinformatics* **8**, 105 (2007).
83. Gómez, M. J., Gómez-Ramos, M. M., Malato, O., Mezcua, M. & Fernández-Alba, A. R. Rapid automated screening, identification and quantification of organic micro-contaminants and their main transformation products in wastewater and river waters using liquid chromatography-quadrupole-time-of-flight mass spectrometry with an accurate-mass. *J. Chromatogr. A* **1217**, 7038–7054 (2010).
84. Thurman, E. M. & Ferrer, I. The isotopic mass defect: A tool for limiting molecular formulas by accurate mass. *Anal. Bioanal. Chem.* **397**, 2807–2816 (2010).
85. Zielinski, A. T. *et al.* A new processing scheme for ultra-high resolution direct infusion mass spectrometry data. *Atmos. Environ.* **178**, 129–139 (2018).
86. Koch, B. P., Dittmar, T., Witt, M. & Kattner, G. Fundamentals of molecular formula assignment to ultrahigh resolution mass data of natural organic matter. *Anal. Chem.* **79**, 1758–1763 (2007).

## Supplemental Information

### S1. Methods and Method Validation

To limit run-to-run variability of a single sample caused by low abundance impurities present in the liquid chromatography solvents, we excluded a comprehensive list of background ions and implemented a strict abundance threshold, as briefly described in the Methods section. Frequently occurring background ions were tracked across a series of 10 positive and negative mode LC-ESI-Q-TOF runs of filter extract blanks, and then excluded from all subsequent analysis (Figure S1). In addition, a conservative abundance threshold was implemented to ensure that all analytes considered in this study are above the method limit of detection (LOD), determined by calibration curve analysis to correspond to a peak volume of  $82,500 \pm 13,400$  counts (peak volume is used by Agilent Mass Hunter software to account for abundance, retention time, and the formation of multiple adducts for a single species). Only analytes with a peak volume greater than 100,000 counts or a corresponding peak height greater than 15,000 counts were considered, which was well above typical signal-to-noise ratios that are set at 3-5 (computing LOD with a signal-to-noise ratio of 3 yields a minimum peak height of 1200 counts). Combined with the data quality control described in the Methods section, implementing a strict LOD threshold and tracking and eliminating low abundance background ions reduced run-to-run variability for sample replicates to less than 8%, on average (Figure S1). This low variability between triplicate runs of the same sample demonstrates that the compositional variability observed when comparing different samples in this study is in fact due to different chemical composition, and not an artifact of analytical methodology.

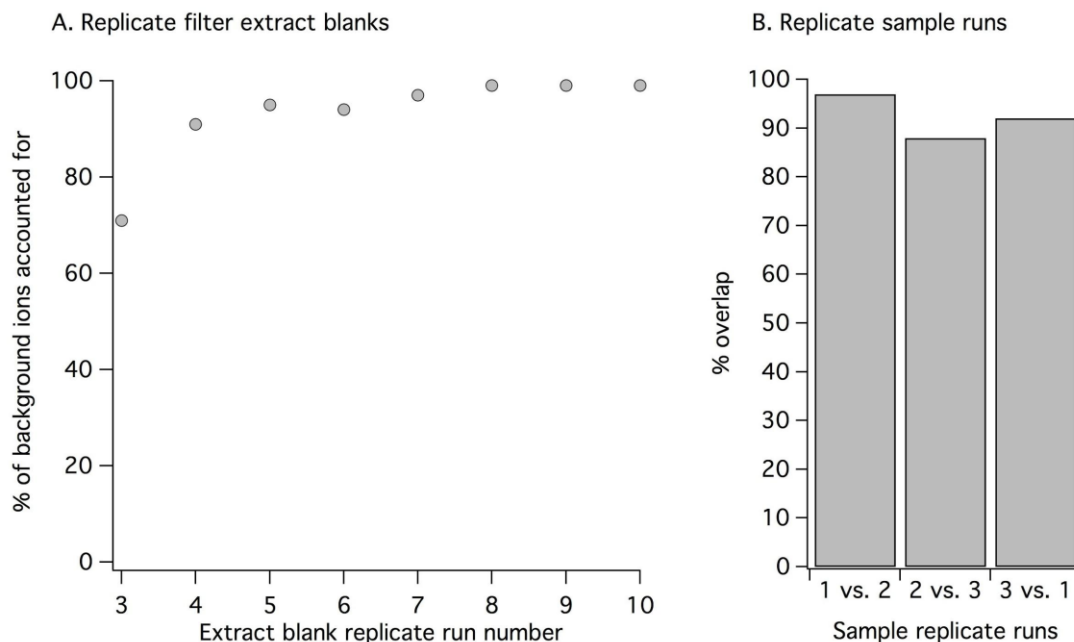


**Figure S1.** (A) A comprehensive list of background ions was compiled from 10 LC-ESI-Q-TOF runs of a filter extract blank, accounting for >99% of observed background ions. This exclusion list, in combination with implementing a peak volume threshold of 100,000 counts and a peak height threshold of 15,000 counts, reduced run-to-run variability for the same sample to less than 8% on average (B), for triplicate runs of the same sample (comparing run 1 versus run 2, run 2 versus run 3, and run 3 versus run 1).

The data quality control discussed above allows only high quality peaks with assigned molecular formulas that pass a strict set of standards to be considered in this analysis (see Methods); this resulted in an average of  $553 \pm 146$  compounds per sample for the forest samples (mean  $\pm$  standard deviation),  $128 \pm 41$  compounds per sample for the Atlanta samples,  $161 \pm 66$  compounds per sample for the New York City samples, and  $240 \pm 35$  compounds per sample for the environmental chamber samples. When the LOD is reduced to -90% in the sensitivity analysis presented here, the height threshold still surpasses the instrument LOD computed with a signal-to-noise ratio of 3 (1500 counts versus 1200 counts, respectively), and an average of  $600 \pm 145$  compounds for the forest,  $175 \pm 51$  for Atlanta,  $268 \pm 107$  for New York City, and  $275 \pm 41$  for the chamber are considered. The

trends in variability observed at the -90% LOD case are less than 6.5% different than the base case LOD threshold, indicating that the variability trends discussed here are not sensitive to LOD or the number of compounds considered. An additional discussion of the sensitivity analysis can be found in section S3 (Figure S18).

Leveraging liquid chromatographic separation to distinguish between isomers was central to this study. Retention times were used to distinguish between two different structures with the same molecular formula. In order to define a retention time window of expected chromatographic drift, five samples were spiked with an internal standard (after first running them on the LC-ESI-Q-TOF to collect compositional variability data). Samples were specifically chosen here, to account for potential matrix effects. A standard was made from the following components, all at 5 ng/ $\mu$ L: limonene epoxide, pinonic acid, pinane diol, 2-decanone, dodecanal, 4-heptanone, octanoic acid, nopinone (all from Sigma Aldrich), N-dodecanol-d25, diethyl phthalate-3,4,5,6-d4, octanoic acid-d15 (all from AccuStandard), and 2-methyltetrols (synthesized by the Surratt group at UNC Chapel Hill).

Spiked samples were run in both ESI positive and negative mode. An average retention time and standard deviation for each component was computed, and are reported in Table S1. The majority (75%) of compounds did not drift more than 0.2 minutes between runs, with only a few outliers exhibiting more significant changes. An expected drift threshold of 0.25 minutes was set (85% of compounds fell below this limit); compounds with the same molecular formula and retention times differing by 0.25 minutes or less were considered to be the same isomer, while compounds with the same molecular formula and

retention times differing by more than 0.25 minutes were classified as isomers. Any very closely eluting isomers (i.e. with retention times that differ by less than 0.25 minutes) were treated as the same compound for this analysis. As a result, this retention time analysis provides a lower limit for variability—if many closely eluting isomers exist, more compositional variability may be observed.

In addition, to estimate the quantity of mass analyzed from each filter sample via LC-ESI-Q-TOF, an average ESI response factor was computed. An internal standard was run on the system, expanding upon the components of the internal standard discussed above, to incorporate a wider range of functional groups (including acids, aldehydes, ketones, alcohols, amines, amides, nitrates, nitriles, ethers, thiols, epoxides, sulfides, sulfates, and phthalates). This standard contained the following components at 5 ng/ $\mu$ L: octanoic acid, citronellol, nopinone, 4-heptanone, N,N-diethyl-meta-toluamide, dodecanal, isobutyl nitrate, isopropyl nitrate, dodecanenitrile, dimethylbenzylamine, diphenyl ether, octanethiol, mentha-8-thiol-3-one, limonene epoxide, dibutyl sulfide, benzene, maleic acid, pinene diol, menthol, benzophenone, octyl sulfate, camphor sulfonic acid, limonene diol, pinonic acid, benzyl butyl phthalate, bis(2-ethylhexyl) phthalate, dibutyl phthalate, di-n-octyl phthalate, diethyl phthalate, and dimethyl phthalate (all from Sigma Aldrich). We studied several isomer pairs (e.g. with the same molecular formula but different structure, such as pinene diol and limonene diol, citronellol and menthol, bis(2-ethylhexyl) phthalate and di-n-octyl phthalate), which were well-separated during LC analysis (>3 minutes between peaks, on average). A response factor (expressed as mass injected/peak volume) for each individual component was computed. Response factors were then

averaged, and the average value multiplied by individual analyte abundances observed in the field samples.

**Table S1.** Constraining expected chromatographic drift to separate isomers via LC

<b>ESI mode</b>	<b>Formula</b>	<b>Average retention time (min)</b>	<b>Standard deviation (min)</b>
Negative	C <sub>10</sub> H <sub>16</sub> O	17.09	0.24
Positive	C <sub>10</sub> H <sub>16</sub> O <sub>3</sub>	11.56	0.21
Negative	C <sub>10</sub> H <sub>16</sub> O <sub>3</sub>	11.33	0.02
Negative	C <sub>10</sub> H <sub>18</sub> O <sub>2</sub>	17.64	0.42
Positive	C <sub>10</sub> H <sub>20</sub> O	18.90	0.31
Negative	C <sub>10</sub> H <sub>20</sub> O	19.06	0.02
Positive	C <sub>12</sub> H <sub>24</sub> O	21.27	0.11
Positive	C <sub>12</sub> H <sub>24</sub> O	21.18	0.10
Negative	C <sub>12</sub> H <sub>24</sub> O	21.45	0.02
Positive	C <sub>12</sub> H <sub>9</sub> D <sub>4</sub> O <sub>4</sub>	12.00	0.67
Positive	C <sub>5</sub> H <sub>12</sub> O <sub>4</sub>	0.91	0.01
Negative	C <sub>5</sub> H <sub>12</sub> O <sub>4</sub>	0.90	0.01
Positive	C <sub>7</sub> H <sub>14</sub> O	21.17	0.10
Negative	C <sub>7</sub> H <sub>14</sub> O	13.67	0.01
Positive	C <sub>8</sub> H <sub>16</sub> O <sub>2</sub>	16.47	0.16
Positive	C <sub>8</sub> H <sub>16</sub> O <sub>2</sub>	16.64	0.16
Negative	C <sub>8</sub> H <sub>16</sub> O <sub>2</sub>	15.66	0.00
Positive	C <sub>9</sub> H <sub>14</sub> O	11.57	0.20
Negative	C <sub>9</sub> H <sub>14</sub> O	14.14	0.01

## **S2. Limited temporal variability in bulk chemical speciation of OA**

LC-ESI-Q-TOF elemental ratios and elemental composition (Figures 1, S2, S3) remain relatively consistent throughout each campaign. This is consistent with AMS O/C data from the forest and Atlanta (Figures 1, S2-S4). Both AMS instruments sampled PM<sub>1</sub> particles, in contrast with the filter measurements discussed in this study, which collected

PM<sub>10</sub>. Figure S4 shows data from the forest and Atlanta for the total submicron organic fraction concentration and for O/C. The total organic components observed is somewhat variable (particularly at the Atlanta site). However, with a few short exceptions for the forest campaign, O/C varies within a narrow range throughout both campaigns, especially over hourly (Figure S4) to 8 hour (Figures S2, S3) time resolution.

There is good agreement between the PM<sub>10</sub> O/C estimate and the PM<sub>1</sub> AMS O/C estimate for the Atlanta site, but the forest estimates diverge more significantly from each other. Inlets at the Atlanta site were vertically co-located, whereas inlets at the forested site, though both above the canopy, were offset by 2 m. Furthermore, in Atlanta, the sampling height was 4.5 m above the ground, whereas at the forested site, the sampling height was 28-30 m above the ground. The most important hypothesized driving factor behind these different O/C ratios is the different PM size cuts that are sampled by the AMS and by the filters analyzed by LC-ESI-Q-TOF. The distribution of organic compounds across the PM<sub>1</sub> size range (measured by AMS) and the PM<sub>10</sub> size range (measured by LC-ESI-Q-QTOF) appears to have been more similar at the Atlanta site than at the forested site. At the forested site, the particles observed by LC-ESI-Q-TOF may include more larger diameter functionalized POA than the particles sampled by AMS (for example, primary biogenic aerosol with a diameter greater than PM<sub>1</sub> but less than PM<sub>10</sub>, which may include compounds related to fungal spores, bacteria, small plant fragments, etc.,<sup>1</sup> all of which are likely to be present in a forested environment). This could contribute to some of the observed O/C difference between the two types of measurements. However, there was a significant range of compounds observed at both sites, and when accounting for the

standard deviation of O/C at the forested site (Table S2), many of the values approach the AMS values within the 28% AMS uncertainty (shown in light green shading, discussed below). Relative to each other, the AMS O/C values are as expected; the forested site AMS O/C is larger, as the forested site is more rural and sees more influence from SOA, while the Atlanta site O/C is smaller, as the Atlanta site seems more influence from POA which lowers the average O/C.

All combined, the difference in PM size cut, differences in site-to-site sampling height, and differences in site-to-site size-dependent chemical composition of particles drive the forest LC-ESI-Q-TOF and AMS O/C data to stray farther apart from each other, while remaining more similar in the Atlanta case.

Unweighted elemental ratios are presented in Figure S2, where elemental ratios were computed for each compound and then averaged, with all compounds treated equally. Weighting O/C ratios by abundance to determine mixture-wide O/C has been shown to improve the accuracy of O/C estimates.<sup>1</sup> This assumes roughly equal ionization efficiencies between compounds in the electrospray source. Despite some variance in ionization efficiency between compounds with different functionality (observed in this study as well as in the literature), an extensive comparison of O/C in the literature obtained by high resolution mass spectrometry and by AMS shows that the assumption of equal ionization efficiency is reasonable.<sup>1</sup> Weighting the elemental ratios computed here by abundance has a variable effect (Figure S3); on average, O/C is increased by  $18.7 \pm 28.0\%$ , O/N is increased by  $10.1 \pm 33.5\%$ , and O/S is decreased by  $7.8 \pm 16.1\%$ .

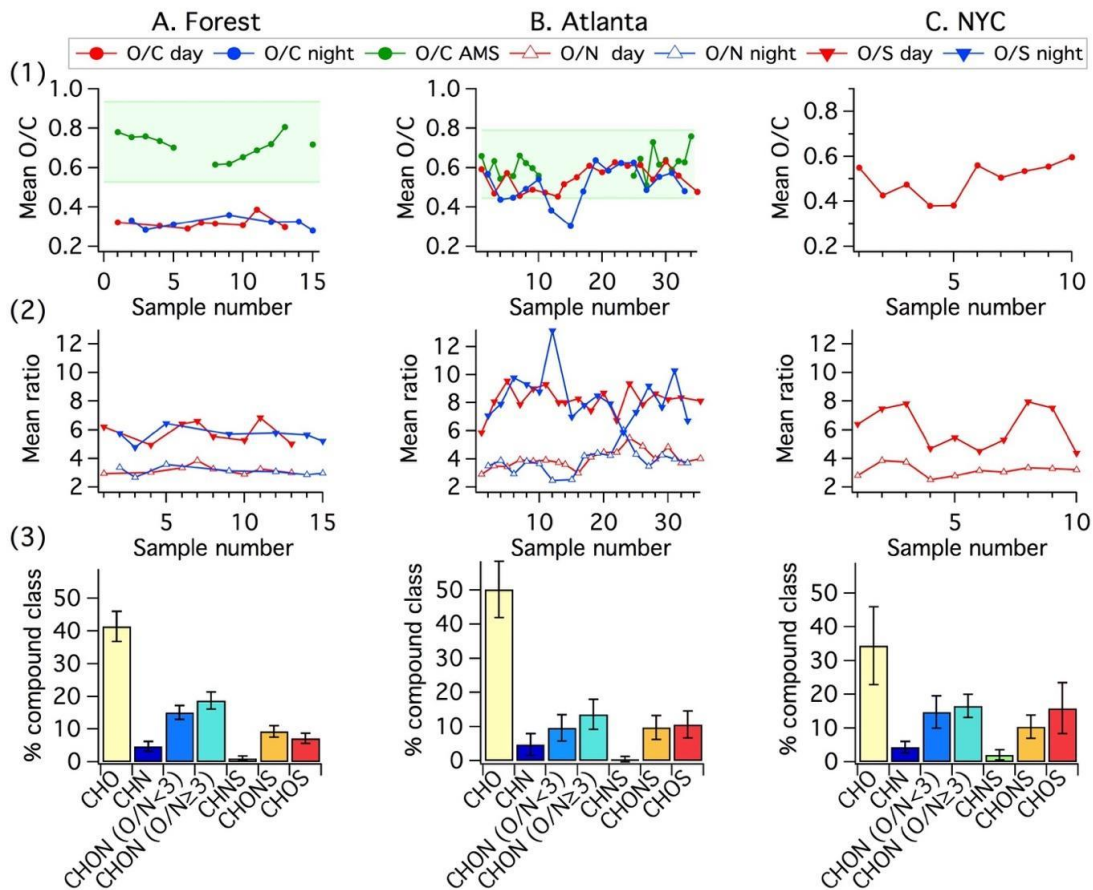


**Figure S2.** Bulk mixture properties for samples at each of 3 field sites: a forest (column A), in Atlanta (column B), and New York City (column C). Panel 1 shows average O/C values (unweighted) for filter samples analyzed via LC-ESI-Q-TOF during the day (red) and at night (blue), and values recorded by the AMS at each site (green). AMS data are averaged across each filter sampling period, but do not include the  $\pm 28\%$  uncertainty reported in Canagaratna et al. for improved-ambient elemental analysis (light green shading, computed as 28% from the mean).<sup>2</sup>

Panel 2 shows average O/N and O/S values for filter samples analyzed via LC-ESI-Q-TOF during the day and at night, for compounds with 1 or more N-atoms and 1 or more S-atoms, respectively. The weighted mean molecular weights for compounds with  $O/N \geq 3$  (includes organonitrates) and compounds with  $O/S \geq 4$  (includes organosulfates) are  $446.8 \pm 27.2$  g/mol and  $354.2 \pm 58.9$  g/mol, respectively, in the forest (unweighted:  $412.2 \pm 11.4$  g/mol,  $433.0 \pm 13.5$  g/mol),  $342.1 \pm 67.0$  g/mol and  $286.0 \pm 44.2$  g/mol, respectively, in Atlanta

(unweighted:  $368.2 \pm 24.0$  g/mol,  $339.2 \pm 33.6$  g/mol), and  $330.8 \pm 119.1$  g/mol and  $289.9 \pm 105.4$  g/mol, respectively, in New York City (unweighted:  $353.9 \pm 28.0$  g/mol and  $340.8 \pm 16.3$  g/mol). Panel 3 shows the mean compound class distribution at each site (identical to Figure 1). Error bars represent 1 standard deviation from the mean, highlighting limited variation between the compound classes observed from sample to sample at each site.

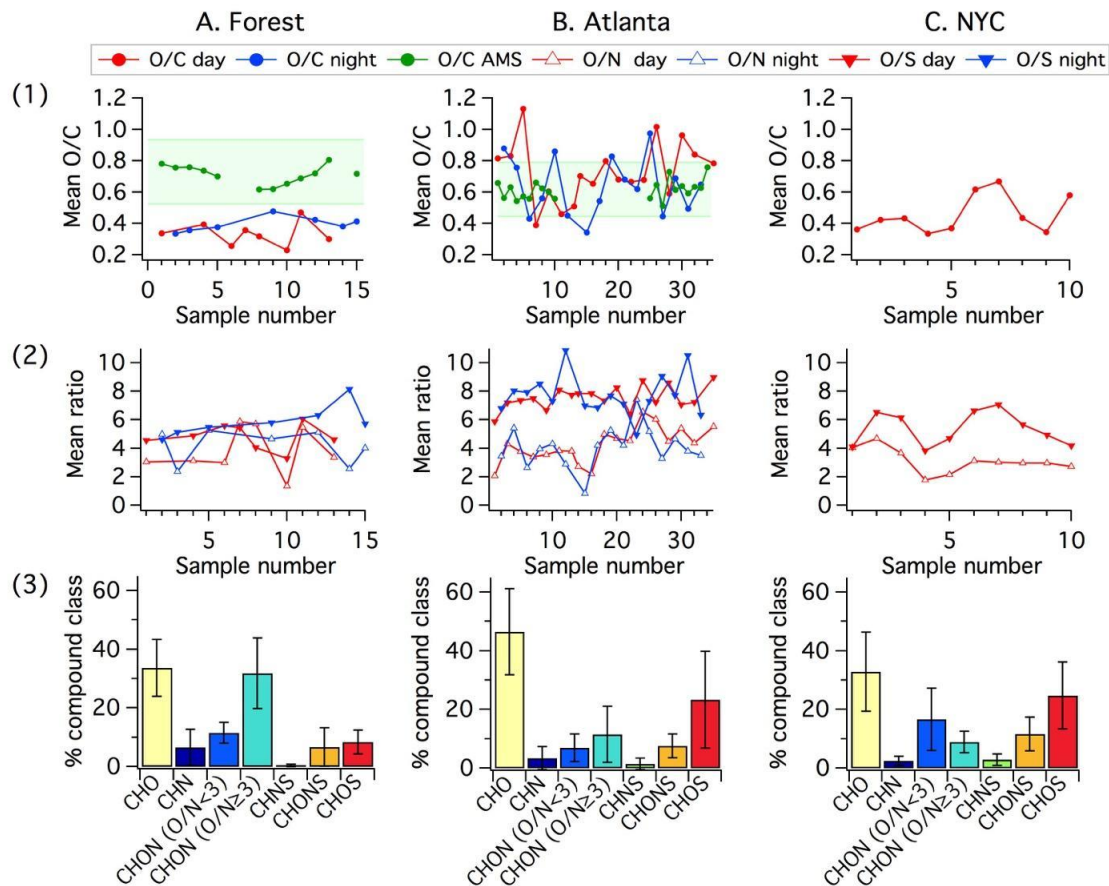


**Figure S3.** Abundance-weighted bulk elemental ratios for samples at each of 3 field sites: a forest (column A), near downtown Atlanta (column B), and New York City (column C). Panel 1 shows average O/C values for filter samples analyzed via LC-ESI-Q-TOF during the day (red) and at night (blue), and values recorded by the AMS at each site (green). Hourly AMS data are averaged across each filter sampling period, but do not include the  $\pm 28\%$  uncertainty reported in Canagaratna et al. for improved-ambient elemental analysis (light green shading, computed as 28% from the mean).<sup>2</sup> Panel 2 shows average O/N and O/S values for filter samples analyzed via LC-ESI-Q-TOF during the day and at night, for compounds with 1 or more N-atoms and 1 or more S-atoms, respectively. All elemental ratios are weighted by the relative abundance of each compound, and then averaged. Panel 3 shows the mean distribution of compound class at each site, weighted by abundance.

Standard deviations for Figures S2 and S3, panels 2 and 3, describe the range of O/C, O/N, and O/S observed at each field site. They are not presented in Figures S2 and S3 as error bars for clarity, but are presented in Table S2.

**Table S2. Standard Deviations Corresponding to Figures S2 and S3**

<b><u>PROPHET Filter</u></b>	<b><u>O/C SD (Fig. S2)</u></b>	<b><u>O/N SD (Fig. S2)</u></b>	<b><u>O/S SD (Fig. S2)</u></b>	<b><u>O/C Weighted SD (Fig. 3)</u></b>	<b><u>O/N Weighted SD (Fig. 3)</u></b>	<b><u>O/S Weighted SD (Fig. 3)</u></b>
Sample 1 Day	0.29	2.87	4.61	0.27	2.74	3.23
Sample 2 Night	0.29	2.72	3.39	0.27	3.90	4.15
Sample 3 Night	0.28	2.54	2.41	0.42	2.39	3.38
Sample 4 Day	0.24	2.47	3.64	0.39	2.11	3.42
Sample 5 Night	0.26	3.07	3.39	0.27	3.83	3.67
Sample 6 Day	0.26	3.06	3.88	0.22	2.46	2.79
Sample 7 Day	0.28	3.12	5.15	0.26	3.84	4.48
Sample 8 Day	0.31	2.98	4.21	0.24	3.70	3.39
Sample 9 Night	0.36	2.75	2.51	0.45	3.79	2.54
Sample 10 Day	0.32	2.95	3.04	0.32	2.01	4.84
Sample 11 Day	0.33	2.89	4.94	0.38	4.12	3.34
Sample 12 Night	0.27	2.54	2.63	0.37	3.90	3.68
Sample 13 Day	0.29	2.79	4.27	0.33	2.31	4.25
Sample 14 Night	0.32	2.65	2.65	0.37	2.51	4.50
Sample 15 Night	0.25	2.82	3.50	0.27	2.75	4.89
<b><u>NYC Filter</u></b>	<b><u>O/C SD (Fig. S2)</u></b>	<b><u>O/N SD (Fig. S2)</u></b>	<b><u>O/S SD (Fig. S2)</u></b>	<b><u>O/C Weighted SD (Fig. 3)</u></b>	<b><u>O/N Weighted SD (Fig. 3)</u></b>	<b><u>O/S Weighted SD (Fig. 3)</u></b>
Day 1	0.43	2.10	4.21	0.39	2.90	2.61
Day 2	0.33	2.86	3.91	0.34	3.25	4.03
Day 3	0.38	2.66	3.46	0.40	2.64	3.53
Day 4	0.33	2.38	4.91	0.36	1.91	4.60
Day 5	0.36	2.48	4.55	0.34	2.11	4.15
Day 6	0.48	2.68	4.75	0.49	2.16	5.00
Day 7	0.47	2.79	5.36	0.54	2.56	5.11
Day 10	0.40	2.63	5.43	0.39	2.45	4.23
Day 11	0.47	2.49	5.13	0.40	2.37	4.24
Day 14	0.55	2.84	4.81	0.53	2.15	4.23
<b><u>Atlanta Filter</u></b>	<b><u>O/C SD (Fig. S2)</u></b>	<b><u>O/N SD (Fig. S2)</u></b>	<b><u>O/S SD (Fig. S2)</u></b>	<b><u>O/C Weighted</u></b>	<b><u>O/N Weighted</u></b>	<b><u>O/S Weighted</u></b>

				<b><u>SD (Fig. 3)</u></b>	<b><u>SD (Fig. 3)</u></b>	<b><u>SD (Fig. 3)</u></b>
Day 1	0.48	2.67	3.03	0.56	1.99	2.37
Night 1	0.46	2.98	3.12	0.58	2.68	1.95
Day 2	0.39	3.33	3.45	0.59	3.76	2.36
Night 2	0.36	3.32	3.75	0.52	3.52	2.50
Day 3	0.46	2.70	4.33	0.59	2.44	2.98
Night 3	0.39	2.47	4.67	0.39	2.02	4.76
Day 4	0.38	3.54	5.10	0.40	3.32	4.47
Night 4	0.41	3.13	4.18	0.48	3.07	3.06
Day 5	0.39	2.61	4.68	0.54	2.59	3.14
Night 5	0.43	3.43	4.53	0.56	3.65	2.69
Day 6	0.40	2.85	4.70	0.46	2.96	3.84
Night 6	0.38	3.14	2.70	0.46	2.71	2.23
Day 7	0.32	3.25	4.09	0.29	3.24	3.20
Day 8	0.39	2.29	4.97	0.48	2.28	3.91
Night 8	0.28	2.16	4.03	0.30	2.31	3.82
Day 9	0.51	2.32	4.21	0.56	2.04	2.46
Night 9	0.41	3.75	5.47	0.41	3.37	4.59
Day 10	0.47	3.12	3.52	0.49	3.96	2.76
Night 10	0.46	3.28	4.53	0.45	3.72	2.58
Day 11	0.44	2.98	3.95	0.44	3.31	3.15
Night 11	0.46	3.03	4.59	0.48	2.82	3.40
Day 12	0.47	3.01	4.80	0.49	3.51	4.01
Night 12	0.42	3.11	2.83	0.46	3.32	2.43
Day 13	0.39	3.62	3.88	0.33	3.52	2.79
Night 13	0.41	3.33	3.52	0.49	3.61	2.17
Day 14	0.43	3.47	3.87	0.52	4.00	2.05
Night 14	0.39	3.27	4.29	0.40	3.13	3.18
Day 15	0.37	3.30	4.42	0.35	3.72	3.17
Night 15	0.37	3.34	3.22	0.40	3.37	2.42
Day 16	0.44	3.40	3.74	0.51	3.53	2.14
Night 16	0.36	2.66	3.25	0.32	2.62	1.95
Day 17	0.41	3.10	4.39	0.52	3.58	3.10
Night 17	0.36	3.04	3.99	0.43	3.22	3.30
Day 18	0.35	2.69	5.07	0.43	3.17	6.02

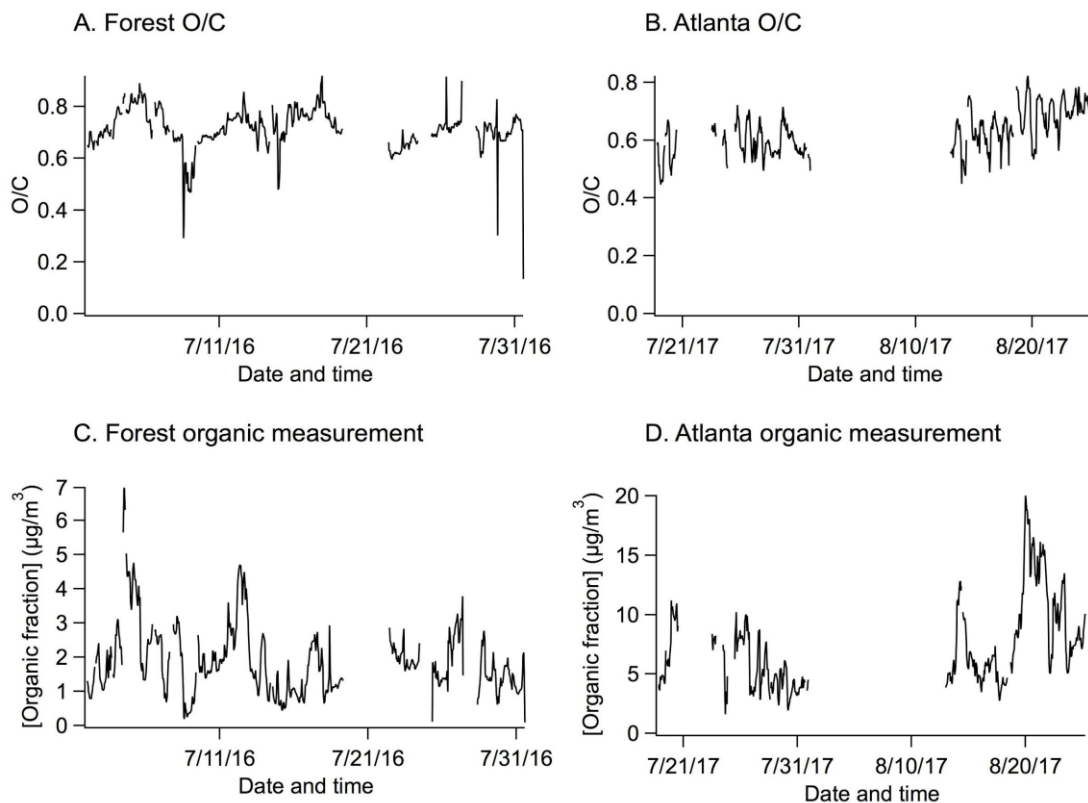


**Figure S4.** Hourly AMS data from the forest and Atlanta, showing O/C (A-B) and the concentration of the organic components (C-D) throughout each field campaign.

### S3. Molecular-level speciation reveals extensive temporal variability in OA composition

Comparisons of consecutive samples and samples collected at similar times (e.g. all daytime, all nighttime) show significant temporal compositional variability (Figures 2, S5, S6), despite similar bulk mixture properties across each field campaign (Figures S2-S3, S10-S11). Consecutive samples, which may be expected to share many of their products due to the long atmospheric lifetime of OA, exhibit significant compositional variability across days and nights, with  $67 \pm 9\%$ ,  $65 \pm 13\%$ ,  $69 \pm 7\%$  distinct samples in the forest, Atlanta, and New York City, respectively.

Figures 2, S5, and S6 highlight the significant sample-to-sample compositional variability observed across all three field campaigns. The distinct compounds observed represent a significant portion of the OA mass (that was able to ionizable via ESI), as shown in Figure S6b (for the Atlanta field campaign). On average, across the three campaigns, distinct compounds represent  $59 \pm 17\%$  of the mass observed on each filter sample for consecutive sample comparisons. Additional visualizations of compositional variability are shown with Van Krevelen diagrams and overlaid average mass spectra for select samples in Figures S7-S9.

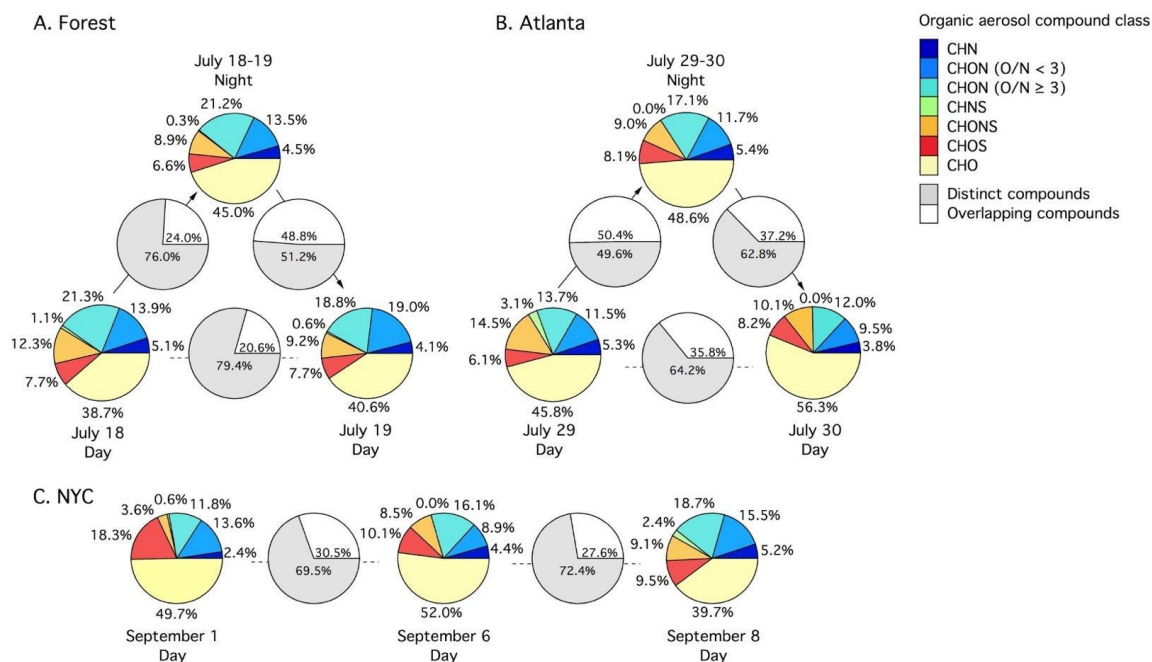


**Figure S5.** Individual sample-to-sample comparisons show that the majority of compounds in consecutive samples are distinct. The colored pie charts show the elemental composition of each sample, while the grey and white pie charts show the percentage of compounds that are distinct (grey) or overlapping (white) for each comparison.

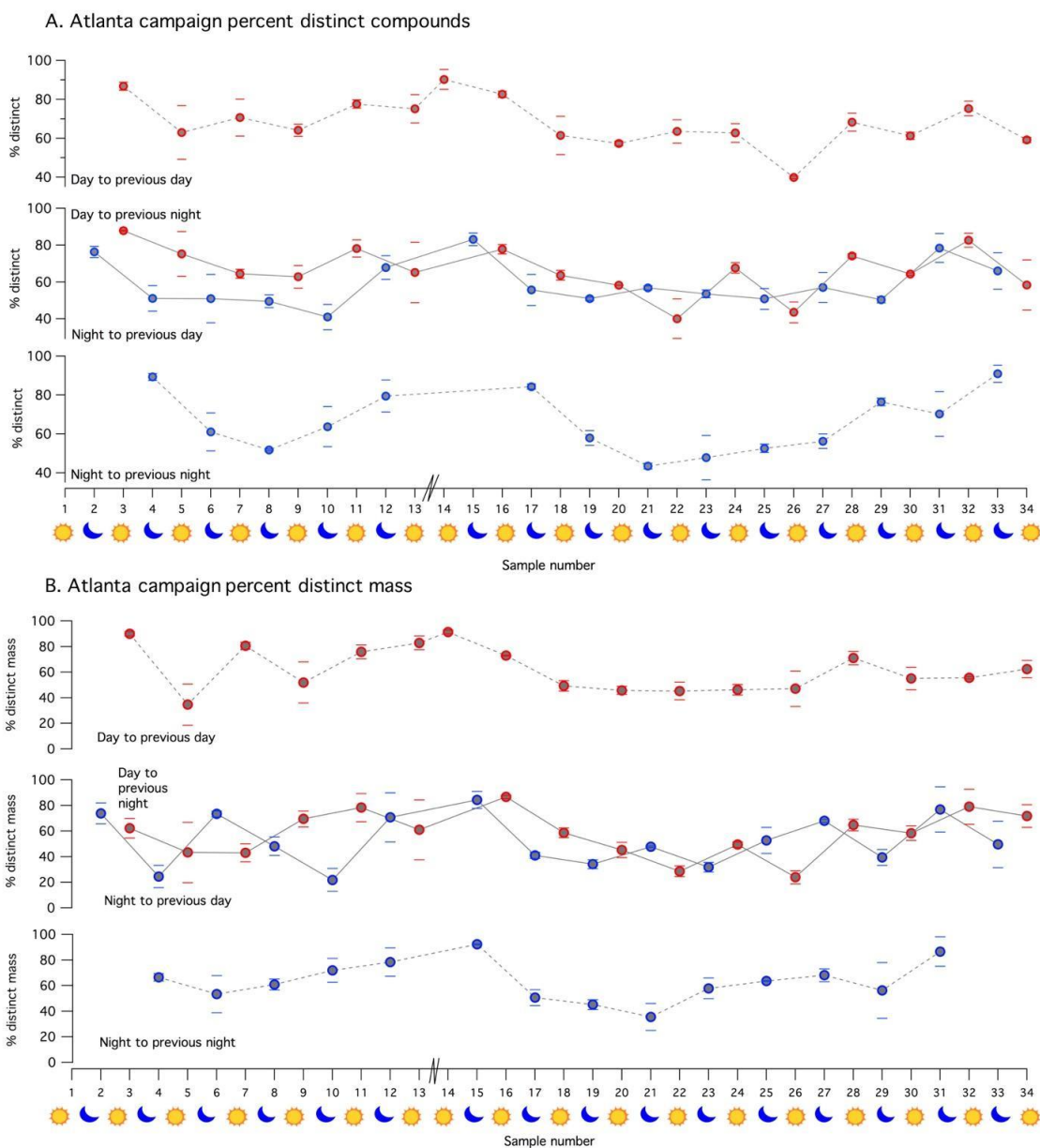


**Figure S6.** Average OA compositional variability (shown as percent distinct compounds) for the Atlanta campaign (A) and average abundance of all distinct compounds in each sample-to-sample comparison (B). The majority of compounds in each sample-to-sample comparison are distinct, and these compounds represent a significant portion of the mass in each sample. In both panels, line markers above each point represent the fraction of distinct compounds with respect to each individual sample in the comparison, while circular markers represent the average between the two.

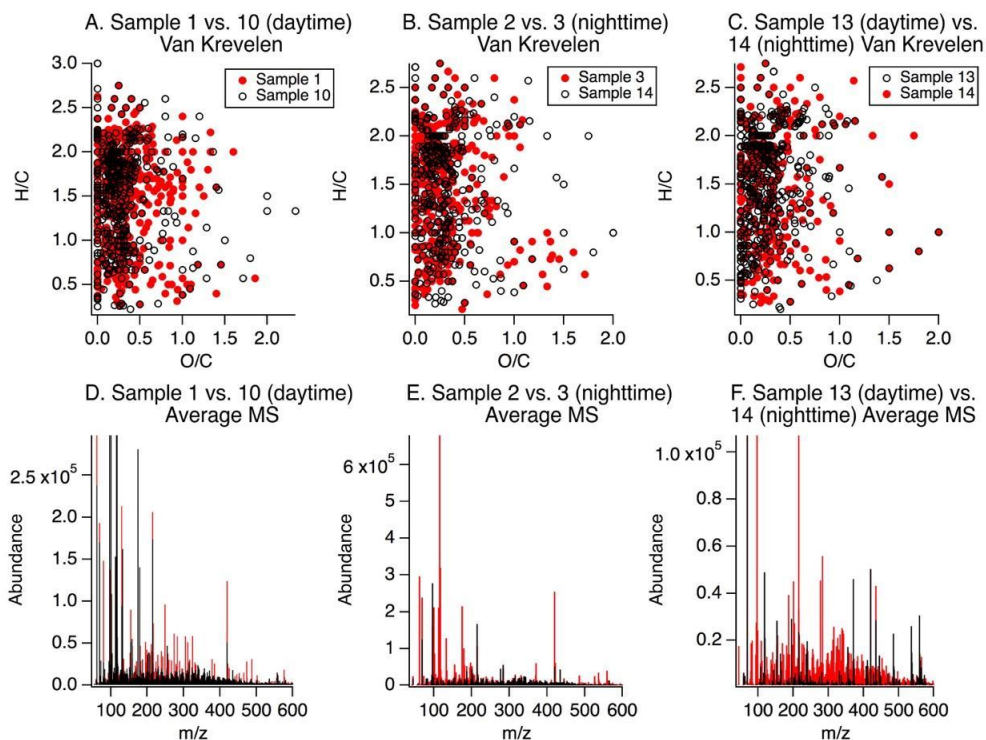


**Figure S7.** Van Krevelen diagrams and overlaid mass spectra for three sample comparisons at the forested site. Two daytime samples (A, D), two nighttime samples (B, E) and one daytime and one nighttime sample (C, F) are shown here to illustrate the observed compositional variability. These sample-to-sample comparisons yield 65% distinct compounds (Sample 1 vs. 10, panels A and D), 68% distinct compounds (Sample 2 vs. 3, panels B and E), and 66% distinct compounds (Sample 13 vs. 14, panels C and E). Comparisons in A and D are included in “All days”, B and E in “All nights”, and C and F in “All consecutive” in Figure 2A.

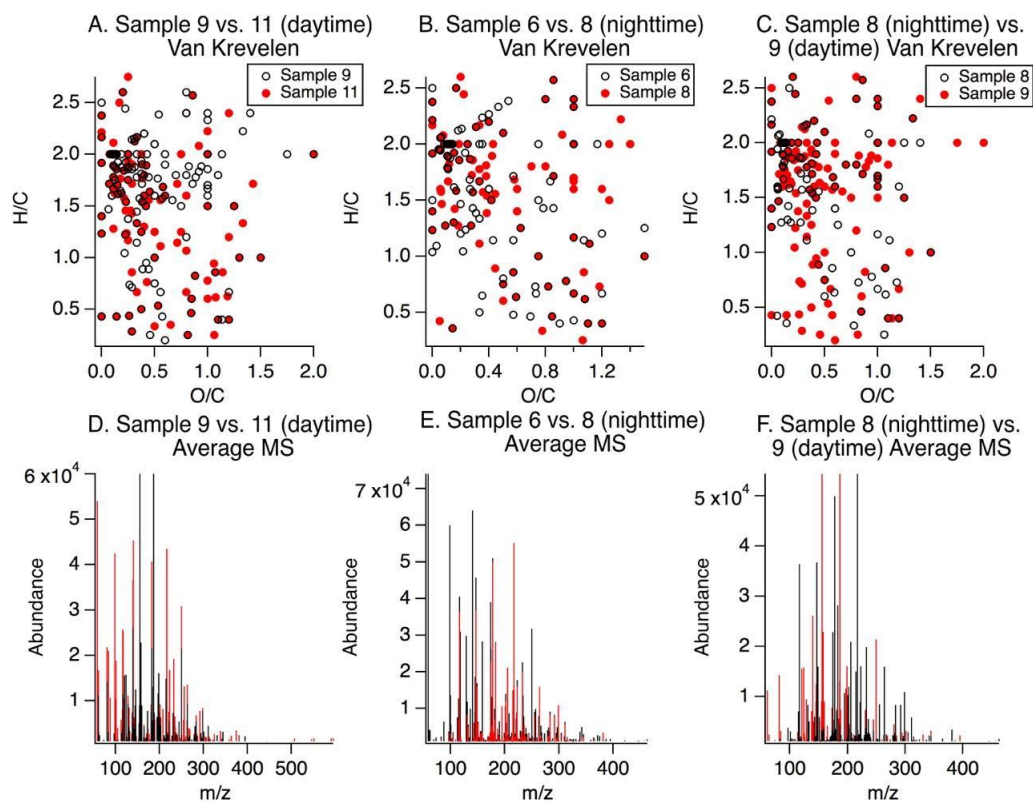


**Figure S8.** Van Krevelen diagrams and overlaid mass spectra for three sample comparisons at the Atlanta site. Two daytime samples (A, D), two nighttime samples (B, E) and one daytime and one nighttime sample (C, F) are shown here to illustrate the observed compositional variability. These sample-to-sample comparisons yield 78% distinct compounds (Sample 9 vs. 11, panels A and D), 52% distinct compounds (Sample 6 vs. 8, panels B and E), and 63% distinct compounds (Sample 8 vs. 9, panels C and E). Comparisons in A and D are included in both “All days” and “All consecutive days”, B and E in both “All nights” and “All consecutive nights”, and C and F in both “All consecutive” and “All consecutive nights to days” in Figure 2A.

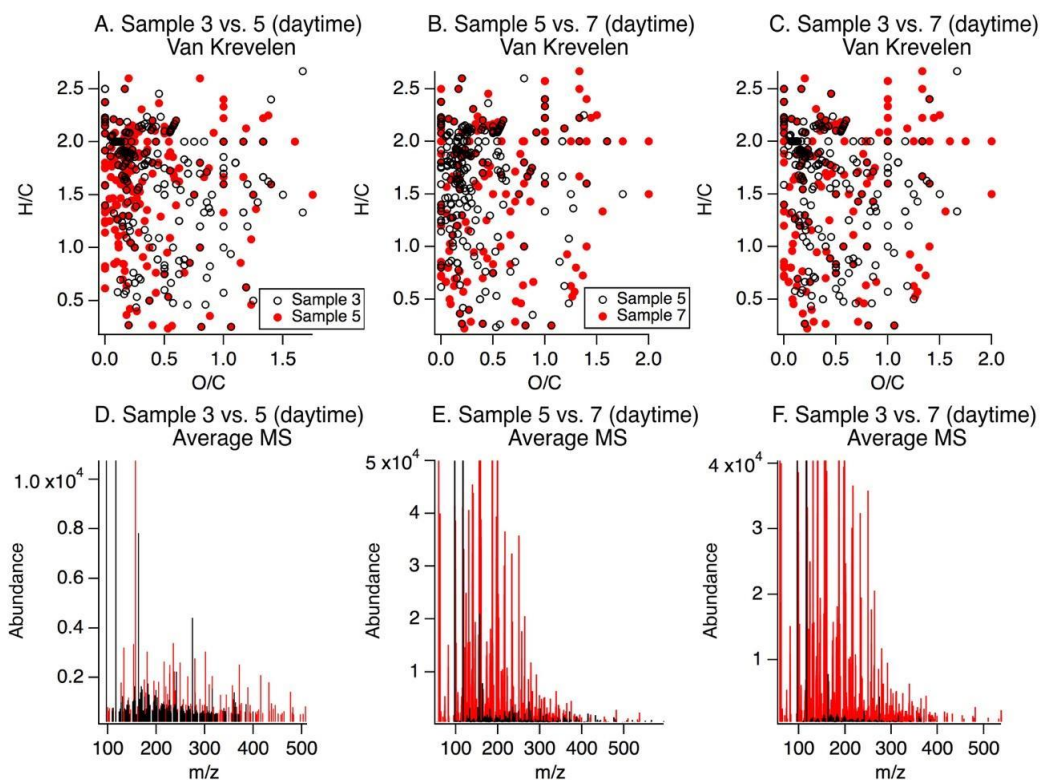


**Figure S9.** Van Krevelen diagrams and overlaid mass spectra for three sample comparisons at the New York City site. Two daytime samples (A, D), two nighttime samples (B, E) and one daytime and one nighttime sample (C, F) are shown here to illustrate the observed compositional variability. These sample-to-sample comparisons yield 72% distinct compounds (Sample 3 vs. 5, panels A and D), 69% distinct compounds (Sample 5 vs. 7, panels B and E), and 73% distinct compounds (Sample 3 vs. 7, panels C and E). Comparisons in A and D as well as B and E are included in “All days” and “All consecutive days”, and C and F in “All days” in Figure 2A.

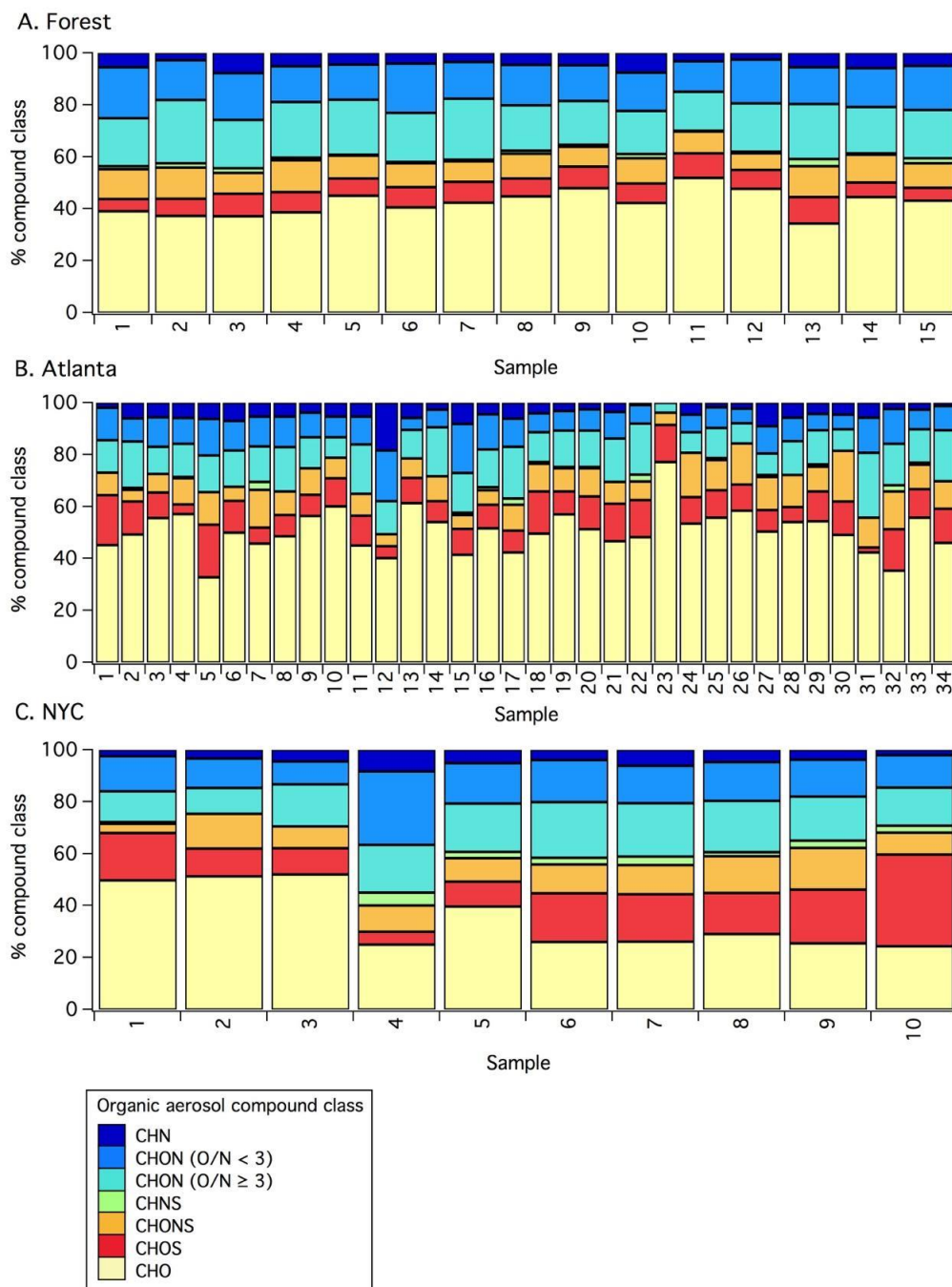


**Figure S10.** Elemental composition for all samples across each field site, reported by unweighted number count. CH and CHS compounds are omitted from this analysis, as they are not readily ionized by the electrospray source.

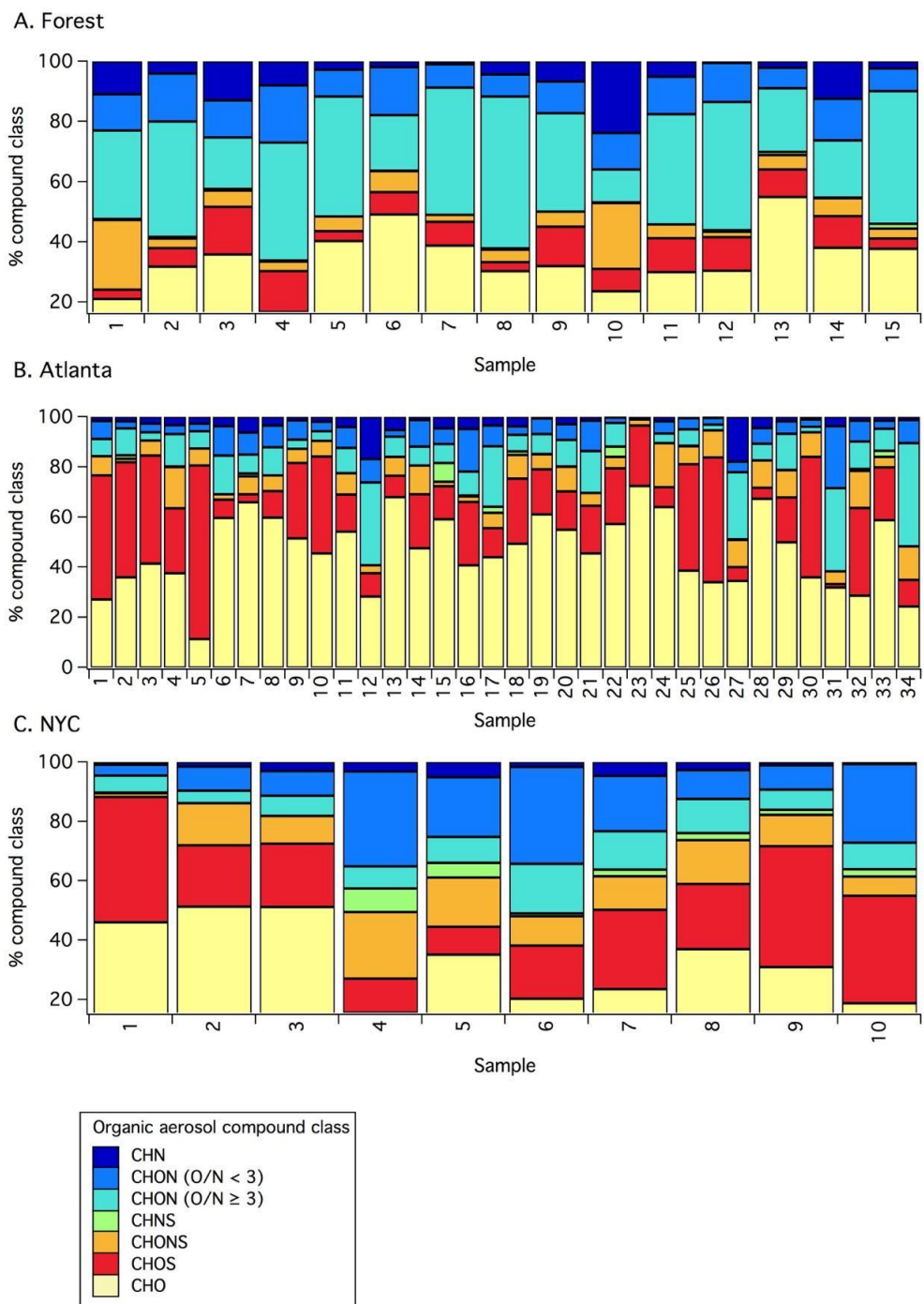


**Figure S11.** Elemental composition for all samples across each field site, weighted by abundance, exhibits more variability than the unweighted version (Figure S7). CH and CHS compounds are omitted from this analysis, as they are not readily ionized by the electrospray source.

A large fraction of the compounds observed did not repeat in multiple samples, as shown in Figure S12. This trend was observed across the three field studies discussed in this work, once again illustrating the significant sample-to-sample variability presented in Figure 2. Despite this variability, we observe several prominent molecular formulas spread across multiple isomers, corresponding to common monoterpene and isoprene oxidation products observed in previous field and laboratory studies (observed at the forest and in Atlanta),<sup>3-6</sup> as well as anthropogenic SOA tracers commonly observed in the particle phase (observed in New York City),<sup>7-9</sup> shown in Table S3.

Tracking individual isomers across each field campaign, we observe compounds with isomers in sets of 8 or fewer (i.e. with 8 or fewer distinct retention times), with the majority of compounds detected in sets of 3 or fewer (Figure S13).

The variability in Figure S12 shows that some markers of oxidized organic aerosol do not appear in all samples. This could be due to variations in the isomers present for a general source (i.e. monoterpene SOA) or relatively minimal presence of a source factor below the LOD, which is consistent with AMS source apportionment studies with positive matrix factorization (PMF). While there are clear diurnal patterns in PMF factors like IEPOX-OA in past studies, minima in the IEPOX-OA factor with very low contributions were reported over multi-day periods during the summer.<sup>10,11</sup> Additionally, there is significant variability in the relative contributions of each of the three reported PMF factors from the forest campaign (Figure S14). This variability can be partially attributed to environmental conditions—even for the relatively simple molecule isoprene, a diversity of

oxidation products (including oligomers) have been observed with a strong dependence on chemical-physical conditions (i.e. aerosol liquid water content; pH; oxidant; sulfate/nitrate, and  $\text{NO}_x$  concentrations) and yields that vary from 1% to 50% with these conditions across a range of structural isomers.<sup>12–15</sup>

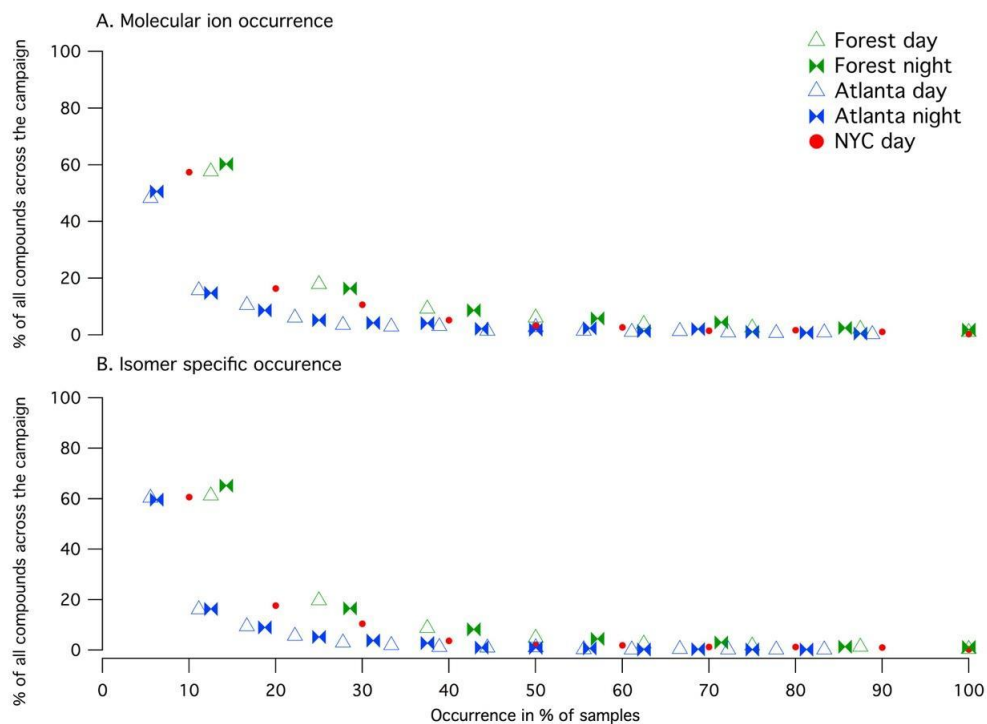


**Figure S12.** Many of the analytes observed at each of the 3 field sites do not reappear across multiple samples, yet the frequency patterns are similar across all 3 sites. Distribution plots are shown here for both (A) molecular ion occurrence and (B) isomer-specific occurrence. Individual compounds were tracked across all samples for each field campaign (in (A), molecular formulas were tracked, not accounting for isomers; in (B), both molecular formulas and retention times were tracked to account for isomers). The number of samples in which a compound was observed was counted for each field campaign, and is shown as a fraction of the total samples collected at each campaign on the x-axis. Each campaign has a different total number of samples, so points do not necessarily align on the x-axis. Percentages are displayed as a number count, where the steep decrease of occurrence towards 0% indicates that fewer and fewer compounds are present in most samples.

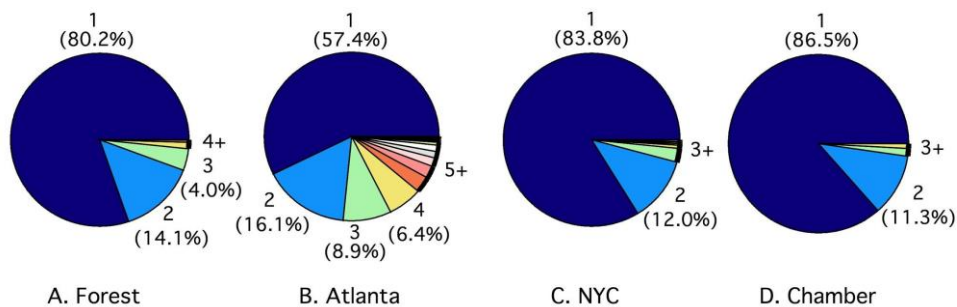


**Figure S13.** Tracking isomers across each field campaign, most compounds above LOD thresholds were detected as a single isomer. Compounds with multiple isomers most frequently have 3 isomers or fewer. Compounds with up to 8 isomers were observed in all 3 field sites, though these contributed minimally to the total number of compounds observed.

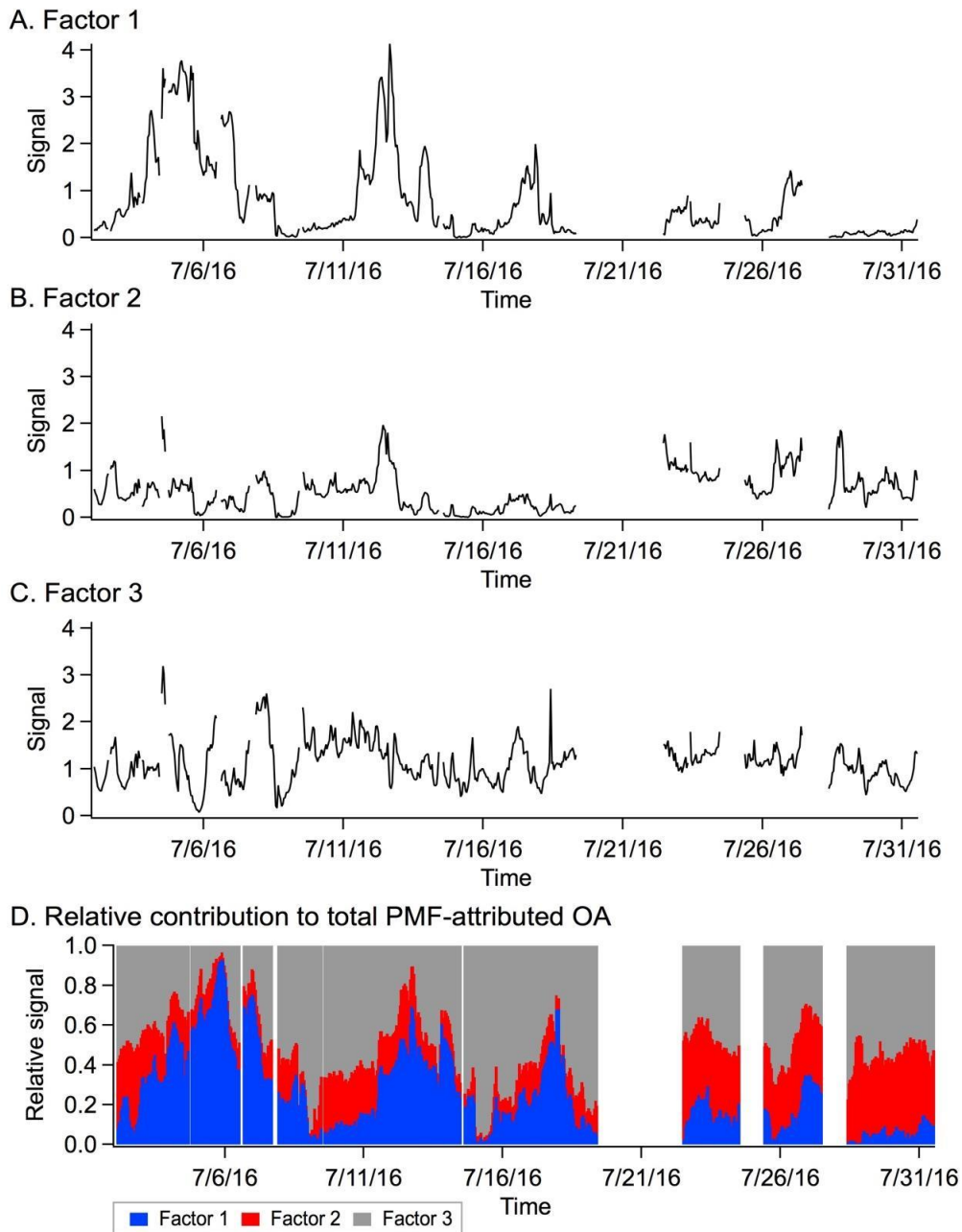


**Figure S14.** 1-hour averaged AMS PMF factors from the forest site (A-C) show variability in their relative contribution to total PMF-attributed OA across the campaign, with the relative importance of individual factors becoming very low for hours to days throughout the sampling period (D). Factors represent more oxidized oxygenated OA (factor 1), IEPOX-derived OA (factor 2), and monoterpene-derived OA (factor 3). Additional OA compositional variability can be expected within each of the statistically-derived PMF source factors.

**Table S3.** Top 10 most prominent biogenic and anthropogenic target species observed at the forested site, in Atlanta, and in New York City. Other notable target compounds

observed include common markers of isoprene and monoterpene oxidation, such as methyltetrols<sup>f,a</sup>, methylglyceric acid<sup>a,n</sup>, pinonic acid<sup>f</sup>, pinic acid<sup>f,a,n</sup>, norpinic acid<sup>f,a,n</sup>, and 3-methyl-1,2,3-butanetricarboxylic acid (MBTCA)<sup>f,a,n</sup> (and their isomers).

Site	Sample time	Formula	Number of isomers observed	% samples with molecular ion occurrence	Source (with past observations)
Forest	Day	C <sub>14</sub> H <sub>26</sub> O <sub>4</sub>	2	100	Monoterpenes <sup>5</sup>
Forest	Day	C <sub>18</sub> H <sub>34</sub> O <sub>4</sub>	4	100	Monoterpenes <sup>5</sup>
Forest	Night	C <sub>12</sub> H <sub>24</sub> O <sub>3</sub>	3	100	Monoterpenes <sup>5</sup>
Forest	Night	C <sub>13</sub> H <sub>25</sub> NO <sub>3</sub>	2	100	Monoterpenes <sup>5</sup>
Forest	Night	C <sub>14</sub> H <sub>24</sub> O <sub>5</sub>	2	100	Monoterpenes <sup>4</sup>
Forest	Night	C <sub>16</sub> H <sub>30</sub> O <sub>4</sub>	1	100	Monoterpenes <sup>5</sup>
Forest	Day	C <sub>10</sub> H <sub>16</sub> O	3	87.5	Monoterpenes <sup>5</sup>
Forest	Night	C <sub>10</sub> H <sub>18</sub> O <sub>3</sub>	3	85.7	Monoterpenes <sup>5</sup>
Forest	Night	C <sub>11</sub> H <sub>20</sub> O <sub>3</sub>	1	85.7	Monoterpenes <sup>5</sup>
Forest	Night	C <sub>9</sub> H <sub>16</sub> O <sub>4</sub>	1	85.7	Monoterpenes <sup>5</sup>
Atlanta	Night	C <sub>14</sub> H <sub>28</sub> O <sub>2</sub>	4	75	Monoterpenes <sup>5</sup>
Atlanta	Night	C <sub>5</sub> H <sub>12</sub> O <sub>4</sub>	2	75	Isoprene <sup>3</sup>
Atlanta	Day	C <sub>14</sub> H <sub>28</sub> O <sub>2</sub>	5	72.2	Monoterpenes <sup>5</sup>
Atlanta	Night	C <sub>10</sub> H <sub>16</sub> O <sub>6</sub>	4	68.8	Monoterpenes <sup>5</sup>
Atlanta	Night	C <sub>8</sub> H <sub>12</sub> O <sub>6</sub>	8	68.8	Monoterpenes <sup>5</sup>
Atlanta	Night	C <sub>9</sub> H <sub>14</sub> O <sub>4</sub>	6	68.8	Monoterpenes <sup>5</sup>
Atlanta	Night	C <sub>9</sub> H <sub>16</sub> O <sub>4</sub>	4	68.8	Monoterpenes <sup>5</sup>
Atlanta	Day	C <sub>13</sub> H <sub>25</sub> NO <sub>2</sub>	4	66.7	Monoterpenes <sup>5</sup>
Atlanta	Day	C <sub>16</sub> H <sub>32</sub> O <sub>2</sub>	5	66.7	Monoterpenes <sup>5</sup>
Atlanta	Night	C <sub>9</sub> H <sub>16</sub> O <sub>3</sub>	4	62.5	Monoterpenes <sup>5</sup>
NYC	Day	C <sub>5</sub> H <sub>8</sub> O <sub>5</sub>	3	70	Toluene <sup>7</sup>
NYC	Day	C <sub>8</sub> H <sub>6</sub> O <sub>4</sub>	6	70	PAH <sup>7</sup>
NYC	Day	C <sub>4</sub> H <sub>8</sub> O <sub>4</sub>	2	60	Isoprene <sup>7</sup>
NYC	Day	C <sub>9</sub> H <sub>8</sub> O <sub>4</sub>	3	50	PAH <sup>7</sup>
NYC	Day	C <sub>8</sub> H <sub>4</sub> O <sub>3</sub>	3	30	PAH <sup>8</sup>
NYC	Day	C <sub>10</sub> H <sub>7</sub> NO <sub>4</sub>	1	20	PAH <sup>9</sup>
NYC	Day	C <sub>6</sub> H <sub>5</sub> NO <sub>3</sub>	1	20	Nitroaromatic <sup>7</sup>
NYC	Day	C <sub>6</sub> H <sub>5</sub> NO <sub>4</sub>	1	20	Nitroaromatic <sup>7</sup>
NYC	Day	C <sub>7</sub> H <sub>7</sub> NO <sub>4</sub>	2	20	Nitroaromatic <sup>7</sup>
NYC	Day	C <sub>10</sub> H <sub>7</sub> NO <sub>3</sub>	1	20	PAH <sup>9</sup>

Notes: <sup>f</sup> Forest field site, <sup>a</sup> Atlanta field site, <sup>n</sup> New York City field site

Distinct compounds in all sample-to-sample comparisons exist across a range of abundances, volatility bins, and compound classes (Figures 2, S15, S16). While there is a distribution of distinct compounds across volatility bins, SVOCs and ELVOCs tend to dominate (Figures S15a, S16a, Table S4). Distinct compounds exist across a range of abundances, representing compounds across both low and high relative abundance in each sample comparison (Figures S15b, S16b). Distinct compounds fall into a variety of compound classes, typically dominated by CHO compounds (Figures S15c, S16c). However, there is rarely a statistically significant difference between the relative fraction of each compound class with compositional variability (Figure S17).

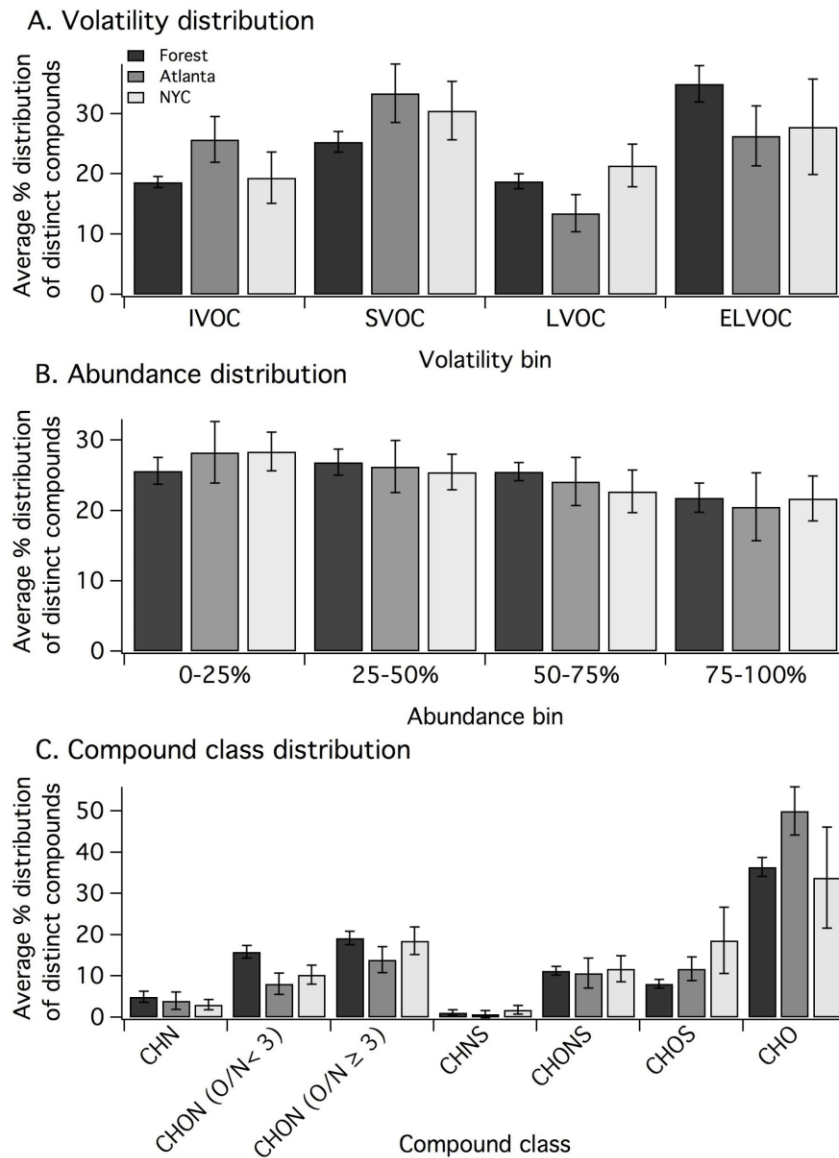


**Figure S15.** Average unweighted distribution of distinct compounds from each sample-to-sample comparison, separated by field campaign.

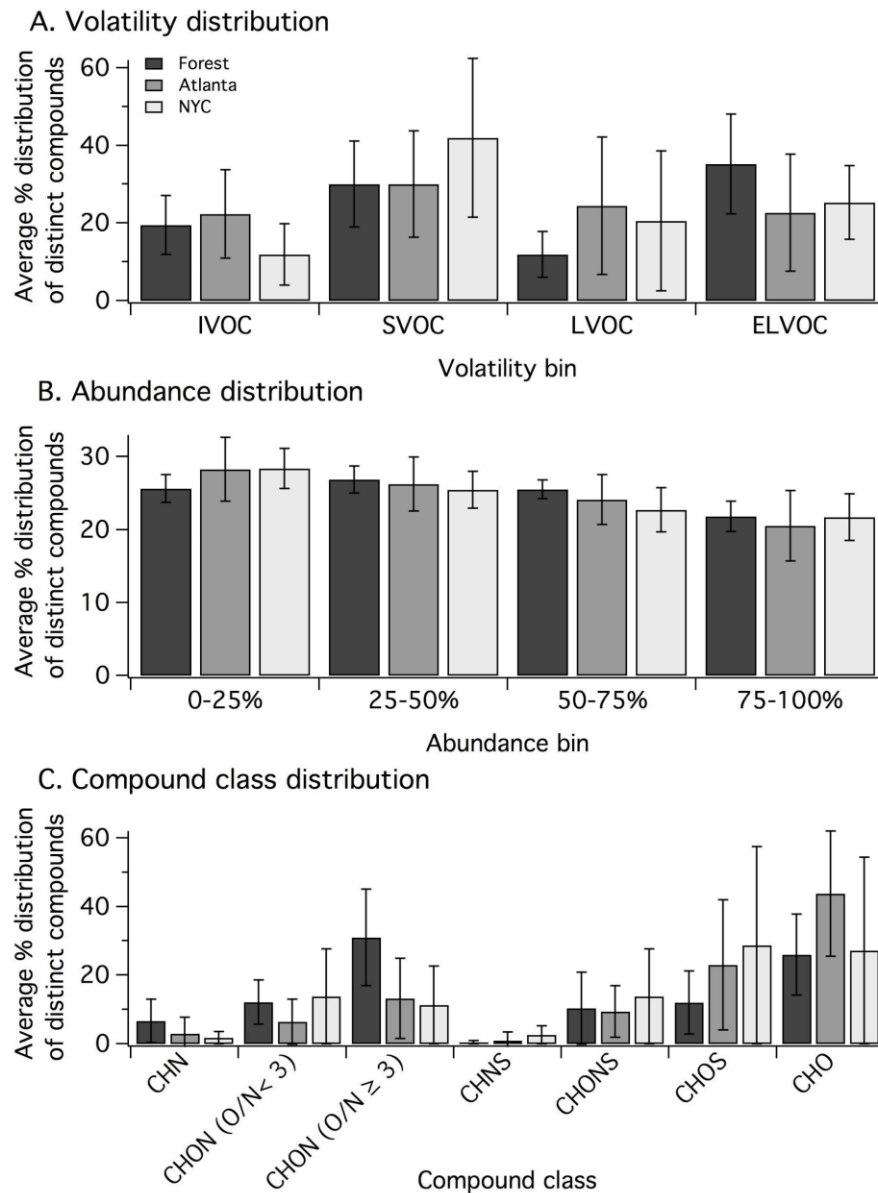


**Figure S16** Average distribution of distinct compounds from each sample-to-sample comparison, separated by field campaign, weighted by abundance (A and C).

**Table S4.** Fraction of distinct compounds falling in each volatility bin. A small contribution from VOCs is omitted here ( $\leq 2\%$ , likely fragments).

<u>Forest</u>	Number % of distinct compounds	Mass % of distinct compounds (unweighted)	Mass % of distinct compounds (weighted)
IVOC	19 ± 1	18 ± 2	21 ± 5
SVOC	25 ± 2	29 ± 8	25 ± 5
LVOC	19 ± 1	12 ± 3	14 ± 5
ELVOC	35 ± 3	39 ± 9	37 ± 10
<u>Atlanta</u>	Number % of distinct compounds	Mass % of distinct compounds (unweighted)	Mass % of distinct compounds (weighted)
IVOC	26 ± 4	22 ± 8	24 ± 10
SVOC	33 ± 5	31 ± 9	33 ± 12
LVOC	14 ± 3	26 ± 13	25 ± 15
ELVOC	26 ± 5	20 ± 8	18 ± 9
<u>NYC</u>	Number % of distinct compounds	Mass % of distinct compounds (unweighted)	Mass % of distinct compounds (weighted)
IVOC	19 ± 4	13 ± 7	13 ± 5
SVOC	31 ± 5	40 ± 2	47 ± 18
LVOC	21 ± 4	22 ± 1	20 ± 14
ELVOC	28 ± 8	24 ± 4	20 ± 5

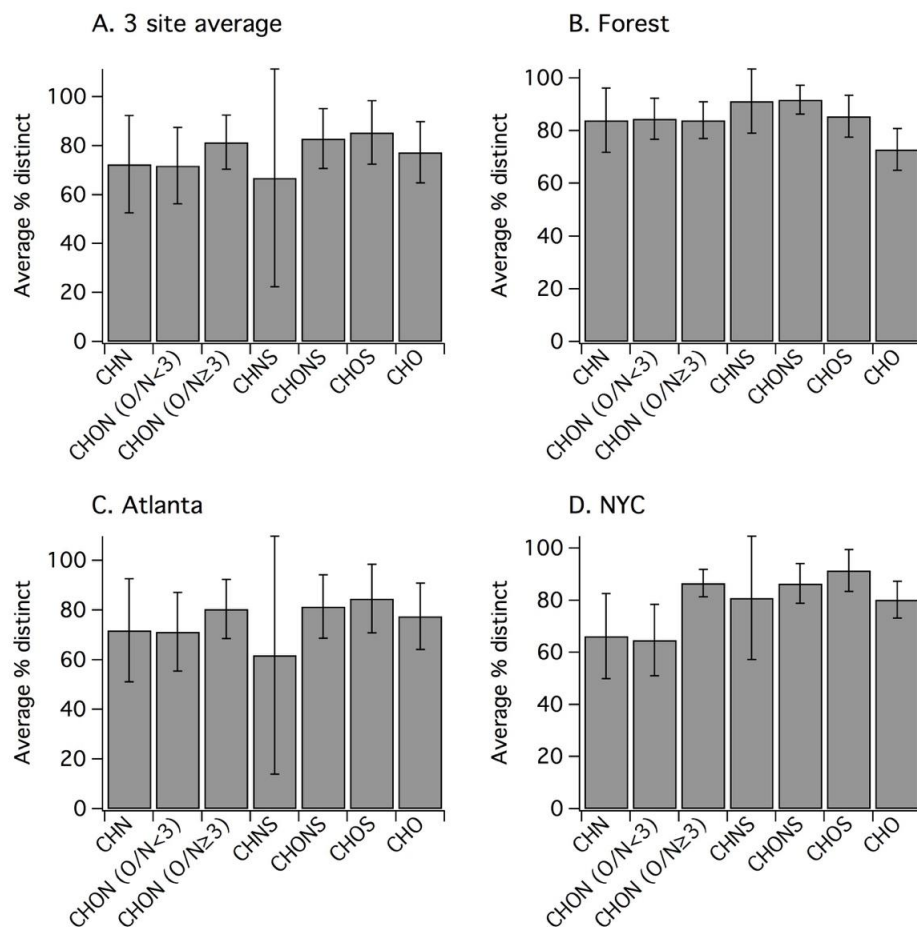


**Figure S17.** The relative occurrence of compositional variability is statistically-similar across all compound classes. Panels A-D show the average fraction of each compound class that is distinct, for all sample-to-sample comparisons across the three field campaigns. Error bars represent 1 standard deviation from the mean. There is rarely a statistically significant difference between the relative occurrence of distinct compounds in each compound class.

A sensitivity analysis was performed to evaluate the effect of instrument/method LODs on the results of the sample-to-sample comparisons presented in this study. The height threshold was varied with volume at its base case threshold (100,000 counts), as well as with no initial volume threshold. In addition, the volume threshold was varied with height at its base case threshold (15,000 counts), as well as with no initial height threshold.

Finally, height and volume were varied together. Sample-to-sample compositional variability results varied by less than 6.5% in all cases (Figures 3, S18), indicating that the results of the sample-to-sample comparisons here are not sensitive to the LOD thresholds that were implemented in this study.

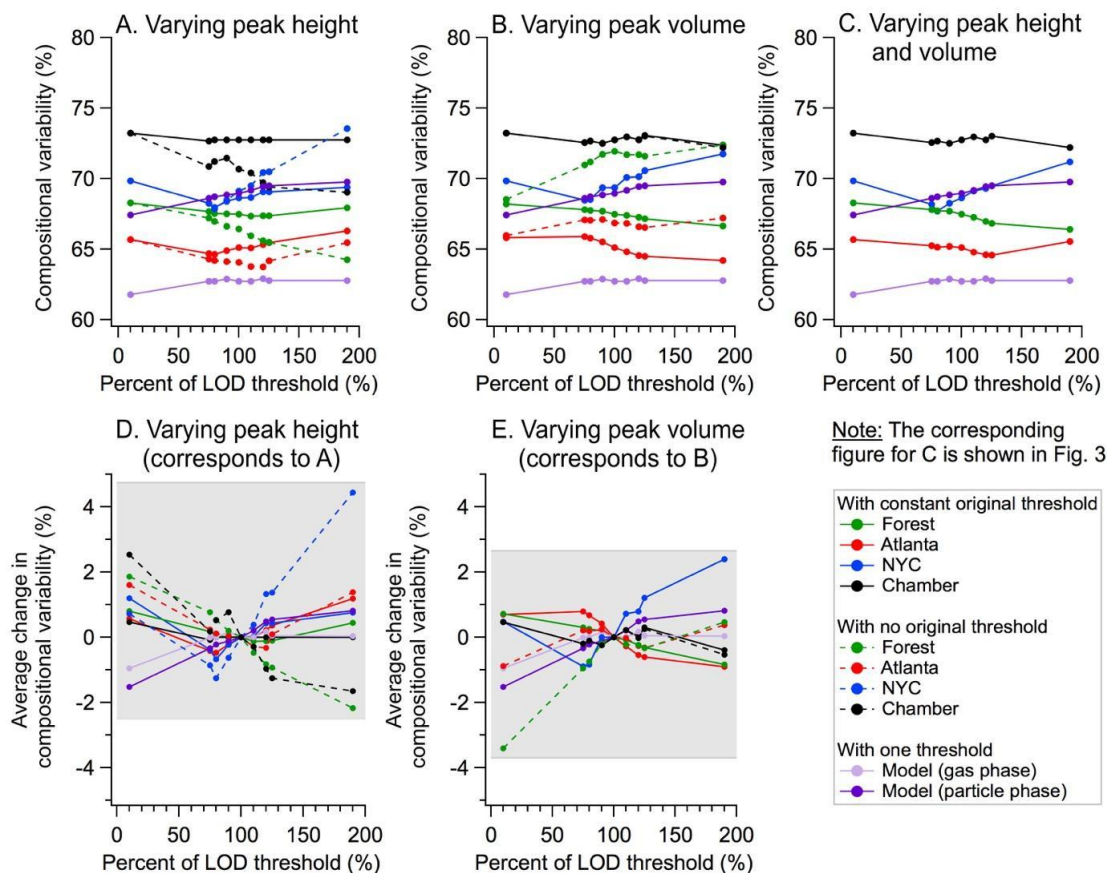


**Figure S18.** A sensitivity analysis performed for ambient, chamber, and model results by varying the LOD thresholds by  $\pm 10\%$ ,  $20\%$ ,  $25\%$ , and  $90\%$  shows less than  $4.5\%$  change in the fraction of distinct compounds observed in each sample-to-sample comparison. All consecutive sample-to-sample comparisons were considered for this sensitivity analysis, and average change in compositional variability for each LOD threshold test is presented here. For all ambient and chamber analysis, the base case volume threshold was set to 100,000 counts and the base case height threshold to 15,000 counts. For model analyses, the base case abundance threshold was set to 10,000 molecules/cm<sup>3</sup>. In this analysis, peak height was varied (resulting compositional variability shown in A, and average deviation from the base case in D; both with and without a base peak volume threshold), peak volume was varied (B and D; both with and without a base peak height threshold), and both peak height and volume were varied together (C and Figure 3). Only one abundance threshold was altered for the model data. As a result, the model data presented in A-C is identical, as is the model data presented in D-E and Figure 3. The last time point in each model simulation was used for all model run comparisons. In addition to the data presented here, the model abundance threshold was reduced by 1-3 orders of magnitude and increased by 1-3 orders of magnitude; these changes resulted in less than  $6.6\%$  change in compositional variability (shown in Figure 3).

In addition, we compared LC-ESI-Q-TOF measurements to measurements from other forested sites (other ultra-high resolution MS data and CIMS data), and show that a large fraction of the chemical diversity observed or modeled in this study is inaccessible with the current capabilities of many online MS instruments (Figure 3b). The distribution shown for LC-ESI-Q-TOF in Figure 3b includes all unique species across the forest field campaign (similar to the CIMS mass list presented). The distribution of compounds below 0.5 MS peak half-widths for the LC-ESI-Q-TOF data depends on the number of samples collected and the number of unique compounds detected in the samples (i.e. more compounds detected results in smaller average distance between compound masses). So, the distribution of compounds in any of the 2-sample comparisons in this study would have a smaller fraction of analytes in the 0-0.5 half-width range than the aggregated campaign data.

#### **S4. Potential driving factors explored via field, chamber, and modeling data**

Figure S19 shows the distribution of overlapping compounds in the set of chamber experiments, comparing oxidation products of  $\alpha$ -pinene and  $\beta$ -pinene under two different chemical conditions ( $\text{NO}_3^*$  initiated oxidation, followed by further oxidation by  $\text{NO}_3^*$  or  $\text{HO}_2^*$ ). O/C ratios of products observed in these 4 chamber experiments range from O/C of 0 to O/C of 2, and most overlapping compounds have an O/C <  $\sim 0.5$  (Figure S19).

The overlapping and distinct fractions shown in Figure S19 account for the presence of isomers by comparing both molecular formulas and retention times across samples. A non-isomer specific analysis (i.e. ignoring retention time and considering only

the molecular formula) yields slightly lower distinct fractions between experiments: 69.3% distinct ( $\alpha$ -pinene-HO<sub>2</sub><sup>\*</sup> versus  $\beta$ -pinene-HO<sub>2</sub><sup>\*</sup>), 76.2% distinct ( $\alpha$ -pinene-NO<sub>3</sub><sup>\*</sup> versus  $\beta$ -pinene-NO<sub>3</sub><sup>\*</sup>), 56.1% distinct ( $\alpha$ -pinene-NO<sub>3</sub><sup>\*</sup> versus  $\alpha$ -pinene-HO<sub>2</sub><sup>\*</sup>), and 46.5% distinct ( $\beta$ -pinene-NO<sub>3</sub><sup>\*</sup> versus  $\beta$ -pinene-HO<sub>2</sub><sup>\*</sup>). These experiments (with and without isomer-specific tracking) suggest that altering precursor results in greater compositional variability than altering oxidation conditions. This is consistent with the modeling results shown in Table 1.

The overlapping compounds in Figure S19 have similar abundances; they fall along a 1:1 line, and are often constrained by 2:1 and 1:2 lines (dotted lines above and below 1:1 line, respectively). A similar analysis for two of the modeling experiments does not yield the same trend, and shows an increased abundance for these overlapping compounds for the NO<sub>3</sub><sup>\*</sup> oxidation experiment (Figure S20).

Equivalent simulation time points are compared in all cases for the modeling analysis presented in Table 1 and Figure 4. An additional time point (at 4 hours of simulation time) for the  $\beta$ -pinene NO<sub>3</sub><sup>\*</sup> is included to reach the same equivalent NO<sub>3</sub><sup>\*</sup> exposure as the parallel  $\alpha$ -pinene experiment, and is compared to the final time point of relevant experiments (i.e. at 2 hours of simulation time hours, for comparisons with  $\beta$ -pinene HO<sub>2</sub><sup>\*</sup> and  $\alpha$ -pinene NO<sub>3</sub><sup>\*</sup>, in Table 1, Figure 4, and Figure S20b).

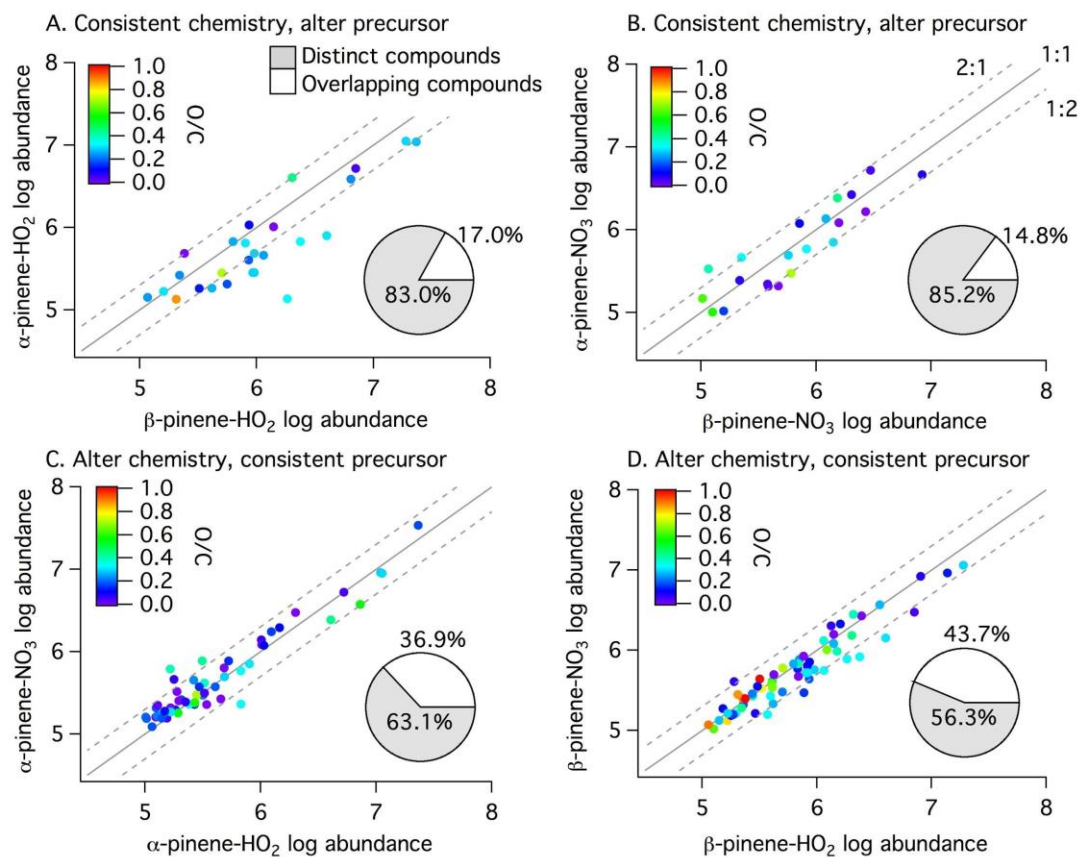


**Figure S19.** Examining chemistry as a driving factor of sample to sample variability in oxidation products. The axes show log abundance for each experiment in question. The following experiments were compared: (A)  $\alpha$ -pinene versus  $\beta$ -pinene with  $\text{HO}_2^*$ -controlled  $\text{RO}_2^*$  fate, (B)  $\alpha$ -pinene versus  $\beta$ -pinene with  $\text{NO}_3^*$ -controlled  $\text{RO}_2^*$  fate, (C)  $\alpha$ -pinene with  $\text{RO}_2^*$  fate controlled by either  $\text{NO}_3^*$  or  $\text{HO}_2^*$ , and (D)  $\beta$ -pinene with  $\text{RO}_2^*$  fate controlled by either  $\text{NO}_3^*$  or  $\text{HO}_2^*$ . Overlapping compounds fall along a 1:1 line, and are often constrained by 2:1 and 1:2 lines (dotted lines above and below 1:1 line, respectively). Pie charts represent the fraction of overlapping (white) and distinct (grey) compounds between each set of experiments. Markers are colored by O/C.

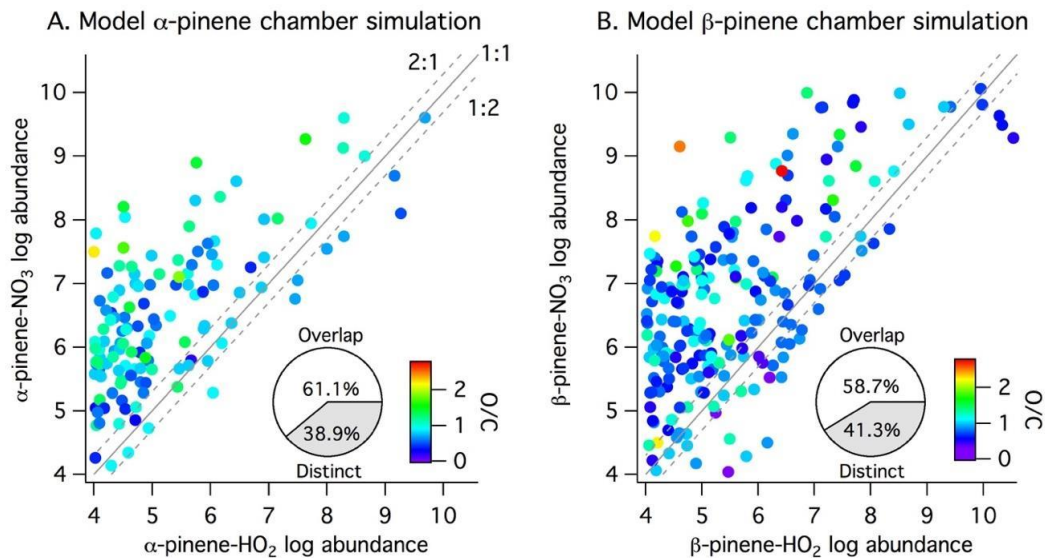


**Figure S20.** Examining chemistry as a driving factor of sample to sample variability in oxidation products through GECKO-A modeling. The axes show log abundance for each experiment in question. Initial particle-phase composition was compared (i.e. before any particle-phase chemistry occurs, as this chemistry is excluded from GECKO-A), using the final simulation time point for each experiment. The following chamber simulation experiments were compared: (A)  $\alpha$ -pinene with RO<sub>2</sub><sup>\*</sup> fate controlled by either NO<sub>3</sub><sup>\*</sup> or HO<sub>2</sub><sup>\*</sup>, and (B)  $\beta$ -pinene with RO<sub>2</sub><sup>\*</sup> fate controlled by either NO<sub>3</sub><sup>\*</sup> or HO<sub>2</sub><sup>\*</sup>. Overlapping compounds generally fall above the 1:1 line here, and are more abundant as products of the NO<sub>3</sub><sup>\*</sup> oxidation experiment. Pie charts represent the fraction of overlapping and distinct compounds between each set of experiments. Markers are colored by O/C.

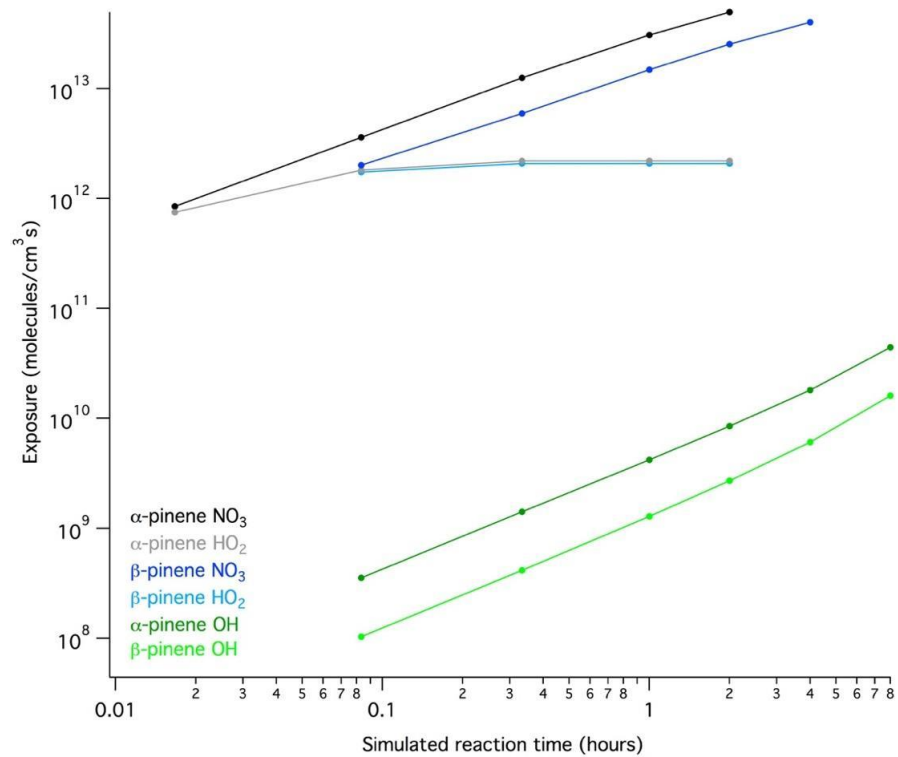


**Figure S21.** Correlation between simulated reaction time and equivalent oxidant exposure (OH<sup>•</sup> exposure for experiments denoted as  $\alpha$ - or  $\beta$ -pinene OH above, or NO<sub>3</sub><sup>•</sup> exposure, for experiments denoted as  $\alpha$ - or  $\beta$ -pinene NO<sub>3</sub> or HO<sub>2</sub> above).

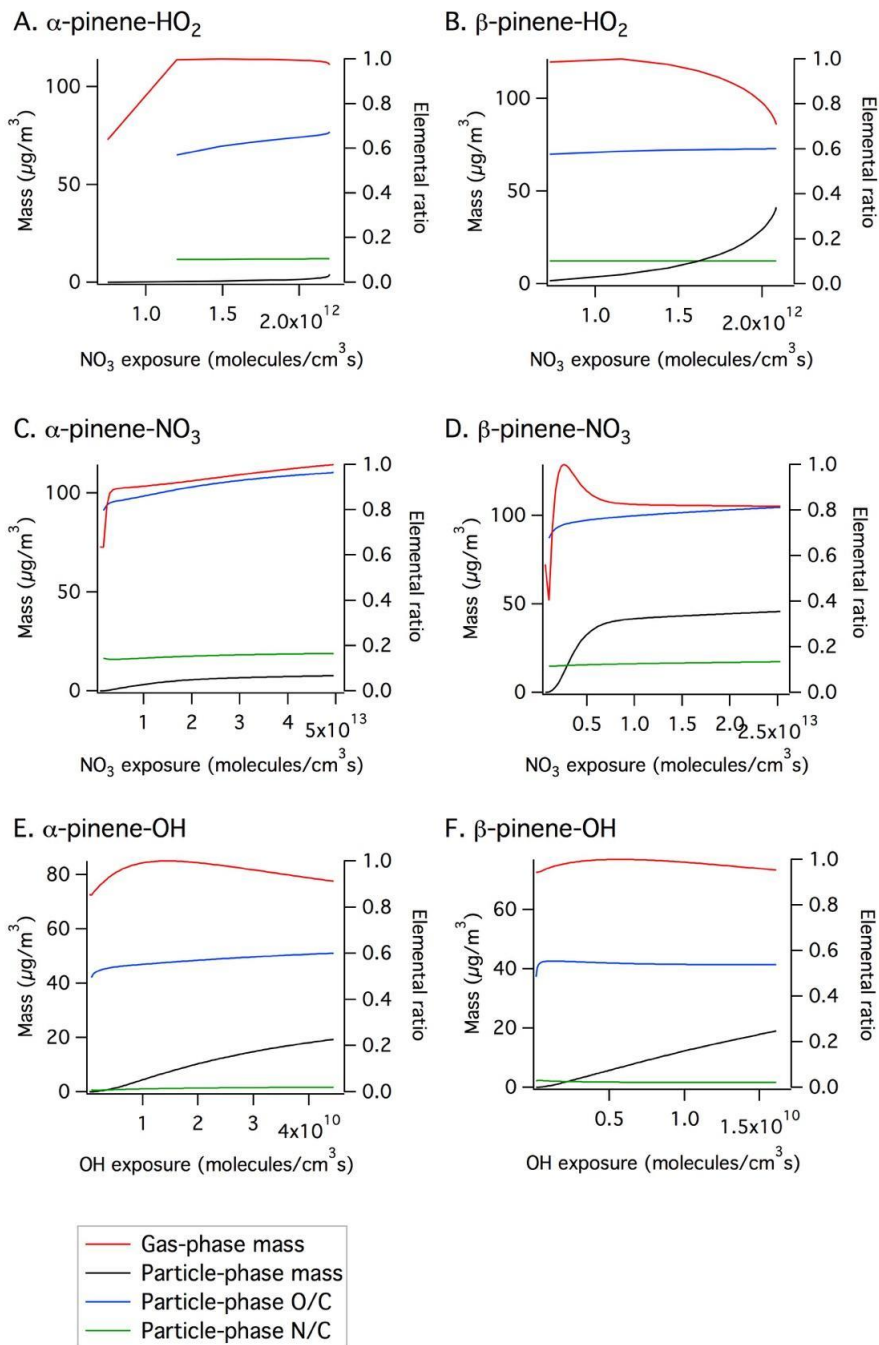


**Figure S22.** Evolution of gas and particle phase compounds ( $\#C > 1$ ) for each modeling experiment using GECKO-A. Panels A-D represent the chamber simulation (i.e. with  $\text{NO}_3^\bullet$  or  $\text{HO}_2^\bullet$  oxidation), while E-F represent the forest (ambient) simulation (i.e. OH oxidation).

A subset of the compounds observed in each chamber experiment discussed here were also observed in the forest and in Atlanta, and exist across a range of O/C and H/C ratios (Figure

S23). These two sites were chosen for comparison with the chamber data because of the prominence of BVOC precursors, particularly  $\alpha$ - and  $\beta$ -pinene, at both locations. For  $\alpha$ -pinene- $\text{HO}_2^\bullet$  experiments, 13.5% of compounds were observed in the forest samples, on average (daytime and nighttime), and only 4% were observed in the Atlanta samples. For  $\alpha$ -pinene- $\text{NO}_3^\bullet$  experiments, 9.5% of compounds were observed in the forest samples, on average, with only 3% of compounds observed in the Atlanta samples. For  $\beta$ -pinene- $\text{HO}_2^\bullet$  experiments, 12% of compounds were observed in the forest samples, on average, with 5.5% observed in the Atlanta samples. For  $\beta$ -pinene- $\text{NO}_3^\bullet$  experiments, 18% of compounds were observed in the forest samples, on average, and 9.5% of compounds were observed in the Atlanta samples.

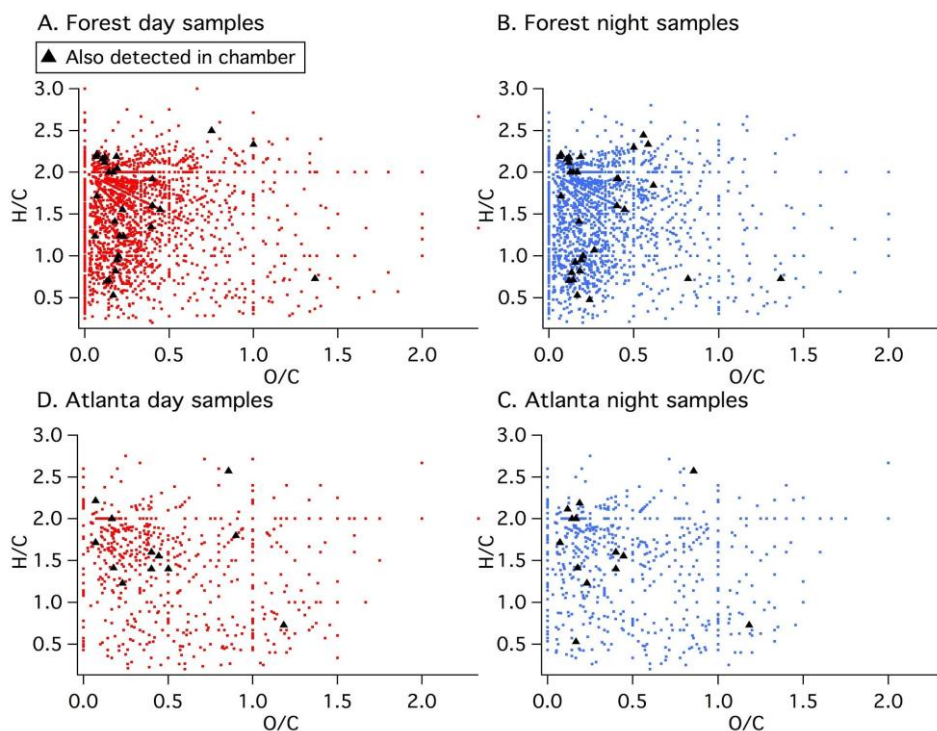


**Figure S23.** Intercomparison of chamber experiments with forest and Atlanta field sites, where BVOC precursors are prominent.

Additional comparisons were made between all samples at each field site, with associated changes in temperature, relative humidity, wind speed, wind direction, and AMS organic and inorganic concentrations, where data were available. Little correlation exists between changes in these factors and the observed chemical compositional variability (Figure S24).

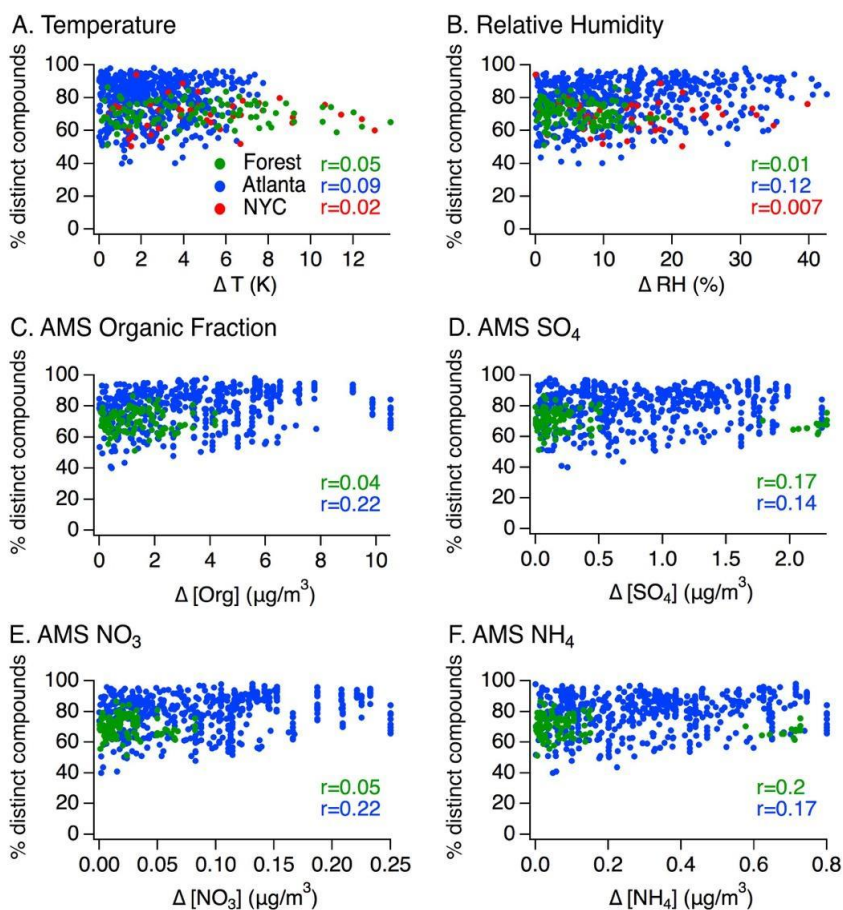


**Figure S24.** A study of compositional variability with respect to changes in meteorological and chemical conditions, where data were available, shows minimal correlation between the compositional variability observed and the meteorological and chemical conditions studied. Temperature and relative humidity (panels A and B) are averaged across the last 6 hours of HYSPLIT backward trajectories for each sample. Wind direction is considered via a more thorough backward trajectory analysis, discussed below and shown in Figure S25 and S26. AMS data are shown in panels C-F because they better represent the concentrations of the ions shown for a longer period of time than local gas-phase concentrations.

## S5. Potential driving factors explored via backward trajectory analysis

To evaluate the similarity between air parcels impacting each field site, we ran 24-hour HYSPLIT models for each daytime and nighttime sample, with backward trajectories computed every hour for the duration of each sample. A final height of 50 m above ground level was selected to compute each trajectory, and only trajectory points below 1 km in height were considered. Trajectory points were grouped into 20 km latitude by 20 km longitude bins. Figure S25 shows the degree of backward trajectory similarity at each of the 3 field sites. In general, backward trajectories are similar close to the site, and differ more significantly with distance.

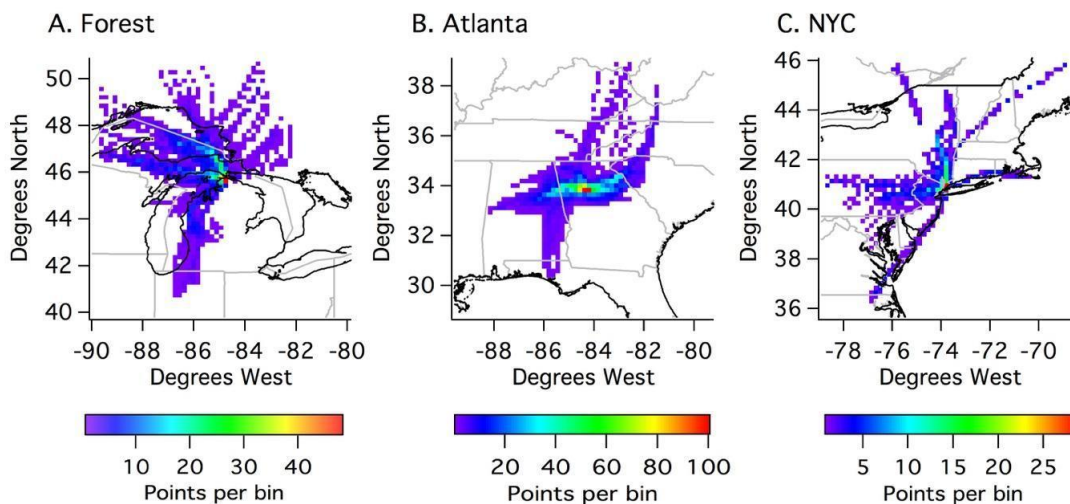


**Figure S25.** 24-hour backward trajectories for every hour corresponding to a filter sampling time period at each of the three field sites. Though there are some prevailing backward trajectories observed at each site, there is still significant diversity in air parcel path. Some difference in precursor emissions and meteorology along these paths is expected, with each path therefore contributing a diverse set of oxidized organic compounds to the sampling site.

To compute the percent similarity or difference between 2 backward trajectories, the number of bins populated by at least 1 point from both backward trajectories was tallied, and divided by the total number of populated latitude and longitude bins for each trajectory.

These bins were then all weighted by the number of points they contained to reduce the impact of bins with few trajectory points (i.e. where air parcels did not spend much time) and increase the impact of bins with many trajectory points (i.e. where air parcels may have stalled). Percentile values for the number of points per bin ( $n$ ) were defined, and bins were weighted according to the following, adapted from Polissar et al. and Gentner et al.: 1 ( $n \geq Q90$ ), 0.7 ( $n \geq Q75$ ), 0.42 ( $n \geq Q50$ ), 0.17 ( $n < Q50$ ).<sup>16,17</sup>

For each field campaign, all daytime samples were compared to each other, and all nighttime samples were compared to each other, with respect to both chemical composition and HYSPLIT backward trajectories. There is no observed correlation between dissimilar backward trajectories and chemical compositional variability (Figure S26,  $r=0.02$  to  $r=0.5$ ), suggesting that though air parcel history (including precursor emissions, associated chemical processing and meteorology) is important, it does not solely control OA compositional variability.

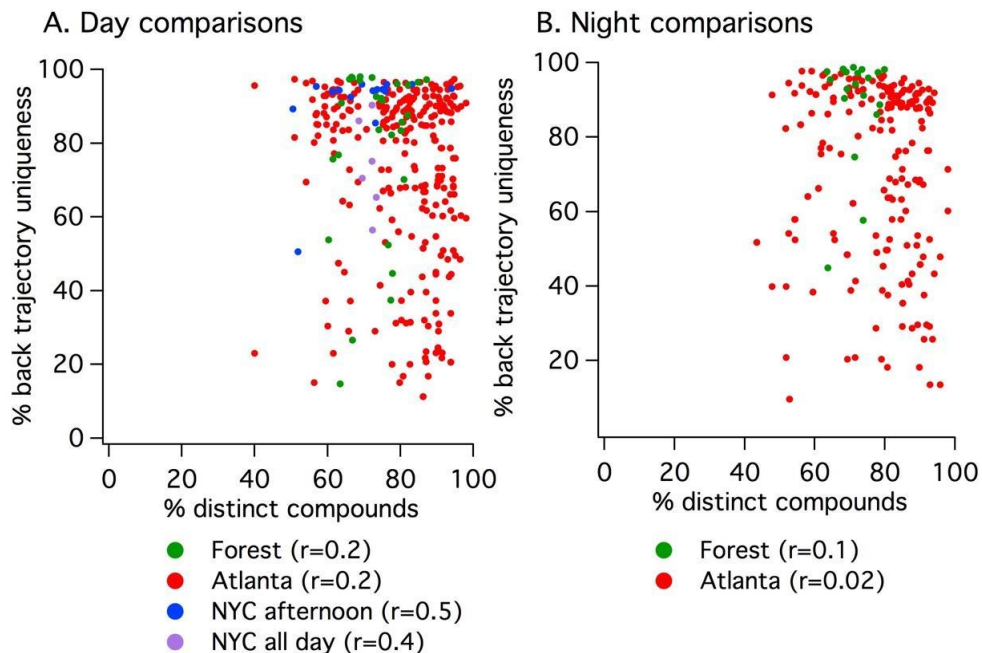


**Figure S26.** Correlation between backward trajectory uniqueness and chemical compositional variability for (A) all daytime and (B) nighttime sample-to-sample comparisons. There is no correlation between the chemical compositional variability observed between individual sample-to-sample comparisons and the degree of uniqueness of their backward trajectories ( $r=0.02-0.5$ ), though clustering of points at very high OA compositional variability and very high backward trajectory uniqueness does occur.

## References

1. Bateman, A. P., Laskin, J., Laskin, A. & Nizkorodov, S. A. Applications of High-Resolution Electrospray Ionization Mass Spectrometry to Measurements of Average Oxygen to Carbon Ratios in Secondary Organic Aerosols. *Environ. Sci. Technol.* **46**, 8315–8324 (2012).
2. Canagaratna, M. R. *et al.* Elemental ratio measurements of organic compounds using aerosol mass spectrometry: characterization, improved calibration, and implications. *Atmos. Chem. Phys.* **15**, 253–272 (2015).
3. Surratt, J. D. *et al.* Reactive intermediates revealed in secondary organic aerosol formation from isoprene. *Proc. Natl. Acad. Sci.* **107**, 6640–6645 (2010).
4. Zhang, X. *et al.* Formation and evolution of molecular products in  $\alpha$ -pinene secondary organic aerosol. *Proc. Natl. Acad. Sci.* **112**, 14168–14173 (2015).
5. Draper, D. C., Farmer, D. K., Desyaterik, Y. & Fry, J. L. A qualitative comparison of secondary organic aerosol yields and composition from ozonolysis of monoterpenes at varying concentrations of NO<sub>2</sub>. *Atmos. Chem. Phys.* **15**, 12267–12281 (2015).
6. Ehn, M. *et al.* Gas phase formation of extremely oxidized pinene reaction products in chamber and ambient air. *Atmos. Chem. Phys.* **12**, 5113–5127 (2012).

7. Al-Naiema, I. M. & Stone, E. A. Evaluation of anthropogenic secondary organic aerosol tracers from aromatic hydrocarbons. *Atmos. Chem. Phys.* **17**, 2053–2065 (2017).
8. Riva, M. *et al.* Gas- and Particle-Phase Products from the Chlorine-Initiated Oxidation of Polycyclic Aromatic Hydrocarbons. *J. Phys. Chem. A* **119**, 11170–11181 (2015).
9. Kautzman, K. E. *et al.* Chemical Composition of Gas- and Aerosol-Phase Products from the Photooxidation of Naphthalene. *J. Phys. Chem. A* **114**, 913–934 (2010).
10. Budisulistiorini, S. H. *et al.* Real-time Continuous Characterization of Secondary Organic Aerosol Derived from Isoprene Epoxydiols in Downtown Atlanta, Georgia, Using the Aerodyne Aerosol Chemical Speciation Monitor. *Environ. Sci. Technol.* **47**, 5686–5694 (2013).
11. Karambelas, A., Pye, H. O. T., Budisulistiorini, S. H., Surratt, J. D. & Pinder, R. W. Contribution of Isoprene Epoxydiol to Urban Organic Aerosol: Evidence from Modeling and Measurements. *Environ. Sci. Technol. Lett.* **1**, 278–283 (2014).
12. Jacobs, M. I., Darer, A. I. & Elrod, M. J. Rate constants and products of the OH reaction with isoprene-derived epoxides. *Environ. Sci. Technol.* **47**, 12868–12876 (2013).
13. Darer, A. I., Cole-Filipiak, N. C., O'Connor, A. E. & Elrod, M. J. Formation and stability of atmospherically relevant isoprene-derived organosulfates and organonitrates. *Environ. Sci. Technol.* **45**, 1895–1902 (2011).
14. Eddingsaas, N. C., Vandernelde, D. G. & Wennberg, P. O. Kinetics and products of the acid-catalyzed ring-opening of atmospherically relevant butyl epoxy alcohols. *J. Phys. Chem. A* **114**, 8106–8113 (2010).
15. Carlton, A. G., Wiedinmyer, C. & Kroll, J. H. A review of Secondary Organic Aerosol (SOA) formation from isoprene. *Atmos. Chem. Phys.* **9**, 4987–5005 (2009).
16. Polissar, A. V., Hopke, P. K. & Harris, J. M. Source Regions for Atmospheric Aerosol Measured at Barrow, Alaska. *Environ. Sci. Technol.* **35**, 4214–4226 (2001).
17. Gentner, D. R. *et al.* Emissions of organic carbon and methane from petroleum and dairy operations in California's San Joaquin Valley. *Atmos. Chem. Phys.* **14**, 4955–4978 (2014).

## REFERENCES

2016. Criteria air pollutants naaqs table.

Aljawhary, D., A. K. Y. Lee, J. P. D. Abbatt. 2013. High-resolution chemical ionization mass spectrometry (tof-cims): Application to study soa composition and processing. *Atmos. Meas. Tech.* 6:3211-3224. doi: 10.5194/amt-6-3211-2013.

Allan, D. W. 1966. Statistics of atomic frequency standards. *Proceedings of the Institute of Electrical and Electronics Engineers* 54:221-&. doi: 10.1109/proc.1966.4634.

Atlas, E. 1988. Evidence for  $\geq$  c 3 alkyl nitrates in rural and remote atmospheres. *Nature* 331:426-428. doi.

Bean, J. K. and L. Hildebrandt Ruiz. 2016. Gas-particle partitioning and hydrolysis of organic nitrates formed from the oxidation of alpha-pinene in environmental chamber experiments. *Atmos. Chem. Phys.* 16:2175-2184. doi: 10.5194/acp-16-2175-2016.

Beaver, M. R., J. M. S. Clair, F. Paulot, K. M. Spencer, J. D. Crouse, B. W. LaFranchi, K. E. Min, S. E. Pusede, P. J. Wooldridge, G. W. Schade, C. Park, R. C. Cohen, P. O. Wennberg. 2012. Importance of biogenic precursors to the budget of organic nitrates: Observations of multifunctional organic nitrates by cims and td-lif during bearpex 2009. *Atmos. Chem. Phys.* 12:5773-5785. doi: 10.5194/acp-12-5773-2012.

Bradshaw, J., S. Sandholm, R. Talbot. 1998. An update on reactive odd-nitrogen measurements made during recent nasa global tropospheric experiment programs. *J. Geophys. Res.-Atmos.* 103:19129-19148. doi: 10.1029/98jd00621.

Browne, E. C. and R. C. Cohen. 2012. Effects of biogenic nitrate chemistry on the nox lifetime in remote continental regions. *Atmos. Chem. Phys.* 12:11917-11932. doi: 10.5194/acp-12-11917-2012.

Buhr, M. P., D. D. Parrish, R. B. Norton, F. C. Fehsenfeld, R. E. Sievers, J. M. Roberts. 1990. Contribution of organic nitrates to the total reactive nitrogen budget at a rural eastern united-states site. *J. Geophys. Res.-Atmos.* 95:9809-9816. doi: 10.1029/JD095iD07p09809.

Carrington, R. 1960. The infra-red spectra of some organic nitrates. *Spectrochimica Acta* 16:1279-1293. doi.

- Chen, Y., M. Takeuchi, T. Nah, L. Xu, M. R. Canagaratna, H. Stark, K. Baumann, F. Canonaco, A. S. H. Prévôt, L. G. Huey, R. J. Weber, N. L. Ng. 2020. Chemical characterization of secondary organic aerosol at a rural site in the southeastern U.S.: Insights from simultaneous hr-tof-ams and figaero-cims measurements. *Atmos. Chem. Phys. Discuss.* 2020:1-40. doi: 10.5194/acp-2020-126.
- D'Anna, B., A. Wisthaler, O. Andreasen, A. Hansel, J. Hjorth, N. R. Jensen, C. J. Nielsen, Y. Stenstrom, J. Viidanoja. 2005. Atmospheric chemistry of c-3-c-6 cycloalkanecarbaldehydes. *J. Phys. Chem. A* 109:5104-5118. doi: 10.1021/jp044495g.
- Darley, E. F., K. A. Kettner, E. R. Stephens. 1963. Analysis of peroxyacyl nitrates by gas chromatography with electron capture detection. *Anal. Chem.* 35:589-591. doi.
- Day, D. A., M. B. Dillon, P. J. Wooldridge, J. A. Thornton, R. S. Rosen, E. C. Wood, R. C. Cohen. 2003. On alkyl nitrates, o-3, and the "missing noy". *J. Geophys. Res.-Atmos.* 108:10. doi: 10.1029/2003jd003685.
- Day, D. A., S. Liu, L. M. Russell, P. J. Ziemann. 2010. Organonitrate group concentrations in submicron particles with high nitrate and organic fractions in coastal southern California. *Atmos. Environ.* 44:1970-1979. doi: 10.1016/j.atmosenv.2010.02.045.
- Day, D. A., P. J. Wooldridge, M. B. Dillon, J. A. Thornton, R. C. Cohen. 2002. A thermal dissociation laser-induced fluorescence instrument for in situ detection of no<sub>2</sub>, peroxy nitrates, alkyl nitrates, and hno<sub>3</sub>. *J. Geophys. Res.-Atmos.* 107:14. doi: 10.1029/2001jd000779.
- Fahey, D. W., G. Hubler, D. D. Parrish, E. J. Williams, R. B. Norton, B. A. Ridley, H. B. Singh, S. C. Liu, F. C. Fehsenfeld. 1986. Reactive nitrogen species in the troposphere - measurements of no, no<sub>2</sub>, hno<sub>3</sub>, particulate nitrate, peroxyacetyl nitrate (pan), o-3, and total reactive odd nitrogen (noy) at Niwot Ridge, Colorado. *J. Geophys. Res.-Atmos.* 91:9781-9793. doi: 10.1029/JD091iD09p09781.
- Farmer, D. K., A. Matsunaga, K. S. Docherty, J. D. Surratt, J. H. Seinfeld, P. J. Ziemann, J. L. Jimenez. 2010. Response of an aerosol mass spectrometer to organonitrates and organosulfates and implications for atmospheric chemistry. *Proceedings of the National Academy of Sciences* 107:6670-6675. doi: 10.1073/pnas.0912340107.
- Fisher, J. A., D. J. Jacob, K. R. Travis, P. S. Kim, E. A. Marais, C. C. Miller, K. R. Yu, L. Zhu, R. M. Yantosca, M. P. Sulprizio, J. Q. Mao, P. O. Wennberg, J. D. Crouse, A. P. Teng, T. B. Nguyen, J. M. St Clair, R. C. Cohen, P. Romer, B. A. Nault, P. J. Wooldridge, J. L. Jimenez, P. Campuzano-Jost, D. A. Day, W. W. Hu, P. B. Shepson, F. L. Z. Xiong, D. R. Blake, A. H. Goldstein, P. K. Misztal, T. F. Hanisco, G. M. Wolfe, T. B. Ryerson, A. Wisthaler, T. Mikoviny. 2016. Organic nitrate chemistry and its implications for nitrogen budgets in an isoprene- and

- monoterpene-rich atmosphere: Constraints from aircraft (seac(4)rs) and ground-based (soas) observations in the southeast us. *Atmos. Chem. Phys.* 16:5969-5991. doi: 10.5194/acp-16-5969-2016.
- Flocke, F. M., A. J. Weinheimer, A. L. Swanson, J. M. Roberts, R. Schmitt, S. Shertz. 2005. On the measurement of pans by gas chromatography and electron capture detection. *J. Atmos. Chem.* 52:19-43. doi: 10.1007/s10874-005-6772-0.
- Fry, J. L., D. C. Draper, K. J. Zarzana, P. Campuzano-Jost, D. A. Day, J. L. Jimenez, S. S. Brown, R. C. Cohen, L. Kaser, A. Hansel, L. Cappellin, T. Karl, A. H. Roux, A. Turnipseed, C. Cantrell, B. L. Lefer, N. Grossberg. 2013. Observations of gas- and aerosol-phase organic nitrates at beachon-rombas 2011. *Atmos. Chem. Phys.* 13:8585-8605. doi: 10.5194/acp-13-8585-2013.
- Fry, J. L., A. Kiendler-Scharr, A. W. Rollins, P. J. Wooldridge, S. S. Brown, H. Fuchs, W. Dube, A. Mensah, M. dal Maso, R. Tillmann, H. P. Dorn, T. Brauers, R. C. Cohen. 2009. Organic nitrate and secondary organic aerosol yield from no<sub>3</sub> oxidation of beta-pinene evaluated using a gas-phase kinetics/aerosol partitioning model. *Atmos. Chem. Phys.* 9:1431-1449. doi: 10.5194/acp-9-1431-2009.
- Goldstein, A. H. and I. E. Galbally. 2007. Known and unexplored organic constituents in the earth's atmosphere. *Environ. Sci. Technol.* 41:1514-1521. doi: 10.1021/es072476p.
- Guenther, A., C. N. Hewitt, D. Erickson, R. Fall, C. Geron, T. Graedel, P. Harley, L. Klinger, M. Lerdau, W. A. McKay, T. Pierce, B. Scholes, R. Steinbrecher, R. Tallamraju, J. Taylor, P. Zimmerman. 1995. A global-model of natural volatile organic-compound emissions. *J. Geophys. Res.-Atmos.* 100:8873-8892. doi: 10.1029/94jd02950.
- Guenther, A. B., X. Jiang, C. L. Heald, T. Sakulyanontvittaya, T. Duhl, L. K. Emmons, X. Wang. 2012. The model of emissions of gases and aerosols from nature version 2.1 (megan2.1): An extended and updated framework for modeling biogenic emissions. *Geosci. Model Dev.* 5:1471-1492. doi: 10.5194/gmd-5-1471-2012.
- Hallquist, M., J. C. Wenger, U. Baltensperger, Y. Rudich, D. Simpson, M. Claeys, J. Dommen, N. M. Donahue, C. George, A. H. Goldstein, J. F. Hamilton, H. Herrmann, T. Hoffmann, Y. Iinuma, M. Jang, M. E. Jenkin, J. L. Jimenez, A. Kiendler-Scharr, W. Maenhaut, G. McFiggans, T. F. Mentel, A. Monod, A. S. H. Prevot, J. H. Seinfeld, J. D. Surratt, R. Szmigielski, J. Wildt. 2009. The formation, properties and impact of secondary organic aerosol: Current and emerging issues. *Atmos. Chem. Phys.* 9:5155-5236. doi.
- Hao, L. Q., A. Kortelainen, S. Romakkaniemi, H. Portin, A. Jaatinen, A. Leskinen, M. Komppula, P. Miettinen, D. Sueper, A. Pajunoja, J. N. Smith, K. E. J. Lehtinen, D.

- R. Worsnop, A. Laaksonen, A. Virtanen. 2014. Atmospheric submicron aerosol composition and particulate organic nitrate formation in a boreal forestland–urban mixed region. *Atmos. Chem. Phys.* 14:13483-13495. doi: 10.5194/acp-14-13483-2014.
- Hildebrandt, L., K. M. Henry, J. H. Kroll, D. R. Worsnop, S. N. Pandis, N. M. Donahue. 2011. Evaluating the mixing of organic aerosol components using high-resolution aerosol mass spectrometry. *Environ. Sci. Technol.* 45:6329-6335. doi: 10.1021/es200825g.
- Jayne, J. T., D. C. Leard, X. F. Zhang, P. Davidovits, K. A. Smith, C. E. Kolb, D. R. Worsnop. 2000. Development of an aerosol mass spectrometer for size and composition analysis of submicron particles. *Aerosol Sci. Technol.* 33:49-70. doi: 10.1080/027868200410840.
- Kanakidou, M., J. H. Seinfeld, S. N. Pandis, I. Barnes, F. J. Dentener, M. C. Facchini, R. Van Dingenen, B. Ervens, A. Nenes, C. J. Nielsen, E. Swietlicki, J. P. Putaud, Y. Balkanski, S. Fuzzi, J. Horth, G. K. Moortgat, R. Winterhalter, C. E. L. Myhre, K. Tsigaridis, E. Vignati, E. G. Stephanou, J. Wilson. 2005. Organic aerosol and global climate modelling: A review. *Atmos. Chem. Phys.* 5:1053-1123. doi: 10.5194/acp-5-1053-2005.
- Kastler, J. and K. Ballschmiter. 1998. Bifunctional alkyl nitrates - trace constituents of the atmosphere. *Fresenius J. Anal. Chem.* 360:812-816. doi: 10.1007/s002160050815.
- Kebabian, P. L., E. C. Wood, S. C. Herndon, A. Freedman. 2008. A practical alternative to chemiluminescence-based detection of nitrogen dioxide: Cavity attenuated phase shift spectroscopy. *Environ. Sci. Technol.* 42:6040-6045. doi: 10.1021/es703204j.
- Kiendler-Scharr, A., A. A. Mensah, E. Friese, D. Topping, E. Nemitz, A. S. H. Prevot, M. Aijala, J. Allan, F. Canonaco, M. Canagaratna, S. Carbone, M. Crippa, M. Dall'Osto, D. A. Day, P. De Carlo, C. F. Di Marco, H. Elbern, A. Eriksson, E. Freney, L. Hao, H. Herrmann, L. Hildebrandt, R. Hillamo, J. L. Jimenez, A. Laaksonen, G. McFiggans, C. Mohr, C. O'Dowd, R. Otjes, J. Ovadnevaite, S. N. Pandis, L. Poulain, P. Schlag, K. Sellegri, E. Swietlicki, P. Tiitta, A. Vermeulen, A. Wahner, D. Worsnop, H. C. Wu. 2016. Ubiquity of organic nitrates from nighttime chemistry in the European submicron aerosol. *Geophys. Res. Lett.* 43:7735-7744. doi: 10.1002/2016gl069239.
- Kirchner, F., A. Mayer-Figge, F. Zabel, K. H. Becker. 1999. Thermal stability of peroxy nitrates. *Int. J. Chem. Kinet.* 31:127-144. doi: 10.1002/(sici)1097-4601(1999)31:2<127::Aid-kin6>3.0.Co;2-l.
- Kwok, E. S. C., S. M. Aschmann, J. Arey, R. Atkinson. 1996. Product formation from the reaction of the NO<sub>3</sub> radical with isoprene and rate constants for the reactions of

methacrolein and methyl vinyl ketone with the  $\text{NO}_3$  radical. *Int. J. Chem. Kinet.* 28:925-934. doi.

- Lee, B. H., F. D. Lopez-Hilfiker, C. Mohr, T. Kurtén, D. R. Worsnop, J. A. Thornton. 2014. An iodide-adduct high-resolution time-of-flight chemical-ionization mass spectrometer: Application to atmospheric inorganic and organic compounds. *Environ. Sci. Technol.* 48:6309-6317. doi: 10.1021/es500362a.
- Lee, B. H., C. Mohr, F. D. Lopez-Hilfiker, A. Lutz, M. Hallquist, L. Lee, P. Romer, R. C. Cohen, S. Iyer, T. Kurten, W. W. Hu, D. A. Day, P. Campuzano-Jost, J. L. Jimenez, L. Xu, N. L. Ng, H. Y. Guo, R. J. Weber, R. J. Wild, S. S. Brown, A. Koss, J. de Gouw, K. Olson, A. H. Goldstein, R. Seco, S. Kim, K. McAvey, P. B. Shepson, T. Starn, K. Baumann, E. S. Edgerton, J. M. Liu, J. E. Shilling, D. O. Miller, W. Brune, S. Schobesberger, E. L. D'Ambro, J. A. Thornton. 2016. Highly functionalized organic nitrates in the southeast United States: Contribution to secondary organic aerosol and reactive nitrogen budgets. *Proc. Natl. Acad. Sci. U. S. A.* 113:1516-1521. doi: 10.1073/pnas.1508108113.
- Logan, J. A. 1983. Nitrogen-oxides in the troposphere - global and regional budgets. *J. Geophys. Res.-Oceans* 88:785-807. doi: 10.1029/JC088iC15p10785.
- Luxenhofer, O., M. Schneider, M. Dambach, K. Ballschmiter. 1996. Semivolatile long chain  $\text{C}_6\text{-C}_{17}$  alkyl nitrates as trace compounds in air. *Chemosphere* 33:393-404. doi: 10.1016/0045-6535(96)00205-6.
- Nah, T., J. Sanchez, C. M. Boyd, N. L. Ng. 2016. Photochemical aging of  $\alpha$ -pinene and  $\beta$ -pinene secondary organic aerosol formed from nitrate radical oxidation. *Environ. Sci. Technol.* 50:222-231. doi: 10.1021/acs.est.5b04594.
- Ng, N. L., S. S. Brown, A. T. Archibald, E. Atlas, R. C. Cohen, J. N. Crowley, D. A. Day, N. M. Donahue, J. L. Fry, H. Fuchs, R. J. Griffin, M. I. Guzman, H. Herrmann, A. Hodzic, Y. Iinuma, J. L. Jimenez, A. Kiendler-Scharr, B. H. Lee, D. J. Luecken, J. Q. Mao, R. McLaren, A. Mutzel, H. D. Osthoff, B. Ouyang, B. Picquet-Varrault, U. Platt, H. O. T. Pye, Y. Rudich, R. H. Schwantes, M. Shiraiwa, J. Stutz, J. A. Thornton, A. Tilgner, B. J. Williams, R. A. Zaveri. 2017. Nitrate radicals and biogenic volatile organic compounds: Oxidation, mechanisms, and organic aerosol. *Atmos. Chem. Phys.* 17:2103-2162. doi: 10.5194/acp-17-2103-2017.
- Niki, H., P. Maker, C. Savage, L. Breitenbach. 1978. FTIR spectroscopic observation of peroxyalkyl nitrates formed via  $\text{ROO}^+ + \text{NO}_2 \rightarrow \text{ROONO}_2$ . *Chemical Physics Letters* 55:289-292. doi.
- Paul, D., A. Furgeson, H. D. Osthoff. 2009. Measurements of total peroxy and alkyl nitrate abundances in laboratory-generated gas samples by thermal dissociation cavity ring-down spectroscopy. *Rev. Sci. Instrum.* 80:8. doi: 10.1063/1.3258204.

- Perring, A. E., S. E. Pusede, R. C. Cohen. 2013. An observational perspective on the atmospheric impacts of alkyl and multifunctional nitrates on ozone and secondary organic aerosol. *Chem. Rev.* 113:5848-5870. doi: 10.1021/cr300520x.
- Pinault. 2017. Estimates and 25-year trends of the global burden of disease attributable to ambient air pollution: An analysis of data from the global burden of diseases study 2015 (vol 389, pg 1907, 2016). *Lancet* 389:E15-E15. doi.
- Roberts, J. M. 1990. The atmospheric chemistry of organic nitrates. *Atmospheric Environment Part a-General Topics* 24:243-287. doi: 10.1016/0960-1686(90)90108-y.
- Robinson, A. L., N. M. Donahue, M. K. Shrivastava, E. A. Weitkamp, A. M. Sage, A. P. Grieshop, T. E. Lane, J. R. Pierce, S. N. Pandis. 2007. Rethinking organic aerosols: Semivolatile emissions and photochemical aging. *Science* 315:1259-1262. doi: 10.1126/science.1133061.
- Rollins, A. W., E. C. Browne, K. E. Min, S. E. Pusede, P. J. Wooldridge, D. R. Gentner, A. H. Goldstein, S. Liu, D. A. Day, L. M. Russell, R. C. Cohen. 2012. Evidence for nox control over nighttime soa formation. *Science* 337:1210-1212. doi: 10.1126/science.1221520.
- Rollins, A. W., J. L. Fry, A. Kiendler-Scharr, P. J. Wooldridge, S. S. Brown, H. Fuchs, W. P. Dube, A. Mensah, R. Tillmann, H. P. Dorn, T. Brauers, R. C. Cohen. 2009. Isoprene oxidation by nitrate radical: Alkyl nitrate and secondary organic aerosol yields. *Abstr. Pap. Am. Chem. Soc.* 237:288-288. doi.
- Rollins, A. W., S. Pusede, P. Wooldridge, K. E. Min, D. R. Gentner, A. H. Goldstein, S. Liu, D. A. Day, L. M. Russell, C. L. Rubitschun, J. D. Surratt, R. C. Cohen. 2013. Gas/particle partitioning of total alkyl nitrates observed with td-lif in bakersfield. *J. Geophys. Res.-Atmos.* 118:6651-6662. doi: 10.1002/jgrd.50522.
- Rollins, A. W., J. D. Smith, K. R. Wilson, R. C. Cohen. 2010. Real time in situ detection of organic nitrates in atmospheric aerosols. *Environ. Sci. Technol.* 44:5540-5545. doi: 10.1021/es100926x.
- Rubinstein, R. Y. and D. P. Kroese. 2016. *Simulation and the monte carlo method*: Wiley Publishing.
- Sadanaga, Y., R. Takaji, A. Ishiyama, K. Nakajima, A. Matsuki, H. Bandow. 2016. Thermal dissociation cavity attenuated phase shift spectroscopy for continuous measurement of total peroxy and organic nitrates in the clean atmosphere. *Rev. Sci. Instrum.* 87:6. doi: 10.1063/1.4958167.
- Sanchez, J., D. J. Tanner, D. X. Chen, L. G. Huey, N. L. Ng. 2016. A new technique for the direct detection of ho2 radicals using bromide chemical ionization mass

- spectrometry (br-cims): Initial characterization. *Atmos Meas Tech* 9:3851-3861. doi: 10.5194/amt-9-3851-2016.
- Schlag, P., A. Kiendler-Scharr, M. J. Blom, F. Canonaco, J. S. Henzing, M. Moerman, A. S. H. Prévôt, R. Holzinger. 2016. Aerosol source apportionment from 1-year measurements at the cesar tower in cabauw, the netherlands. *Atmos. Chem. Phys.* 16:8831-8847. doi: 10.5194/acp-16-8831-2016.
- Schneider, M., O. Luxenhofer, A. Deissler, K. Ballschmiter. 1998. C-1-c-15 alkyl nitrates, benzyl nitrate, and bifunctional nitrates: Measurements in california and south atlantic air and global comparison using c2cl4 and chbr3 as marker molecules. *Environ. Sci. Technol.* 32:3055-3062. doi: 10.1021/es980132g.
- Slusher, D. L., L. G. Huey, D. J. Tanner, F. M. Flocke, J. M. Roberts. 2004. A thermal dissociation-chemical ionization mass spectrometry (td-cims) technique for the simultaneous measurement of peroxyacyl nitrates and dinitrogen pentoxide. *J. Geophys. Res.-Atmos.* 109:13. doi: 10.1029/2004jd004670.
- Sparks, T. L., C. J. Ebben, P. J. Wooldridge, F. D. Lopez-Hilfiker, B. H. Lee, J. A. Thornton, E. E. McDuffie, D. L. Fibiger, S. S. Brown, D. D. Montzka, A. J. Weinheimer, J. C. Schroder, P. Campuzano-Jost, J. L. Jimenez, R. C. Cohen. 2019. Comparison of airborne reactive nitrogen measurements during winter. *J. Geophys. Res.-Atmos.* 124:10483-10502. doi: 10.1029/2019jd030700.
- Sun, Y. L., Q. Zhang, J. J. Schwab, T. Yang, N. L. Ng, K. L. Demerjian. 2012. Factor analysis of combined organic and inorganic aerosol mass spectra from high resolution aerosol mass spectrometer measurements. *Atmos. Chem. Phys.* 12:8537-8551. doi: 10.5194/acp-12-8537-2012.
- Takeuchi, M. and N. L. Ng. 2018. Organic nitrates and secondary organic aerosol (soa) formation from oxidation of biogenic volatile organic compounds, in *Multiphase environmental chemistry in the atmosphere*, 105-125: American Chemical Society.
- Takeuchi, M. and N. L. Ng. 2019. Chemical composition and hydrolysis of organic nitrate aerosol formed from hydroxyl and nitrate radical oxidation of  $\alpha$ -pinene and  $\beta$ -pinene. *Atmos. Chem. Phys.* 19:12749-12766. doi: 10.5194/acp-19-12749-2019.
- Thieser, J., G. Schuster, J. Schuladen, G. J. Phillips, A. Reiffs, U. Parchatka, D. Pöhler, J. Lelieveld, J. N. Crowley. 2016. A two-channel thermal dissociation cavity ring-down spectrometer for the detection of ambient no<sub>2</sub>, ro<sub>2</sub>no<sub>2</sub> and rono<sub>2</sub>. *Atmos. Meas. Tech.* 9:553-576. doi: 10.5194/amt-9-553-2016.
- Warneck, P. and T. Zerbach. 1992. Synthesis of peroxyacetyl nitrate in air by acetone photolysis. *Environ. Sci. Technol.* 26:74-79. doi: 10.1021/es00025a005.

- Womack, C. C., J. A. Neuman, P. R. Veres, S. J. Eilerman, C. A. Brock, Z. C. J. Decker, K. J. Zarzana, W. P. Dube, R. J. Wild, P. J. Wooldridge, R. C. Cohen, S. S. Brown. 2017. Evaluation of the accuracy of thermal dissociation crds and lif techniques for atmospheric measurement of reactive nitrogen species. *Atmos. Meas. Tech.* 10:1911-1926. doi: 10.5194/amt-10-1911-2017.
- Wooldridge, P. J., A. E. Perring, T. H. Bertram, F. M. Flocke, J. M. Roberts, H. B. Singh, L. G. Huey, J. A. Thornton, G. M. Wolfe, J. G. Murphy, J. L. Fry, A. W. Rollins, B. W. LaFranchi, R. C. Cohen. 2010a. Total peroxy nitrates ( $\sigma$ pns) in the atmosphere: The thermal dissociation-laser induced fluorescence (td-lif) technique and comparisons to speciated pan measurements. *Atmos. Meas. Tech.* 3:593-607. doi: 10.5194/amt-3-593-2010.
- Wooldridge, P. J., A. E. Perring, T. H. Bertram, F. M. Flocke, J. M. Roberts, H. B. Singh, L. G. Huey, J. A. Thornton, G. M. Wolfe, J. G. Murphy, J. L. Fry, A. W. Rollins, B. W. LaFranchi, R. C. Cohen. 2010b. Total peroxy nitrates ( $\sigma$ pns) in the atmosphere: The thermal dissociation-laser induced fluorescence (td-lif) technique and comparisons to speciated pan measurements. *Atmos. Meas. Tech.* 3:593-607. doi: 10.5194/amt-3-593-2010.
- Xu, L., H. Y. Guo, C. M. Boyd, M. Klein, A. Bougiatioti, K. M. Cerully, J. R. Hite, G. Isaacman-VanWertz, N. M. Kreisberg, C. Knote, K. Olson, A. Koss, A. H. Goldstein, S. V. Hering, J. de Gouw, K. Baumann, S. H. Lee, A. Nenes, R. J. Weber, N. L. Ng. 2015a. Effects of anthropogenic emissions on aerosol formation from isoprene and monoterpenes in the southeastern united states. *Proc. Natl. Acad. Sci. U. S. A.* 112:37-42. doi: 10.1073/pnas.1417609112.
- Xu, L., S. Suresh, H. Guo, R. J. Weber, N. L. Ng. 2015b. Aerosol characterization over the southeastern united states using high-resolution aerosol mass spectrometry: Spatial and seasonal variation of aerosol composition and sources with a focus on organic nitrates. *Atmos. Chem. Phys.* 15:7307-7336. doi: 10.5194/acp-15-7307-2015.
- Zhang, Q., J. L. Jimenez, M. R. Canagaratna, J. D. Allan, H. Coe, I. Ulbrich, M. R. Alfarra, A. Takami, A. M. Middlebrook, Y. L. Sun, K. Dzepina, E. Dunlea, K. Docherty, P. F. DeCarlo, D. Salcedo, T. Onasch, J. T. Jayne, T. Miyoshi, A. Shimono, S. Hatakeyama, N. Takegawa, Y. Kondo, J. Schneider, F. Drewnick, S. Borrmann, S. Weimer, K. Demerjian, P. Williams, K. Bower, R. Bahreini, L. Cottrell, R. J. Griffin, J. Rautiainen, J. Y. Sun, Y. M. Zhang, D. R. Worsnop. 2007. Ubiquity and dominance of oxygenated species in organic aerosols in anthropogenically-influenced northern hemisphere midlatitudes. *Geophys. Res. Lett.* 34:6. doi: 10.1029/2007gl029979.
- Zheng, W., F. M. Flocke, G. S. Tyndall, A. Swanson, J. J. Orlando, J. M. Roberts, L. G. Huey, D. J. Tanner. 2011. Characterization of a thermal decomposition chemical ionization mass spectrometer for the measurement of peroxy acyl nitrates (pans) in

the atmosphere. *Atmos. Chem. Phys.* 11:6529-6547. doi: 10.5194/acp-11-6529-2011.